

# **Nanoparticles for use in imaging, catalysis and phthalocyanine synthesis**

**Mogammad Luqmaan Samsodien**

---

**Supervisor: Professor E. Antunes**

**Co-Supervisors: Professor D. Beukes, Professor M. Meyer**



**UNIVERSITY *of the*  
WESTERN CAPE**

**A thesis submitted in conformity with the requirements  
for  
Master of Science in Nanoscience**

**Department of Biotechnology  
University of the Western Cape  
2018**

## DECLARATION

I declare that “**Application of nanoparticles for use in imaging, catalysis and phthalocyanine synthesis**” is my own work and has not in its entirety, or in part, been submitted for any degree or examination in any other university. All the resources that I have quoted have been indicated and fully acknowledged by complete references.

**Full Name: Mogamaad Luqmaan Samsodien**

**Date : 28/02/2018**

**Signed: MLS**



UNIVERSITY *of the*  
WESTERN CAPE

## Acknowledgements

- ❖ Firstly, I would like to thank GOD Almighty for bestowing blessings on me and guiding me over the course of this degree and throughout my life.
- ❖ I would like to thank my parents and grandparents for everything they have given me and for moulding me into the person I am today.
- ❖ I would like to give the biggest thank you to Professor Antunes and Professor Beukes, the two most knowledgeable people I have ever met, who have welcomed me into the research group with open arms. It's truly a privilege to be under the guidance of such great supervisors. Thank you for the kindness, patience and the knowledge passed on to me.
- ❖ Thank you to one of the nicest people I have met, Dr. Botha who was always ready to help me with the TEM samples. Everything she has done is very much appreciated.
- ❖ I would like to thank Dr. Bucher, Professor Kroon and Mr Lesch for running samples for me.
- ❖ I would like to thank the Marine Biodiscovery Research Group who has become my UWC family. Thank you for helping me and supporting me during this period.
- ❖ Thank you to all the friends I made during the course work period of the nanoscience program. Thank you for the memories made which I will never forget.
- ❖ Thank you to all the lecturers and staff who taught, helped and inspired me in the nanoscience programme
- ❖ Lastly, I would like to thank the University of the Western Cape and the National Nanoscience Postgraduate Teaching and Training Platform for giving me the opportunity to further my education.

## Abstract

Nanoscience and nanotechnology are known to be interdisciplinary, crossing and combining various fields and disciplines in pursuit of desirable outcomes. This has brought about applications of nanoscience and nanotechnology in multitudes of industries, spanning from the health, pharmaceutical to industrial industry. Within the health industry, the medical field has seen much advancement through nanoscience and nanotechnology. The importance of finding cures to diseases is top priorities within the medical field, along with advancements in understanding and diagnosing diseases. Due to these outcomes, we see the emergence of imaging techniques playing a crucial role. The work covered in this thesis looks at a prospective luminescent agent applicable in the medical field for bio-imaging, but also at a possible phthalocyanine sensitizer for treatment of cancer through photodynamic therapy. Another area where nanoscience and nanotechnology are found is in industry, where nanoparticles are utilised as catalysts in many synthetic reactions. Highly desirable catalysts in industry are those involved in oxidative reactions where we explore a metal nanoparticle catalyst within this work.

Upconversion nanoparticles have gained interest in medical bio-imaging, specifically those with properties having the ability to improve present day methods. The nanoparticles considered as luminescent contrast agents are those that use rare earth metals doped into a crystalline host to generate unique optical properties. The work in this thesis covers the synthesis of five different upconversion nanoparticles; namely NaYF<sub>4</sub>:Yb/Er; NaYF<sub>4</sub>:Yb/Ho; NaScF<sub>4</sub>:Yb/Er; LiYF<sub>4</sub>:Yb/Er and KYF<sub>4</sub>:Yb/Er; utilising a microwave solvothermal method. The nanoparticles were synthesized on a small as well as a larger scale where there were noticeable differences within the two sets of synthesized nanoparticles. This was observed in the TEM images with large amounts of agglomeration present. The XRD patterns of the nanoparticles matched crystalline structures of standard references relating to the cubic, tetragonal and monoclinic phase which were found for the nanoparticles with the NaYF<sub>4</sub>, KYF<sub>4</sub> and NaScF<sub>4</sub> host lattice, respectively. The LiYF<sub>4</sub> nanoparticles did not match any standard reference pattern found in literature.

The solid state NMR data showed broad powder like patterns for the <sup>23</sup>Na NMR spectra of the NaYF<sub>4</sub> UCNPs. The signals were distributed between 7 and -25 ppm, with maximum intensities at -18.4 ppm and a shoulder at -13.4 ppm as observed for all samples except the NaYF<sub>4</sub>:Yb/Er

small scale sample. This NaYF<sub>4</sub>:Yb/Er sample also showed two maximum intensity, sharp signals at -0.5 and -12.7 ppm. The powder pattern obtained for NaScF<sub>4</sub>:Yb/Er NPs small scale sample was different however, due to the contributions of the various parameters. Four possible sites were identified for the small scale sample with two main peaks and two apparent shoulders. In the steady state fluorescence spectra, the NaYF<sub>4</sub>:Yb/Er and NaScF<sub>4</sub>:Yb/Er nanoparticles showed three strong emission bands in the spectra corresponding to the green and red emission bands. Unlike any of the other samples, an additional strong emission band was observed for the NaScF sample centred at  $\lambda_{em} = 810$  nm. The transitions observed for the NaYF<sub>4</sub>:Yb/Er samples showed four emission bands at slightly different wavelengths correlating to green, red and NIR emission bands. The KYF and LiYF host nanoparticles gave almost no upconversion luminescence.

A phthalocyanine, 4-[4-(hydroxymethyl)phenyl] Zinc Phthalocyanine, was synthesized to evaluate its potential as a sensitizer for photodynamic therapy as well as utilise it as a catalyst support, with silver nanoparticles (NPs) imbedded on it. The spectroscopic and photophysical properties of the synthesized phthalocyanine and the catalyst were investigated. The extinction coefficient of the phthalocyanine in DMSO and DMF was found to have a log  $\epsilon$  of 4.88 and 4.75, respectively. The fluorescence quantum yield stokes shift and fluorescence lifetime for the phthalocyanine was found to be 0.34, 11 nm and 3.79 ns, respectively. The phthalocyanine imbedded silver nanoparticles were found to have fluorescence quantum yields, stokes shifts and fluorescence lifetimes of 0.30, 10 nm and 3.11 ns, respectively, showing only a slight difference caused by the presence of the silver nanoparticles. On the other hand, the effect of the NPs on the singlet oxygen generation ability in DMSO was more pronounced. A value of  $\Phi_{\Delta}$  1.17 was obtained for the Pc alone indicating the involvement of radicals (since the quantum yield was greater than 1), whereas the Pc supported AgNPs had a  $\Phi_{\Delta}$  of 0.67 indicating possible quenching by the NPs.

The catalytic ability of the synthesized catalysts was evaluated by the oxidative dehydrogenation coupling of aniline to produce an azobenzene. The catalysts were composed of silver nanoparticles (NPs) imbedded onto a support in the form of carbon or the synthesized phthalocyanine. The nanoparticles synthesized revealed an SPR band in the UV/Visible spectra

at 410 nm, with an average NP size of 10 - 12 nm. The XRD pattern for the silver nanoparticles matched perfectly with a face centred cubic crystal phase silver standard reference pattern. The azobenzene product was formed successfully, with heat being an important parameter in the successful production of azobenzene within the reaction.

**Keywords:** Nanoscience, nanotechnology, bio-imaging, upconversion nanoparticles, photodynamic therapy, phthalocyanines, catalysts and silver nanoparticles



UNIVERSITY *of the*  
WESTERN CAPE

# Table of Contents

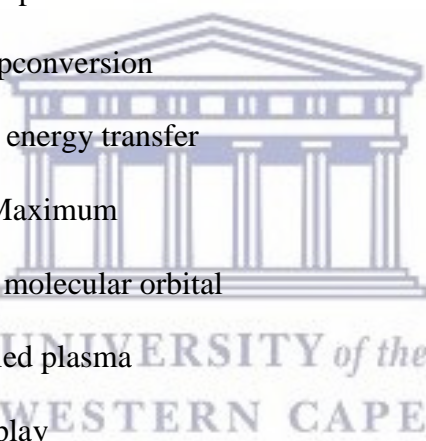
DECLARATION.....	I
ACKNOWLEDGEMENTS .....	II
ABSTRACT.....	III
TABLE OF CONTENTS .....	VI
LIST OF ABBREVIATIONS.....	IX
LIST OF SYMBOLS .....	XI
LIST OF FIGURES .....	XIII
LIST OF SCHEMES .....	XXIII
LIST OF TABLES.....	XXV
<b>CHAPTER 1: INTRODUCTION.....</b>	<b>1</b>
1.1 NANOTECHNOLOGY .....	1
1.2 PART A: .....	2
1.2.1. UPCONVERSION NANOPARTICLES.....	2
1.3 PART B: .....	2
1.3.1 SILVER NANOPARTICLES AS CATALYSTS .....	2
1.3.2. PHTHALOCYANINES .....	3
1.4 AIMS, OBJECTIVES AND HYPOTHESES OF THE STUDY.....	3
1.4.1 <i>Aims</i> .....	3
1.4.2 <i>Objectives</i> .....	4
1.4.3 <i>Hypotheses</i> .....	4
1.5 RESEARCH QUESTIONS .....	5
1.6 THESIS OUTLINE .....	5
<b>CHAPTER 2: LITERATURE REVIEW .....</b>	<b>7</b>
2.1 NANOSCIENCE AND NANOTECHNOLOGY .....	7
2.2 APPLICATIONS OF NANOPARTICLES AND NANOTECHNOLOGY IN THE MEDICAL FIELD .....	8
2.3. PART A: .....	10
2.3.1 FLUORESCENCE.....	10
2.3.2 FLUOROPHORES .....	12
2.3.2.1 <i>Inorganic fluorophores</i> .....	14
2.3.2.2 <i>Upconversion</i> .....	16
2.4. PART B:.....	28
2.4.1 PHTHALOCYANINES .....	28
2.4.1.1 <i>Phthalocyanine synthesis</i> .....	30
2.4.1.2 <i>Absorbance properties of phthalocyanines</i> .....	34
2.4.1.3 <i>Fluorescence quantum yield and lifetimes</i> .....	35
2.4.1.4 <i>Singlet oxygen production within phthalocyanines</i> .....	37
2.4.1.6 <i>Phthalocyanine applications</i> .....	42
2.4.2 NANOPARTICLES AS CATALYSTS .....	45
2.4.2.1 <i>Silver nanoparticles</i> .....	46

2.4.2.2 Silver nanoparticle synthesis .....	47
2.4.2.3 Applications of silver nanoparticles .....	49
2.5 CHARACTERIZATION OF NANOPARTICLES AND COMPOUNDS SYNTHESIZED .....	51
2.5.1 TRANSMISSION ELECTRON MICROSCOPY .....	52
2.5.2 X-RAY POWDER DIFFRACTION .....	53
2.5.3 UV/VISIBLE SPECTROSCOPY .....	54
2.5.4 FOURIER TRANSFORM-INFRARED SPECTROSCOPY .....	54
2.5.5 NUCLEAR MAGNETIC RESONANCE SPECTROSCOPY .....	55
2.5.6 MASS SPECTROSCOPY .....	57
2.5.7 INDUCTIVELY COUPLED PLASMA SPECTROSCOPY .....	58
<b>CHAPTER 3: MATERIALS AND METHODS .....</b>	<b>59</b>
3.1 MATERIALS .....	59
3.2 INSTRUMENTATION .....	59
3.2.1 NMR .....	59
3.2.2 XRD .....	60
3.2.3 UV/Visible spectroscopy .....	60
3.2.4 FT-IR spectroscopy .....	61
3.2.5 TEM .....	61
3.2.6 ICP-AES .....	61
3.2.7 Mass spectroscopy .....	62
3.2.8 Fluorescence spectroscopy .....	62
3.2.9 Microwave setup .....	63
3.2.10 Elemental analysis .....	63
3.2.11 Singlet oxygen quantum yields $\Phi_{\Delta}$ .....	63
3.3 METHODS .....	64
3.3.1 Phthalocyanine synthesis .....	64
3.3.1.1 Synthesis of 4-[4-(hydroxymethyl)phenyl] phthalonitrile .....	64
3.3.1.2 Preparation of phthalocyanines .....	65
3.3.1.2.1 Synthesis of zinc phthalocyanine (complex 4) .....	65
3.3.1.2.2 Synthesis of 4-[4-(hydroxymethyl)phenyl] Zinc Phthalocyanine (complex 5) .....	66
3.3.1.3 Synthesis of silver nanoparticles .....	67
3.3.1.3.1 Preparation of silver nanoparticles (6) .....	67
3.3.1.3.2 Preparation of AgNPs/C (7) and AgNPs/Pc (8) as modified supports .....	67
3.3.1.4 Synthesis of upconversion nanoparticles .....	68
3.3.2 Fluorescence quantum yield and lifetime determinations .....	70
3.3.3 Singlet oxygen quantum yield determinations for phthalocyanine (5) and the Pc supported AgNPs (8) .....	71
3.3.4 Catalytic reactions .....	71
3.3.4.1 Catalytic reactions utilising AgNPs/C (7) .....	71
<b>PART A: .....</b>	<b>72</b>
<b>CHAPTER 4: UPCONVERSION NANOPARTICLES .....</b>	<b>72</b>
4.1 SYNTHESIS OF THE UPCONVERSION NANOPARTICLES .....	72
4.2 CHARACTERIZATION OF THE UCNPs .....	75

4.2.1 Transmission electron microscopy (TEM) and Energy Dispersive X – Ray Spectroscopy (EDX).....	75
4.2.2 X-ray powder diffraction (PXRD).....	82
4.2.3 Solid State NMR.....	89
4.2.4 Steady state fluorescence spectroscopy .....	94
4.2.4 Summary and Conclusion .....	100
<b>PART B:.....</b>	<b>102</b>
<b>CHAPTER 5: SYNTHESIS AND CHARACTERISATION OF MPCs AND THE MODIFIED NP SUPPORT.....</b>	<b>102</b>
5.1 SYNTHESIS AND CHARACTERIZATION OF MPCs .....	102
5.1.1 Synthesis and characterisation of ZnPc (4) standard.....	102
5.1.2 Synthesis and characterisation of 4-(4-hydroxymethyl)phthalocyanine Zn(II) (HMPZnPc) (5).....	104
5.1.2.1 Synthesis and characterisation of phthalonitrile precursor 4-(4-hydroxymethyl)-phthalonitrile (3).....	104
5.1.2.2 Synthesis and characterisation of HMPZnPc (5) .....	111
5.2 GROUND STATE ABSORPTION SPECTRA OF MPCs AND MODIFIED AGNPs/PC (8) SUPPORT. 113	
5.3 CHARACTERISATION OF AGNPs (6) AND THE AGNP SUPPORTS (7) AND AGNPs/PC (8) ....	116
5.4 PHOTOPHYSICAL CHARACTERIZATION OF MPCs AND MODIFIED AGNPs/PC SUPPORT (8). 120	
5.4.1 Extinction coefficient determination .....	121
5.4.2 Fluorescence quantum yield and lifetimes.....	124
5.4.3 Singlet Oxygen quantum yield ( $\Phi_{\Delta}$ ).....	125
5.4.4 Summary and conclusions.....	128
<b>CHAPTER 6: CATALYTIC REACTIONS.....</b>	<b>129</b>
6.1 INTRODUCTION.....	129
6.2 AZOBENZENE CATALYTIC REACTIONS .....	129
6.3 SUMMARY AND CONCLUSION.....	134
<b>CHAPTER 7: CONCLUSION AND FUTURE PROSPECTS.....</b>	<b>135</b>
<b>APPENDIX.....</b>	<b>137</b>

## List of abbreviations

ADMA	anthracene-9,10-diyl-bis-methylmalonate
AgNPs	silver nanoparticles
CR	cross relaxation
CSU	cooperative sensitization upconversion
DBU	1,8-diazabicyclo[5,4,0]undec-7-ene
DMAE	<i>N,N</i> -dimethylaminoethanol
DPBF	diphenylisobenzofuran
ESA	excited-state absorption
ETU	energy transfer upconversion
FRET	Forster resonance energy transfer
FWHM	Full Width Half Maximum
HOMO	highest occupied molecular orbital
ICP	inductively coupled plasma
LCD	liquid crystal display
LRET	luminescence resonance energy transfer
LUMO	lowest unoccupied molecular orbital
MALDI-TOF	matrix-assisted laser desorption ionization-time of time of flight
MS	mass spectroscopy
MB	methylene blue
MPc	metal phthalocyanine
NIR	near infrared
NMR	nuclear magnetic resonance

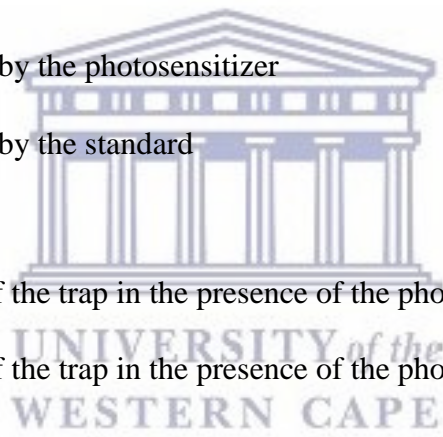


OPV	organic solar/voltaic cells
PA	photon avalanche
Pc	phthalocyanine
PDT	photodynamic therapy
PL	photoluminescence
PS	photosensitizer
SPPR	surface plasmon polariton resonances
SPR	surface plasmon resonance
TEM	transmission electron microscope
UC	upconversion
UCNPs	upconversion nanoparticles
XRD	X-ray diffraction



## List of symbols

$\Phi_{\Delta}$	singlet oxygen quantum yield
$\Phi_{\Delta}^{\text{Std}}$	singlet oxygen quantum yield of the standard
$c$	speed of light
$E$	energy
E1	energy level 1
E2	energy level 2
G	ground level
$h$	Plank's constant
$I_{\text{abs}}$	rate of light absorbance by the photosensitizer
$I_{\text{abs}}^{\text{Std}}$	rate of light absorbance by the standard
$^1\text{O}_2$	singlet oxygen
R	photodegradation rate of the trap in the presence of the photosensitizer
$R^{\text{Std}}$	photodegradation rate of the trap in the presence of the photosensitizer and standard respectively
$S_0$	ground state
$S_1$	first excited state
$S_n$	$n^{\text{th}}$ (2, 3 etc.) excited states
$T_1$	first triplet state ( $T_1$ )
$\lambda$	wavelength of photon
$\Phi_{\text{F}}$	fluorescence quantum yield
$\Phi_{\text{Std}}$	fluorescence quantum yield of the standard
F	area under the fluorescence emission curve for the sample



$F_{Std}$  area under the fluorescence emission curve for the standard

$A_{Std}$  rate of light absorbance by the standard

$A$  rate of light absorbance by the sample

$\eta_{Std}^2$  the refractive indices of the standard

$\eta^2$  the refractive indices of the sample

$\tau_F$  fluorescence lifetimes

$\tau_0$  natural radiative lifetimes

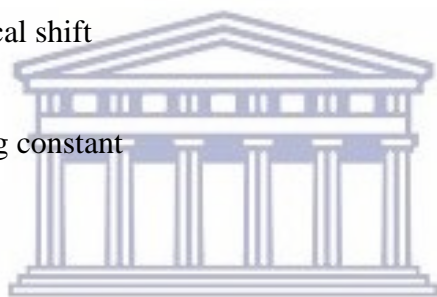
$\delta_{CG}$  peak position or center of gravity

$\delta_{iso}$  the true isotropic chemical shift

$C_Q$  the quadrupolar coupling constant

$\nu_0$  Larmor frequency

$\eta_Q$  the asymmetry parameter of the quadrupolar coupling tensor



UNIVERSITY of the  
WESTERN CAPE

## List of Figures

**Figure 2.1:** Jablonski diagram illustrating the excited states of a molecule and various levels within each state (Lichtman and Conchello 2009).

**Page no. 12**

**Figure 2.2:** Jablonski diagram illustrating the emission processes a molecule during fluorescence or phosphorescence with reference to a time scale of the different processes (Lichtman and Conchello, 2009).

**Page no. 14**

**Figure 2.3:** Upconversion processes for lanthanide-doped upconversion nanoparticles (Chen *et al.*, 2014).

**Page no. 17**

**Figure 2.4:** Illustration of a cross section of core/shell upconversion nanoparticle (Chen *et al.*, 2014).

**Page no. 20**

**Figure 2.5:** Upconversion Mechanism of the Lanthanide UCNPs doped with (a) Yb<sup>3+</sup> and Er<sup>3+</sup>, (b) Yb<sup>3+</sup> and Tm<sup>3+</sup>, or (c) Yb<sup>3+</sup> and Ho<sup>3+</sup> (Zhou *et al.*, 2015).

**Page no. 23**

**Figure 2.6:** Numbering system of the Metallated Phthalocyanine showing the covalent and partial bonds between the central metal and the nitrogen atoms and (b)  $\alpha$  and  $\beta$  positions on the di hydrogen Phthalocyanine.

**Page no. 29**

**Figure 2.7:** Possible synthesis routes of symmetrical Phthalocyanines through several 1,2-disubstituted benzene species (Kadish *et al.*, 2003).

**Page no. 31**

**Figure 2.8:** Schematic illustration of the statistical condensation which involves the use of two differently substituted phthalonitriles to produce a mixture of Pc six compounds (Kadish *et al.*, 2003).

**Page no. 33**

**Figure 2.9:** Absorption spectra of the metallated phthalocyanine (red line) and unmetallated phthalocyanine (blue line) (Kadish *et al.*, 2003).

**Page no. 34**

**Figure 2.10:** (a) The electronic transitions of the B band as well as the Q band electronic transition for metallated phthalocyanines (b) Q band electronic transitions for the two peaks found in the unmetallated phthalocyanine (Kadish *et al.*, 2003).

**Page no. 35**

**Figure 2.11:** Schematic Jablonski's diagram showing PDT's mechanism of action. Following light absorption, the PS reaches an excited singlet state. After an intersystem crossing, the PS, now in a triplet excited state, can react in two ways: react with biomolecules through a hydrogen atom (electron) transfer to form radicals, which react with molecular oxygen to generate ROS (type I reaction); or, the PS in its triplet state can react directly with oxygen through energy transfer, generating singlet oxygen (Type II reaction) (Calixto *et al.*, 2016).

**Page no. 39**

**Figure 2.12:** Various applications of phthalocyanines (Sakamoto and Ohno-Okumura, 2009).

**Page no. 42**

**Figure 2.13:** Various applications of silver nanoparticles (Keat *et al.*, 2015).

**Page no. 50**

**Figure 3.1:** Singlet oxygen set up (Kuznetsova *et al.*, 2000).

**Page no. 64**

**Figure 4.1:** The mechanism of action for the upconversion nanoparticle synthesis. (Mi *et al.*, 2011).

**Page no. 74**

**Figure 4.2:** TEM images obtained for the (A -C) NaYF<sub>4</sub>:Yb/Er ss, (D - F) NaYF<sub>4</sub>:Yb/Ho us, (G - I) NaScY<sub>2</sub>:Yb/Er ss UCNP samples.

**Page no. 76 - 77**

**Figure 4.3:** TEM images obtained for the (A - C) KYF<sub>4</sub>:Yb/Er ss and (D - F) LiYF<sub>4</sub>:Yb/Er ss UCNP samples.

**Page no. 78**

**Figure 4.4:** Representative TEM-EDX spectra of A) NaYF<sub>4</sub>:Yb/Er us, B) NaYF<sub>4</sub>:Yb/Ho ss, C) NaScF<sub>4</sub>:Yb/Er ss, D) LiY<sub>x</sub>F<sub>y</sub>:Yb/Er us and E) KY<sub>x</sub>F<sub>y</sub>:Yb/Er us UCNPs.

**Page no. 79 - 81**

**Figure 4.5:** The XRD powder patterns obtained for the samples containing the NaYF<sub>4</sub> crystal lattice, together with the corresponding reference data from JCPDS, indicating that all four samples are mainly cubic phase.

**Page no. 83**

**Figure 4.6:** The XRD powder patterns obtained for the samples containing the NaScF<sub>4</sub> crystal lattice, together with the pattern for NaYF<sub>4</sub>:Yb/Er ss and, for comparison, the reference data from JCPDS for cubic (JCPDS No. 77-2042) and hexagonal (JCPDS No.28-1192) phases for the NaYF<sub>4</sub> crystal lattice (Zeng *et al.*, 2013).

**Page no. 85**

**Figure 4.7:** The XRD powder patterns obtained for the samples containing the  $\text{LiY}_x\text{F}_y$  crystal lattice, together with the pattern for  $\text{NaYF}_4:\text{Yb}/\text{Er}$  ss and, for comparison, the reference data from JCPDS for the  $\text{NaYF}_4$  cubic (JCPDS No. 77-2042) and  $\text{LiYF}_4$  (JCPDS No. 81-2254) phases (Gao *et al.*, 2014).

**Page no. 86**

**Figure 4.8:** The XRD powder patterns obtained for the samples containing the  $\text{KY}_x\text{F}_y$  crystal lattice, together with the pattern for  $\text{NaYF}_4:\text{Yb}/\text{Er}$  ss and, for comparison, the reference data from JCPDS for the  $\text{KYF}_4$  and  $\text{KY}_3\text{F}_{10}$  patterns (Mahalingam *et al.*, 2009).

**Page no. 88**

**Figure 4.9:**  $^{23}\text{Na}$  MAS NMR spectra obtained at a spinning speed of 11 kHz for the  $\text{NaYF}_4$  nanoparticles at 11.7 T. The parameters obtained for these spectra are listed in Table 6.2. \*indicate spinning side bands.

**Page no. 90**

**Figure 4.10:**  $^{23}\text{Na}$  MAS NMR spectra of  $\text{NaYF}_4$  nanoparticles at 21.1 T (900 MHz) (A) undoped, (B) doped with 1 mol %  $\text{Er}^{3+}$ , (C) doped with 2 mol %  $\text{Er}^{3+}$  as reported by Arnold *et al.* (2013).

**Page no. 91**

**Figure 4.11:**  $^{23}\text{Na}$  MAS NMR spectra obtained at a spinning speed of 11 kHz for the  $\text{NaYF}_4:\text{Yb}/\text{Er}$  NPs as a comparison and for the  $\text{NaScF}_4:\text{Yb}/\text{Er}$  us nanoparticles at 11.7 T. Spectra for the  $\text{NaScF}_4:\text{Yb}/\text{Er}$  ss sample was also obtained but subsequently lost due to hardware issues. The parameters obtained for these spectra are listed in Table 6.2. \*indicate spinning side bands.

**Page no. 92**

**Figure 4.12:**  $^{45}\text{Sc}$  MAS NMR spectra obtained at various spinning speeds i.e. 6, 7 and 10 kHz for the  $\text{NaScF}_4:\text{Yb}/\text{Er}$  NPs us as a comparison and for the  $\text{NaScF}_4:\text{Yb}/\text{Er}$  us nanoparticles at 11.7 T.

**Page no. 94**

**Figure 4.13:** Upconversion luminescence spectra for the NaYF<sub>4</sub>:Yb/Er and NaScF<sub>4</sub>:Yb/Er UCNPs under 980 nm laser excitation.

**Page no. 96**

**Figure 4.14:** Upconversion luminescence spectra for the NaYF<sub>4</sub>:Yb/Ho and NaYF<sub>4</sub>:Yb/Er UCNPs under 980 nm laser excitation.

**Page no. 97**

**Figure 4.15:** Upconversion luminescence spectra for the KY<sub>x</sub>F<sub>y</sub>:Yb/Er and LiY<sub>x</sub>F<sub>y</sub>:Yb/Er UCNP powder samples under 980 nm laser excitation.

**Page no. 98**

**Figure 4.16:** Upconversion luminescence spectra for the NaScF<sub>4</sub>:Yb/Er UCNP sample, in powder form as well as in ethanol and water, under 980 nm laser excitation. The graph is plotted on a logarithmic scale.

**Page no. 99**

**Figure 5.1:** A) The UV/Visible spectrum of the ZnPc in DMSO and B) the FTIR spectrum of the ZnPc.

**Page no. 103**

**Figure 5.2:** <sup>1</sup>H NMR (400 MHz) data acquired at 298K for A) 4-iodophthalonitrile (**1**, in CDCl<sub>3</sub>), B) phthalonitrile product (**3**, in CDCl<sub>3</sub>), C) phthalonitrile product (**3**, in DMSO-*d*<sub>6</sub>) and D) 4-(hydroxymethyl)phenyl boronic acid (**4**, in DMSO-*d*<sub>6</sub>).

**Page no. 106**

**Figure 5.3:** <sup>13</sup>C NMR (400 MHz) data acquired at 298K for A) 4-iodophthalonitrile (**1**, in CDCl<sub>3</sub>), B) phthalonitrile product (**3**, in CDCl<sub>3</sub>), C) phthalonitrile product (**3**, in DMSO-*d*<sub>6</sub>) and D) 4-(hydroxymethyl)phenyl boronic acid (**4**, in DMSO-*d*<sub>6</sub>).

**Page no. 108**

**Figure 5.4:** HMBC spectrum acquired on a 400 MHz NMR instrument at 298 K in DMSO-*d*<sub>6</sub>. Key correlations observed for compound **3** are shown.

**Page no. 109**

**Figure 5.5:** Important HMBC correlations observed for compound **3**.

**Page no. 109**

**Figure 5.6:** FTIR spectra of 4-(4-hydroxymethyl)phenyl-phthalonitrile (**3**).

**Page no. 111**

**Figure 5.7:** <sup>1</sup>H NMR (400 MHz) spectrum acquired for complex **5** (HMPZnPc) in DMSO-*d*<sub>6</sub> at 323 K with water presaturation.

**Page no. 112**

**Figure 5.8:** FTIR spectra of the synthesized phthalocyanine (**5**).

**Page no. 113**

**Figure 5.9:** The spectra of the phthalocyanine (**5**) in different polar solvents which also show the slight shifting of the Q and B bands in the various solvents.

**Page no. 114**

**Figure 5.10:** Absorption (A) and emission (B) spectra of the MPcs (**4** and **5**) and the AgNPs/Pc (**8**) in DMSO to enable comparison.

**Page no. 115**

**Figure 5.11:** The synthesis of silver nanoparticles with oleylamine capping agent (Abbas *et al.*, 2012).

**Page no. 116**

**Figure 5.12:** Spectra and images obtained for the synthesized silver nanoparticles. A) The UV/Visible spectra of the AgNPs in hexane; B) EDX spectra for the AgNPs; and C – D) the TEM images of the synthesized silver nanoparticles and E) histogram illustrating the size distribution of the silver nanoparticles.

**Page no. 117 - 118**

**Figure 5.13:** The XRD powder patterns obtained for silver nanoparticles on carbon and the phthalocyanine together with the standard reference pattern of silver (JCPDS 00-004-0783). A) AgNPs on carbon (**7**); B) AgNPs on the phthalocyanine (**8**); C) Standard reference pattern of silver (JCPDS 00-004-0783), and D) the standard reference pattern for ZnO (JCPDS 36-1451).

**Page no. 119 - 120**

**Figure 5.14:** UV/Visible spectra (A) of a series of dilutions of complex **5** over a concentration range of  $1.30 \times 10^{-5}$  M to  $7.54 \times 10^{-6}$  M in DMSO. The linear behaviour of the absorbance vs concentration for the complex **5** at 690 nm, 606 nm and 348 nm was determined with the gradient used to calculate the extinction coefficient at each point.

**Page no. 122**

**Figure 5.15:** UV/Visible spectra (A) of a series of dilutions of complex **5** over a concentration range of  $2.00 \times 10^{-5}$  M to  $1.16 \times 10^{-6}$  M in DMF. (B) The linear behaviour of the absorbance vs concentration for the complex **5** at 684 nm, 604 nm and 350 nm was determined with the gradient used to calculate the extinction coefficient at each point.

**Page no. 123**

**Figure 5.16:** The absorbance and emission spectra for A) synthesized ZnPc (**4**), B) the HMPZnPc (**5**) and (C) the AgNPs/Pc (**8**) in DMSO.  $\lambda_{exc} = 615\text{nm}$ .

**Page no. 124**

**Figure 5.17:** UV/Visible spectra for the determination of singlet oxygen quantum yields ( $\Phi_{\Delta}$ ) in DMSO using complex **5**.

**Page no. 126**

**Figure 5.18:** UV/Visible spectra for the determination of singlet oxygen quantum yields ( $\Phi_{\Delta}$ ) in DMSO using the AgNPs/Pc (**8**) catalyst.

**Page no. 127**

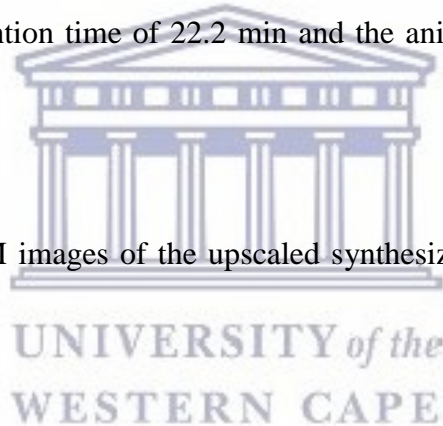
**Figure 6.1:** GC-MS results obtained for the standard catalytic reaction (Table 6.1, reaction 1) of aniline using AgNPs/C (**7**). A) Shows the total ion chromatogram (TIC) of the product and B) shows the mass spectrum of the peak at 22.2 min, indicating successful formation of the azobenzene.

**Page no. 131**

**Figure 6.2:** TICs obtained for the various catalytic reactions where parameters are changed (Table 6.1) for A) reaction 2. B) reaction 3. C) reaction 4. D) reaction 5. E) reaction 6. The azobenzene product has a retention time of 22.2 min and the aniline starting material retention time is at 12.1 min.

**Page no. 133**

**Figure A4.1:** A - C) The TEM images of the upscaled synthesized NaYF:Yb/Er upconversion nanoparticles.



**Page no. 137**

**Figure A4.2:** A - C) The TEM images of the upscaled synthesized NaYF:Yb/Ho upconversion nanoparticles.

**Page no. 137**

**Figure A4.3:** A - C) The TEM images of the synthesized NaScF<sub>4</sub>:Yb/Er upconversion nanoparticles.

**Page no. 138**

**Figure A4.4:** A - C) The TEM images of the upscaled synthesized LiY<sub>x</sub>F<sub>y</sub>:Yb/Er upconversion nanoparticles.

**Page no. 138**

**Figure A4.5:** A - C) The TEM images of the upscaled synthesized  $KY_xF_y:Yb/Er$  upconversion nanoparticles.

**Page no. 139**

**Figure A4.6:** The EDX of the small scale synthesized  $NaYF_4:Yb/Er$  upconversion nanoparticles.

**Page no. 139**

**Figure A4.7:** The EDX of the upscaled synthesized  $NaYF_4:Yb/Ho$  upconversion nanoparticles.

**Page no. 140**

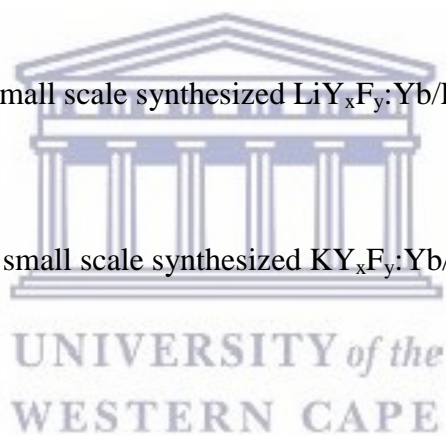
**Figure A4.8:** The EDX of the upscaled synthesized  $NaScF_4:Yb/Er$  upconversion nanoparticles.

**Page no. 140**

**Figure A4.9:** The EDX of the small scale synthesized  $LiY_xF_y:Yb/Er$  upconversion nanoparticles.

**Page no. 141**

**Figure A4.10:** The EDX of the small scale synthesized  $KY_xF_y:Yb/Er$  upconversion nanoparticles.



**Page no. 141**

**Figure A4.11:** The XRD powder patterns obtained for the samples synthesized in this work showing the true intensities of the reflections obtained.

**Page no. 142**

**Figure A4.12:** Upconversion luminescence spectra for all powdered UCNPs under 980 nm laser excitation. The graph is on a log-scale which enables small peaks to be identified.

**Page no. 143**

**Figure A4.13:** (A) Upconversion luminescence emission spectra of the  $KY_3F_{10}:Yb/Er$  nanoparticles synthesized in the powder form and the relevant transitions. (B) Logarithmic scaled emission spectra of the nanoparticles synthesized in the powder form.

**Page no. 144**

**Figure A4.14:** (A) Upconversion luminescence emission spectra of the  $LiY_xF_y:Yb/Er$  nanoparticles synthesized in the powder form and the relevant transitions. (B) Logarithmic scaled emission spectra of the nanoparticles synthesized in the powder form.

**Page no. 145**

**Figure A5.1:** COSY spectra of 4-(4-hydroxymethyl)-phthalonitrile (**3**).

**Page no. 147**

**Figure A5.2:** HSQC spectra of 4-(4-hydroxymethyl)-phthalonitrile (**3**).

**Page no. 148**

**Figure A5.3:** DEPT-135 spectra of 4-(4-hydroxymethyl)-phthalonitrile (**3**).

**Page no. 149**

**Figure A5.4:** UV/Visible spectra for the determination of the  $R^{Std}$  in DMSO using the standard ZnPc, (complex **4**).

**Page no. 149**

**Figure A6.1:** GC-EI MS chromatograms obtained for the catalyst reactions yielding the azobenzene molecular ion. The TICs illustrating the azobenzene molecular ion at the 22 minute time frame with a peak at  $182 m/z$  in A) reaction 3, B) reaction 4 and C) with the reaction 6.

**Page no. 151**

## List of schemes

**Scheme 3.1:** Illustration of the Suzuki coupling reaction of 4-iodophthalonitrile and (hydroxymethyl)phenylboronic acid.

**Page no. 64**

**Scheme 3.2:** Zinc phthalocyanine (4) synthesis using the unmetallated phthalocyanine product and zinc acetate as the metal source.

**Page no. 65**

**Scheme 3.3:** Phthalocyanine (5) synthesis using the Suzuki coupling phthalocyanine product, DBU and zinc acetate.

**Page no. 66**

**Scheme 3.4:** Illustration of the azobenzene catalytic reaction.

**Page no. 71**

**Scheme 4.1:** Possible UC emission mechanisms for A) NaYF<sub>4</sub>:Yb/Er and NaScF<sub>4</sub>:Yb/Er UCNPs and B) NaYF<sub>4</sub>:Yb/Ho UCNPs under 980 nm laser excitation.

**Page no. 96**

**Scheme 6.1:** Mechanism for Ag NPs-catalyzed oxidative coupling of aniline as proposed by Cai *et al.* (2013).

**Page no. 130**

**Scheme A5.1:** Illustration of correlating protons found within the COSY spectra (400 MHz, DMSO-*d*<sub>6</sub>, 298 K).

**Page no. 146**

**Scheme A5.2:** Illustration of correlating protons to the respective carbons found within the HSQC spectra (400 MHz, DMSO- $d_6$ , 298 K).

**Page no. 147**



UNIVERSITY *of the*  
WESTERN CAPE

## List of tables

**Table 3.1:** The reagents, moles and masses utilized for each of the synthesis of upconversion nanoparticles on a small scale (ss) or large (us).

**Page no. 69**

**Table 3.2:** The yields obtained for each of the different UCNP samples.

**Page no. 70**

**Table 4.1:** Particle size of the UCNPs as extracted from the TEM images as well as those calculated based on the Debye-Scherrer equation (equation 2.6) from XRD

**Page no. 78**

**Table 4.2:** Isotopic Chemical Shifts  $\delta_{\text{iso}}$  (ppm), Quadrupolar Coupling Constants ( $C_Q$ , MHz) and Asymmetry ( $\eta$ ) parameters as extracted from  $^{23}\text{Na}$  and  $^{45}\text{Sc}$  one-dimensional NMR Spectra for the various upconversion nanoparticles

**Page no. 93**

**Table 5.1:**  $^1\text{H}$ ,  $^{13}\text{C}$ , HSQC, COSY and HMBC data acquired for 4-(4-hydroxymethyl)phthalonitrile (**3**) at 400 MHz in  $\text{DMSO-}d_6$  at 298K. The correlations observed in the 2D spectra for the various proton signals.

**Page no. 110**

**Table 5.2:** Absorption and photophysical data obtained for complexes **4** and **5** as well as the ZnPc (**4**) standard.

**Page no. 121**

**Table 5.3:** Log  $\epsilon$  determinations for complex **5** in DMSO and DMF

**Page no. 121**

**Table 6.1:** Catalytic reaction conditions with varied parameters and product formation

**Page no. 131**

# Chapter 1: Introduction

This chapter serves as a summary of the work undertaken in the thesis, providing insight into the different research aspects which are detailed more extensively in the ensuing chapters. This chapter will include important topics such as nanotechnology, upconversion nanoparticles, the use of silver nanoparticles as a catalyst and phthalocyanines; all of which are the topics around which the thesis is built. The thesis is thus divided into two parts: Part A will cover upconversion nanoparticles, while Part B will cover the section on silver nanoparticles and phthalocyanines. There will also be some information which aims to clarify the rationale and motivation of the research undertaken.

## 1.1 Nanotechnology

The research area of nanotechnology is interdisciplinary, covering a wide variety of subjects ranging from chemistry, physics to biology, and within each discipline, we find the emergence of different types of nanoparticles (Whitesides, 2005). For example, in chemistry, structures such as buckytubes, silicon nanorods, and semiconductor quantum dots have emerged as particularly interesting classes of nanostructures. In biology, the usage of nanocarriers in the form of biodegradable liposomes and solid lipid nanoparticles are found. In physics, nanoscience is often associated with quantum behavior and the behavior of electrons and photons in nanoscale structures (Whitesides, 2005; Poole and Owens, 2006).

A nanometer is described as a billionth of a meter and hence nanotechnology is attributed to the application of particles less than 100 nanometers in size that display new chemistry and physics, leading to new properties and behavior which relates to their size (Whitesides, 2005; Brechignac *et al.*, 2006). For example, the electronic structure, conductivity, reactivity, melting temperature, and mechanical properties have all been observed to change when particles become smaller than a critical size, displaying new properties and behavior compared to the bulk state of the particle (Whitesides, 2005; Poole and Owens, 2006). There are two methods associated with regards to the production of nanoparticles, namely the bottom-up approach and the top-down approach (Brechignac *et al.*, 2006). In the former, one assembles atoms and molecules into structures, and

from there, an increase in the size of the structure. In the latter, one considers the change in the properties of a sample as its size is whittled down from the macroscopic toward nanometric lengths (Brechignac *et al.*, 2006).

## **1.2 Part A:**

### **1.2.1. Upconversion nanoparticles**

The medical field has become a prominent area where the interdisciplinary aspects of nanotechnology are witnessed (Davis *et al.*, 2008), where nanoparticles are used in various disciplines such as drug delivery and medical bio-imaging, to name a few. Upconversion nanoparticles (UCNPs) have gained great interest in medical bio-imaging specifically, since they possess properties and have the ability to improve present day methods. The nanoparticles are considered as luminescent agents that use rare earth metals doped into a crystalline host to generate unique optical properties (Gainer and Romanowski 2014). They have the ability to convert near-infrared (NIR) excitation to tuneable shorter-wavelength luminescence and have other favourable outcomes including their ability to overcome many of the problems associated with more traditionally used luminescent agents, such as photobleaching, auto fluorescence, cytotoxicity and phototoxicity (Li *et al.*, 2008). For these reasons, UCNPs have attracted a great deal of attention from researchers due to their unique properties including tunable multicolor emission, photo stability, deep tissue penetration and low *in vitro* and *in vivo* toxicity (Li *et al.* 2008).

## **1.3 Part B:**

### **1.3.1 Silver nanoparticles as catalysts**

Another use of nanotechnology comes in the form of catalysts which are present and active in many parts of industry. Metal nanoparticles have been attracting much attention, not only for its catalytic ability but also the possibility of these catalysts being produced using chemical synthetic procedures which are clean, nontoxic and environmentally acceptable i.e. “green chemistry” methods (Jiang *et al.*, 2005; Evanoff and Chumanov, 2005). There is evidence that metal nanoparticles have high catalytic activities for hydrogenation, hydroformylation,

carbonylation, olefin polymerization, desulfurization, ammonia synthesis and oxidation (Jiang *et al.*, 2005; Evanoff and Chumanov, 2005). Metal nanoparticles also have unique optical, electrical and thermal properties which allows their application in various fields (Kelly *et al.*, 2003). Their optical properties specifically, attract a lot of attention, especially for silver nanoparticles (AgNPs) (Kelly *et al.*, 2003). This optical property results from the collective oscillations of conduction electrons, due to excitation by electromagnetic radiation, is called surface plasmon polariton resonances (SPPR) or surface plasmon resonance (SPR). The SPPR band appears at around 400 nm for spherical silver nanoparticles in the UV/Visible absorption spectrum.

### **1.3.2. Phthalocyanines**

The catalytic properties of nanoparticles can also be utilised in the synthesis of phthalocyanines (Pcs) which are molecules that have found use in the medical field for photodynamic therapy. Photodynamic therapy is a clinical treatment that utilizes photosensitizers to produce singlet oxygen that can oxidize critical cellular macromolecules, including lipids, nucleic acids, and amino acids (Guo *et al.*, 2010). This leads to cellular permeability alterations with the consequence of cell death by necrosis or apoptosis, or both, in diseased cells (Guo *et al.*, 2010). There are many photosensitizers to choose from, with the choice of photosensitizer being critical for successful treatment (Calixto *et al.*, 2016). One such group of photosensitizers that can produce singlet oxygen is the phthalocyanines which are a family of aromatic macrocycles based on an extensive delocalized two-dimensional 18 pi-electron system that exhibit many unique properties (Torres *et al.*, 1998). They are highly stable and versatile compounds, capable of including various metallic and non-metallic ions in the ring cavity (Torres *et al.*, 1998). Phthalocyanines are found to be exceptionally stable to acids, alkalies, moisture, heat, light and solvent, and they generally only decompose by pyrolysis at or above 500°C (Engel *et al.*, 1997; Sekkat *et al.*, 2012).

## **1.4 Aims, objectives and hypotheses of the study**

### **1.4.1 Aims**

- To synthesize five different upconversion nanoparticles and assess their ability to produce UV/Visible emissions from NIR light excitation.

- To synthesize a phthalocyanine and assess its spectroscopic and photophysical properties.
- To synthesize silver nanoparticles on a carbon support and a phthalocyanine support and assess their catalytic abilities.

#### 1.4.2 Objectives

- Synthesize five different upconversion nanoparticles, on a small and large scale, each with a different host lattice or dopant.
- Characterize the upconversion nanoparticles using XRD, TEM and solid state NMR, taking note of the differences produced depending on the scale of the synthesis.
- Obtain the fluorescence emission spectra of the large scale synthesis upconversion nanoparticles.
- Synthesize and characterize a zinc phthalocyanine analogue.
- Synthesize silver nanoparticles and imbed the silver nanoparticles on a carbon or phthalocyanine support to create the catalyst.
- Characterize the silver nanoparticles using TEM, XRD and UV/Visible spectroscopy.
- Determine the amount of silver imbedded on carbon and the phthalocyanine using ICP-AES.
- Determine the spectroscopic and photophysical properties of the phthalocyanine and the silver nanoparticles imbedded on the phthalocyanine.
- Determine the catalytic abilities of the AgNPs imbedded on carbon or Pc support using the oxidative dehydrogenation coupling of anilines for azobenzenes.

#### 1.4.3 Hypotheses

- Upconversion nanoparticles with different host lattices and dopants can each convert NIR light into UV/Visible emission, where their efficiency of upconversion may differ due to their composition.
- The silver nanoparticles imbedded on the phthalocyanine may alter the Pc's spectroscopic and photophysical properties.

- A silver metal nanoparticle imbedded on carbon support will enable aniline coupling for azobenzene synthesis through oxidative dehydrogenation.

## 1.5 Research Questions

- Can upconversion nanoparticles with different host lattices and dopants each convert NIR light to higher energy UV/Visible emissions?
- What are the photophysical properties of the phthalocyanine and will silver nanoparticles imbedded in the phthalocyanine alter the Pc's photophysical properties?
- Will a silver metal nanoparticle imbedded on the carbon or Pc catalyst successfully be able to couple anilines for azobenzene synthesis through oxidative dehydrogenation by producing oxygen?

## 1.6 Thesis Outline

### Chapter 1

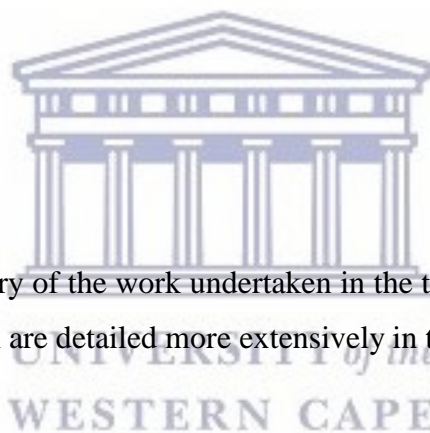
This chapter serves as a summary of the work undertaken in the thesis, providing insight into the different research aspects which are detailed more extensively in the ensuing chapters.

### Chapter 2

This chapter encompasses the literature dealing with the relevant topics associated with the research such as Nanoscience and Nanotechnology, Applications of Nanotechnology in the medical field, Fluorescence, Phthalocyanines, Nanoparticles as catalysts and Characterisation of nanoparticles as well as their respective sub-headings.

### Chapter 3

This chapter includes all the necessary Materials and Methods as well as equipment involved in the research.



## Chapter 4

This chapter encompasses the synthesis of the upconversion nanoparticles and the analysis of the different characterization techniques.

## Chapter 5

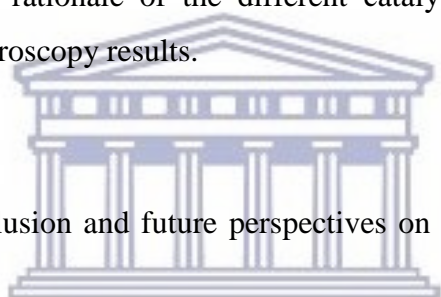
This chapter includes the spectroscopic and photophysical characterisation of the precursors used in the Pc synthesis, the phthalocyanine itself, silver nanoparticles as well as the results obtained for the silver nanoparticles imbedded with the phthalocyanine.

## Chapter 6

This chapter encompasses the rationale of the different catalytic reactions run with altered parameters and their mass spectroscopy results.

## Chapter 7

This chapter includes the conclusion and future perspectives on the research carried out in the thesis



UNIVERSITY *of the*  
WESTERN CAPE

## Chapter 2: Literature Review

### 2.1 Nanoscience and nanotechnology

Across history we find events that led to discoveries having such a great impact that it proved to be the turning points in life. There is a possibility that history is repeating itself and we are witnessing “something” which could revolutionize not one but various disciplines within science (Poole and Owens, 2006). This “something” appears in the form of nanotechnology and in recent years has brought about advancements in fields such as physics, chemistry, engineering and biology (Poole and Owens, 2006). It shows great promise for providing us with many breakthroughs that will change the direction of technology in a wide range of applications (Poole and Owens, 2006). Although this surge of nanotechnology within the scientific world has occurred recently, it is not clear when humans first began to take advantage of nano-sized materials. It is known that in the fourth-century A.D., Roman glassmakers were fabricating glasses containing nano-sized metals where an artifact from this period called the Lycurgus cup resides in the British Museum in London. This cup is found to be made from soda lime glass containing silver and gold nanoparticles. (Poole and Owens, 2006).

Nanotechnology only received recognition of such artifacts centuries later and was spearheaded on into existence with the help of a man by the name of Richard Feynman. Although a scientist, his help did not come in the form of scientific contributions to the field of nanotechnology but through a lecture which is now popular amongst nanotechnology researchers as one scientist commented, “it was so visionary that it did not connect with people until the technology caught up with it” (Poole and Owens, 2006). Richard Feynman was awarded the Nobel Prize in physics in 1965 for his contributions to quantum electrodynamics (Poole and Owens, 2006). In 1960, he presented a visionary and prophetic lecture at a meeting of the American Physical Society, entitled “There is Plenty of Room at the Bottom,” where he speculated on the possibility and potential of nano-sized materials. He envisioned many scientific scenarios which would later on become true and change the direction of science. (Poole and Owens, 2006).

The term “nano” is responsible for the definition ascribed to nanotechnology, with regards to size in meters (Whitesides, 2005). A nanometer is described as a billionth of a meter and hence we attribute nanotechnology to the application of particles less than the size of 100 nanometers that display new chemistry and physics, leading to new properties and behavior relating to their size (Whitesides, 2005; Poole and Owens, 2006). For example, the electronic structure, conductivity, reactivity, melting temperature, and mechanical properties have all been observed to change when particles become smaller than a critical size, displaying new properties and behavior compared to the bulk state of the particle (Whitesides, 2005). There are two methods associated with regards to producing nanoparticles, namely the bottom-up approach and the top-down approach (Brechignac *et al.*, 2006). In the bottom-up approach, one assembles atoms and molecules into structures, which then increase the size of the structure. The relevant parameter becomes the size rather than the exact number of atoms contained in the structure. In the top-down approach, one considers the change of the properties of a sample as its size is whittled down from macroscopic toward nanometric lengths. The dependence of the behavior on the particle sizes can allow one to engineer their properties (Brechignac *et al.*, 2006).

## **2.2 Applications of nanoparticles and nanotechnology in the medical field**

The research area of nanotechnology is interdisciplinary covering a wide variety of subjects ranging from the chemistry of nano-sized catalysts, the physics of the quantum dot laser, to DNA, subcellular organelles and gap junctions all of which are considered as biological nanostructures (Whitesides, 2005). As a result, researchers in any one particular area needs to reach beyond their expertise in order to appreciate the broader implications of nanotechnology (Whitesides, 2005). Within each discipline we find the emergence of different types of nanoparticles (Whitesides, 2005). For example, in chemistry structures such as buckytubes, silicon nanorods, and semiconductor quantum dots have emerged as particularly interesting classes of nanostructures. In biology, we find the usage of nanocarriers in the form of biodegradable liposomes and solid lipid nanoparticles. In physics, nanoscience is most often associated with quantum behavior, and the behavior of electrons and photons in nanoscale structures. (Whitesides, 2005).

The medical field has become a prominent area where the interdisciplinary aspects of nanotechnology is witnessed (Davis *et al.*, 2008). Drug delivery systems for therapeutic use in cancer treatment would include biologically stable nanoparticles and the therapeutic entities. (Davis *et al.*, 2008). The incorporated therapeutic entities are situated either on the surface or inside the nanoparticle with such nanoparticles having shown enhanced anticancer effects, compared to the therapeutic entities alone, *via* improved pharmacokinetics and pharmacodynamics, and active intracellular delivery (Davis *et al.*, 2008).

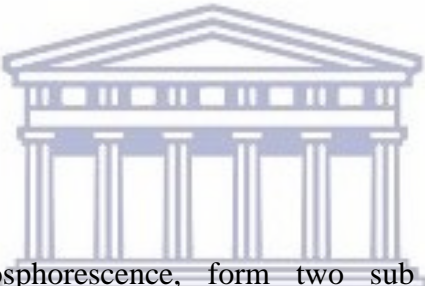
Drug delivery is not the “end of the road” when it comes to nanotechnology in this field. There is an interesting concept which looks to integrate imaging and therapy into a single platform called theranostics (Chen *et al.*, 2014). Incorporation of therapeutic functions into imaging contrast agents is the end goal of theranostics (Chen *et al.*, 2014). The therapeutic aspect of theranostics would include drug delivery strategies utilizing nanoparticles where the actual release mechanism of therapeutic entities or therapy itself can be light-activated such as photodynamic therapy (PDT) (Chen *et al.*, 2014). This form of treatment requires a photosensitizer (PS) that is administered and activated by a light of a specific wavelength, which causes selective damage to surrounding cells (Calixto *et al.*, 2016). An issue arises when selecting a photosensitizer, as UV and visible light, which is needed to activate the photosensitizers, has a low penetration depth in biological tissues therefore acting as a limiting factor to its therapeutic use (Calixto *et al.*, 2016). In this regard, nanotechnology provides a possible solution in the form of upconversion nanoparticles (UCNPs). UCNPs converts near infrared light into UV and visible light (Chen *et al.*, 2014). This is ideal as near infrared light is low energy and has better penetration of biological tissue. It therefore is not a limiting factor to the use of photosensitizers (Chen *et al.*, 2014). Taking into consideration that UCNPs are fluorescent nanoparticles they could also fulfill the role required for imaging within theranostics as it overcomes many of the problems associated with more traditionally used luminescent contrast agents, such as photobleaching, auto fluorescence, cytotoxicity and phototoxicity (Chen *et al.*, 2014).

Fluorescent nanoparticles show great potential in many disciplines, especially in conjunction with photoluminescence (PL) spectroscopy. This specific partnership has been directed towards medical diagnostics where nanoparticles with fluorescent properties are being applied in tissue

imaging (Liu *et al.*, 2013) and fluorescence sensing (Li *et al.*, 2011). Diagnostics utilizing photoluminescence (PL) spectroscopy became an important technique in scientific disciplines such as biochemistry and molecular biology (Chen *et al.*, 2014). It then evolved and developed into the more dominant methods which revolutionized medical diagnostics, bioassays, DNA sequencing, and genomics (Chen *et al.*, 2014). It is still currently in use today in order for scientists to study a wide range of biological specimens, from cells to *in vivo* tissue samples, and to *in vivo* imaging of live objects; it can also cover a broad range of length scale, from sub micrometer-sized bacteria, to macroscopic-sized live biological species (Chen *et al.*, 2014). Thus, PL imaging has provided a powerful noninvasive tool to visualize morphological details in tissue with subcellular resolution and, with the use of fluorescent nanoparticles, there is a possibility to improve the efficiency of our current methods- even replacing them (Chen *et al.*, 2014).

## 2.3. Part A:

### 2.3.1 Fluorescence



Fluorescence along with phosphorescence, form two sub categories within the term photoluminescence (Valeur, 2001). The definition of photoluminescence can be broken down into two parts, namely “photo” and “luminescence”. Luminescence is defined as the emission of ultraviolet, visible or infrared photons from an electronically excited species. There are various types of luminescence, with the method of excitation usually defining the type of luminescence found. In photoluminescence, excitation is obtained through the absorbance of photons and it is for this reason the term “photo” is used (Valeur, 2001). In order to differentiate between the two sub categories within photoluminescence, a closer look at the spin multiplicity of each sub-category with regards to their decay processes which occur *via* the loss of photons is warranted (Lakowicz, 1999). Spin multiplicity refers to “the number of possible orientations, calculated as  $2S + 1$ , of the spin angular momentum corresponding to a given total spin quantum number  $S$ ” (Braslavsky, 2006). In the process of fluorescence, emissions generally originate from the lowest vibrational level of the lowest excited state (Lakowicz, 1999). After the excitation of a molecule, the spin multiplicity in fluorescence is retained as the electrons drop to the ground state (Lakowicz, 1999). In phosphorescence, emission occurs from the first triplet state ( $T_1$ )

(Lakowicz, 1999). After the excitation of a molecule, the spin multiplicity undergoes a spin conversion as the electrons drop to the first triplet state ( $T_1$ ) called intersystem crossing (Lakowicz, 1999). The transition from  $T_1$  to the ground state involves a transition between states of different multiplicities that requires an electronic spin flip, which is quantum mechanically forbidden, and only occurs as a result of spin orbit coupling (Lakowicz, 1999).

The processes that emerge when photons are absorbed and emitted can be described by the Jablonski diagram which is a good tool to use in understanding how photoluminescence occurs (Lakowicz, 1999). The Jablonski diagram can be seen as a universal one, although different forms of the diagrams exist, illustrating various molecular processes which can occur in excited states (Lakowicz, 1999). The outlay of the diagram includes the annotations  $S_0$ ,  $S_1$  and  $S_n$  representing the ground state, first excited state and  $n^{\text{th}}$  (2, 3 etc.) excited states respectively.  $S_0$  is the ground state and represents the energy of a molecule that is not being excited by photons.  $S_1$  and  $S_n$  are excited singlet states in which an outer electron is boosted into a different orbital.  $S_n$  contains more energy than  $S_1$  and  $S_1$  more energy than the ground state. Each electronic state also encompasses several smaller vibrational states (Valeur, 2001; Lakowicz, 1999). Absorption of a photon results in the promotion of an electron occupying a lower state, to a higher excited state. Absorption usually occurs from the lowest vibrational level of the ground state to another vibrational level of a higher excited state (Lakowicz, 1999). The higher probability of electron occupancy of the lowest vibrational level of the ground state is predicted by the Boltzmann distribution (Lakowicz, 1999). Figure 2.1, pg. 12 displays the excited states and associated energy transfer processes of the two spin multiplicities which exist for neutral organic molecules. For singlet states, the total spin is equal to 0 while for triplet states, 2 unpaired electrons with parallel spins result in a total spin of 1. These states maintain the paired  $+\frac{1}{2}$  and  $-\frac{1}{2}$  spin states of the electrons, with each electron in a pair having opposite spins (Braslavsky, 2006).

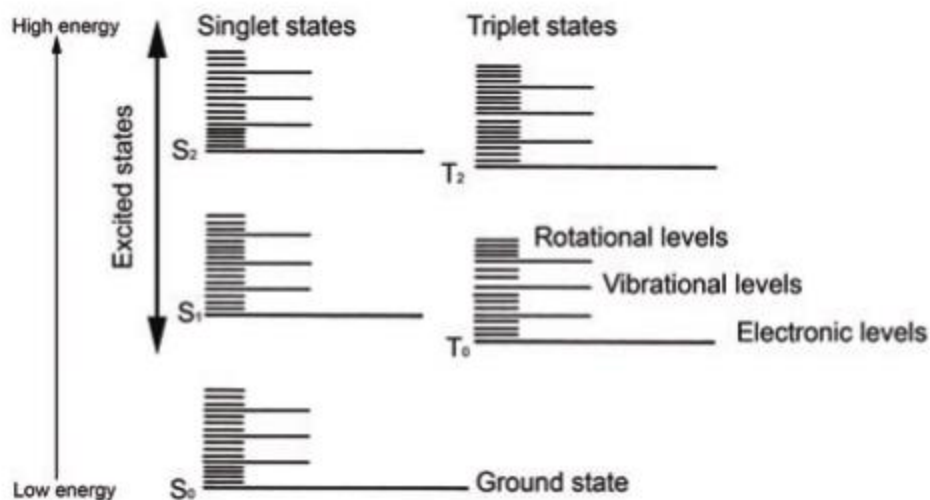


**Figure 2.1:** Jablonski diagram illustrating the excited states of a molecule and various levels within each state (Lichtman and Conchello 2009).

## 2.3.2 Fluorophores

A fluorophore is a term used for naming molecules which possess fluorescent properties (Lichtman and Conchello, 2009). The absorption and emission wavelengths and fluorescent efficiency are determined by the outermost electrons fluorophore molecule (Lichtman and Conchello, 2009). The absorption of photons allows the movement of an electron into a different orbital farther away from the nucleus. This transition to an excited state occurs within femtoseconds after the absorption of photons. The absorbed energy is eventually released through vibrational relaxation and fluorescence emission, which are the main ways a fluorophore returns to its low-energy ground state (Lichtman and Conchello, 2009). During the absorption of photons, all the energy possessed by a photon is transferred to the fluorophore. This energy is inversely related to the photon's wavelength and can be described by Equation 2.1:

$$E = h \times c / \lambda \quad (2.1)$$

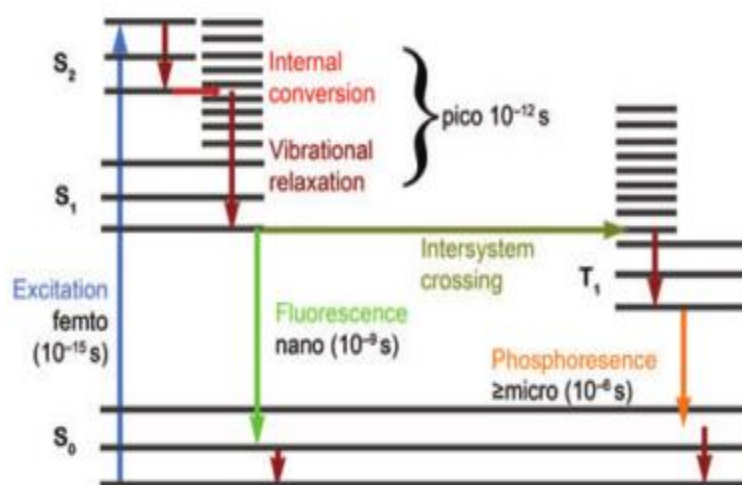
where  $h$  is Plank's constant and  $c$  and  $\lambda$  are the speed of light and wavelength of photon, respectively (Lichtman and Conchello, 2009). If the absorbed photon's energy is larger than the

energy needed to transition from the ground state to the lowest energy level of  $S_1$ , the molecule will move into an even higher electronic orbital with or without undergoing changes in vibration or rotation (Lichtman and Conchello, 2009). The transition of an electron from  $S_0$  to  $S_1$  is known as the minimum amount of energy a molecule needed for fluorescence. It is also possible for multiple photons to combine their energy to bring a molecule to the excited state. This can occur when two photons with half the energy of that needed to reach the excited state reach a molecule at the same time, combine and provide for two-photon excitation (Lichtman and Conchello, 2009).

After excitation, the molecule uses several different pathways to return to the ground state as shown in Figure 2.2, pg. 14 (Lichtman and Conchello, 2009). The internal conversion pathway occurs between electron orbital states such as  $S_2$  to  $S_1$  which allows isoenergetic transitions from low vibrational energies of one electronic state to high vibrational modes of a lower electronic state, so no energy is lost during this transition, but the extra energy is eventually released through vibrational relaxation (Lichtman and Conchello, 2009). During vibrational relaxation, the vibrational energy in the fluorophore is transferred to nearby molecules *via* direct interactions. Internal conversion and vibrational relaxation takes picoseconds and typically bring the molecule back to the lowest energy level of  $S_1$ . The excited molecule now has a similar vibrational state as it did in the ground state, but the outer electron orbital still contains extra energy (Lichtman and Conchello, 2009). For most fluorophores the energy difference between the ground state vibrational modes and first singlet excited state is so large that internal conversion is not preferred.

The majority of fluorophores releases a photon with the energy that covers the gap between the lowest vibrational state of  $S_1$  and any one of the vibrational or rotational states of  $S_0$  (Lichtman and Conchello, 2009). The emission starts from the lowest level of  $S_1$ , therefore the energy of the emitted photon is typically less than the absorbed photon as vibrational relaxation and internal conversion remove the excess energy. This observation is referred to as a Stokes shift and results from the fact that, regardless of the energy used to excite a particular system, the primary emission will always originate from the first (or lowest) excited state as stipulated by Kasha's rule (Kasha, 1950; Lichtman and Conchello, 2009). Generally, large shifts have the advantage of

easier separation of the exciting and emitted light. Not all fluorescent emission occurs at longer wavelengths than the exciting light. On some occasions fluorophores find themselves in one of the higher vibrational states of  $S_0$  when they are excited (Lichtman and Conchello, 2009). In these cases, a photon can drop back in a larger energy jump than was needed to reach  $S_1$ , accounting for the overlap of the emission and excitation spectra. This occurs according to the Franck-Condon principle, where all electronic transitions occur without change in the position of the nuclei (Lakowicz, 1999).



UNIVERSITY of the  
WESTERN CAPE

**Figure 2.2:** Jablonski diagram illustrating the emission processes a molecule during fluorescence or phosphorescence with reference to a time scale of the different processes (Lichtman and Conchello, 2009).

### 2.3.2.1 Inorganic fluorophores

There are thousands of fluorophores in existence, each having their own spectral properties varying with their application (Lakowicz, 1999). The use of fluorophores as fluorescent probes has shown to be an important tool in fluorescence spectroscopy. They are either added to the sample to provide fluorescence for the detection of a target molecule, or the target molecule has a fluorescence capability itself due to its fluorophore properties (Lakowicz, 1999). Detection of molecules within a sample such as aromatic amino acids, NADH and flavins are examples of

target molecules which possess fluorescence capabilities. Molecules which would add fluorescence to the sample and aid in detection of the target molecules of interest are rhodamine, fluorescein and dansyl chloride (Lakowicz, 1999). Fluorescent tagging of cells and biomolecules is an example where we find the use of fluorophores as fluorescent probes. However, there are certain limitations in the use of fluorophores especially in live cell applications. These limitations come in the form of narrow excitation spectra, broad emission spectra, photobleaching and customized chemistry for conjugation of biomolecules, all of which affects the number of fluorescent probes utilized (Lakowicz, 1999). Inorganic fluorophores are a class of fluorophores which are also utilized and have shown greater efficiency compared to certain fluorophores (Alivisatos, 1996). Semiconducting quantum dots for instance have shown brighter signals compared to some organic fluorophores due to greater adsorption of the excitation light and high photobleaching threshold (Alivisatos, 1996).

Inorganic fluorophores consist of a crystalline host material, either uniform in composition or containing small amounts of specific impurities, such as activators and sensitizers (dopants), that can be diffused in the host material at elevated temperatures by a process called doping (Ronda, 2008). For the latter kind of inorganic fluorophores, the activators are primarily responsible for luminescence. However, this is not achieved single handedly as the sensitizer aids the activator which cannot directly emit photons from the excited light (Bunzli *et al.*, 2007). Instead, the sensitizer absorbs the excitation energy and then transfers this energy to the activator non-radiatively *via* resonance (Bunzli *et al.*, 2007). This form of fluorescence differs from band model fluorescence, in that emissions occur as a result of electronic transitions taking place at, or within, impurity centres (dopants) and not between valence and conduction bands where electrons are delocalised across a solid crystal lattice as in semiconducting quantum dots. The luminescence and lifetimes of these fluorophores are determined by the concentration of these ions or activators in the matrix (Ronda, 2008).

A large number of these types of inorganic fluorophores have been synthesized with rare earth ions or rare earth host lattices (Ronda *et al.*, 1998). Quite a few of these materials have found their way into applications and in many cases, rare earth host lattices dramatically improved the performance of devices in which they were applied (Ronda *et al.*, 1998). In most cases, the

emission of rare earth ions is due to optical transitions within the f-orbitals (e.g.  $Tb^{3+}$  ( $4f^8$ ), on  $Gd^{3+}$  ( $4f^7$ ) and  $Eu^{3+}$  ( $4f^7$ ) (Ronda *et al.* 1998). The f-electrons are well shielded from the chemical environment by the outer 5s and 5p subshells and do not participate directly in bonding and therefore have almost retained their atomic character (Ronda *et al.*, 1998). As a consequence, the f–f emission spectra consist of sharp lines and their transitions are partially forbidden with many of them also spin forbidden (Ronda *et al.*, 1998). Therefore, these optical transitions are generally very slow, in the range of microseconds to milliseconds, and occur with low probability displaying weak absorption spectra (Ronda *et al.*, 1998). For a number of rare earth ions broad emission bands are also known, with prominent examples being  $Eu^{2+}$  ( $4f^7$ ) and  $Ce^{3+}$  ( $4f^1$ ) (Ronda *et al.*, 1998). In these cases, emission is due to 5d–4f optical transitions (Ronda *et al.* 1998). As d electrons participate in the chemical bonding, their nuclear and electronic configurations are highly sensitive to their immediate environment (Bunzli *et al.*, 2007). Furthermore, the d–f optical transitions are allowed and are consequently very fast, in the range of milliseconds or less (Ronda *et al.*, 1998). As most rare earth metal atoms possess a vast ladder-like arrangement of excited states, they are often able to produce more than one emission band and, together, their emissions range from the UV to the NIR regions (DeLuca, 1980).

### 2.3.2.2 Upconversion

When one goes down to the nanoscale, inorganic fluorophores, with unique attributes owing to its dopant containing architecture, are found. One of those attributes is the ability to emit higher-energy photons under excitation with lower-energy photons (Wang and Liu, 2009). A few processes have been found to possess the ability to generate this anti-Stokes photoluminescence with upconversion (UC) being one of those distinct anti-Stokes processes (Wang and Liu, 2009). Upconversion can be described as a process characterized by the successive absorption of two or more photons through intermediate long-lived energy states followed by the emission of higher energy photons than the excitation of lower photon energy (Wang and Liu, 2009; Chen *et al.*, 2014). This concept was first recognized and formulated by Auzel, Ovsyankin, and Feofilov in the mid-1960s, where the research has been directed to the conversion of infrared light into visible light (Wang and Liu, 2009).

UC is a nonlinear process that utilizes the sequential absorption of multiple photons due to long lifetimes and real ladder-like energy levels of trivalent lanthanide (rare earth) ions imbedded in an appropriate inorganic host lattice to produce higher energy anti-Stokes luminescence (Zhou *et al.*, 2015; Chen and Zhou, 2012). It thereby converts two or more low-energy excitation photons, which are generally NIR light, into shorter wavelength emissions (Zhou *et al.*, 2015; Chen and Zhou, 2012). The efficiency of an UC process is greater than that of nonlinear multiphoton absorption, thus enabling UC to be produced by a low-cost continuous-wave diode laser, standard xenon or halogen lamp instead of the need of ultrashort pulsed lasers for nonlinear multiphoton excitation (Zhou *et al.*, 2015; Chen and Zhou, 2012). This process is different from nonlinear multiphoton absorption in organic dyes and quantum dots, which involves simultaneous absorption of two or more photons (Zhou *et al.*, 2015; Chen and Zhou, 2012). UC luminescence includes a metastable intermediate excited state which is expected to have a relatively long lifetime so as to maintain a high population in the intermediate excited state ahead of the second excitation energy (Zhou *et al.*, 2015; Chen and Zhou, 2012).

There are five mechanisms related to the occurrence of upconversion. These are excited-state absorption (ESA), energy transfer upconversion (ETU), cooperative sensitization upconversion (CSU), cross relaxation (CR), and photon avalanche (PA) (Chen *et al.*, 2014). These mechanisms are depicted graphically in Figure 2.3, pg. 17.

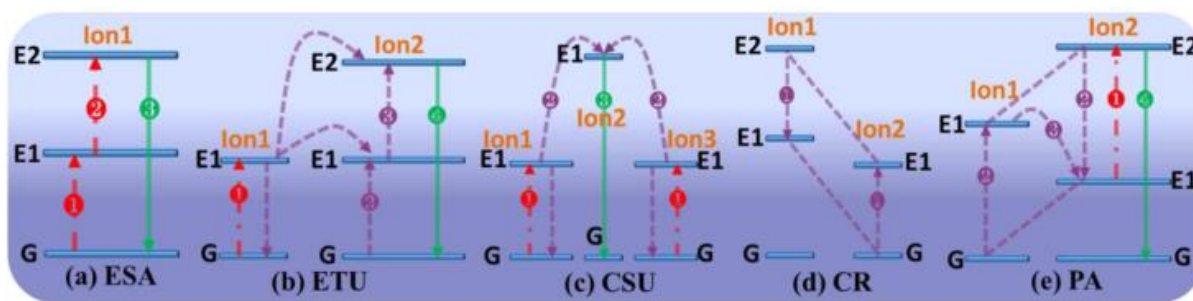


**Figure 2.3:** Upconversion processes for lanthanide-doped upconversion nanoparticles (Chen *et al.*, 2014).

Excited-state absorption (ESA) takes the form of successive absorption of photons due to the ladder-like structure of a simple multilevel system (Chen *et al.*, 2014; Chen and Zhou, 2012).

The occurrence of this mechanism is due to the equal distance from ground level (G) to energy level 1 (E1) and from E1 to energy level 2 (E2) as well as the reservoir capability of the intermediate level E1 (Chen *et al.*, 2014; Chen and Zhou, 2012). When an ion is excited from the ground state to the E1 level, another photon has a high possibility of promoting the ion from E1 to the higher-lying state E2 due to the long lifetime of E1 state, before its decay to the ground state. Consequently, upconverted emission will occur from the E2 level (Chen *et al.*, 2014; Chen and Zhou, 2012). To achieve highly efficient ESA, a ladder-like arrangement of the energy states of lanthanide is required (Chen *et al.*, 2014). Only a few lanthanide ions such as erbium (Er<sup>3+</sup>), holmium (Ho<sup>3+</sup>), thulium (Tm<sup>3+</sup>) and neodymium (Nd<sup>3+</sup>) have such energy level structures, which also find a good excitation wavelength match at ~975 and/or 808 nm (Chen *et al.*, 2014; Chen and Zhou, 2012).

Energy transfer upconversion (ETU) differs from ESA in the amount of ions present (Chen *et al.*, 2014; Chen and Zhou, 2012). ESA occurs within a single lanthanide ion, while ETU involves two neighboring ions (Chen *et al.*, 2014). In an ETU process, ion 1, known as the sensitizer, is first excited from the ground state to its metastable level E1 by absorbing a photon. It then successively transfers its harvested energy to the excited-state E1 of ion 2, known as the activator, exciting ion 2 to its upper emitting state E2 (Chen *et al.*, 2014; Chen and Zhou, 2012). The upconversion efficiency of an ETU process is sensitive to the average distance between the neighboring sensitizer-activator, which is determined by the concentrations of dopants (Chen *et al.*, 2014; Chen and Zhou, 2012). The sensitizer and activator pairing that have been commonly found to enhance excitation at ~975 nm are Yb<sup>3+</sup>/Tm<sup>3+</sup>, Yb<sup>3+</sup>/Er<sup>3+</sup>, and Yb<sup>3+</sup>/Ho<sup>3+</sup> (Chen *et al.*, 2014; Chen and Zhou, 2012).

Cooperative sensitization upconversion (CSU) is a process involving the interaction of three ion centers, with ion 1 and ion 3 generally being of the same type (Chen *et al.*, 2014; Chen and Zhou, 2012). After absorbing excitation photons, both ion 1 and ion 3 can be excited to the excited state, respectively (Chen *et al.*, 2014; Chen and Zhou, 2012). Both ion 1 and ion 3 then can interact with ion 2 simultaneously, cooperatively transfer the contained energy, and excite ion 2 to a higher state (Chen *et al.*, 2014). The excited ion 2 can relax back to its ground state by emitting an upconverted photon (Chen *et al.*, 2014; Chen and Zhou, 2012). The efficiency of

CSU is generally orders of magnitude lower than the ESA or ETU process (Chen *et al.*, 2014v). The CSU mechanism has been reported for Yb<sup>3+</sup>/Tb<sup>3+</sup>, Yb<sup>3+</sup>/Eu<sup>3+</sup>, and Yb<sup>3+</sup>/Praseodymium (Pr<sup>3+</sup>) ion pairs (Chen *et al.*, 2014; Chen and Zhou, 2012).

Cross relaxation (CR) is an energy transfer process, resulting from ion-ion interaction in which ion 1 transfers part of its excited energy to ion 2 through a process of E2 (ion 1) + G (ion 2) → E1 (ion1) + E1 (ion 2) (Chen *et al.*, 2014; Chen and Zhou, 2012). Ion 1 and ion 2 can be either the same or different, and ion 2 can also be in its excited state in some cases (Chen *et al.*, 2014; Chen and Zhou, 2012). The CR process is a fundamental result of ion-ion interaction; its efficiency is in close relation with the dopant concentration (Chen *et al.*, 2014; Chen and Zhou, 2012). CR is the main reason for the well-known “concentration quenching mechanism” of emission, but it can be intentionally used to tune the color output in UCNPs or construct efficient photon avalanche (PA) mechanism (Chen *et al.*, 2014; Chen and Zhou, 2012).

PA is a process that produces UC above a certain threshold of excitation power. Below the threshold very little up-converted fluorescence is produced (Chen *et al.*, 2014; Chen and Zhou, 2012). The PA is a looping process that involves processes of ESA for excitation light and an efficient CR that produces feedback (Chen *et al.*, 2014; Chen and Zhou, 2012). The level E1 of ion 2 is initially populated by non-resonant weak ground-state absorption (Chen *et al.*, 2014; Chen and Zhou, 2012). The looping process starts with the ESA process to elevate ion 2 at the level E1 to the emitting level E2. An efficient CR process of E2 (ion 2) + G (ion 1) → E1 (ion 2) + E1 (ion 1) between ion 1 and ion 2 then occurs. Lastly, ion 1 transfers its energy to ion 2 to populate its level E1, forming a complete loop (Chen *et al.*, 2014; Chen and Zhou, 2012). The net effect of the looping process is that one ion 2 at metastable E1 state produces two ion 2's at this state (Chen *et al.*, 2014; Chen and Zhou, 2012). When the looping process ensues, two ion 2's at the E1 state will produce four; four will produce eight, evoking an avalanche effect for populating ion 2 in its E1 state, and thus the PA UC from the emitting level of E2 (Chen *et al.*, 2014; Chen and Zhou, 2012).

### *Upconversion nanoparticles and its architecture*

The name given to these nanoscale upconverting inorganic fluorophores are upconversion nanoparticles (UCNPs). They come in different shapes and sizes as well as composition, all of

which affects the properties, effectiveness and efficiency of the nanoparticles (Li *et al.*, 2008; Wang and Liu, 2009). The important constituents of the nanoparticle are the crystalline host material, sensitizers and activators (Figure 2.4, pg. 20).

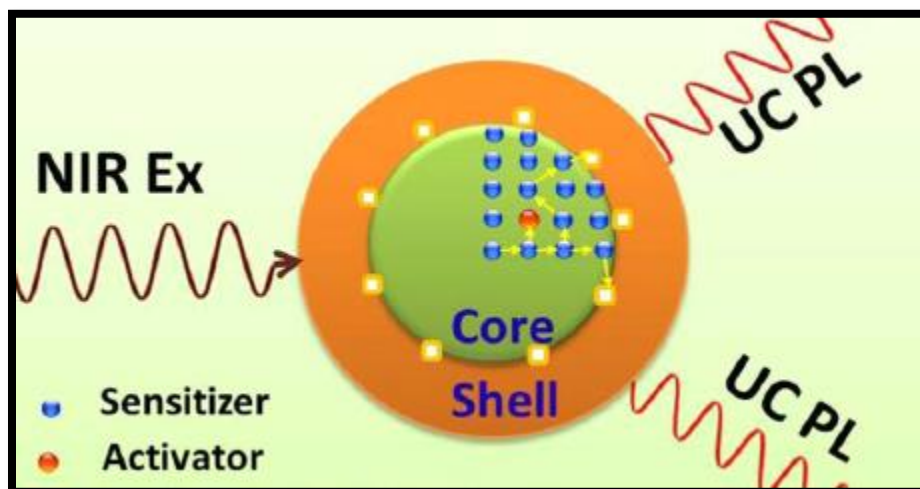


**Figure 2.4:** Illustration of a cross section of core/shell upconversion nanoparticle (Chen *et al.*, 2014).

Host materials are essential for high efficiency UC emissions where an ideal host material should be transparent in the spectral range of interest, have high optical damage threshold, and be chemically stable (Chen *et al.*, 2014). When selecting host materials, the required close lattice match to dopant ions need to be considered, and the matrix should also have low phonon energies (Chen *et al.*, 2014; Chen and Zhou, 2012). As all trivalent rare earth ions exhibit similar ionic size and chemical properties, their inorganic compounds are ideal host materials for upconverting lanthanide dopant ions. In addition, alkaline earth ions ( $\text{Ca}^{2+}$ ,  $\text{Sr}^{2+}$ , and  $\text{Ba}^{2+}$ ) and some transition metal ions ( $\text{Zr}^{4+}$  and  $\text{Ti}^{4+}$ ) also exhibit close ionic size to lanthanide ions (Chen *et al.*, 2014; Chen and Zhou, 2012). Therefore, inorganic compounds containing these ions are also frequently used as host materials for UC processes (Chen *et al.*, 2014; Chen and Zhou, 2012).

The host lattice can affect the UC efficiency in two ways, namely by phonon dynamics and the local crystal field (Chen *et al.*, 2014; Chen and Zhou, 2012). Phonon dynamics refers to phonon energies, where low phonon energies are a requirement to minimize non-radiative loss and

maximize the radiative emission (Chen *et al.*, 2014; Chen and Zhou, 2012). The larger the number of phonons needed to convert the excitation energy into phonon energy, the lower the efficiency of the nonradiative process. Hence, to enhance the emission efficiency by reducing nonradiative rate, it is desirable to have the dopants incorporated into a dielectric host of very low frequency phonons (Chen *et al.*, 2014; Chen and Zhou, 2012). Among investigated hosts, fluoride materials have the lowest phonon cutoff energy ( $350\text{ cm}^{-1}$ ) and generally exhibit the highest UC efficiency due to the minimization of nonradiative losses in the intermediate states or the emitting states (Chen *et al.*, 2014; Chen and Zhou, 2012). Other hosts include heavy halides like chlorides, bromides and iodides that generally exhibit low phonon energies of less than  $300\text{ cm}^{-1}$ . However, they are hygroscopic and are of limited use (Chen *et al.*, 2014; Chen and Zhou, 2012). Oxides exhibit high chemical stability, but their phonon energies are relatively high and generally larger than  $500\text{ cm}^{-1}$  due to the stretching vibration of the host lattice (Chen *et al.*, 2014; Chen and Zhou, 2012).

The crystal field of the host material has a profound effect on the UC efficiency of lanthanide emitters, as the local crystal symmetry surrounding a lanthanide ion strongly influences its optical properties (Chen *et al.*, 2014; Chen and Zhou, 2012). A less symmetric crystal phase is generally favorable for the UC efficiency, as the intermixing of the lanthanide ion's f states with higher electronic configurations can be more manifested (Chen *et al.*, 2014; Chen and Zhou, 2012). The uneven components enhance the electronic coupling between 4f energy levels and higher electronic configuration and subsequently increase f–f transition probabilities of the dopant ions (Chen *et al.*, 2014; Chen and Zhou, 2012). For example, hexagonal  $\text{NaYF}_4:\text{Yb}^{3+}/\text{Er}^{3+}$  microcrystals exhibit visible upconversion PL, which is 4.4 times higher than its cubic counterparts, and monoclinic  $\text{ZrO}_2$  nanoparticles emit higher UC PL than the tetragonal phase nanoparticles (Chen *et al.*, 2014). In addition, the decrease in cation size or unit-cell volume of the host can cause an increase in the crystal-field strength around the dopant ions and lead to enhanced UC efficiency. For example, the bulk material of  $\text{NaYF}_4:\text{Yb}^{3+}/\text{Er}^{3+}$  exhibits a UC luminescence two times stronger than that of  $\text{NaLaF}_4:\text{Yb}^{3+}/\text{Er}^{3+}$  (Chen *et al.*, 2014).

The requirement of multiple metastable levels for UC makes the lanthanides well-suited for this (Wang and Liu, 2009). The lanthanides, which are associated with the filling of the 4f-shell,

commence with the element lanthanum (La) and end with the element lutetium (Lu) (Wang and Liu 2009; Wang *et al.*, 2011). They essentially exist in their most stable oxidation state as trivalent ions ( $\text{Ln}^{3+}$ ) (Wang and Liu, 2009; Wang *et al.*, 2011). The shielding of the 4f electrons of  $\text{Ln}^{3+}$  by the completed filled  $5s^2$  and  $5p^6$  sub-shells results in weak electron–phonon coupling that is responsible for phenomena such as sharp and narrow f–f transition bands (Wang and Liu, 2009; Wang *et al.*, 2011). In addition, the f–f transitions are Laporte forbidden, resulting in low transition probabilities and substantially long-lived (up to 0.1 s) excited states (Wang and Liu, 2009). With the exception of  $\text{La}^{3+}$ ,  $\text{Ce}^{3+}$ ,  $\text{Yb}^{3+}$ , and  $\text{Lu}^{3+}$ , the lanthanide ions commonly have more than one excited 4f energy level (Wang and Liu 2009; Wang *et al.*, 2011). As a consequence, UC emission can be theoretically expected for most lanthanide ions (Wang and Liu, 2009). However, to generate practically useful UC emission, the energy difference between each excited level and its lower-lying intermediate level (ground level) should be close enough to facilitate photon absorption and energy transfer steps involved in UC processes (Wang and Liu, 2009).

The enhancement of UC luminescence efficiency is also dependent on a sensitizer with a sufficient absorption cross-section in the NIR region which is usually co-doped along with an activator to take advantage of the upconversion processes between the two (Wang and Li, 2007; Wang *et al.*, 2011). Trivalent Yb possesses only one excited 4f level of  $^2\text{F}_{5/2}$  (Wang and Li, 2007; Chen and Zhou, 2012). The absorption band of  $\text{Yb}^{3+}$  that is located around 980 nm due to the  $^2\text{F}_{7/2} - ^2\text{F}_{5/2}$  transition (Figure 2.5, pg. 23) has a larger absorption cross section than that of other lanthanide ions (Wang and Li, 2007; Chen and Zhou, 2012). Additionally, the  $^2\text{F}_{7/2} - ^2\text{F}_{5/2}$  transition of  $\text{Yb}^{3+}$  is well resonant with many f–f transitions of typical upconverting lanthanide ions, thus facilitating efficient energy transfer from  $\text{Yb}^{3+}$  to other ions (Wang and Li, 2007; Chen and Zhou, 2012). These optical characteristics make  $\text{Yb}^{3+}$  particularly suitable for use as a UC sensitizer (Wang and Li, 2007; Chen and Zhou, 2012). The sensitizer content is normally kept high (20 mol%) in doubly or triply doped nanocrystals, while the activator content is relatively low (2 mol%), minimizing cross relaxation energy loss (Wang and Li, 2007; Chen and Zhou, 2012).

Dopant ions  $\text{Er}^{3+}$ ,  $\text{Tm}^{3+}$ , and  $\text{Ho}^{3+}$  with their ladder-like arranged energy levels are frequently selected as activators to generate upconversion emission (Zhou *et al.*, 2015). The  ${}^2\text{F}_{7/2} \rightarrow {}^2\text{F}_{5/2}$  transition of  $\text{Yb}^{3+}$  is conveniently resonant with many f–f transitions of  $\text{Er}^{3+}$ ,  $\text{Tm}^{3+}$ , and  $\text{Ho}^{3+}$ , thus facilitating efficient energy transfer from  $\text{Yb}^{3+}$  to these ions (Figure 2.5, pg. 23) (Zhou *et al.*, 2015; Chen and Zhou, 2012).

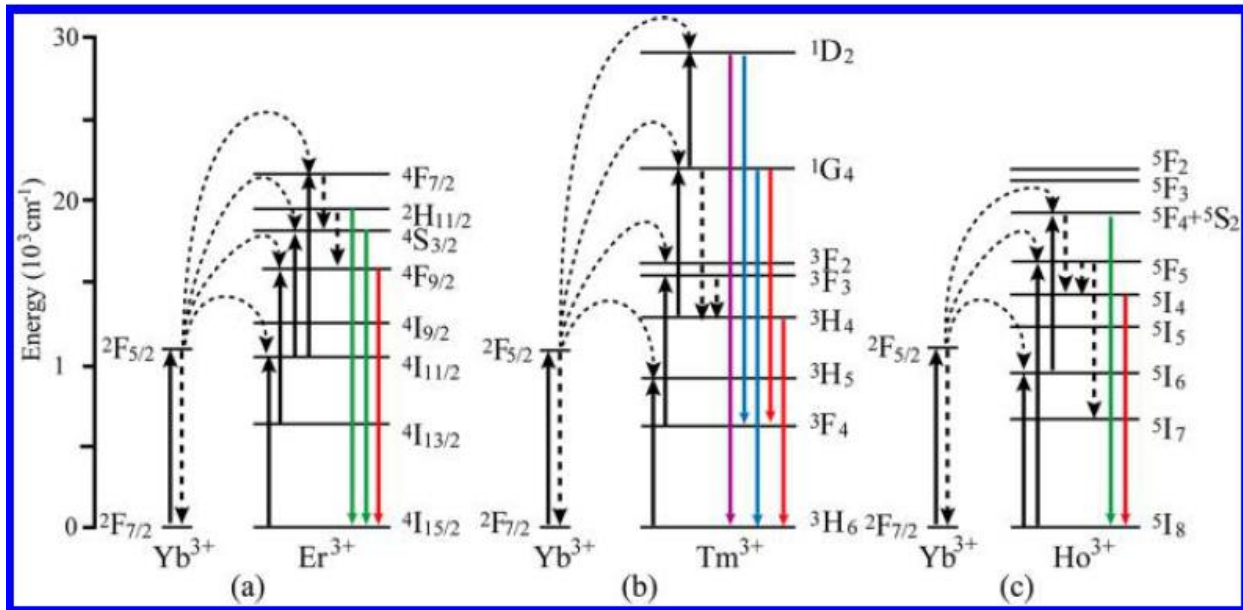
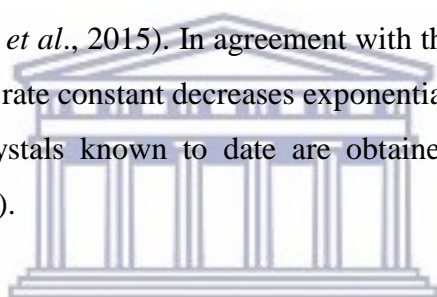


**Figure 2.5:** Upconversion Mechanism of the Lanthanide UCNPs doped with (a)  $\text{Yb}^{3+}$  and  $\text{Er}^{3+}$ , (b)  $\text{Yb}^{3+}$  and  $\text{Tm}^{3+}$ , or (c)  $\text{Yb}^{3+}$  and  $\text{Ho}^{3+}$  (Zhou *et al.*, 2015).

Thus,  $\text{Yb}^{3+}$  is often codoped with  $\text{Er}^{3+}$ ,  $\text{Tm}^{3+}$ , or  $\text{Ho}^{3+}$  as a sensitizer to enhance upconversion emission (Figure 2.5) (Zhou *et al.*, 2015). A continuous wave 980 nm laser is applied as the excitation source to match the  ${}^2\text{F}_{7/2} \rightarrow {}^2\text{F}_{5/2}$  transition of  $\text{Yb}^{3+}$  (Zhou *et al.*, 2015). For  $\text{Yb}^{3+}$  and  $\text{Er}^{3+}$  codoped UCNPs, green upconversion emissions in the region 510–570 nm are attributable to the transitions from the  ${}^2\text{H}_{11/2}$  and  ${}^4\text{S}_{3/2}$  excited states to the  ${}^4\text{I}_{15/2}$  ground state, with the peaks centered at 520 and 542 nm, respectively (Zhou *et al.*, 2015). A red emission centered at 660 nm is observed, for the transition from the  ${}^4\text{F}_{9/2}$  excited state to the ground state (Zhou *et al.*, 2015). Weak blue emissions are also observed at 445–505 nm from the  ${}^4\text{F}_{5/2} \rightarrow {}^4\text{I}_{15/2}$  (centered at 450 nm) and  ${}^4\text{F}_{7/2} \rightarrow {}^4\text{I}_{15/2}$  (centered at 495 nm) transitions (Zhou *et al.*, 2015). In addition, because of a four-photon process, emission bands at 390 and 410 nm can be observed under high excitation

power density with a high concentration of  $\text{Yb}^{3+}$  (Zhou *et al.*, 2015). For  $\text{Yb}^{3+}/\text{Tm}^{3+}$ -co-doped UCNPs, upconversion emission bands at 451, 481, 646, and 800 nm can be ascribed to the  $^1\text{D}_2 \rightarrow ^3\text{F}_4$ ,  $^1\text{G}_4 \rightarrow ^3\text{H}_6$ ,  $^1\text{G}_4 \rightarrow ^3\text{F}_4$ , and  $^3\text{H}_4 \rightarrow ^3\text{H}_6$  transitions, respectively (Zhou *et al.*, 2015). In addition, upconversion emissions in the UV region at 345 and 365 nm can be assigned to the  $^1\text{D}_2 \rightarrow ^3\text{H}_6$  transitions (Zhou *et al.*, 2015). Generally, for  $\text{Yb}^{3+}/\text{Tm}^{3+}$ -co-doped UCNPs, the upconversion emission intensity at 800 nm is the largest (Zhou *et al.*, 2015). For  $\text{Yb}^{3+}/\text{Ho}^{3+}$ -co-doped UCNPs, a blue upconversion emission centered at 486 nm from the  $^4\text{F}_3 \rightarrow ^5\text{I}_8$  transition and green emissions at 510–570 nm ascribed to the  $^5\text{F}_4, ^5\text{S}_2 \rightarrow ^5\text{I}_8$  transitions are observed (Zhou *et al.*, 2015). A red emission centered at 647 nm is observed for the transition from the  $^5\text{F}_5$  excited state to the ground state  $^5\text{I}_8$  (Zhou *et al.*, 2015). NIR upconversion emission observed at 751 nm can be ascribed to the  $^5\text{F}_4, ^5\text{S}_2 \rightarrow ^5\text{I}_7$  transitions (Zhou *et al.*, 2015).  $\text{Er}^{3+}$  and  $\text{Tm}^{3+}$  have relatively large energy gaps and thus low probabilities of non-radiative transitions among various excited levels of the ions (Zhou *et al.*, 2015). In agreement with the energy gap law, which states that the multiphonon relaxation rate constant decreases exponentially with increasing energy gap, the most efficient UC nanocrystals known to date are obtained with  $\text{Er}^{3+}$  and  $\text{Tm}^{3+}$  as the activators (Wang and Liu, 2009).



UNIVERSITY of the  
WESTERN CAPE

### *Synthesis protocols*

The earliest form of UCNPs came in the presence of upconverting lanthanoid materials such as phosphors or as bulk materials (Heer *et al.*, 2003). It was only in 2003 when the first synthetic method for the synthesis of stable suspensions of UCNPs was reported by Heer *et al.* (2003). The UCNPs were in the size range of 7 nm where the composition of the nanoparticles were  $\text{YbPO}_4:\text{Er}$  and  $\text{LuPO}_4:\text{Yb,Tm}$  (Heer *et al.*, 2003). The composition of the upconversion was later changed, most notably in the host lattice, to  $\text{NaYF}_4$  (Heer *et al.*, 2004). This change from phosphate crystal lattices to  $\text{NaYF}_4$  showed a remarkable difference in luminescence intensity (Heer *et al.*, 2004). Since the publication of the paper by Heer *et al.*, (2004), different kinds of UCNPs have been synthesized, with many more synthetic methods produced as well. The majority of these methods produced UCNPs stabilized with a hydrophobic capping ligand, which lead to the need for the modification of the UCNP surface to render them hydrophilic and thus make them biocompatible (Lin *et al.*, 2012). The ability to disperse a UCNPs in water or biological media is often considered a necessity for any of its application within the medical field

(Lin *et al.*, 2012). As important as hydrophilicity of the UCNPs is, surface functionality is also possible in the field of UCNP surface modification (Haase and Schäfer, 2011). Common functional groups include amines, thiols and carboxylic acids, due to the ease with which they may be reacted with many biologically relevant molecules (Lin *et al.* 2012). Surface modification of UCNPs has derived multiple techniques capable of rendering UCNPs water dispersible. Surface modification methods investigated can be divided into five categories namely ligand exchange, ligand modification, adsorption of amphiphilic molecule and growth of a silica shell (Lin *et al.*, 2012; Dong *et al.*, 2010; Wilhelm *et al.*, 2015)

One of the most popular methods of UCNP synthesis used over the years has been thermal decomposition (Plohl *et al.*, 2015). This synthesis protocol involves the heating of lanthanoid activators and sensitizers in nonpolar solvents with high boiling points in the presence of the intended host matrix materials (Plohl *et al.*, 2015). A capping ligand is usually used to manage nanoparticle growth and stabilize the growing nanoparticles in solution (Plohl *et al.*, 2015). Commonly reported within thermal decomposition methods, is the use of oleic acid in conjunction with either oleylamine or octadecene (Plohl *et al.*, 2015). Due to the high temperatures involved and the general sensitivity of UCNPs to oxygen impurities, control over the reaction must be precise in order to produce good quality nanocrystals of a narrow, monodisperse size (Plohl *et al.*, 2015). Parameters that influence nanocrystal morphology, size and crystal phase include temperature, pressure, capping ligand, precursor composition, heating rate, cooling rate, reaction time, solvent, and reagent concentrations (Plohl *et al.*, 2015). The careful selection of these parameters allows for control over UCNP size and crystal phase. However, the large number of variables also makes the elimination of errors and reproducible syntheses exceptionally challenging (Plohl *et al.*, 2015). Although thermal decomposition produces good UCNPs, it also produces toxic byproducts (Plohl *et al.*, 2015).

Coprecipitation, compared to thermal decomposition, is a much more user-friendly synthetic method, as there are fewer toxic byproducts and the temperatures required during the initial synthesis are around 120 – 160 °C which is not as extreme as the 270-320 °C temperatures used for thermal decomposition (Wang *et al.*, 2011). This method does, on the other hand, have its own negative aspects with lower UCNP quality immediately following synthesis, often requiring

additional annealing to achieve good photon upconversion (Wang et al., 2011). A typical protocol involves the rapid injection of a lanthanoid-EDTA complex into a solution made up of NaF in deionized water, resulting in immediate nucleation (Gainer and Romanowski, 2014). This is then allowed to react at room temperature for 1 hour which is followed by precipitation of the UCNPs by centrifugation and several wash steps (Gainer and Romanowski, 2014). The dry nanoparticles are then annealed at 400 °C to promote the transition from cubic to hexagonal phase (Gainer and Romanowski, 2014). Two similar synthetic procedures to coprecipitation, include the hydrothermal and solvothermal synthetic protocols with respect to the requirement of lower temperatures and production of fewer toxic byproducts than the thermal decomposition methods (Wang et al., 2011). The main requirement for hydrothermal synthesis is an autoclave, which is necessary in order to bring the polar solvents used to temperatures and pressures above their critical points (Wang et al., 2011). Organic solvents may be added to these reactions to help control crystal growth and directionality, although high quality nanoparticles can still be synthesized without them (Wang et al., 2011). There are other known synthetic methods such as ion thermal, sol-gel, combustion and flame synthesis (Wang et al., 2011; Qin *et al.*, 2007; Liu *et al.*, 2009). Although each of these synthetic methods has its own virtues, the nanoparticles produced are, in general, not as good as those produced by the methods described previously (Wang et al., 2011).

### *Upconversion nanoparticle applications*

The application of upconversion nanoparticles spans various fields, mostly due to their unique properties. The fields range from sensing to therapeutic (Chen *et al.*, 2014). Being a considerably young prospect in science, its true potential has yet to be untapped.

With regards to bio-sensing and bioassays, UCNPs are promising for these endeavors due to their unique converting capability of biocompatible NIR light which is not harmful to tissues (Wang *et al.*, 2010). They have the potential to reach a high detection sensitivity located deeply in living body systems (Wang *et al.*, 2010). The PL of UCNPs is not directly related to any biochemical property of a system, but in combination with recognition elements, it can be useful to detect biochemical processes which is the fundamental process in chemical sensing (Wang *et*

*al.*, 2010). The recognition element of a biosensor may consist of an enzyme, an antibody, a polynucleotide, or even living cells (Wang *et al.*, 2010). The process of biochemical recognition needs to be transduced into an optical signal given by the UCNPs and the transduction must then be implemented by a Forster resonance energy transfer (FRET) and/or Forster resonance energy transfer (LRET) mechanism (Wang *et al.*, 2010). Within laboratories, the utilization of UCNPs is seen in *in vitro* temperature sensing; detection of ions such as cyanide, mercury, sensing of small gas molecules such as oxygen, carbon dioxide, ammonia; as well as UCNP-based bioassays for biomolecules like avidin, ATP, DNA, RNA (Chen *et al.*, 2008; Hao *et al.*, 2013; Chen and Zhao, 2012; Wang *et al.*, 2010). This has shown promising results, but it needs further development. The UCNPs improved the limit of detection of current assays down to about 1 order of magnitude or more when compared to that of conventional methods involving latex particles, gold nanoparticles and organic dyes (Chen *et al.*, 2014). There is still an issue with the efficiency of UCNPs, which restrains the limit of detection in some of these assays (Chen *et al.*, 2014). Development of more efficient UCNPs can further increase the nanoparticles' potential (Chen *et al.*, 2014). In addition, multiplexed detections of a variety of analytes or multiplexed sensing of biochemical entities using multicolor emissions of UCNPs could be revolutionary (Zhou *et al.*, 2010).

Another application involves PL imaging, which plays an important role in biomedical research, being extremely useful for early detection, screening, and image-guided therapy of life-threatening diseases (Davis *et al.*, 2008). In combination with UCNPs, this has emerged as a new generation of promising bioimaging nanomaterials for endeavors in toxicity assessment, cellular imaging, whole body PL imaging, optical tomography and multimodal imaging (Chen *et al.*, 2014; Davis *et al.*, 2008; Na *et al.*, 2009; Sun *et al.*, 2013; Wang *et al.*, 2010). This combination has been successfully tested in laboratories to a certain extent, however, there are still several interesting or important aspects that need to be explored or improved upon. Despite few works on active target bioimaging, most investigations on PL or multimodal imaging are limited (Zhou *et al.*, 2010). Future work on targeted imaging needs to be explored using UCNPs in animal models to help solve practical biological or medical problems and optical tomography using UCNPs has been limited to reconstruct 3-D images in tissue (Chen *et al.*, 2014). Extensions of the nanoparticles into biological tissues, living biological bodies, or human tissues would be an

appealing area (Chen *et al.*, 2014). Although there are a few successful examples, the development of multifunctional nanoprobe based on UCNPs for multimodal imaging is still in its infancy. It remains a challenge to construct multimodal probes with compatible design (Chen *et al.*, 2014). Development of a multifunctional nanoprobe for simultaneous bioimaging covering optical imaging, MRI, PET, SPECT and CT monitoring would be an interesting topic (Chen *et al.*, 2014). Most importantly, more efficient UCNPs with clearable capability will be required. This would be achievable through a systematic optimization of present systems including the small size, the appropriate surface chemistry, the high efficiency and the long circulation capability (Chen *et al.*, 2014).

Drug delivery and therapeutics has benefited from the use of nanotechnology and will continue to do so (Davis *et al.*, 2008; Wang *et al.*, 2010; González-Béjar *et al.*, 2016). UCNPs will hopefully play a role as their therapeutic applications have shown promising results in drug delivery, light-regulated drug release, photothermal therapy, and PDT (Davis *et al.*, 2008; Wang *et al.*, 2010; González-Béjar *et al.*, 2016). Most of these therapeutic results have been done *in vitro* with limited works *in vivo*. This has to be improved with more research in animal models where the combined use of PDT and photothermal in UCNPs might be able to result in an impressive therapeutic improvement (Davis *et al.*, 2008; Wang *et al.*, 2010; González-Béjar *et al.*, 2016). This could lead to theranostic agents for simultaneous medical diagnosis and therapy with an extensive exploration of imaging-guided delivery or therapy to treat cancers or malignant diseases (Davis *et al.*, 2008; Wang *et al.*, 2010; González-Béjar *et al.*, 2016).

## **2.4. Part B:**

### **2.4.1 Phthalocyanines**

Phthalocyanines (Figure 2.6, pg 29) are a family of aromatic macrocycles based on an extensive, delocalized, two-dimensional 18 pi-electron system which exhibit many unique properties (Torres *et al.*, 1998). They are highly stable and versatile compounds, capable of including various metallic and non-metallic ions in the ring cavity (Torres *et al.*, 1998). It is possible to have a variety of peripheral substituents around the phthalocyanine core, as well as to replace some of the four isoindole units by other heterocyclic moieties, giving rise to different

phthalocyanine analogues (Torres *et al.*, 1998). The neat fit of the central metal atom in the phthalocyanine, the coordination and covalent coordination of the metal central atom, and the high degree of aromaticity of the surrounding nitrogen and benzene structures which form the molecule may explain the unusual stability of the phthalocyanines (Engel *et al.*, 1997; Sekkat *et al.*, 2012). Phthalocyanines are found to be exceptionally stable to acids, alkalies, moisture, heat, light and solvent where they generally decompose by pyrolysis at or above 500°C (Engel *et al.*, 1997; Sekkat *et al.*, 2012).

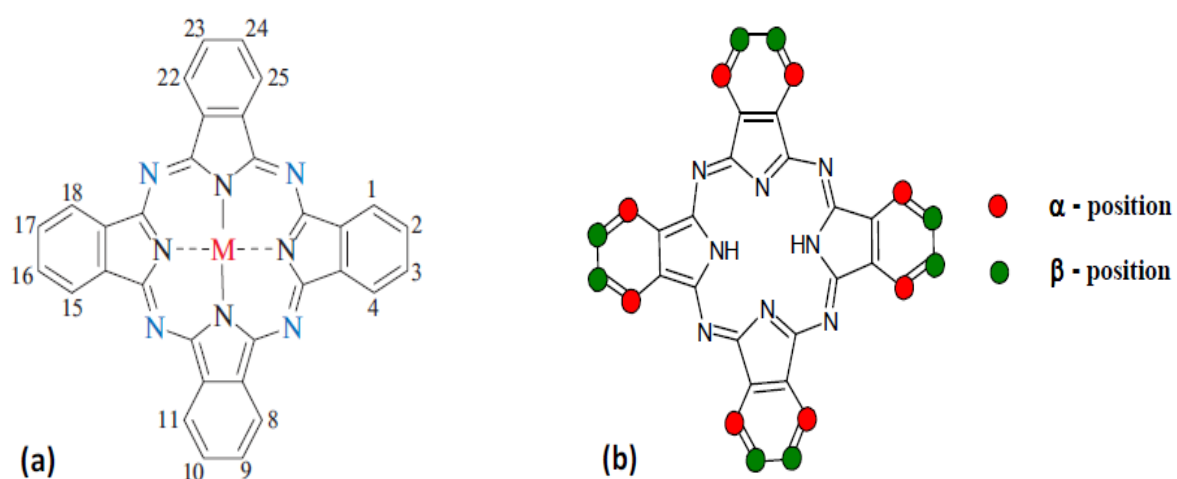


**Figure 2.6:** Numbering system of the Metallated Phthalocyanine showing the covalent and partial bonds between the central metal and the nitrogen atoms and (b)  $\alpha$  and  $\beta$  positions on the di- hydrogen Phthalocyanine.

Phthalocyanines made three appearances before its structure was known and even before it received its name. The first appearance of phthalocyanines was reported in 1907 by Braun and Tcherniac at the South Metropolitan Gas Company, in the United Kingdom, where they were attempting to synthesize *o*-cyanobenzamide but obtained a blue, insoluble compound instead (Engel *et al.*, 1997; Sekkat *et al.*, 2012). In 1927, phthalocyanines appeared again through Diesbach and von der Weid at the University of Fribourg, in Switzerland, where they reported a blue product as they were attempting to synthesize nitriles of benzene by reacting *o*-cyanobenzamide with cuprous cyanide (Engel *et al.*, 1997; Sekkat *et al.*, 2012). In 1928, it

appeared during the course of the industrial production of phthalimide in the Grangemouth works of Messrs, Scottish Dyes, Ltd. The process consisted in passing ammonia into molten phthalic anhydride in iron vessels and it was found that, during certain preparations, traces of a dark blue substance were formed in the molten imide (Engel *et al.*, 1997; Sekkat *et al.*, 2012). This material was stable, crystalline and contained iron which was not eliminated by treatment with concentrated sulphuric acid (Engel *et al.*, 1997; Sekkat *et al.*, 2012).

After remaining unknown for years, it was in 1934 where Professor Linstead in collaboration with Imperial Chemical Industries became the first to characterize the chemical structure of this phthalocyanine molecule (Engel *et al.*, 1997). The molecular structure of phthalocyanines proposed by Linstead and co-workers, went on to develop improved synthetic methods for several metal phthalocyanines (MPcs) from 1929 to 1939 (Gümrukçü *et al.*, 2014). The structure of the phthalocyanine molecule was confirmed by X-ray structure determination by Professor Robertson and co-workers, where they observed that Pcs form monoclinic crystals, space groups P2/a, with two molecules per unit cell, each with center symmetry (Engel *et al.*, 1997; Sekkat *et al.*, 2012). They also noted that the entire molecule lies in the same plane, with the possible exception of the two central hydrogen atoms in di hydrogen phthalocyanine (H<sub>2</sub>Pc) (Engel *et al.*, 1997).

#### 2.4.1.1 Phthalocyanine synthesis

There are various aspects one looks into when considering phthalocyanines. Phthalocyanines can be synthesized either as unmetallated or metallated Pcs, as well as with different substituent groups on the outer subunits. The basic unmetallated structure of the Pc consists of four isoindole subunits where the protons on the peripheral benzene rings can be substituted with various groups on either the peripheral ( $\alpha$ ) or non-peripheral ( $\beta$ ) positions (Kadish *et al.*, 2003). The successful addition of desired functional groups allows for the manipulation of the physical, chemical and electronic properties of the Pc (Kadish *et al.*, 2003). A variety of metals can also be introduced into the centre of the Pc ring, forming two partial bonds with opposing nitrogen atoms (Kadish *et al.*, 2003). MPcs possess high thermal stability due to both interlinking nitrogen atoms (Kadish *et al.*, 2003). If the Pc is substituted on all the  $\alpha$  or  $\beta$  positions, the Pc is referred to as

octa-substituted and if the Pc is substituted on only one position, at either the alpha or the beta positions, then the Pc is known as tetra-substituted (Kadish *et al.*, 2003).

Pcs that are synthesized unmetallated or metallated can be symmetrical or unsymmetrical depending on the arranged substituents during synthesis. Symmetrical Pcs are manufactured from several precursors, as shown in Figure 2.7, pg. 31, through cyclotetramerization reactions that take place in the presence of a metal salt (Kadish *et al.*, 2003).

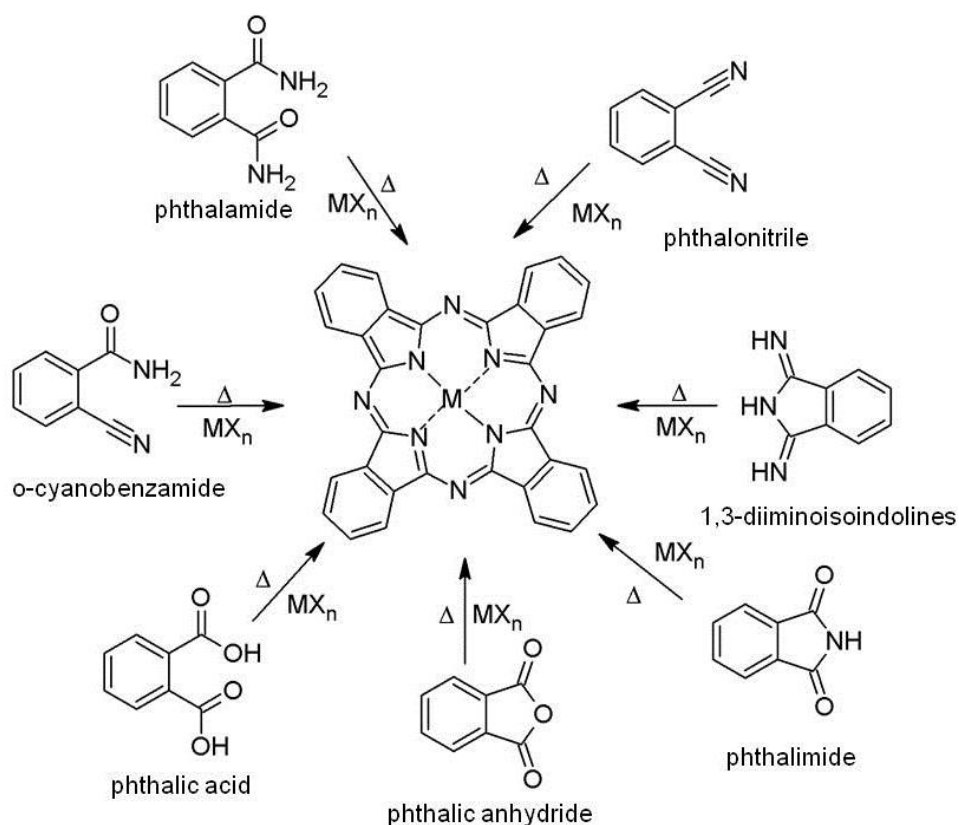


**Figure 2.7:** Possible synthesis routes of symmetrical Phthalocyanines through several 1,2-disubstituted benzene species (Kadish *et al.*, 2003).

There is a possibility that some of these precursors may occur as intermediates in synthesis reactions of other Pcs (Kadish *et al.*, 2003). Certain precursors are preferred compared to others depending on factors relative to the need of the Pcs (Kadish *et al.*, 2003). In industry the cost of production is a high priority where the cheapest alternative for production of their product is

more attractive (Kadish *et al.*, 2003). It is for this reason that trend of phthalimides, phthalic acids and phthalic anhydrides are more frequently used owing to their relatively cheap production costs when compared to the more expensive phthalonitriles which are more popular in small scale synthetic operations and in academia (Kadish *et al.*, 2003).

Phthalonitriles possess superior qualities as phthalocyanine precursors where they are produced in high purity and good yields *via* reasonably simple reactions (Kadish *et al.*, 2003). These reactions are done using several different approaches (Kadish *et al.*, 2003). One such example includes phthalonitriles added to metals or metal salts and heated to high temperatures as solid state mixtures or dissolved in a suitable high boiling point solvent such as quinoline, where they may be combined with an appropriate reducing agent such as hydroquinone, or strong bases like 1,8-diazabicyclo[5,4,0]undec-7-ene (DBU), or a basic solvent such as N,N-dimethylaminoethanol (DMAE) (Snow and Griffith, 1984; Thompson *et al.*, 1993; Uchida *et al.*, 2003). The use of DBU in alcoholic solvents like pentanol facilitates the synthesis of Pcs using significantly lower reaction temperatures and results in high purity products (Snow and Griffith, 1984; Thompson *et al.*, 1993; Uchida *et al.*, 2003). The unmetallated Pcs can be synthesized using the same procedure mentioned previously but without the addition of a metal or metal salt (Snow and Griffith, 1984; Thompson *et al.*, 1993; Uchida *et al.*, 2003). Although they can also be generated through the cyclization of phthalonitriles with labile metals such as lithium and magnesium, which can be easily removed using acid (Sorokin, 2013). The presence of labile metals also makes possible the inclusion of new metals in the macrocycle centre *via* a metal ion exchange (Sorokin, 2013).

Unsymmetrical Pcs can be synthesized using the method of statistical condensation which involves the use of two differently substituted isoindoles or phthalonitriles, at a molar ratio of 3:1, which produces a mixture of six compounds requiring lengthy chromatographic techniques for their isolation (Figure 2.8, pg. 33) (Kadish *et al.*, 2003).

The reason for a 3: 1 molar ratio is due to statistical considerations which predict, for two different phthalonitrile derivatives of similar reactivity, a mixture of products in the following percentages: A<sub>4</sub> (33%), A<sub>3</sub>B (44%) and the remaining cross-condensation products (23%), with

the production of the unsymmetrical phthalocyanine being the major product (Kadish *et al.*, 2003). In cases where the reactivity of A and B differ, the molar ratios of A:B can be modified. For example where B is much more reactive than A, a molar ratio of 9:1 (A:B) or higher may be used; although an increase in the amount of A<sub>4</sub> occurs, reducing the number of products with more than one B subunit (Kadish *et al.*, 2003). Chromatographic separation of the resultant phthalocyanines can be difficult due to the enormous tendency of these molecules towards aggregation (Kadish *et al.*, 2003). Substitution at the β position and the use of bulky or rigid groups as substituents on phthalocyanines have resulted in easier chromatographic separation (Kadish *et al.*, 2003).

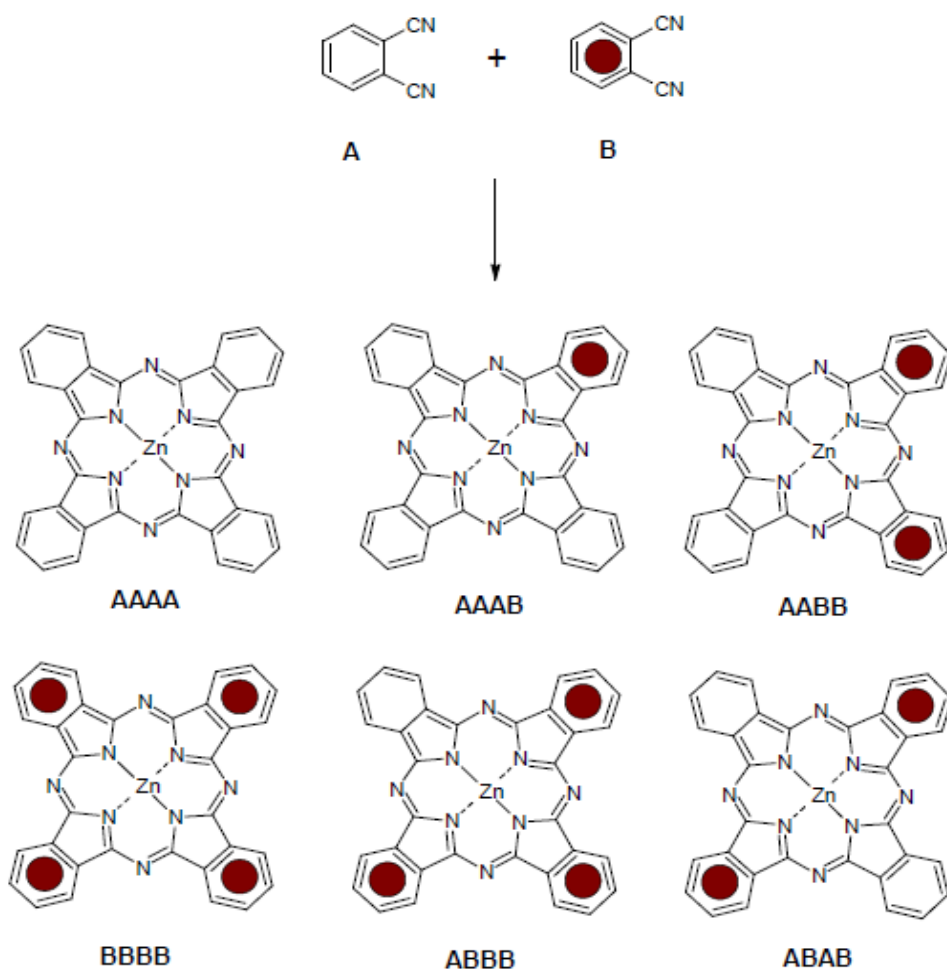


**Figure 2.8:** Schematic illustration of the statistical condensation which involves the use of two differently substituted phthalonitriles to produce a mixture of six Pc compounds (Kadish *et al.*, 2003).

### 2.4.1.2 Absorbance properties of phthalocyanines

The absorption spectra for phthalocyanines contain two main bands, B (soret) and Q, in the region of 300 – 400 nm and 600 – 700 nm, respectively (Kadish *et al.*, 2003). The absorption spectra can be used to differentiate between the metallated and unmetallated phthalocyanines as the band in the region of 600 – 700 nm differ between the two phthalocyanines (Kadish *et al.*, 2003). For the metallated phthalocyanines a single peak is obtained whereas the unmetallated phthalocyanine contains two neighboring peaks (Figure 2.9, pg. 34) (Kadish *et al.*, 2003).

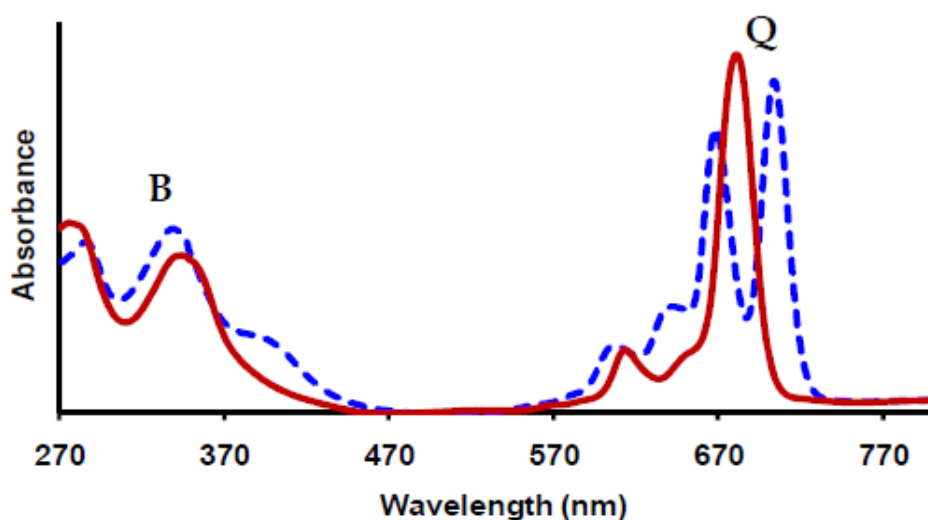


**Figure 2.9:** Absorption spectra of the metallated phthalocyanine (red line) and unmetallated phthalocyanine (blue line) (Kadish *et al.*, 2003).

Within the phthalocyanines, the Q band arises from a transition between the highest occupied molecular orbital (HOMO),  $a_{1u}$ , and the degenerate lowest unoccupied molecular orbitals (LUMO and LUMO+1),  $e_g$  (Figure. 2.11). The weaker Q bands, in the form of shoulder peaks, are thought to arise from a transition involving excited state vibrational levels (Kadish *et al.*, 2003). The broad B band comprises two bands,  $B_1$  and  $B_2$ , which originate from  $a_{2u}$  to  $e_g$  and  $b_{2u}$  (HOMO-1) to  $e_g$  level transitions (Kadish *et al.*, 2003). The degeneracy of the LUMO and LUMO+1 orbitals can be attributed to the  $D_{4h}$  symmetry of the planar, metallated Pc ring (Kadish *et al.*, 2003). The split Q band of the unmetallated phthalocyanine is a result of a

degenerate LUMO (eg, due to the hydrogen atoms in the center of the ring which lowers the symmetry from  $D_{4h}$  to  $D_{2h}$  of the phthalocyanine (Kadish *et al.*, 2003). The shape and position of the Q band of phthalocyanines are influenced by several factors including Pc ring substituents, metal centres, axial ligands, solubility and solvent characteristics (Kadish *et al.*, 2003).

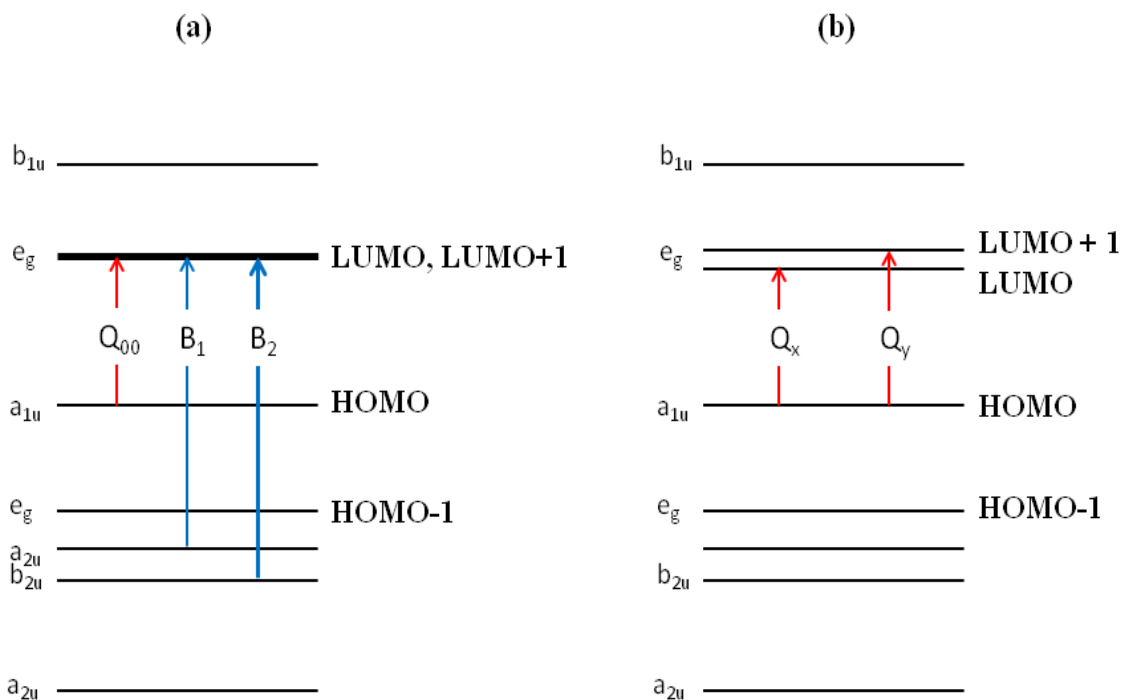


**Figure 2.10:** (a) The electronic transitions of the B band as well as the Q band electronic transition for metallated phthalocyanines (b) Q band electronic transitions for the two peaks found in the unmetallated phthalocyanine (Kadish *et al.*, 2003).

#### 2.4.1.3 Fluorescence quantum yield and lifetimes

Fluorescence emissions may be expressed quantitatively utilizing quantum yields. Quantum yields are utilized to assess the effectiveness of the fluorescent emission compared to other radiative and non-radiative de-excitation processes (Yanik *et al.*, 2016). The fluorescence quantum yield ( $\Phi_f$ ) is defined as the number of photons emitted in relation to the number of photons absorbed or in other words the ratio of molecules fluorescing to the number of photons absorbed. Typically, quantum yields possess a value of less than one, owing to energy loss *via* competing

decay mechanisms, and may be described as either relative or absolute where these terms refer to the experimental methods used in quantum yield acquisition (Yanik *et al.*, 2016). Relative quantum yields are measured by comparing a sample's fluorescent emissions with that of a known standard (Gümrukçü *et al.*, 2014). Quantum yields in this work have been calculated using the standard comparison method and Equation 2.2 (Gümrukçü *et al.*, 2014) :

$$\Phi_F = \Phi_{Std} \frac{F \cdot A_{Std} \cdot \eta^2}{F_{Std} \cdot A \cdot \eta_{Std}^2} \quad (2.2)$$

Here,  $\Phi_F$  is the quantum yield of the sample and  $\Phi_{Std}$  that of the standard; F and  $F_{Std}$  represent the area under the fluorescence emission curve for the sample and standard respectively; A and  $A_{Std}$  refer to the rates of light absorbance of the sample and standard and  $\eta$  and  $\eta_{Std}$  are the refractive indices of the sample and standard solutions, respectively (Gümrukçü *et al.*, 2014). Fluorescence quantum yields as well as lifetimes depend on a number of factors such as the central metal, the nature of the substituents, the refractive indices of the solvents, as well as the pH and temperature.

The fluorescence lifetime refers to the time spent by a system in the excited state from which decay by fluorescence occurs and is equal to the reciprocal of the sum of the decay constants for all the relaxation processes acting upon the excited state (Yanik *et al.*, 2016). The fluorescence lifetimes ( $\tau_F$ ) for MPCs are generally of the order of picoseconds to nanoseconds (Berezin *et al.*, 2012). They are widely used to investigate the radiative and non-radiative decay rates acting on fluorophore excited states, the interaction of these states with the environment (i.e. with solvents), as well as excited state reaction rates (Berezin *et al.*, 2012). One of the methods used for determining fluorescence lifetimes is through the use of the program PhotochemCAD (Du *et al.*, 1998) in the absence of having a fluorescence lifetime spectrometer available. This is a software package that utilizes the Strickler-Berg Equation to calculate the fluorescence lifetimes using the acceptor absorption and donor emission spectra (Du *et al.*, 1998). The equation however is only valid for molecules that which do not interact with the solvent and those that do not undergo geometric changes when excited (Du *et al.*, 1998). Natural radiative lifetimes ( $\tau_0$ ), described as the lifetime of an excited molecular entity in the absence of radiationless transitions,

are determined with the PhotochemCAD program using the Strickler-Berg Equation followed by the evaluation of the fluorescence lifetimes ( $\tau_F$ ) using Equation 2.3 (Du *et al.*, 1998):

$$\Phi_F = \frac{\tau_F}{\tau_0} \quad (2.3)$$

#### 2.4.1.4 Singlet oxygen production within phthalocyanines

Singlet oxygen is produced by photosensitizers using light of the appropriate energy (Calixto *et al.*, 2016). Phthalocyanines are one example of photosensitizers that, when excited from a ground singlet state to an excited singlet state, undergoes intersystem crossing to a longer-lived triplet state which then reacts with a nearby oxygen molecule to produce a  $^1O_2$  (Calixto *et al.*, 2016). The processes of photosensitization may be accomplished *via* two mechanisms, namely Type I and Type II (Calixto *et al.*, 2016). After an intersystem crossing (ICS), the photosensitizer, now in a triplet excited state, can react in two ways leading to the different mechanisms (Calixto *et al.*, 2016). Type I involves the reaction with biomolecules through a hydrogen atom (electron) transfer to form radicals, which react with molecular oxygen to generate reactive oxygen species (Calixto *et al.*, 2016). In Type II, the PS in its triplet state can react directly with oxygen through energy transfer, generating singlet oxygen (Type II reaction) (Calixto *et al.*, 2016). The metastability of the lowest singlet excited state is as a result of relaxation to the triplet ground state being spin forbidden (Calixto *et al.*, 2016). This imparts a relatively long lifetime to molecular singlet oxygen, allowing it to participate in a great number of chemical reactions (Calixto *et al.*, 2016). In comparison to molecules occupying the ground (triplet) state, singlet oxygen is highly electrophilic and has found use as an oxidizing agent for numerous organic reagents including some sulfides, phosphides, amines, alkenes and a number of cyclic compounds (Clennan and Pace, 2005).

The efficiency in which a phthalocyanine, or more generally a photosensitizer, can generate singlet oxygen is determined as the singlet oxygen quantum yield, designated  $\Phi_\Delta$  (Durmus, 2012). Experiments undertaken for singlet oxygen quantum yield determinations are usually done utilizing a standard such as zinc phthalocyanine (Durmus, 2012). Experimentally, the photodegradation rate of a singlet oxygen trap such as diphenylisobenzofuran (DPBF) (in

organic solvents) or anthracene-9,10-diyl-bis-methylmalonate (ADMA) (in aqueous solvents) is examined by exciting a mixture of a photosensitizer and chemical trap for a series of specific time intervals (Durmus, 2012). This is then compared to the photodegradation rate induced by the standard and a quantum yield can be obtained using Equation 2.4:

$$\Phi_{\Delta} = \Phi_{\Delta}^{\text{Std}} \cdot \frac{RI_{\text{abs}}^{\text{Std}}}{R^{\text{Std}}I_{\text{abs}}} \quad (2.4)$$

where  $\Phi_{\Delta}^{\text{Std}}$  is the singlet oxygen quantum yield of the standard,  $I_{\text{abs}}$  and  $I_{\text{abs}}^{\text{Std}}$  are the rates of light absorbance by the photosensitizer and standard respectively, and  $R$  and  $R^{\text{Std}}$  are the photodegradation rates of the trap in the presence of the photosensitizer and standard, respectively (Durmus, 2012). Other singlet oxygen detection methods involve the examination of singlet oxygen luminescence spectra which typically display a broad peak at 1270 nm upon relaxation to the ground state (Ogilby and Foote, 1983). This approach may also be used to calculate quantum yields by comparing the integrated area under the singlet oxygen luminescence curves produced by the photosensitizer and a standard (Ogilby and Foote, 1983). Lifetime measurements may also be used to establish the presence of singlet oxygen as well as to probe environmental effects on the excited state stability (Ogilby and Foote, 1983).

#### 2.4.1.5 Photodynamic therapy

PDT is a clinical treatment that utilizes photosensitizers to produce singlet oxygen that can oxidize critical cellular macromolecules, including lipids, nucleic acids, and amino acids (Guo *et al.*, 2010). This will lead to cellular permeability alterations with the consequence of cell death by necrosis or apoptosis or both in diseased cells (Guo *et al.*, 2010). Crucial elements of PDT treatments include three components, namely the photosensitizer (PS), the light source and the oxygen within the tissue at the disease site (Guo *et al.*, 2010). Under appropriate light excitation, the photosensitizer can be excited from a ground singlet state to an excited singlet state, which undergoes intersystem crossing to a longer-lived triplet state and then reacts with nearby oxygen molecules to produce highly cytotoxic singlet oxygen ( $^1\text{O}_2$ ) (Figure 2.11, pg. 39) (Calixto *et al.*, 2016). PDT has been used for therapy in prostate, lung, head and neck, or skin cancers (Calixto *et al.*, 2016). However, conventional PDT is limited by the penetration depth of visible light

needed for its activation. NIR light can penetrate significantly deeper into tissues than visible light, because absorbance and light scattering for most body constituents are minimal in this range (Guo *et al.*, 2010).

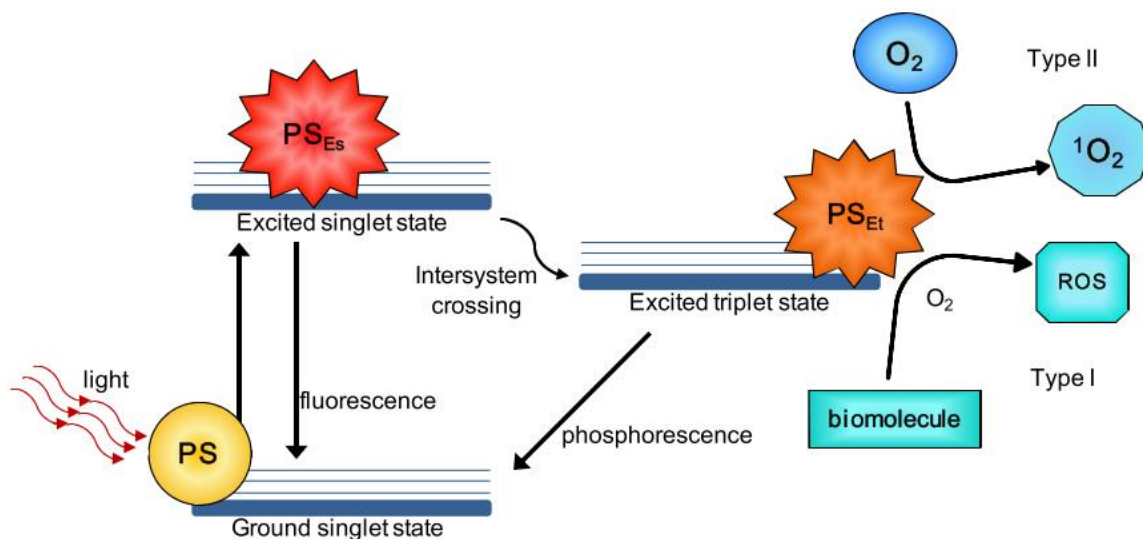


**Figure 2.11:** Schematic Jablonski's diagram showing PDT's mechanism of action. Following light absorption, the PS reaches an excited singlet state. After an intersystem crossing, the PS, now in a triplet excited state, can react in two ways: react with biomolecules through a hydrogen atom (electron) transfer to form radicals, which react with molecular oxygen to generate reactive oxygen species (ROS) (type I reaction); or, the PS in its triplet state can react directly with oxygen through energy transfer, generating singlet oxygen (Type II reaction) (Calixto *et al.*, 2016).

Nanotechnology-based PDT represents an emerging approach to improve the outcome of the treatment (Calixto *et al.*, 2016). Development of the nanotechnology-based drug delivery systems can facilitate precise intracellular delivery and has advantages such as improved delivery of a poorly water-soluble PS; facilitating transcytosis of PS across tight epithelial and endothelial barriers; delivery of large macromolecular PS to intracellular sites of action; and co-delivery of two or more drugs for combination therapy (Calixto *et al.*, 2016). UCNPs is an example of potential nanotechnology based PDT as it can efficiently convert the deeply penetrating near-infrared light to visible light that can excite photosensitizer to produce cytotoxic singlet oxygen

(Chen *et al.*, 2014). This was applied in a study by Guo *et al.*, (2010) where mesoporous silica was coated onto NaYF<sub>4</sub> upconversion nanoparticles to form a core-shell structure and was then loaded with the photosensitizer zinc (II)-phthalocyanine into the porous silica (Guo *et al.*, 2010). Upon irradiation with 980-nm near-infrared light, their efficiency in activating the loaded zinc (II)-phthalocyanine to generate singlet oxygen molecules was confirmed *in vitro* (Guo *et al.*, 2010). The cytotoxic effect of the released singlet oxygen from the nanoparticles showed a strong photodynamic effect on aurothelial carcinoma cell line (Guo *et al.*, 2010). This showed the possibility of upconversion nanoparticles as a carrier for photosensitizers and their use in photodynamic therapy of cancer and other diseases (Guo *et al.*, 2010).

There are various photosensitizers to choose from with the choice of photosensitizer being critical for successful treatment (Calixto *et al.*, 2016). Critical points need to be addressed when selecting PS which include the excitation light that should be able to reach the PS within tissue, the PS should not cause cell death in the absence of light, must be selectively captured and retained by the target cells and be able to induce immunogenic cell death (Calixto *et al.*, 2016). Examples of photosensitizers originated in nature are as follows: Chlorins and bacteriochlorins are PS that have a strong light absorption between 640 and 700 nm and are found in natural products (Calixto *et al.*, 2016). For example, chlorins are found in chlorophyll-a, present in some species of *Spirulina*, and bacteriochlorins are found in *Rhodobacter capsulatus* bacteria (Calixto *et al.*, 2016). Chlorins are hydrophilic, reduced porphyrins; therefore, their basic structure is similar to porphyrins. Several chlorin derivatives have been studied for use as PSs, including mono-L-aspartyl chlorin e6 (Calixto *et al.*, 2016). It has two important properties, a high quantum yield of singlet oxygen and an intense light absorption in wavelengths within 650 and 680 nm range (Calixto *et al.*, 2016). Some synthetic chlorins exist, such as meso-tetrakis (m-hydroxyphenyl) chlorin (m-THPC) and a benzoporphyrin derivative (BPDMA), which show promising biological activity (Calixto *et al.*, 2016). The PS Curcumin is a polyphenolic compound isolated from *Curcuma longa* that has been used for centuries as a medicine, dye and spice (Calixto *et al.*, 2016). Curcumin has a variety of pharmaceutical applications in wound treatment, liver diseases, blood purification, joint inflammation, and for antimicrobial effects (Calixto *et al.*, 2016). Curcumin is another example where it has a wide light absorption range from 300 to 500 nm (maximum peak at 430 nm) and exerts its biological activity in micromolar

concentrations (Calixto *et al.*, 2016). Hypericin is a naturally occurring red plant pigment extracted from *Hypericum perforatum*, which has been used for centuries in traditional medicine (Calixto *et al.*, 2016). It has drawn increased interest as a PS due to its photochemical properties, such as high quantum yields of singlet oxygen, light absorption close to the therapeutic window (590 nm), tumor selectivity, and low production costs (Calixto *et al.*, 2016). It shows low photobleaching, low cytotoxicity in the absence of light, and no mutagenicity (Calixto *et al.*, 2016).

Synthetically derived PS include Methylene blue (MB), which is an organic dye with both fluorescent and photosensitizing properties (Calixto *et al.*, 2016). The positive charge and its low molecular weight promote an enhanced interaction with bacteria and mammalian cells (Calixto *et al.*, 2016). The hydrophilic/lipophilic balance and net positive charge on MB allows it to easily penetrate the biological membranes and is most commonly used as a PS in antimicrobial PDT, for the treatment of *Candida albicans*, *Enterococcus faecalis*, and *Escherichia coli* infections (Calixto *et al.*, 2016). The last PS example, which will be elaborated on further, is the phthalocyanines which are second-generation PSs-similar to porphyrins (Calixto *et al.*, 2016). They have superior photophysical and photochemical properties and the possibility of modification to alter hydrophilicity; high photo- and chemical-stability; long-wavelength absorption with high extinction coefficients (much more intense absorption in the 650–750 nm region); and high singlet oxygen quantum yields (Calixto *et al.*, 2016). Like porphyrins, phthalocyanines coordinate metal ions within their core, which offers numerous options to control their physical properties by synthetic modifications (Calixto *et al.*, 2016). However, phthalocyanines lack tumor cell specificity (Calixto *et al.*, 2016). To address this drawback, phthalocyanines have been conjugated to tumor-targeting peptides or through the use of nanotechnology (Calixto *et al.*, 2016). Systems combining a PS and metal nanoparticles (hybrid nanostructures) are also highly attractive for cancer treatment due to the extended PDT capabilities (Calixto *et al.*, 2016). The hybrid nanostructures containing phthalocyanines and metal nanoparticles enhance the therapeutic effects by increasing the singlet oxygen quantum yield; the synergistic effect by means of metal nanostructures and singlet oxygen generated by phthalocyanine; and facilitating in phthalocyanine cellular uptake (Calixto *et al.*, 2016).

### 2.4.1.6 Phthalocyanine applications

Although discovered in 1924, singlet molecular oxygen became the focus of laboratory study only after 1963 (DeRosa and Crutchley, 2002). Since then, the physical, chemical, and biological properties of this energetically rich form of molecular oxygen obtained serious attention with applications ranging in various fields (DeRosa and Crutchley, 2002). In particular, the photosensitized production of singlet oxygen showed significance in a range of areas such as photooxidation, DNA damage, photodynamic therapy of cancer, to polymer science (DeRosa and Crutchley, 2002). With the increasing interest in singlet oxygen, interest arose in compounds which are able to produce singlet oxygen as well, such as phthalocyanines (Sakamoto and Ohno-Okumura, 2009). Phthalocyanine derivatives have been utilized in important functional materials in many fields as shown in Figure 2.12, pg. 42 (Sakamoto and Ohno-Okumura, 2009). Their useful properties are attributed to their efficient electron transfer abilities due to their 18 pi electron conjugated ring system found in their molecular structure (Sakamoto and Ohno-Okumura, 2009).

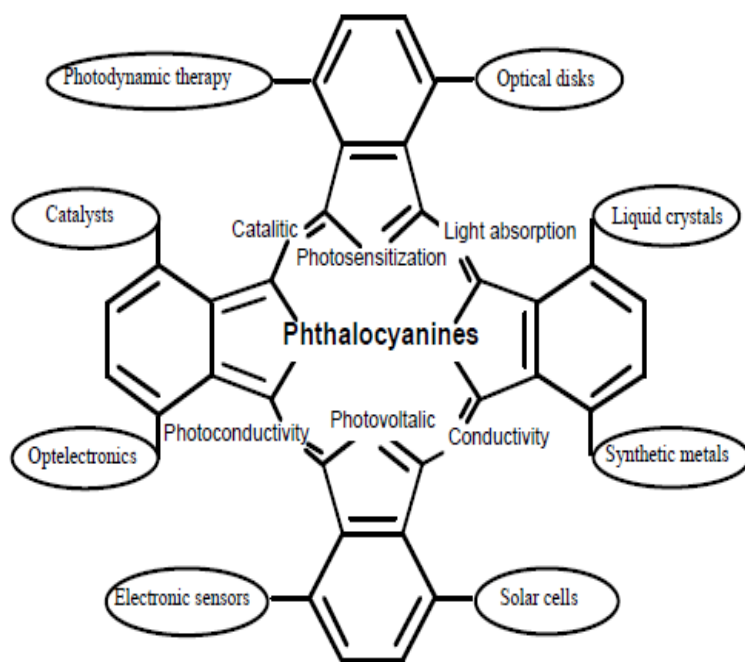


**Figure 2.12:** Various applications of phthalocyanines (Sakamoto and Ohno-Okumura, 2009).

Phthalocyanines were predominantly used as blue and green colorants for decades before being used for other applications (Wöhrle *et al.*, 2012). The usage of colorants is found in printing inks, varnish, paints, for coloring plastics, textiles and finishes (Wöhrle *et al.*, 2012). An important issue for colorants is the absorption of photons in the visible region up to the NIR which is characteristic for the most intense HOMO/LUMO transition (Q band) (Wöhrle *et al.*, 2012). Phthalocyanines are superior for coloration because they show good stability against decomposition and are absorbing in depending on the kind of substituents present, between  $\lambda$  ~650 and ~750 nm with high extinction coefficients (Wöhrle *et al.*, 2012). Although, monomolecular dissolved macrocycles exhibit an increase of the absorption wavelength by extending the  $\pi$ -system, a disadvantage is that the stability decreases dramatically with extension of the  $\pi$ -system (Wöhrle *et al.*, 2012). Examples of phthalocyanines used as colorants include the unsubstituted copper phthalocyanine which is used as a blue pigment where the halogenated form produces green pigments (Wöhrle *et al.*, 2012). The use of these phthalocyanines as well as ones with various modifications in the form of powders, pastes or suspensions is very wide for printing inks, paints, coatings, plastics, textiles, etc. (Wöhrle *et al.*, 2012). Phthalocyanines are also used as dyes, which are soluble colorants having an affinity to a substrate to be dyed, such as paper, textile fiber, leather, etc., with water-soluble phthalocyanine sulfonic acids used for dyeing cotton (Wöhrle *et al.*, 2012).

The development of liquid crystal displays (LCDs) began in the early 1970s which led, in the late 1990s, to flat screens and from 2002 to flat television screens (Wöhrle *et al.*, 2012). In the LCDs metallated phthalocyanines display two of the three color components that are responsible for their intense color and absorption of visible light in certain wavelength ranges (Wöhrle *et al.*, 2012). For the primary color blue, the copper phthalocyanine 1 is employed and for the primary color green the halogenated copper phthalocyanine-Cl~4 Br~12 is used (Wöhrle *et al.*, 2012). The colorants of the three primary colors requirements are color fastness, color uniformity, color intensity and color stability (Wöhrle *et al.*, 2012). To avoid light scattering, the colorants must be present as nanoparticles of about 20 to 30 nm in uniform and globular form that do not grow together to form agglomerates (Wöhrle *et al.*, 2012).

The first copy machine came to market in 1950, and 1973 the first color copier was introduced (Wöhrle *et al.*, 2012). The core of the device is a light-sensitive photo-conductor (Wöhrle *et al.*, 2012). More than 90% organic photoconductors based on the Y-modification of titanyl phthalocyanine is used (Wöhrle *et al.*, 2012). Advantages of this low cost titanium oxide Pc are that it has very good photoconductivity, has excellent photo stability and absorption of light in the long wavelength visible region with high absorbance (Wöhrle *et al.*, 2012). Irradiation is carried out with an efficient, compact and inexpensive LEDs that emit at about 780-800 nm light (Wöhrle *et al.*, 2012). The photoconductive titanium oxide Pc absorbs in this wavelength range with a quantum yield close to 1 (Wöhrle *et al.*, 2012).

Over the past decade the use of large organic molecules as alternatives to inorganic semiconductors has been investigated for many types of electronic and optoelectronic devices including solar cells (Wöhrle *et al.*, 2012; Petritsch *et al.*, 2000). Most of these polymers can be processed from solution, *via* spin coating, at room temperature enabling the manufacture of large area, flexible and light weight devices (Wöhrle *et al.*, 2012; Petritsch *et al.*, 2000). In organic solar/photovoltaic cells (OPVs) the organic semiconductor phthalocyanine is one of the active components (Wöhrle *et al.*, 2012; Petritsch *et al.*, 2000). Phthalocyanines exhibit useful properties for OPVs such as high crystalline order in the solid state, p-conductivity, photoconductivity, absorption in the visible range with a large extinction coefficient, right position of electronic energy levels and good photostability (Wöhrle *et al.*, 2012; Petritsch *et al.*, 2000). They can be used as the intrinsic absorber layer for visible light, where we find zinc phthalocyanines or copper phthalocyanines 1 utilised (Wöhrle *et al.*, 2012; Petritsch *et al.*, 2000). Also 1,8,15,22 tetrafluorophthalocyanine can act as an absorber and conductor, while hexadecafluorophthalocyanine can be employed as an absorber and conductor as well (Wöhrle *et al.*, 2012; Petritsch *et al.*, 2000).

#### 2.4.1.6.1 Phthalocyanine applications in catalysis

One of the most important applications of metallated phthalocyanines has been in catalysis, including large-scale industrial processes (Sorokin, 2013). Metallated phthalocyanines are very attractive due to their accessibility in terms of the cost and straightforward preparation on a large

scale as well as their chemical and thermal stability (Sorokin, 2013). The use of metallated phthalocyanine-based catalysts to prepare valuable products is a very attractive topic (Sorokin, 2013). Although the field is dominated by oxidation, the scope of reactions catalyzed by metal phthalocyanine complexes is rapidly expanding (Sorokin, 2013). A large range of various transformations including reduction, preparation of nitrogen-containing compounds, and various C–C bond formation reactions can be efficiently catalyzed by metallated phthalocyanines (Sorokin, 2013). The catalytic properties of metallated phthalocyanines can be used in large-scale processes for the preparation of bulk chemicals as well as for the synthesis of elaborated fine chemicals up to applications in total synthesis (Sorokin, 2013). The catalytic properties of metallated phthalocyanines depend on the metal and complex structure and can be tuned by appropriate structural modifications (Sorokin, 2013). An example includes the Merox process, referred to as “sweetening” in the petroleum refining industry, involving catalytic oxidation of mercaptans in the presence of sulfonated cobalt phthalocyanines to remove a major part of sulfur from petrol (Sorokin, 2013). An example that is focused towards the degradation of different pollutants involves iron tetrasulfophthalocyanine which was shown to be able to perform oxidative degradation of recalcitrant chlorinated phenols by hydrogen peroxide in aqueous solutions under mild conditions with partial mineralization (Sorokin, 2013).

## 2.4.2 Nanoparticles as catalysts

Another form of catalyst that is present and active in many parts of industry come in the form of nanoparticles. There are various kinds and ways in which these catalysts are used, with one example dating back to the 1970s (Bell, 2003). Found inside the automotive converter, under the floor of every new car manufactured in the United States in the early 1970s, the walls were coated with porous alumina (Bell, 2003). The alumina wash coat was impregnated with nanoparticles of platinum, rhodium, cerium, zirconium, lanthanum, and barium, each having a specific role (Bell, 2003). The platinum was used to oxidize hydrocarbons and carbon monoxide where the rhodium reduced  $\text{NO}_x$ . (Bell, 2003) The cerium, particularly in combination with zirconium, worked as an oxygen storage component, enabling the oxidation of hydrocarbons and carbon monoxide to occur during moments when the engine exhaust is fuel rich (Bell, 2003).

The lanthanum served to stabilize the alumina against a loss of surface area and the barium acts as a trap for sulfur trioxide (Bell, 2003).

Metal nanoparticles have been attracting much attention not only for its catalytic ability but also the possibility of these catalysts being synthesized using chemical synthetic procedures with clean, nontoxic and environmentally acceptable “green chemistry” methods (Jiang *et al.*, 2005; Evanoff and Chumanov, 2005). There is evidence that metal nanoparticles have high catalytic activities for hydrogenation, hydroformylation, carbonylation, olefin polymerization, desulfurization, ammonia synthesis and oxidation (Jiang *et al.*, 2005; Evanoff and Chumanov, 2005). Oxidation reactions are vital and prevalent in nature and prominent in industrial processes. The catalytic process can be explained by an electro-chemical mechanism, where metal nanoparticles- serve as an electron relay for an oxidant and a reductant, and electron transfer occurs *via* the metal particles (Jiang *et al.*, 2005; Evanoff and Chumanov, 2005). The catalytic efficiency of a metal nanoparticle for an electron-transfer process is closely related to the size-dependent redox properties that control its roles as an electron relay (Jiang *et al.*, 2005; Evanoff and Chumanov, 2005). Developing efficient nanoparticle catalysts for the activation of oxygen is an area which has seen a great deal of development over the years. However, with metal nanoparticle catalysts, they tend to congregate during catalytic processes, as nano-sized metal particles in the solution are active and prone to coalesce due to van der Waals forces and high surface energy unless they are protected (Jiang *et al.*, 2005; Evanoff and Chumanov, 2005). In this regard, surface modification using polymers, complex ligands, surfactants or the immobilization of the metal nanoparticles onto a desired substrate from a colloidal solution are frequently used to stabilize metal catalysts (Jiang *et al.*, 2005; Evanoff and Chumanov, 2005).

#### 2.4.2.1 Silver nanoparticles

Metal nanoparticles have unique optical, electrical and thermal properties which allows their application in various fields (Kelly *et al.*, 2003). The optical property specifically, attracts a lot of attention when mentioning these nanoparticles, especially for silver nanoparticles (Kelly *et al.*, 2003). This property within silver nanoparticles originate from the collective oscillations of conduction electrons, due to excitation by electromagnetic radiation, is called surface plasmon

polariton resonances (SPPR) or more simply the SPR band. The electric field of the incident electromagnetic radiation displaces the particle's electrons from equilibrium and produces a restoring force that results in oscillatory motion of the electrons with a characteristic frequency, called the SPPR frequency (Evanoff and Chumanov, 2005). At the same time, the oscillating electrons induce polarization of the opposite direction in the surrounding medium, and this polarization reduces the restoring force for the electrons thereby shifting the SPPR to a lower frequency (Evanoff and Chumanov, 2005). The SPPR band appears at around 400 nm for spherical silver nanoparticles, although the spherical silver nanoparticles' SPPR band can be tuned from 400 nm to 530 nm by changing the particle size and the local refractive index near the particle surface (Kelly *et al.*, 2003). Even larger shifts of the SPR peak wavelength out into the infrared region of the electromagnetic spectrum can be achieved by producing silver nanoparticles with rod or plate shapes (Kelly *et al.*, 2003).

The factors that collectively lead to these oscillations are the acceleration of the conduction electrons by the electric field of incident radiation, presence of restoring forces that result from the induced polarization in both the particle and surrounding medium, and confinement of the electrons to dimensions smaller than the wavelength of light (Evanoff and Chumanov, 2005). When SPPRs are excited, the oscillating electrons generate an electromagnetic field consisting of two components, namely a local non-radiative field around the particles that is enhanced as compared to the incident field and a radiative electromagnetic field due to resonant scattering (Evanoff and Chumanov, 2005). The distance to which the local field extends from the particle surface plays a major role in various surface-enhanced phenomena as molecules placed within this field experience increased induced polarization (Evanoff and Chumanov, 2005). At the same time, the molecules perturb the field by affecting the local dielectric environment and, because the oscillating electrons and the local field are inseparable parts of the same system, the frequency of electron oscillations is changed (Evanoff and Chumanov, 2005).

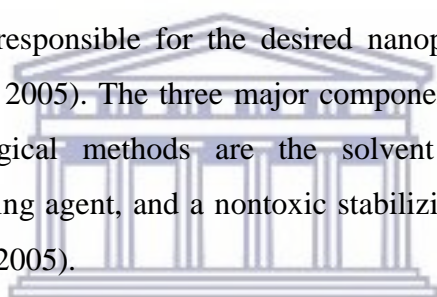
#### 2.4.2.2 Silver nanoparticle synthesis

There are many different methods in use for the synthesis of AgNPs where we can broadly categorize them as traditional and non-traditional (Evanoff and Chumanov, 2005). Traditional methods include solution phase synthesis techniques in which different silver salts and reducing

agents are used (Evanoff and Chumanov, 2005). Examples of traditional methods include the Lee– Meisel method where  $\text{AgNO}_3$  is used as the metal source. Another example, and the most common method for the synthesis of nano-sized silver particles, is the reduction of silver nitrate with sodium borohydride, referred to as the Creighton method (Evanoff and Chumanov, 2005). Non-traditional methods include silver particle synthesis through high-temperature reduction in porous solid matrices, vapor-phase condensation of a metal onto a solid support, laser ablation of a metal target into a suspending liquid, photoreduction of silver ions, and electrolysis of an silver salt solution (Evanoff and Chumanov, 2005).

One of the simpler syntheses methods involve the chemical reduction of the metal salt silver tetrafluoroborate by sodium borohydride in water. Other methods include the electrochemical method which involves the electroreduction of  $\text{AgNO}_3$  in aqueous solution in the presence of polyethylene glycol (Prabhu and Poulouse, 2012). Sonodecomposition involves the usage of ultrasonic waves to induce cavitation, a phenomenon whereby the passage of ultrasonic waves through an aqueous solution yields microscopic bubbles that expand and ultimately burst (Prabhu and Poulouse, 2012). Sonochemical reduction is a method where an aqueous silver nitrate solution is placed in an atmosphere of argon-hydrogen where reduction occurs due to the generation of hydrogen radicals during the sonication process (Prabhu and Poulouse, 2012). Silver nanoparticles are also synthesized within aqueous foams as a template (Prabhu and Poulouse, 2012). The method involves electrostatically complexing silver ions with an anionic surfactant aerosol in highly stable liquid foam (Prabhu and Poulouse, 2012). The foam is drained off and reduced by introducing sodium borohydride (Prabhu and Poulouse, 2012). The microwave synthesis of silver nanoparticles involves the reduction of silver nanoparticles using variable frequency microwave radiation compared to the conventional heating method (Prabhu and Poulouse, 2012). The method yields a faster reaction and gives a higher concentration of silver nanoparticles with the same temperature and exposure (Prabhu and Poulouse, 2012). There are also many more techniques of synthesizing silver nanoparticles, such as thermal decomposition in organic solvents, chemical and photoreduction in reverse micelles, spark discharge, and cryo- chemical synthesis (Prabhu and Poulouse, 2012).

The popularity of these methods has decreased over the years due to issues arising with the involvement of the use of toxic, hazardous chemicals, which pose potential environmental and biological risks (Prabhu and Poulouse, 2012; Evanoff and Chumanov, 2005). It is an unavoidable fact that there is a need for an environmentally and economically feasible way to synthesize these nanoparticles (Prabhu and Poulouse, 2012; Evanoff and Chumanov, 2005). This brought about the search for such methods which has led to the biomimetic production of silver nanoparticles whereby biological methods are used to synthesize the nanoparticles (Prabhu and Poulouse, 2012; Evanoff and Chumanov, 2005). There are three major sources of synthesizing silver nanoparticles biologically which include bacteria, fungi, and plant extracts (Prabhu and Poulouse, 2012; Evanoff and Chumanov, 2005). These kinds of methods are bottom-up approaches that mostly involves reduction/oxidation reactions. It is mainly the microbial enzymes or the plant phytochemicals with antioxidant or reducing properties that act on the respective compounds that is responsible for the desired nanoparticles (Prabhu and Poulouse, 2012; Evanoff and Chumanov, 2005). The three major components involved in the preparation of nanoparticles using biological methods are the solvent medium for synthesis, the environmentally friendly reducing agent, and a nontoxic stabilizing agent (Prabhu and Poulouse, 2012; Evanoff and Chumanov, 2005).



UNIVERSITY of the  
WESTERN CAPE

#### 2.4.2.3 Applications of silver nanoparticles

The applications of silver nanoparticles are widespread, which can be seen from the previously mentioned catalytic capabilities to their emergence in consumer products that includes advantages with its use (Figure 2.13, pg. 50) (Ahamed *et al.*, 2010). An example of this is seen in the catalytic use of AgNPs in the industrial epoxidation of ethylene (Mitsudome *et al.*, 2010). Deoxygenation of epoxides into alkenes is important reaction in both organic synthesis and biological chemistry; such as the deprotection of oxirane rings and in the reproduction of vitamin K in the vitamin K cycle (Mitsudome *et al.*, 2010). There are methods available for the deoxygenation of epoxides, however, it usually involves reagents that are toxic or employed in large excess, resulting in the production of undesired waste (Mitsudome *et al.*, 2010). Silver NPs imbedded on hydrotalcite has reported to catalyse the deoxygenation of epoxides into alkenes using alcohols (Mitsudome *et al.*, 2010). The AgNP catalyst also offers a green protocol for

removing oxygen from epoxides with the following advantages: 1) high catalytic activity and selectivity; 2) the use of safe and easy-to-handle catalysts and reducing reagents; 3) applicability to a wide range of epoxides; 4) a simple purification procedure owing to easy separation of the solid catalysts from the reaction mixtures; and 5) recyclability of the catalysts without any loss in their efficiency (Mitsudome *et al.*, 2010).

Other examples of AgNPs utilization found in many day-to-day applications in human life range from disinfecting medical devices, home appliances, water treatment, house cleaning chemicals, in fabric cleaners, as antireflection coatings, to improve the transfer of heat from collectors of solar energy to their fuel tanks and to produce high performance delicate electronics (Morones *et al.*, 2005; Prabhu and Poulouse, 2012; Ahamed *et al.*, 2010; Xia *et al.*, 2013; Rai *et al.*, 2009).

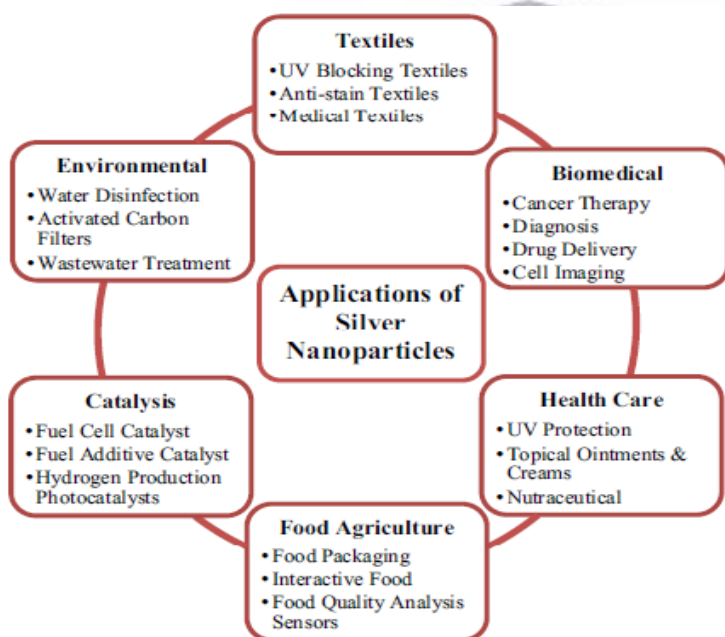


**Figure 2.13:** Various applications of silver nanoparticles (Keat *et al.*, 2015).

Although all these are important applications of silver nanoparticles, perhaps their need is most desired in the medical field (Kelly *et al.*, 2003). Their unique plasmon-resonance optical scattering properties allow AgNPs to be used in biosensing and imaging applications (Kelly *et al.*, 2003). One of topics of importance is the potential for the application of AgNPs in the treatment of diseases that require maintenance of circulating drug concentration or targeting of

specific cells or organs (Ahamed *et al.*, 2010). Their application in this regard has shown potential due to the important aspect of the nanoparticles which is the small size of the nanoparticles providing for a larger surface area for the particle and hence increasing the effect (Ahamed *et al.*, 2010). The nano-size of the particles also increases the penetration potential of the silver particles, hence again aiding in better utilization of the metal properties (Ahamed *et al.*, 2010).

The antimicrobial property, along with its useful anti-inflammatory property, is the most exploited nature of silver nanoparticles in the medical field. Dr. Robert Burrell developed the world's first AgNPs-based wound dressing in 1995 (Prabhu and Poulose, 2012). The AgNPs within the wound dressing is effective since it has a much better effect on the bacteria that tend to infect the wound and because it can easily penetrate the wound through the body fluids (Prabhu and Poulose, 2012). AgNPs also has the capacity to be used in biosensing due to the plasmonic properties of AgNPs dictated by its shape, size, and the dielectric medium that surrounds it (Prabhu and Poulose, 2012). Its properties in the dielectric medium can be exploited making it an effective candidate for detecting a large number of proteins (Prabhu and Poulose, 2012). This unique advantage that AgNPs has, can also be utilized for detecting various abnormalities and diseases in the human body including cancer (Prabhu and Poulose, 2012). The plasmonic properties of AgNPs also make it an excellent candidate for bioimaging as they, contrary to commonly used fluorescent dyes, do not undergo photobleaching and can be used to monitor dynamic events over an extended period of time (Prabhu and Poulose, 2012). The plasmonic nature of AgNPs can also be used to destroy targeted cells. The NPs can be conjugated to the target cells and then be used to absorb light and convert it to thermal energy; which can lead to thermal ablation of the target cells (Prabhu and Poulose, 2012).

## **2.5 Characterization of nanoparticles and compounds synthesized**

The use of scientific instrumentation is synonymous with nanotechnology particularly when characterization is involved. Some would consider nanotechnology “instrumentation heavy” as many various pieces of instrumentation are required to confirm that nanoparticles have been

successfully synthesized. Once that is achieved any modification of the nanoparticles would also require further confirmation of success through instrumentation (Joshi *et al.*, 2008). Although there has always been the use of instrumentation within science, the reliance of nanotechnology and its emergence has been, to a certain extent, dependent on instrumentation (Joshi *et al.*, 2008). One instrument which is designed for the nanoscale is the atomic force microscope (Luykx *et al.*, 2008). This form of scanning probe microscopy quantitatively measures the surface roughness and can be used for visualizing the surface on many types of material surfaces including polymer nanocomposites and nano-finished or nanocoated textiles (Joshi *et al.*, 2008). This kind of microscopy is a nondestructive technique and it has a very high three-dimensional spatial resolution (Luykx *et al.*, 2008). The techniques used to characterize the nanoparticles synthesized in this work are briefly described below.

### **2.5.1 Transmission electron microscopy**

There are many instruments that are utilized amongst nano-researchers. One of the more popular ones, when it comes to imaging, is transmission electron microscopy (TEM). Within the microscope, electrons that pass through the sample provide information not only about particle size and shape, but also about the lattice structure and the chemical composition of individual particles (Joshi *et al.*, 2008; Luykx *et al.*, 2008). The principle of the technique involves an incident electron beam that is transmitted through a very thin foil specimen, during which the incident electrons interacting with specimen are transformed to unscattered electrons, elastically scattered electrons or inelastically scattered electrons (Lin *et al.*, 2014). The magnification of TEM is mainly determined by the ratio of the distance between objective lens and the specimen and the distance between objective lens and its image plane (Lin *et al.*, 2014). The scattered or unscattered electrons are focused by a series of electromagnetic lenses and then projected on a screen to generate an electron diffraction, amplitude-contrast image, a phase-contrast image or a shadow image of varying darkness according to the density of unscattered electrons (Lin *et al.*, 2014). The source of radiation is generated using an electron gun. The resulting beam of electrons is focused into a tight, coherent beam by multiple electromagnetic lenses and apertures. The lens system is designed to eliminate stray electrons as well as to control and focus the electron beam (Joshi *et al.*, 2008; Luykx *et al.*, 2008).

## 2.5.2 X-ray powder diffraction

X-ray diffraction (XRD) is a method which utilizes X-rays and is a versatile, nondestructive technique that reveals detailed information about the chemical composition and crystallographic structure of natural and manufactured materials (Joshi *et al.*, 2008; Luykx *et al.*, 2008). X-rays are electromagnetic radiation similar to light, but with a much shorter wavelength. They are produced when electrically charged particles of sufficient energy are decelerated. In an X-ray tube, the high voltage maintained across the electrodes draws electrons toward a metal target. X-rays are produced at the point of impact, and radiate in all directions (Joshi *et al.*, 2008; Luykx *et al.*, 2008). X-ray crystallography yields high-resolution structures of biomolecules and complexes from the solid phase based on their atomic structure. During this XRD analysis, X-ray beams are reflected off the parallel atomic layers within a molecule over a range of diffraction angles. Because the X-ray beam has a single specific wavelength, constructive or destructive interference can occur. At certain angles, the reflected rays are in phase (constructive interference), and this will give a peak in a diffractogram. From the diffraction pattern, one can identify the molecule or mixture of molecules (Joshi *et al.*, 2008; Luykx *et al.*, 2008). More or less like a “fingerprint”, every molecule has its own distinct set of diffraction peaks that can be used to identify it. Identification of the molecules is usually done by comparing the measured diffractogram with a database of known diffraction data (Joshi *et al.*, 2008; Luykx *et al.*, 2008).

There are number of crystalline nanoparticles that can be characterized with X-ray diffraction such as metals, metal oxides, semiconductors, layered nanomaterials and crystalline polymers (Lin *et al.*, 2014). In the case of nanomaterials, diffraction peaks appear much broader compared to their bulk counterparts (Langford *et al.*, 2000). This broadening can be used to calculate the minimum particle sizes of the nanoparticles from the XRD diffraction pattern using the Debye-Scherrer equation, Equation 2.6:

$$d = \frac{k\lambda}{\beta \cos\theta} \quad (2.6)$$

where  $\lambda$  is the X-ray wavelength in nanometer (nm),  $\beta$  is the peak width of the diffraction peak profile at half maximum height resulting from small crystallite size in radians and  $K$  is a constant

related to crystallite shape, normally taken as 0.9. The value of  $\beta$  in  $2\theta$  axis of diffraction profile must be in radians with the  $\theta$  in degrees or radians (Monshi *et al.*, 2012).

### **2.5.3 UV/Visible spectroscopy**

An instrument used within nanoscience specifically for fluorescent nanoparticles and nanoparticles with an SPR band, is UV/Visible spectroscopy (Joshi *et al.*, 2008). This instrument consists of a light source, reference and sample beams, a monochromator and a detector (Joshi *et al.*, 2008). The ultraviolet-visible spectrum for a sample is obtained by exposing a sample of the compound to ultraviolet light from a light source, such as a Xenon lamp (Joshi *et al.*, 2008). The reference beam in the spectrophotometer travels from the light source to the detector without interacting with the sample. The sample beam interacts with the sample exposing it to ultraviolet light of continuously changing wavelength. When the emitted wavelength corresponds to the energy level which promotes an electron to a higher molecular orbital, energy is absorbed. The detector records the ratio between reference and sample beam intensities. The computer determines at what wavelength the sample absorbed a large amount of ultraviolet light by scanning for the largest gap between the two beams (Joshi *et al.*, 2008). When a large gap between intensities is found, where the sample beam intensity is significantly weaker than the reference beam, the computer plots this wavelength as having the highest ultraviolet light absorbance as it prepares the ultraviolet absorbance spectrum (Joshi *et al.*, 2008).

### **2.5.4 Fourier Transform-Infrared spectroscopy**

A method to identify functional groups present in nanomaterials due to modification is a frequent requirement in nanoscience and nanotechnology research. Fourier Transform-Infrared spectroscopy is a popular choice utilised due to its versatility, relative ease of use and ability to use as a quantification tool. Atoms in chemical bonds constantly vibrate (Lin *et al.*, 2014). The vibration frequency depends on the masses of the atoms that contributes to a bond and cohesiveness of the bond. Since bonds have atoms with different shapes and sizes and different strength, each combination of atoms in each type of bond has a unique harmonic frequency. This natural frequency lies in the range of infrared region (Lin *et al.*, 2014). When the infrared

radiation with the same harmonic frequency of the bond shines upon the bond, the bond vibration is amplified by increased transfer of energy from the infrared radiation (Lin *et al.*, 2014). When a range of infrared frequencies is given to the material, it only absorbs infrared frequencies that correspond to the natural frequencies of the bonds that exist in the sample (Lin *et al.*, 2014). Others are not absorbed and can be analysed using an Infrared spectrometer, which informs the user of the frequencies that are absorbed by the sample. This therefore provides important information about the functional groups present in the sample (Lin *et al.*, 2014).

## 2.5.5 Nuclear Magnetic Resonance Spectroscopy

Another method which can be used for nanoparticles is Nuclear Magnetic Resonance (NMR), although it is more popularly used for the determination of organic chemical structures (Luykx *et al.*, 2008). NMR is based upon the measurement of the absorption of radiofrequency radiation by atomic nuclei with non-zero spins in a strong magnetic field (Luykx *et al.*, 2008). The absorption of the atomic nuclei is affected by the surrounding atoms, which cause small local modifications to the external magnetic field (Luykx *et al.*, 2008). Among nuclei with non-zero spins, the isotopes of  $^1\text{H}$  and  $^{13}\text{C}$  are the most used in NMR, although other isotopes such as  $^{15}\text{N}$ ,  $^{17}\text{F}$ , or  $^{31}\text{P}$  are also frequently employed (Luykx *et al.*, 2008). NMR is synonymous with certain characteristics which include being a nondestructive method that makes it possible to perform different analyses on the same sample; it is able to detect different nuclei, allowing a study of the sample from different perspectives; it is structure-sensitive, that is, capable of investigating structural features in the solution phase and solid phase; and it is sensitive to dynamics, which allows differentiation between molecules or portions of molecules with different mobility (Luykx *et al.*, 2008).

Solid-state NMR has proven to be a useful tool for the analysis of structure and dynamics in solids. It is commonly used in tandem with other techniques such as X-ray crystallography and powder X-ray diffraction where calculations are used in order to correlate NMR parameters with bonding and structure (Laws *et al.*, 2002). The NMR parameters of solids are very sensitive to the changes in the local environment of nuclei and therefore, any changes in bond lengths, angles and molecular symmetry will have significant effects on NMR spectra (Laws *et al.*, 2002). In

solution NMR spectra, sharp, well-resolved peaks are normally observed due to the fast, isotropic (orientation-independent) molecular tumbling that serves to average the anisotropic (orientation-dependent) NMR interactions. In solid state NMR, anisotropic NMR interactions generally lead to very broad powder patterns that reduce both resolution and sensitivity (Laws *et al.*, 2002). The broadening can be attributed to interactions like the quadrupolar interactions which involve nuclei with a spin-quantum number of  $I > \frac{1}{2}$  (Laws *et al.*, 2002). Other interactions attributed to the solid state NMR spectra include the Zeeman interaction of nuclear spins, direct dipolar spin interactions, indirect spin-spin coupling (*J*-coupling), nuclear-electron spin coupling (paramagnetic), direct spin-lattice interactions, indirect spin-lattice interaction *via* electrons and chemical shielding (Laws *et al.*, 2002; Schwartz *et al.*, 2007).

The broad spectra obtained contain important information about the local chemical and geometrical environments around the nucleus of interest as well as dynamics, which is not available from the solution NMR data (Laws *et al.*, 2002; Schwartz *et al.*, 2007). Advancements in solid-state NMR spectroscopy used to reduce the line broadening of solid-state NMR spectra came about by the introduction of magic-angle spinning (MAS). Magic-angle spinning introduces artificial motion by placing the axis of the sample rotor at the magic angle ( $54.74^\circ$ ) with respect to magnetic field (Laws *et al.*, 2002; Schwartz *et al.*, 2007). The rate of MAS must be greater than or equal to the magnitude of the anisotropic interaction to average it to zero (Laws *et al.*, 2002; Schwartz *et al.*, 2007). Samples are finely powdered and packed tightly into rotors, which are then spun at rates from 1 to 35 kHz, depending on the rotor size and type of experiment being conducted. If the sample is spun at a rate less than the magnitude of the anisotropic interaction, a manifold of spinning sidebands becomes visible, which are separated by the rate of spinning (in Hz) (Laws *et al.*, 2002; Schwartz *et al.*, 2007). A number of other methods have been developed in order to minimize large anisotropic NMR interactions between nuclei and increase signal to noise ratio in nmr spectra include dilution, multiple-pulse sequences and cross polarization (Laws *et al.*, 2002; Schwartz *et al.*, 2007).

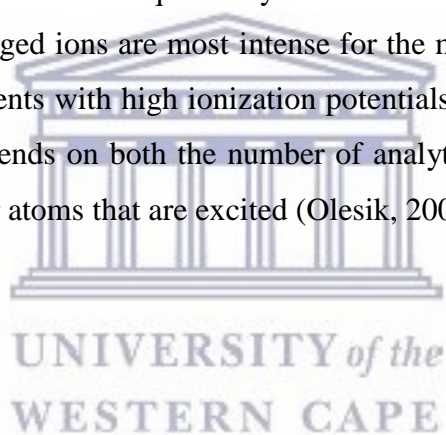
## 2.5.6 Mass spectroscopy

A method also popular for the use in structure identification is Mass spectroscopy (MS) which is a powerful analytical technique for measuring the mass-to-charge ratio of ion (Walch *et al.*, 2008; Watrous *et al.*, 2011; Aichler and Walch, 2015). MS is one of the major analytical techniques used to examine the mass, elemental composition and chemical structure of a particle or a molecule (Lin *et al.*, 2014). The basic principle of MS is to distinguish charged particles with different masses based on their mass-to-charge ratios (Lin *et al.*, 2014). MS provides a high degree of precision and accuracy for molecular weight determination, as well as high detection sensitivity, which only requires  $10^{-9}$  to  $10^{-21}$  mol of a sample (Lin *et al.*, 2014). Several characteristics of nanomaterials and samples can be depicted using various MS procedures, distinguished by their ion sources, separation methods and detector systems (Lin *et al.*, 2014). Among the ionization techniques coupled with MS analyzers, matrix-assisted laser desorption/ionization (MALDI) and electrospray ionization (ESI) are commonly used to ionize and volatilize the sample derivatives instead of introducing significant fragmentation or decomposition of the molecules (Lin *et al.*, 2014). The development of these ionization techniques, such as MALDI, ESI, and desorption electrospray ionization (DESI), has allowed great progress within this instrumentation field (Walch *et al.*, 2008; Watrous *et al.*, 2011; Aichler and Walch, 2015). The pulsed laser used for MALDI makes it an ideal ionization technique for Time of Flight-MS since there is a precisely defined time of ion generation. The ionized molecules are accelerated electrostatically to a defined kinetic energy, and the flight time is determined by a detector positioned at the end of the field-free region. At a fixed kinetic energy, small ions travel at higher speed than large ions, that is, they have a shorter flight time (Walch *et al.*, 2008; Watrous *et al.*, 2011; Aichler and Walch, 2015). Electron impact (EI) is another ionization technique which was one of the first methods used with mass spectroscopy (Griffiths, 2008). It is an energetic ionisation technique that produces fragment ions which are smaller parts of the original molecule (Fenn *et al.*, 1990). The ions are accelerated out of the source and pass through a series of slits to produce a focussed beam. The beam of ions pass through a flight tube which is located between the poles of an electromagnet, and are separated according to their mass/charge ratio by scanning the magnetic field (Fenn *et al.*, 1990). The separated ions are

detected by electron or photomultipliers to produce a plot of intensity versus mass/charge ratio representative of the sample being analysed (Fenn *et al.*, 1990).

## 2.5.7 Inductively Coupled Plasma Spectroscopy

The inductively coupled plasma (ICP) instrument is a source for rapid spectroscopic multielement analysis as a result of a set of attributes, including low detection limits, a wide linear dynamic range, and high precision (Olesik, 2000). The ICP is a partially ionized gas produced in a quartz torch using a 12.5-kW radio frequency power supply. Samples are typically introduced into the center of the plasma as aerosols. Light emitted from a 3- to 5 mm-high region of the plasma is focused onto the entrance slit of a monochromator or polychromator to monitor emission from different elements either sequentially or simultaneously (Olesik, 2000). Spectral lines resulting from singly charged ions are most intense for the majority of elements, and atom lines are most intense for elements with high ionization potentials and the alkali metals (Olesik, 2000). The detected signal depends on both the number of analyte ions or atoms in the plasma and the fraction of those ions or atoms that are excited (Olesik, 2000).



## Chapter 3: Materials and Methods

### 3.1 Materials

The chemicals ytterbium chloride hexahydrate, yttrium nitrate hexahydrate, erbium chloride hexahydrate, holmium oxide, scandium oxide, ammonium fluoride, sodium chloride, ethylene glycol, lithium chloride, olelyamine, cyclohexane, activated charcoal, potassium hydroxide, aniline, diphenylisobenzofuran (DPBF), 4-iodophthalonitrile, (hydroxymethyl)phenyl boronic acid, tetrakis(triphenylphosphine)palladium(0), tetrahydrofuran, zinc acetate dihydrate, pentanol, 4-nitrophthalonitrile, palladium on carbon, 1,8-diazabicyclo[5,4,0]undec-7-ene (DBU), pyridine, 1,2 dicyanobenzene, lithium metal, glacial acetic acid and diphenylisobenzofuran was purchased from Sigma-Aldrich, Steinheim, Germany. The solvents ethanol, methanol and dichloromethane were purchased from Crest Chemicals, Cape Town, South Africa. The chemicals potassium chloride, potassium carbonate and nitric acid were purchased from Kimix, Cape Town, South Africa. Silver nitrate, dimethyl sulfoxide (DMSO), deuterated dimethylsulfoxide and dimethylformamide was purchased from Merck, Wadeville Gauteng, South Africa. Milli-Q water ( $15.0 \text{ M}\Omega\cdot\text{cm}^{-1}$ ) was utilized for all reactions where it was required.

### 3.2 Instrumentation

#### 3.2.1 NMR

NMR analysis in the solution state was achieved through the use of a Bruker 400 MHz Avance IIIHD Nanobay spectrometer equipped with a 5 mm BBO probe at 333 K using standard 1D and 2D NMR pulse sequences. All spectra were referenced to the solvent peaks.

Solid state nmr spectra were recorded at 11.7 T, corresponding to a  $^1\text{H}$  Larmor frequency of 500 MHz. The  $^{23}\text{Na}$  and  $^{45}\text{Sc}$  spectra were recorded on a Bruker Avance III HD spectrometer using either a 2.5 mm triple resonance (Trigamma) or 4 mm BBO magic-angle spinning (MAS) probe and a MAS spinning frequency of 11 kHz for both nuclei. Simple one-pulse  $^{23}\text{Na}$  MAS spectra were acquired using a power level of 100 W, a pulse length of 3.5  $\mu\text{s}$  and 100 to 1000 transients were added with an optimized recycle delay of 4 s.  $^{45}\text{Sc}$  MAS spectra were also acquired using a

one-pulse experiment with a power level 90 W, a pulse length 4.5  $\mu$ s 24 transients were added with an optimized 3 s recycle delay.  $^{23}\text{Na}$  and  $^{45}\text{Sc}$  NMR chemical shifts were externally referenced with respect to solid NaCl and 0.1 M ScCl<sub>3</sub>, respectively, all set to 0 ppm. The data obtained were analysed using the Bruker Topspin 3.2 pl5 software and the data fitted using Sola which is part of the Topspin package. The  $\delta_{\text{QIS}}$  values were calculated for the UCNPs based on the equation

$$\delta_{\text{QIS}} = \delta_{\text{CG}} - \delta_{\text{iso}} = -25000(C_{\text{Q}}^2/\nu_0^2)(1 + \eta_{\text{Q}}^2/3) \quad (3.1)$$

where  $\delta_{\text{CG}}$  (ppm) is the peak position or center of gravity,  $\delta_{\text{iso}}$  (ppm) the true isotropic chemical shift in the absence of quadrupolar coupling,  $C_{\text{Q}}$  (MHz) the quadrupolar coupling constant,  $\nu_0$  (MHz) is the Larmor frequency of the observed nucleus, and  $\eta_{\text{Q}}$  the asymmetry parameter of the quadrupolar coupling tensor.

### 3.2.2 XRD

Analysis utilising X-ray diffraction was achieved through the use of a Bruker AXS (Germany) D8 Advance diffractometer (voltage 40 kV; current 40 mA). The XRD spectra were recorded in the  $2\theta$  range 10-90° using an X-ray source of Cu K $\alpha$  ( $\lambda=0.154$  nm) monochromatic radiation.

### 3.2.3 UV/Visible spectroscopy

Analysis utilising UV/Visible spectroscopy analysis was achieved through the use of a Varian Cary 50E UV-Vis spectrophotometer with Cintral version software. The sample was dispersed in relevant solvent and measured in a quartz cuvette with a path length of 1 cm. The visible range for the measurements was set to be from 200 nm to 800 nm.

### 3.2.4 FT-IR spectroscopy

Fourier transform infrared spectra were acquired through the use of a PerkinElmer Spectrum 400, FT-IR/FT-NIR spectrophotometer with Spectrum software. The powdered measurements were done using an attenuated total reflectance (ATR) accessory on the PerkinElmer Spectrum 400, FT-IR/FT-NIR spectrophotometer, using the instrument software, Spectrum. The range for the measurements was set to be from  $650\text{ cm}^{-1}$  to  $4000\text{ cm}^{-1}$

### 3.2.5 TEM

Analysis utilising transmission electron microscopy was achieved through the use of a FEI Tecnai G2 20 field-emission gun (FEG) transmission electron microscope, operated in bright field mode at an accelerating voltage of 200 kV. Energy dispersive X-ray spectra (EDX) were collected using an EDAX liquid nitrogen cooled lithium-doped silicon detector. The size of the nanoparticles was determined with ImageJ software. The samples were dispersed in the relevant solvent, and then prepared by drop-coating one drop of the specimen solution onto a holey carbon coated copper grid. The specimen solution was then dried under a xenon lamp for about 10 minutes. The sample coated grids were subsequently analyzed under the microscope.

### 3.2.6 ICP-AES

Analysis utilising ICP-AES was achieved through the use of a Thermo ICap 6200 ICP-AES. The samples were prepared for ICP-AES by taking 2.5 mg of sample and adding it to 500  $\mu\text{L}$  of nitric acid where it was heated for 1 hour at  $100\text{ }^{\circ}\text{C}$ . The sample was then accurately made up to 25 mL of deionized water. The instrument was calibrated and validated using traceable standards in order to quantify the upconversion nanoparticles or silver nanoparticles in solution.

### 3.2.7 Mass spectroscopy

#### GC-EI MS:

GC-mass spectroscopic analysis was achieved through the use of a Agilent/ Technologies 7820A coupled 5977E mass spectrometer with a HP5 GC column. The sample was made up to a concentration of 2mg/2 ml in the relevant solvent with a teflon lined cap *vial*. The sample was then injected into the MS column. The times of the different fragmented eluents were recorded where the mass spectrometer analysed each fragments separately.

#### MALDI-TOF MS:

Mass spectral data were acquired on an UltrafleXtreme MALDI TOF/TOF system (Bruker Daltonics, Bremen, Germany). The instrument was operated in reflector positive ion mode between a scan range of 0 -1500 amu and 500 – 1500 amu. The voltages of the ion sources were set at 25 and 22.5 kV for ion sources 1 and 2 respectively, while the lens was set at 8.00 kV. The reflector 1 and 2 voltages were set at 26.55 and 13.45 kV respectively. The spectra were ionised using alpha-cyano-4-hydroxy-cinnamic acid (CHCA) as the MALDI matrix, using a 337 nm nitrogen laser. Spectra were internally calibrated using calibration standard II (Bruker Daltonics, Bremen, Germany). This calibration method provided a mass accuracy of 50 ppm across the mass range 700 Da to 4000 Da. Spectra of accumulated 4,000 shots were automatically processed using FlexAnalysis 3. 4 software (Bruker Daltonics, Bremen, Germany). The Sample was prepared at 0.01 µg/µl in Solvent A (50 % methanol; 0.1 % trifluoroacetic acid). Matrix (CHCA) was prepared at 10 µg/µl in Solvent A. Sample was then diluted to 1 ng/µl and 1 µl of the solution deposited onto a MTP 384 ground steel target plate and allowed to air dry prior to the addition of 1 µl CHCA matrix. The sample was allowed to air dry and following co-crystallization, samples were analyzed by MALDI TOF-MS.

### 3.2.8 Fluorescence spectroscopy

The upconversion luminescence of the nanoparticles was characterized using an Edinburgh Instruments FLS980 fluorescence spectrometer. They were excited using a 980 nm diode laser and the upconversion luminescence was detected using a double monochromator and

photomultiplier detector. The nanoparticles were measured using a laser power of 1 W, a bandpass of 1 nm and an integration time of 1 s. For solutions the laser power was increased to 1.5 W, the bandpass to 2 nm and the integration time to 2 s.

The steady state emission spectra of the phthalocyanines as well as the AgNPs supported on the phthalocyanine was measured utilising a Biotek Synergy Mx fluorescence spectrometer using Gen5 microplate reader software.

### 3.2.19 Microwave setup

The synthesis of the upconversion nanoparticles were achieved using a CEM Discover SP-Microwave Synthesizer. The temperature was set at 160°C for 1 hour with a pressure of 150 psi and 150 W as the power level.

### 3.2.10 Elemental analysis

Elemental analysis was done using a Vario-Elementar Microcube ELIII.

### 3.2.11 Singlet oxygen quantum yields $\Phi_{\Delta}$

A chemical method was employed in this work for  $\Phi_{\Delta}$  determination, using the experimental set-up shown in Figure 3.1, pg. 64. The  $\Phi_{\Delta}$  values were determined by monitoring the change in the absorbance of the singlet oxygen quencher degradation, at 416 nm for DPBF, with time. Values obtained were used to calculate  $\Phi_{\Delta}$  according to Equation 2.4 (ZnP  $\Phi_{\Delta} = 0.67$  in DMSO (Durmus, 2012)). A General Electric Quartz lamp (300 W) was used as an irradiation source. Water filters were used to filter off ultra-violet and far infrared radiations. An interference filter 670 nm with bandpass of 40 nm was placed in the light path just before the cell containing the sample. An air-saturated solution of the MPcs (2.0 mL) with the DPBF singlet oxygen quencher was placed in a 1 cm path length spectrophotometric quartz cell, and photolysed at the Q-band region using a 300 W General electric quartz lamp. The wavelength of the interference filter was chosen such that it was close to the Q band absorption of the MPc.

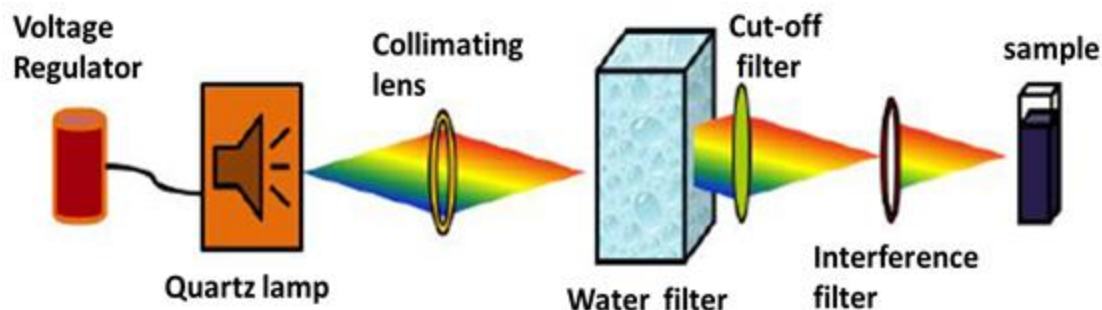
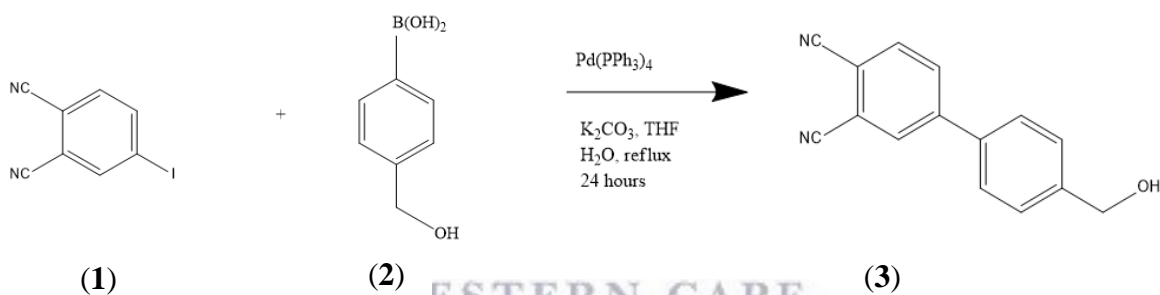


**Figure 3.1:** Singlet oxygen set up (Kuznetsova *et al.*, 2000).

## 3.3 Methods

### 3.3.1 Phthalocyanine synthesis

#### 3.3.1.1 Synthesis of 4-[4-(hydroxymethyl)phenyl] phthalonitrile



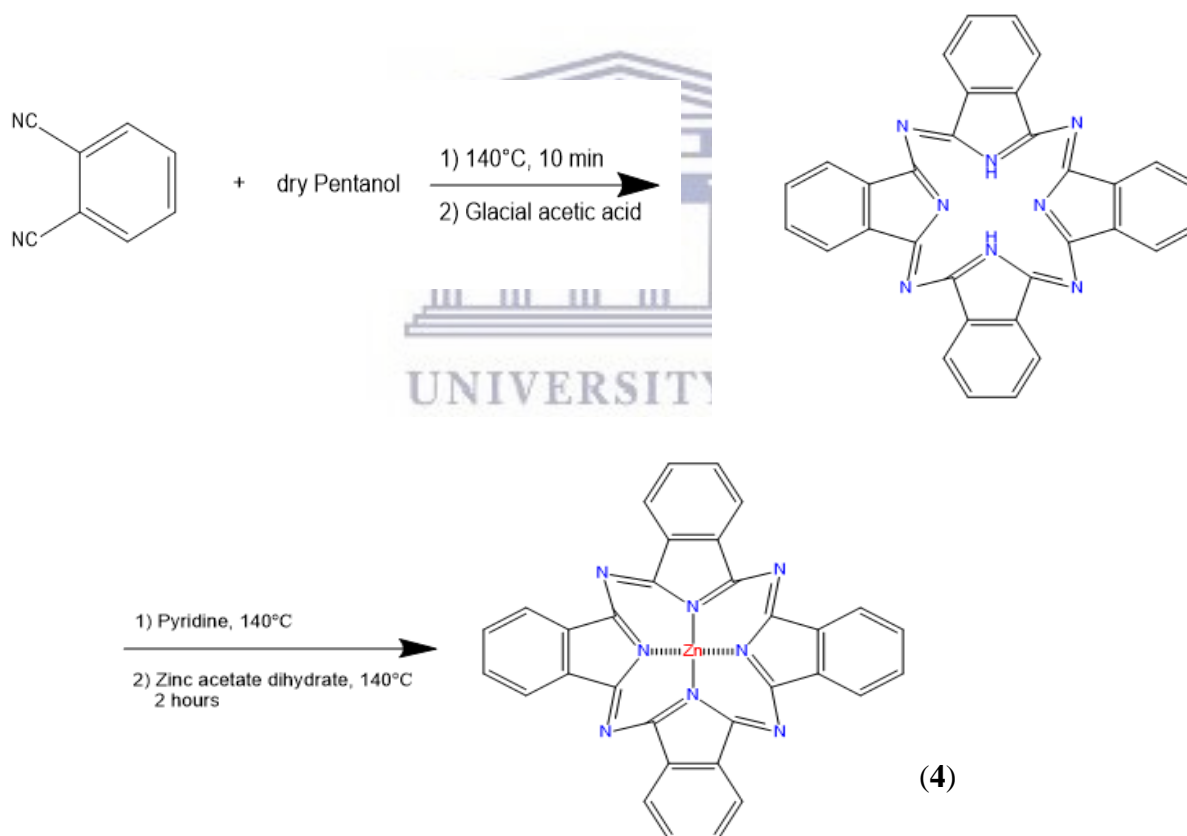
**Scheme 3.1:** Illustration of the Suzuki coupling reaction between 4-iodophthalonitrile and (hydroxymethyl)phenylboronic acid.

The Suzuki coupling reaction utilised is a modified form of the previously described Suzuki coupling reaction method described by Byrd *et al.* (2016). Briefly, 4-iodophthalonitrile (1) (0.335 g, 1.32 mmol) was added to 12 ml tetrahydrofuran. Under an argon atmosphere tetrakis(triphenylphosphine)palladium (0.0305 g, 0.0264 mmol) was added to the solution and the reaction mixture was stirred for 20 min. Afterwards, 4 - (hydroxymethyl)phenylboronic acid (2) (0.2 g, 1.32 mmol), potassium carbonate (0.182 g, 1.32 mmol) and 17 ml of water was added to the reaction mixture and refluxed for 24 hours. The mixture was then cooled to room temperature and the tetrahydrofuran was removed under reduced pressure.

Yield: 0.283 g. (91%). IR:  $\text{mmax/cm}^{-1}$ : 3400 (–OH), 3014, 3086 (Ar–C–H), 2934, 2854 (Aliphatic–C–H), 2260 (C≡N), 1600 (C=N), 1500, 1328, 1064, 792 (C=C), 1250 (C–N).  $^1\text{H}$  NMR (DMSO- $d_6$ , 400 MHz, 298K): 7.80 (2H, d,  $J = 8.3\text{Hz}$ ), 7.49 (2H, d,  $J = 8.3\text{ Hz}$ ), 4.56 (2H, d,  $J = 5.6\text{ Hz}$ ), 5.40 (1H, t,  $J = 5.6\text{ Hz}$ ), 8.21 (1H, dd,  $J = 8.4, 1.7\text{ Hz}$ ), 8.17 (1H, d,  $J = 8.3\text{ Hz}$ ) and 8.48 (1H, d,  $J = 1.6\text{ Hz}$ ).  $^{13}\text{C}$  NMR (DMSO- $d_6$ , 400 MHz, 298K): 127.3 (CH), 127.4 (CH), 144.4 (C), 62.5 (CH<sub>2</sub>), 134.8 (C), 145.2 (C), 131.6 (CH), 134.7 (CH), 115.5 (C), 112.8 (C), 131.9 (CH), 116.3 (C) and 116.2 (C). GC-MS: Calc.  $m/z$ : 234; Found  $m/z$ : 234.23.

### 3.3.1.2 Preparation of phthalocyanines

#### 3.3.1.2.1 Synthesis of zinc phthalocyanine (complex 4)

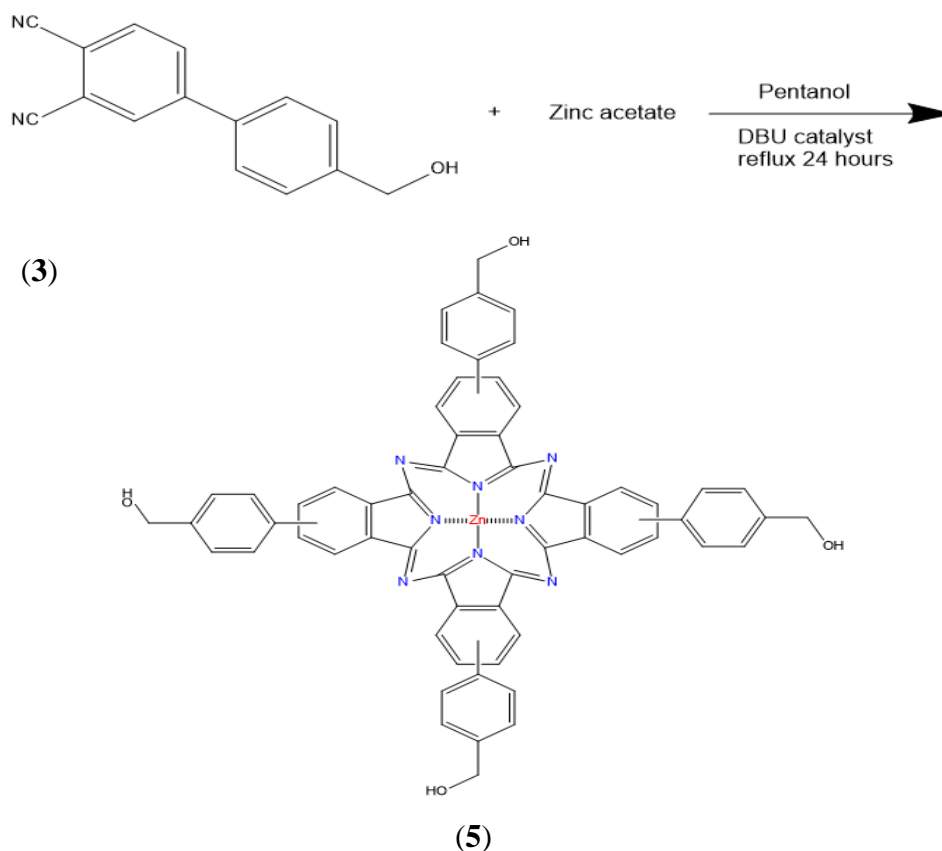


**Scheme 3.2:** Zinc phthalocyanine (4) synthesis using the unmetallated phthalocyanine product and zinc acetate as the metal source.

In 25 ml of dry pentanol, one equivalent of 1,2 dicyanobenzene was stirred under reflux in an argon atmosphere at 140°C for 10 min. Thereafter the reaction mixture was left to cool to room

temperature. 40 ml of glacial acetic acid was added to the mixture resulting in unmetallated phthalocyanine (H<sub>2</sub>Pc). The resulting precipitates were centrifuged and washed with copious amounts of deionized water. H<sub>2</sub>Pc (0.1 mg, 0.19 mmol) was added to 2 ml of pyridine and heated at 140°C under reflux. Zinc acetate dihydrate (0.043 g, 0.2 mmol) was then added and the reaction was stirred and run for 2 hours. After cooling to room temperature excess amounts of deionized water and then centrifuged and the precipitate was collected and stored as the ZnPc. Yield: 0.061 g. (53%). IR: mmax/cm<sup>-1</sup>: 3014, 3086 (Ar-C-H), 1500,1328, 1064, 977 (C=C), 1250 (C-N).

### 3. 3.1.2.2 Synthesis of 4-[4-(hydroxymethyl)phenyl] Zinc Phthalocyanine (complex **5**)



**Scheme 3.3:** Phthalocyanine (**5**) synthesis using the prepared 4-[4-(hydroxymethyl)phenyl] phthalonitrile (**3**), DBU and zinc acetate.

The synthesis of the phthalocyanine was carried out using a modified method as previously described by Nombona *et al.* (2012). Briefly, compound (**3**) (0.140 g, 0.6 mmol) and zinc acetate

(0.092 g, 0.5 mmol) was added to 10 ml of dry pentanol and stirred under a nitrogen atmosphere. The reaction was heated to 60°C and 0.5 ml of the DBU catalyst was added. The reaction was allowed to proceed for a further 24 hours. After cooling to room temperature, the solution was centrifuged at 6000 rpm for 5 minutes and the precipitate collected. The precipitate was washed several times with hexane where it was dried and stored for later use.

Yield: 0.147 mg. (28%). IR:  $\text{max/cm}^{-1}$ : 3500 (–OH), 3014, 3086 (Ar–C–H), 1600 (C=N), 1500, 1328, 1064, 977 (C=C), 1250 (C–N).  $^1\text{H NMR}$  (DMSO- $d_6$ , 400 MHz, 298K): 4.6 (8H, d, CH<sub>2</sub>–OH), 7.4 – 8.2 (28H, m, Aromatic–H), 9.3 (1H, brs, OH). MALDI–TOF MS: Calc.  $m/z$ : 1002.5. Found [M–4H]<sup>+</sup>: 998.5. UV–Vis (DMSO)  $k_{\text{max/nm}}$  (log  $\epsilon$ ) 348 (4.72), 606 (4.33), 690 (4.88). Elemental Anal. Calc. for C<sub>64</sub>H<sub>56</sub>N<sub>8</sub>O<sub>4</sub>Zn(ZnO)\*: C 62.5%, H 4.6%, N 9.2%, O 7.8%, Zn 615.9%. Found: C 60.0%, H 5.1%, N 12.1%. \* ZnO was detected in the XRD spectrum.

### 3.3.1.3 Synthesis of silver nanoparticles

#### 3.3.1.3.1 Preparation of silver nanoparticles (6)

The synthesis of silver nanoparticles was carried out by a slightly modified method as previously described by Cai *et al.* (2013). Briefly, 0.034 g of AgNO<sub>3</sub> (0.034g, 0.2 mmol) was added to oleylamine (1.5 g, 0.006 mol) at 80 °C. The resulting colorless, clear solution was added to oleylamine (6 g, 0.022 mol) at 200 °C under vigorous stirring. After stirring for 10 min, ethanol was used to precipitate the product and the nanoparticles collected by centrifugation. The precipitate was washed with ethanol several times, and the final product was dispersed in cyclohexane for further use.

Yield: 0.023 g. (68%).

#### 3.3.1.3.2 Preparation of AgNPs/C (7) and AgNPs/Pc (8) as modified supports

The synthesis of AgNPs/C (7) was carried out by a method previously described by Cai *et al.* (2013). Briefly, 200 mg of charcoal was dispersed in cyclohexane and stirred under sonication for 1 h. After cooling to room temperature, 10 mg of AgNPs was added and mixed where the slurry was stirred for 24 hours and cyclohexane removed under reduced pressure. The synthesis

of AgNPs/Pc (**8**) was carried out with a slight modification to the method previously described for the AgNPs/C (**7**). Instead of 200 mg of charcoal, 100 mg of the Pc was dispersed in methanol and stirred under sonication for 1 h.

Yield: (**7**) – 0.197 g. (94%).

Yield: (**8**) – 0.096g (87%).

### 3.3.1.4 Synthesis of upconversion nanoparticles

The synthesis of the various upconversion nanoparticles was achieved through a modified microwave-assisted method previously described by Mi *et al.* (2011). The upconversion nanoparticles were synthesized by varying the elements used for the host lattice and the activator, with fluoride and ytterbium the only constant elements in the synthesis of each upconversion nanoparticle. The structure of the upconversion nanoparticles will be described as  $ABF:Yb/C$  where  $A$  will represent either Na/Li/K,  $B$  either Y/Sc and  $C$  either Er/Ho with the different combinations rendering the different upconversion nanoparticles. The following upconversion nanoparticles were synthesized: NaYF:Yb/Er (**9**), NaYF:Yb/Ho (**10**), NaScF:Yb/Er (**11**), LiYF:Yb/Er (**12**) and KYF:Yb/Er (**13**). The synthesis was carried out in ethylene glycol and deionized water. The respective rare earth precursors, as previously mentioned in section 3.1.1, for desired upconversion nanoparticles were used as well as the chloride form of  $C$ . The fluoride source was obtained from the  $NH_4F$  salt.

Firstly, the mixed rare earth precursors were added in a mole ratio of 0.8 mmol of  $B$ , 0.18 mmol of Ytterbium and 0.02 mmol of  $C$ , all of which were dissolved in a solution composed of 10 mL of water and 10 mL of ethylene glycol. Then,  $NH_4F$  (0.185 g, 5 mmol) and 1 mmol of  $A$  were added to the mixture. The mixture was stirred under sonication to form a homogeneous solution and transferred into the microwave vessel and treated at 160 °C for 1 h. After the reaction was complete, the microwave vessel was cooled to room temperature and the reaction solution centrifuged at 6000 rpm/min for 5 min. The obtained pellet was washed with ethanol three times followed by centrifugation and dried in an oven at 80 °C. Once dried the obtained white powder was collected and stored.

**Table 3.1:** The reagents, moles and masses utilized for each of the synthesis of the upconversion nanoparticles on a small scale (ss) or large scale (us).

	Yttrium Nitrate 0.8 mmol/ 8 mmol (g)	Ytterbium Nitrate 0.18 mmol/ 1.8 mmol (g)	Erbium Nitrate 0.02 mmol/ 0.2 mmol (g)	Holmium Oxide 0.02 mmol/ 0.2 mmol (g)	Scandium Oxide 0.8 mmol/ 8 mmol (g)	NaCl 1 mmol/ 10 mmol (g)	LiCl 1 mmol/ 10 mmol (g)	KCl 1 mmol/ 10 mmol (g)	NH <sub>4</sub> F 5 mmol 50 mmol (g)
NaYF <sub>3</sub> :Yb/Er (9) Small Scale	0.31	0.07	0.008	-	-	0.059	-	-	0.185
NaYF <sub>3</sub> :Yb/Er (9) Large Scale	3.10	0.70	0.080	-	-	0.590	-	-	1.850
NaYF <sub>3</sub> :Yb/Ho (10) Small Scale	0.31	0.07	-	0.008	-	0.059	-	-	0.185
NaYF <sub>3</sub> :Yb/Ho (10) Large Scale	3.10	0.70	-	0.080	-	0.590	-	-	1.850
NaScF <sub>3</sub> :Yb/Er (11) Small Scale	-	0.07	0.008	-	0.11	0.059	-	-	0.185
NaScF <sub>3</sub> :Yb/Er (11) Large Scale	-	0.70	0.080	-	1.10	0.590	-	-	1.850
LiYF <sub>3</sub> :Yb/Er (12) Small Scale	0.31	0.07	0.008	-	-	-	0.042	-	0.185
LiYF <sub>3</sub> :Yb/Er (12) Large Scale	3.10	0.70	0.080	-	-	-	0.420	-	1.850
KYF <sub>3</sub> :Yb/Er (13) Small Scale	0.31	0.07	0.008	-	-	-	-	0.074	0.185
KYF <sub>3</sub> :Yb/Er (13) Large Scale	3.10	0.70	0.080	-	-	-	-	0.740	1.850

\* The mmol ratios highlighted in red is indicative of that which was used for the large scale synthesis

\* The deionized water and ethylene glycol remained at 10 ml each for both the ss and us synthesis of the nanoparticles

**Table 3.2:** The yields obtained for each of the different UCNP samples.

<b>Nanoparticle</b>	<b>Yield (g)</b>
<b>NaYF:Yb/Er (9) small scale</b>	0.102
<b>NaYF:Yb/Er (9) large scale</b>	1.123
<b>NaYF:Yb/Ho (10) small scale</b>	0.111
<b>NaYF:Yb/Ho (10) large scale</b>	1.21
<b>NaScF<sub>4</sub>:Yb/Er (11) small scale</b>	0.122
<b>NaScF<sub>4</sub>:Yb/Er (11) large scale</b>	1.411
<b>LiYF:Yb/Er (12) small scale</b>	0.109
<b>LiYF:Yb/Er (12) large scale</b>	1.102
<b>KYF:Yb/Er (13) small scale</b>	0.105
<b>KYF:Yb/Er (13) large scale</b>	1.119

### 3.3.2 Fluorescence quantum yield and lifetime determinations

The fluorescence spectra of the synthesized Pc (**5**) together with the unsubstituted zinc phthalocyanine (ZnPc) (**4**) standard, were prepared such that the absorbance of each, at the wavelength, was  $\sim 0.05$ . The emission spectra of the Pc (**5**), AgNPs (**8**) and ZnPc (**4**) standard were measured in DMSO. The area under the emission curves were measured to calculate the fluorescence quantum yields using Equation 2.2. The ZnPc standard was measured in DMSO ( $\Phi_F = 0.20$ ). The fluorescence lifetimes were determined in DMSO through the use of the program PhotochemCAD (<http://www.photochemcad.com/pages/chemcad/chem-home.html>) as previously described in Chapter 2 section 2.4.3 equation 2.3.

### 3.3.3 Singlet oxygen quantum yield determinations for phthalocyanine (5) and the Pc supported AgNPs (8)

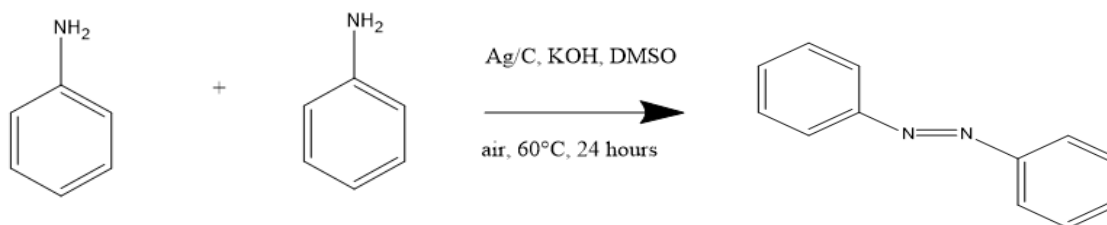
Singlet oxygen quantum yield ( $\Phi_{\Delta}$ ) determinations were carried out using the method described by Gümürükçü *et al.* (2014). Briefly, a 3 ml portion of the phthalocyanine, containing the singlet oxygen quencher DPBF, was irradiated in the Q band region (700 – 720 nm) for intervals of five seconds with 12 readings. The experiment was run in the dark with all other light blocked from the sample. This is then compared to the photodegradation rate induced by the standard and a quantum yield can be obtained using Equation 2.4 as described in section 2.4.4.

### 3.3.4 Catalytic reactions

#### 3.3.4.1 Catalytic reactions utilising AgNPs/C (7)

Catalytic reactions were carried out and the influence of each parameter on the success of the reaction evaluated. The reactions were carried out using a method previously described by Cai *et al.* (2013) with slight modification. Briefly, aniline (0.093 g, 1mmol) potassium hydroxide (0.056 g, 1 mmol) and 10.6 mg of AgNPs/C (7) were added to 2 ml of DMSO. The reaction was then heated to 60°C under a gentle in flow of air for 24 hours. The reaction was repeated with several parameters varied including temperature, the addition of the AgNPs/Pc (8) catalyst, the absence of a catalyst and the availability of air.

Yields: 0.143 g. (78%).



**Scheme 3.4:** Illustration of the azobenzene catalytic reaction.

## Part A:

### Chapter 4: Upconversion Nanoparticles

The following chapter will encompass the different kinds of nanoparticles synthesized and employed for the different characterization techniques as previously explained in chapter 3.3.

#### 4.1 Synthesis of the Upconversion Nanoparticles

The synthesis of high quality upconversion nanoparticles are known to be dependent on different parameters where strict control of these parameters within the syntheses procedures are needed (Gainer and Romanowski, 2014; Yi *et al.*, 2002; B. Zhou *et al.*, 2015). Many articles have reported on the control of these parameters as a factor that affects the reproducibility or inconsistency of the results obtained (Gainer and Romanowski, 2014; Yi *et al.*, 2002; B. Zhou *et al.*, 2015). This was true, as many issues arose when first attempting to synthesize these nanoparticles with this method which was later then aborted for another. The thermal decomposition methods appeared to be very appealing, but issue after issue arose. Reproducibility of the reaction and temperature environment itself could only be controlled to a certain extent where the successful synthesis of nanoparticles produced were not always guaranteed. In addition, difficulties arose when trying to get the nanoparticles to precipitate out of solution, and this in turn spelled out problems with obtaining good TEM images as the levels of hydrocarbons (oleylamine/octadecene etc.) were too high to obtain decent images. The thermal decomposition method was therefore aborted and replaced with a microwave solvothermal method which proved to be successful with the presence of fewer problems experienced. Most methods employed for the synthesis of upconversion nanoparticles, usually involve the preparation of the nanoparticles at high temperatures, i.e. 300°C, or they are time consuming, using time periods of 3 hours and more (Gainer and Romanowski, 2014; Yi *et al.*, 2002; B. Zhou *et al.*, 2015). The microwave solvothermal method offered a controlled reaction environment with other appealing qualities such as eco-friendliness, energy-efficiency, shorter reaction times needed and lower temperatures (Mi *et al.*, 2011).

The UCNPs were synthesized according to a modified method previously reported procedure (Mi *et al.*, 2011) in which a microwave synthesis method was applied using ethylene glycol. The microwave method was chosen instead which, in ethylene glycol in the reaction, problems such as getting the nanoparticles in powder form for obtaining TEM images were eliminated.

The rare earth salts (ytterbium chloride hexahydrate, yttrium nitrate hexahydrate, erbium chloride hexahydrate, holmium oxide, scandium oxide) were used as received from the supplier. Typically, the rare earth salts were dissolved in 10 ml of ethylene glycol and 10 ml of water. The relevant Na/K/Li and fluoride sources were then added to the reaction vessel and then sonicated for 1 hour. After sonification the mixture was transferred to the microwave for 1 hour at 60° C. After 1 hour the solution was cooled down to room temperature and the product separated from the reaction mixture through centrifugation at 6000 rpm for 5 minutes. The pellet obtained was washed with water and ethanol repeatedly and eventually dried at 80°C for 24 hours. A white powder was primarily obtained for the UCNPs, except for the upscaled (us) NaYF<sub>4</sub>:Yb/Ho sample which had a slight pink colour. The small scale syntheses (ss) for LiYF<sub>x</sub>:Yb/Er, NaYF<sub>4</sub>:Yb/Er, KY<sub>x</sub>F<sub>y</sub>:Yb/Er and NaYF<sub>4</sub>:Yb/Ho, which seemed to produce better quality crystals (according to XRD data) were light brown to a dark brown in colour (the latter two). The yields obtained for the different NPs ranged between 100 mg and 1 g for the small-scale and upscaled synthesis respectively. The small-scale synthesis samples will be referred to as the relevant UCNP with “ss” following the name, while the upscaled reaction will have samples named with a “us” following the relevant UCNP name. The concentration chosen for the Er ion was kept low in order to avoid possible cross relaxation processes between the excited sensitizer ions.

The mechanism for the reaction can be divided into three steps as shown in Figure 4.1, pg. 74. All the necessary reactants were added together in water and ethylene glycol in a round bottom flask. The reaction took place as follows: 1) When the temperature was elevated, the precursor decomposed slowly, so that the lanthanide ions were released from the precursor; 2) the free lanthanide ions encountered, proceeded to react with sodium/potassium/lithium and fluoride ions to form particles; 3) the smaller particles gradually grew with increasing reaction time (Mi *et al.*, 2011).

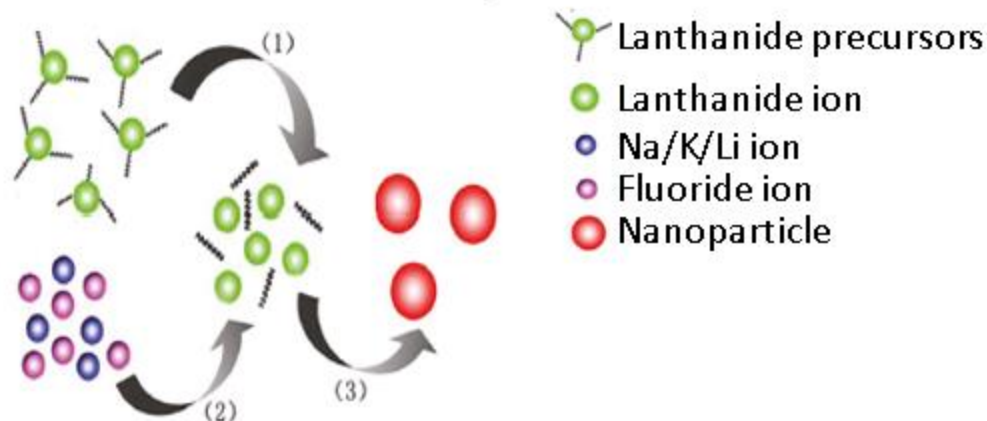


**Figure 4.1:** The mechanism of action for the upconversion nanoparticle synthesis. (Mi *et al.*, 2011).

It should be noted that the authors who reported this method utilized lanthanides in their acetate form. In this thesis lanthanide chloride hexahydrate, nitrate hexahydrate or oxides were used (chapter 3.1). The mole ratio of the lanthanides used were determined based on the most efficient ratio of sensitizer to activator (20%/2%), as reported by multiple articles (Gainer and Romanowski, 2014; Yi *et al.*, 2002; B. Zhou *et al.*, 2015). Thus, the remainder (78%) was made up of either yttrium or scandium. The synthesis procedure was tested for its reproducibility and effect the upscaling the synthesis procedure had on the nanoparticles produced (by a factor of 10 compared to the original reported method). This upscaling would also give us an insight on the consequence of increasing the concentration of reactants. It was reported by Wang *et al.*, (2010) that the reactant concentration has a considerable influence on the shape evolution of the nanoparticles. They found that, in the case of a microwave assisted synthesis of rare earth doped upconverting Na/LiYF<sub>4</sub> nanocrystals, the crystallographic lattice of the particles and the concentration of the reactants governed their morphology (Wang *et al.*, 2010). Low reactant concentrations resulted in very small and monodisperse spherical nanocrystals, whereas nanowires were obtained at a high reactant concentration (Wang *et al.*, 2010). Upon preparing the samples for TEM analysis, it was observed that the nanoparticles did not suspend well in either polar or non-polar solvents. This is attributed to the absence of ineffective capping agents on the nanoparticles where in previous attempts of synthesizing these nanoparticles the capping agents allowed the nanoparticles to be suspended in polar or non-polar solvents depending on the

capping agent. Ethylene glycol was employed in these reactions as the capping and reducing agent. Sonicating the nanoparticles in a polar solvent for an hour prior to reaction helped suspend the prepared nanoparticles to a certain extent (Wang *et al.*, 2010). The resultant solution was used to obtain the TEM images, although the nanoparticles were in an agglomerated state. The agglomeration made it difficult to determine accurate sizes for the nanoparticles using the TEM images, thus the XRD powder pattern was used to determine its size instead. The minimum particle size of the synthesized UCNPs could be calculated from the Debye Scherrer equation, Equation 2.6 (section 3.2.2). The XRD patterns were also compared to those patterns of structures that closely resemble the nanoparticles synthesized found in the literature.

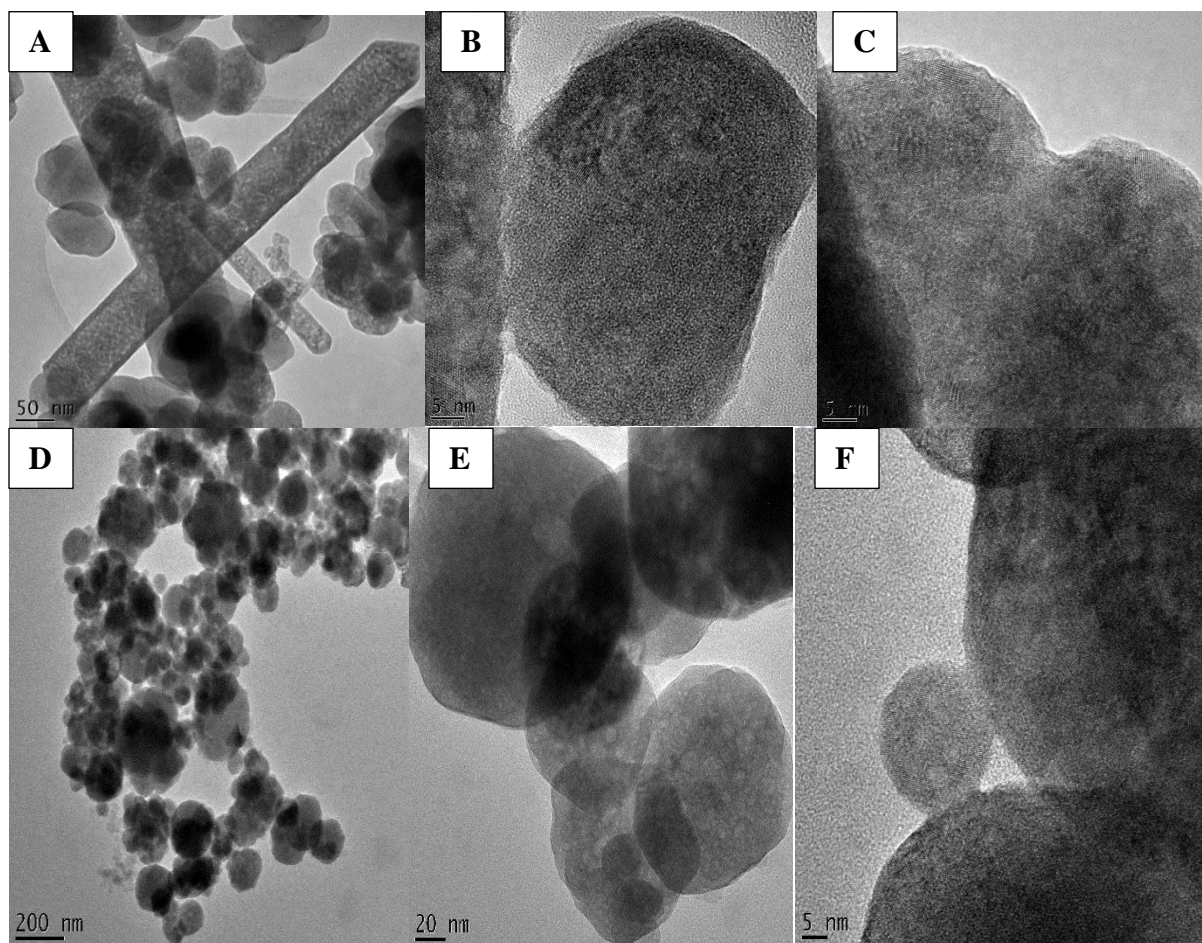
## 4.2 Characterization of the UCNPs

### 4.2.1 Transmission electron microscopy (TEM) and Energy Dispersive X – Ray Spectroscopy (EDX)

The particle size and morphology of the UCNPs were analysed using TEM and EDX. The TEM images (Figure 4.2, pg. 76 - 77) for the NaYF<sub>4</sub> crystal lattice samples (NaYF<sub>4</sub>:Yb,Er and NaYF<sub>4</sub>:Yb/Ho) all show spherical nanoparticles, with one sample, NaYF<sub>4</sub>:Yb/Er ss additionally revealing the formation of rod-like structures (Figure 4.2A, pg. 77). The rods witnessed are commonly found in synthetic methods utilising a microwave (Mi *et al.*, 2011). Additional images are provided in the Appendix Figures A4.1 and A4.2. Although the TEM images revealed that the NPs were highly aggregated, an average of 50 particles in the TEM images were still evaluated, revealing the particle sizes to range in size from 10 – 80 nm. The minimum particle sizes were also calculated from the XRD patterns using the Debye-Scherrer equation (equation 2.6) as this would most likely provide more accurate data. This data is discussed later in the XRD section.

The TEM images obtained for the NaScF<sub>4</sub>:Yb/Er samples are shown in Figure 4.2, pg. 77 (G – D), revealing spherical nanoparticles with sizes ranging from 10 – 50 nm in diameter for the NaScF<sub>4</sub>:Yb/Er ss sample and 40 - 80 nm in diameter for the upscaled sample (us) (Appendix Figure A4.3, pg. 138). Close inspection of the images revealed the presence of lattice fringes,

accounting for the crystalline structure, as well as what appears to be some voids present in the upscaled sample in particular. Similar results are found within metal nanoparticles which can be explained by the Frenkel effect (Kirkendall voiding) as a consequence of the out-diffusion of metal through the forming of a spherical layer of compound being faster than the in-diffusion of other reactants through this growing compound layer. This results in an inward flux of vacancies, which meet inside and form a void (or several voids) in the remaining metallic core (Gusak *et al.*, 2011).



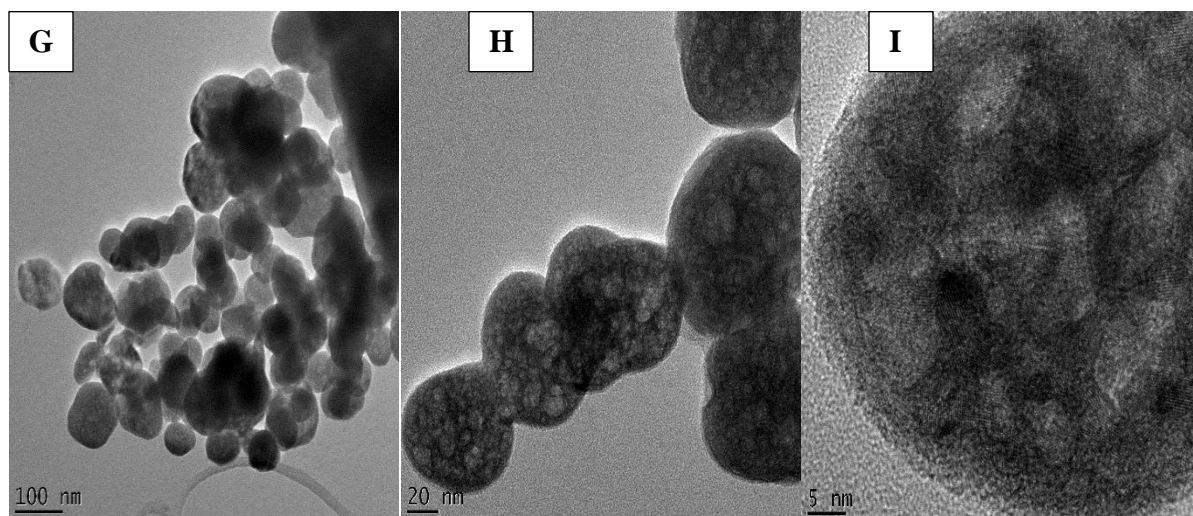


**Figure 4.2:** TEM images obtained for the (A -C)  $\text{NaYF}_4\text{:Yb/Er}$  ss, (D - F)  $\text{NaYF}_4\text{:Yb/Ho}$  us, (G - I)  $\text{NaScF}_4\text{:Yb/Er}$  ss UCNP samples.

The Na ion in the crystal lattice was replaced in the next set of samples with the smaller Li ion and the larger K ion. The TEM images for these nanoparticles are shown in Figure 4.3, pg. 78. The images obtained for these samples show mostly spherical nanoparticles, however the  $\text{LiY}_x\text{F}_y\text{:Yb/Er}$  ss and  $\text{KY}_x\text{F}_y\text{:Yb/Er}$  ss sample shows hexagonal and cubic shaped nanoparticles, respectively, as well. The lattice fringes are also clearly visible in the small-scale nanoparticles. Smaller size ranges were obtained for the small-scale syntheses, i.e. 20 – 80 nm and 10 – 60 nm for the Li and K substituted UCNPs, while larger ranges were obtained for the upscaled synthesis of the  $\text{LiYF}_x$  UCNP (Table 4.1, pg. 78). Interestingly, much smaller sizes (and size ranges) were obtained for the upscaled  $\text{KY}_x\text{F}_y$  UCNP at only 5 – 20 nm in diameter. Table 4.1, pg. 78 shows the particle sizes obtained using both TEM and XRD for comparison. Sizes ranged from 12 to 87 nm in diameter according to the TEM analyses, while XRD sizes were found to be more conservative and slightly smaller, with sizes ranging from 9 to 45 nm in diameter. The scale of the synthetic method used i.e. us or ss, did not appear to influence the size of the NPs, however, although it did affect the morphology of these UCNPs.

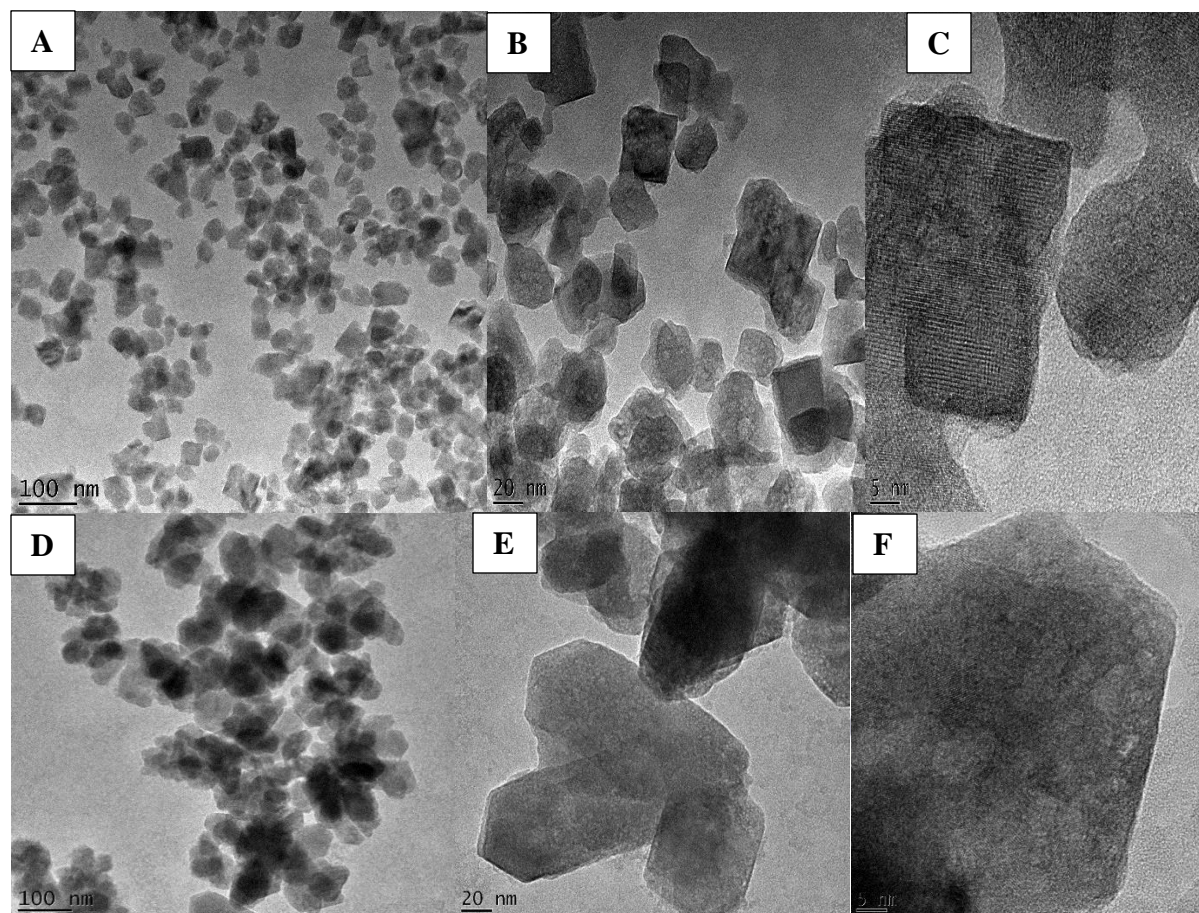


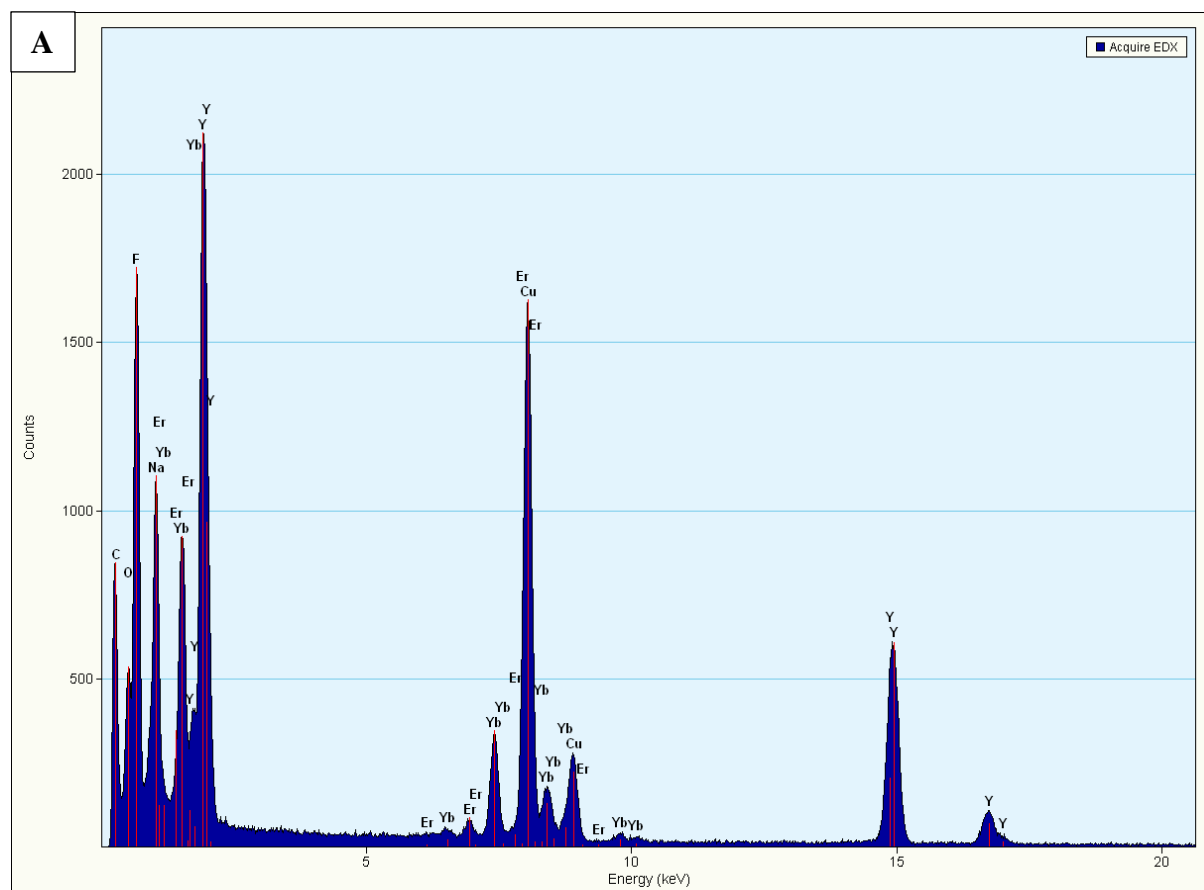
**Figure 4.3:** TEM images obtained for the (A – C) KYF<sub>4</sub>:Yb/Er ss and (D – F) LiYF<sub>4</sub>:Yb/Er ss UCNPs samples.

**Table 4.1** Particle size of the UCNPs as extracted from the TEM images as well as those calculated based on the Debye-Scherrer equation (equation 2.6) from XRD.

Sample	Mean diameter (TEM) / nm	Size range (TEM) / nm	Mean diameter of nanocrystalline domain size (XRD) / nm
NaYF <sub>4</sub> :Yb/Er ss	62	40 – 80	45
NaYF <sub>4</sub> :Yb/Er us	87	50 – 200	34
NaYF <sub>4</sub> :Yb/Ho ss	53	40 – 80	34
NaYF <sub>4</sub> :Yb/Ho us	66	20 – 100	41
NaScF <sub>4</sub> :Yb/Er ss	40	10 – 50	30
NaScF <sub>4</sub> :Yb/Er us	51	40 – 80	40
KY <sub>x</sub> F <sub>y</sub> :Yb/Er ss	38	10 – 60	17
KY <sub>x</sub> F <sub>y</sub> :Yb/Er us	12	5 – 20	9
LiY <sub>x</sub> F <sub>y</sub> :Yb/Er ss	49	20 – 80	23
LiY <sub>x</sub> F <sub>y</sub> :Yb/Er us	64	10 – 200	17

The EDX spectra shown in Figure 4.4, pg. 79 - 81 reveal the expected elemental compositions for each of the NaYF<sub>4</sub> samples, where Er is observed for the NaYF<sub>4</sub>:Yb,Er (Figure 4.4A, pg. 79)

and Ho for the NaYF<sub>4</sub>:Yb/Ho (Figure 4.4B, pg. 80) samples. Some spectra have also been included in the appendix A6.6 and A6.7). The EDX spectrum for the NaScF<sub>4</sub> samples, shown in Figure 4.4C, pg. 80 and in the appendix, reveal the presence of Sc, with no traces of Y detected. The EDX spectra for the Li and K substituted UCNP crystals are shown in Figure 4.4 D and E, pg. 81, respectively. The spectra revealed no traces of Na and only the expected elemental composition, however Li was not detected in either the small-scale or upscaled sample. This is due to the fact that lithium is very reactive and oxidize immediately when exposed to air and the low energy of the characteristic line leads to a low intensity of the peak which is not visible without specialised equipment (Muto and Tatsumi, 2016).





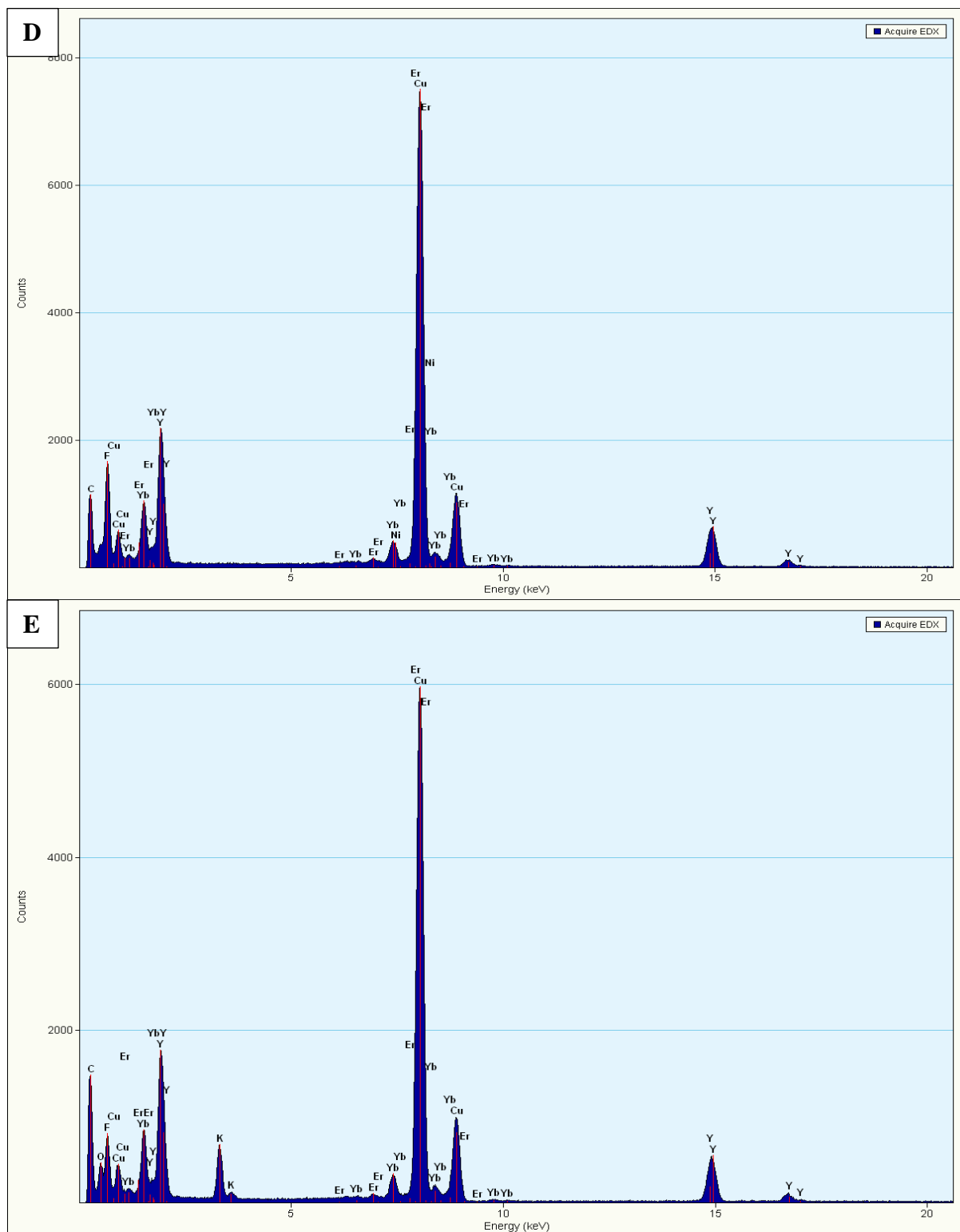


**Figure 4.4:** Representative TEM-EDX spectra of A) NaYF<sub>4</sub>:Yb/Er us, B) NaYF<sub>4</sub>:Yb/Ho ss, C) NaScF<sub>4</sub>:Yb/Er ss, D) LiY<sub>x</sub>F<sub>y</sub>:Yb/Er us and E) KY<sub>x</sub>F<sub>y</sub>:Yb/Er us UCNPs.

#### 4.2.2 X-ray powder diffraction (PXRD)

Since the method and characterisation for the upconversion nanoparticle NaYF<sub>4</sub>:Yb/Er is so well established, this sample was intended to be used as a model UCNP against which the rest of the UCNPs would be compared, particularly with respect to the powder XRD patterns. The synthesized samples were examined by XRD in order to determine the sample's phase composition. Two phases are known for the NaYF<sub>4</sub> host lattice, the cubic ( $\alpha$  -phase) and the hexagonal ( $\beta$  -phase) (Yang *et al.*, 2016). The XRD patterns, together with the Miller indices of the lattice planes for the NaYF<sub>4</sub>:Yb/Er and NaYF<sub>4</sub>:Yb/Ho samples (both the upscaled and small scale syntheses) are shown in Figure 4.5, pg. 83. A comparison of these powder patterns with the database for the International centre of diffraction data (ICDD, or JCPDS, No. 77-2042) showed that these NPs are composed of the cubic (or  $\alpha$  -phase) found for NaYF<sub>4</sub>. Even though mild conditions were employed, the intensity and sharpness of the reflections indicated that a defined crystal lattice had indeed formed. The intensities further alluded to the quality of the crystals produced (shown in Figure A4.11, pg. 142 in the appendix), indicating that the small-scale syntheses produced better quality crystals compared to the upscaled method. In order to enable comparison of the powder patterns, some of the XRD data was magnified and the true intensities are shown only in the appendix (Figure A4.11, pg. 142). Curiously, although exactly the same reaction time, temperature, pressure and materials were used to produce both the small-scale and upscaled samples, a slight shift to lower  $2\theta$  angles was observed for the two samples (i.e. Er and Ho) that were synthesized using the small-scale synthesis method. This may be attributed to larger d spacing associated with an increase in the unit cell lattice parameters (Wang *et al.*, 2010), e.g. when the ionic radii of one ion is larger than another substitute. This was not the case here as it was simply the difference in concentration of the reactants that was different. It is also not likely due to the differences observed in size of the NPs, and so it remains curious. It also appeared that the upscaled samples are starting to show the formation of a small amount of the  $\beta$  -phase or anisotropic crystals.

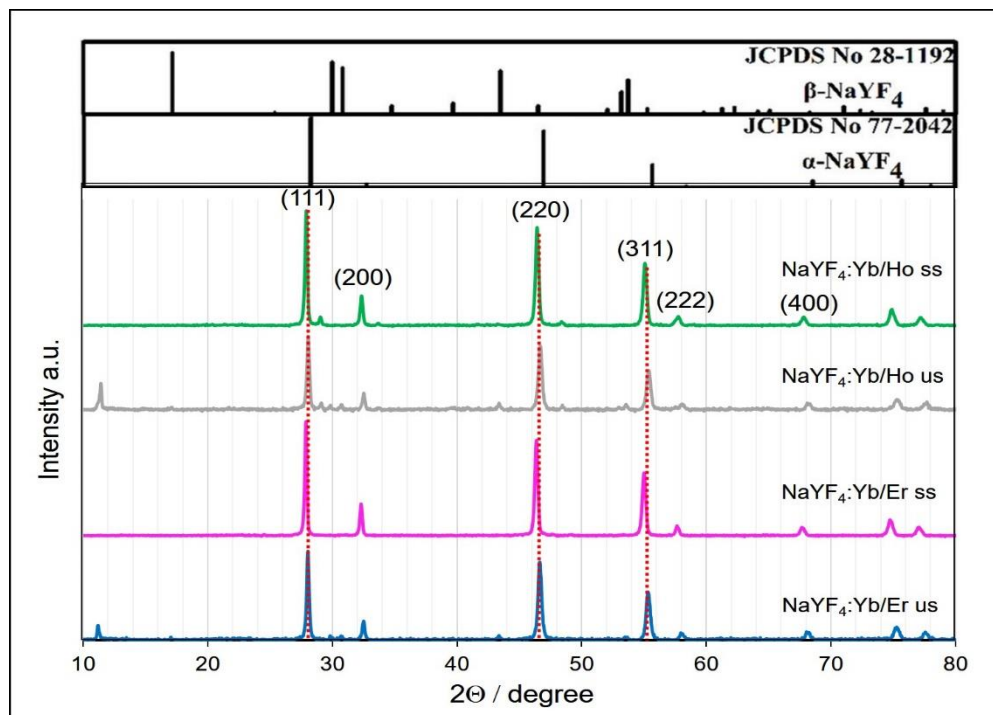


**Figure 4.5.** The XRD powder patterns obtained for the samples containing the  $\text{NaYF}_4$  crystal lattice, together with the corresponding reference data from JCPDS, indicating that all four samples are mainly cubic phase.

As mentioned previously, the Debye-Scherrer equation (equation 2.6) was used to calculate the minimum particle sizes of all the UCNPs as it was more likely that the XRD data could provide a better estimation of the NP sizes compared to the TEM images which only revealed highly aggregated NPs. The mean size of the nanocrystals is shown in Table 4.1, pg. 78 and can be compared to the sizes provided by the TEM images. The average sizes ranged from 30 – 45 nm for all samples. Regardless of the method employed (small- or up-scaled), the average NP size was not determined by the synthesis procedure. However, the size ranges obtained (as shown by the TEM images) were much smaller for the small-scale synthetic procedure, indicating greater control in the reaction conditions.

The powder XRD patterns obtained for the  $\text{NaScF}_4$  crystal phase is given in Figure 4.6, pg. 85 below. The molar equivalent of F present in the sample is at this time unknown and due to time constraints were not determined here. The UCNP is thus referred to as  $\text{NaScF}_4$ . In this sample,

the Y ion is replaced by the smaller Sc ion. There are some reflections at  $2\theta = \sim 28^\circ, 33^\circ, 47^\circ$  and  $56^\circ$  for the  $\text{NaScF}_4:\text{Yb/Er}$  ss sample each corresponding to the specific (221), (113), (224), and (315) planes of the hexagonal  $\text{NaScF}_4$  respectively. However, it is also very apparent that there might be more than one phase present as there are reflections reminiscent of the cubic phase of the  $\text{NaYF}_4$  crystal lattice, although these are shifted to higher  $2\theta$  angles (Pang *et al.*, 2014). Since the ionic radius of Sc is smaller than that of the Y ionic radius, it is expected that a smaller d spacing associated with a decrease in the unit cell lattice parameters occurs (Hao *et al.*, 2012). The upscaled sample in particular appeared to also have more than one phase present although there are reflections pertaining to the hexagonal phase. A search of the literature was done to try and explain these findings and if there are instances of more than one phase present in a synthesis of  $\text{NaScF}_4$  host lattice UCNPs. It was found in one paper that the authors simulated the powder pattern for the Sc UCNPs, since none matched in the database similar to this work (Yu *et al.*, 2013). The authors synthesized  $\text{NaScF}_4$  microcrystals and used CrystalClear software for data reduction and empirical absorption correction to theoretically determine the crystalline structure along with direct methods using SHELXTL (Yu *et al.*, 2013). Once again the average size of the  $\text{NaScF}_4$  nanocrystals were calculated using the Debye-Scherrer equation, Equation 2.6, to be 30 nm and 40 nm in size for the  $\text{NaScF}_4:\text{Yb/Er}$  ss and  $\text{NaScF}_4:\text{Yb/Er}$  us UCNPs, respectively Table 4.1, pg. 78. Taking into account the sizes determined using the TEM images, the  $\text{NaScF}_4$  NPs are relatively smaller in size. The structure and morphology of the different scaled nanoparticles can be attributed to the different concentration of reactants in the reaction (Wang *et al.*, 2010) Further work is needed to optimise the reaction conditions used to synthesize these nanomaterials, however.

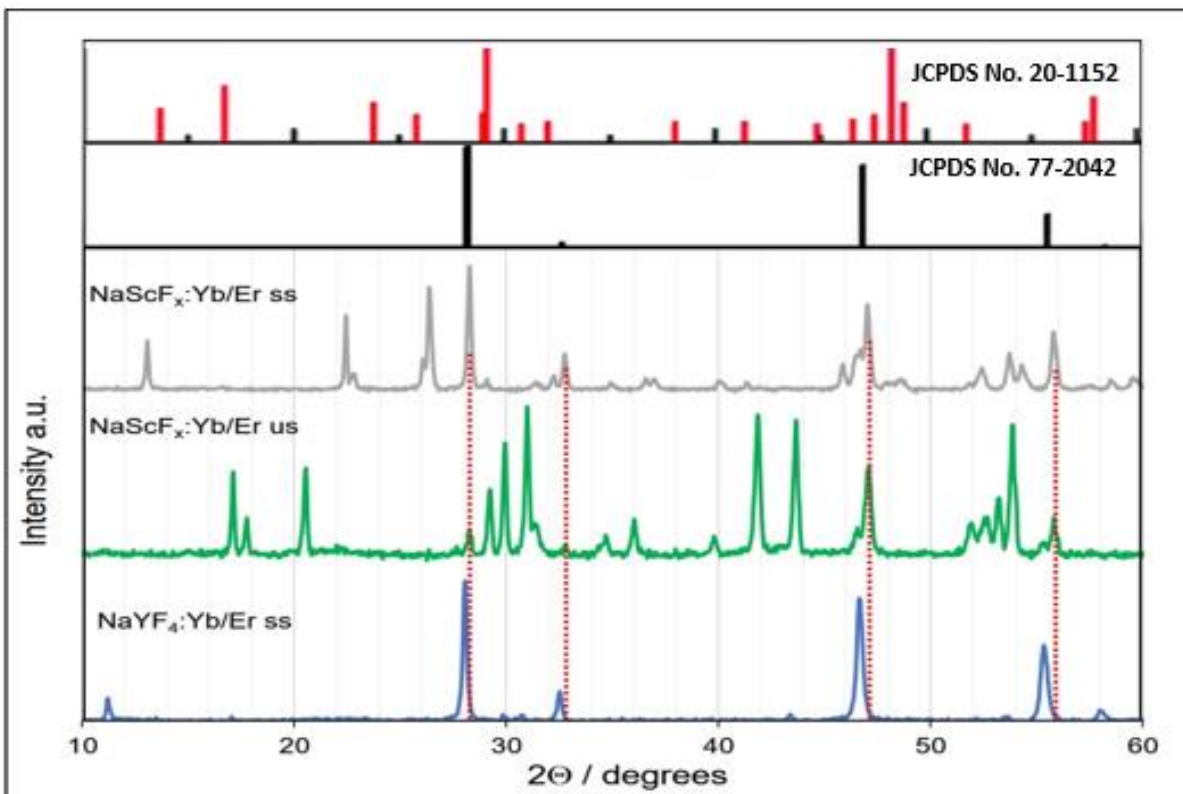


**Figure 4.6:** The XRD powder patterns obtained for the samples containing the NaScF crystal lattice, together with the pattern for NaYF<sub>4</sub>:Yb/Er ss and, for comparison, the reference data from JCPDS for cubic (JCPDS No. 77-2042) and hexagonal (JCPDS No.20-1152) phases for the NaScF crystal lattice (Zeng *et al.*, 2013).

The XRD powder patterns obtained for the LiY<sub>x</sub>F<sub>y</sub> UCNPs are shown in Figure 4.7, pg. 86 and compared to the NaYF<sub>4</sub>:Yb/Er ss sample. Unfortunately, no match against the ICDD database was found in the literature (e.g. JCPDS No. 81-2254), but the small-scale sample does also appear to have reflections reminiscent of those for the NaYF<sub>4</sub> crystal lattice. These reflections found at  $2\theta = 27^\circ$ ,  $44^\circ$  and  $52^\circ$  were found at lower angles compared to the NaYF<sub>4</sub> crystal, however, and remains unexplained. The upscaled sample produced a very different powder pattern and thus the reaction conditions will obviously need to be modified and optimised. These results can be attributed to the reaction conditions which play an important role in the successful synthesis of UCNPs.

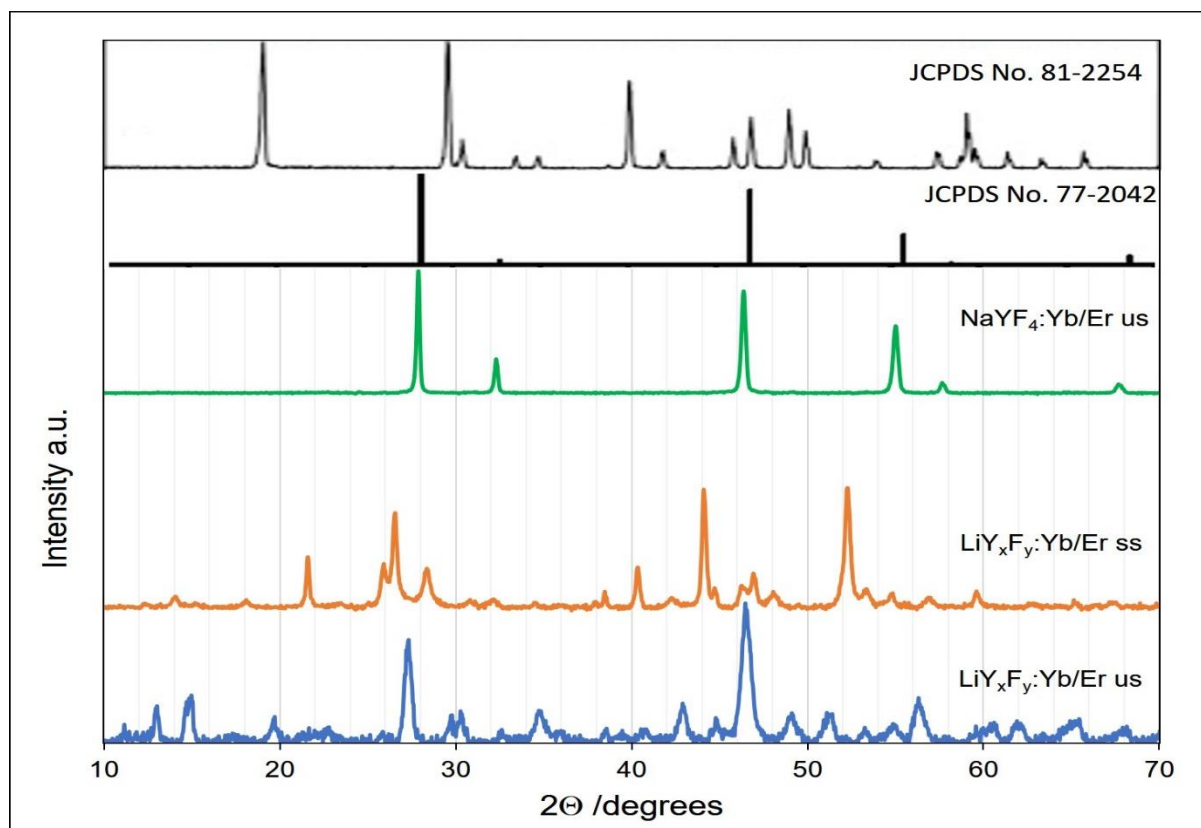


**Figure 4.7:** The XRD powder patterns obtained for the samples containing the LiY<sub>x</sub>F<sub>y</sub> crystal lattice, together with the pattern for NaYF<sub>4</sub>:Yb/Er ss and, for comparison, the reference data from JCPDS for the NaYF<sub>4</sub> cubic (JCPDS No. 77-2042) and LiYF<sub>4</sub> (JCPDS No. 81-2254) phases (Gao *et al.*, 2014).

The effect of various parameters in the synthesis of LiScF<sub>3</sub>: Yb/Er was reported by Liang *et al.*, (2016) utilising a solvothermal method which gives further insight in Li based nanoparticles. They found two parameters that are relevant to the successful synthesis of the nanoparticles, which are the temperature and time (Liang *et al.*, 2016). They concluded that the nanoparticles synthesized with a reaction time of 1 hour yielded impure ScF<sub>3</sub> peaks in the XRD pattern (Liang *et al.*, 2016). The increase in synthesis time showed a decrease in these impurity peaks where the TEM images also showed the disappearance of small uneven shaped nanoparticles and the appearance of uniform and monodisperse nanoparticles (Liang *et al.*, 2016). The authors also reported successful synthesis of the nanoparticles at no less than 270°C (Liang *et al.*, 2016). According to their findings the insufficient time of 1 hour and temperature of 160°C in the

synthesis of the  $\text{LiY}_x\text{F}_y$  could be the reason of the poor results witnessed (Liang *et al.*, 2016). The minimum particle sizes of the NPs were calculated using the Debye-Scherrer equation (equation 2.6) to be 23 nm and 17 nm for the small-scale and upscaled samples, which was expected given that the reflections are broader for the latter.

The XRD patterns, together with the Miller indices of the lattice planes for the  $\text{KY}_x\text{F}_y:\text{Yb/Er}$  samples (both the upscaled and small scale syntheses) are shown in Figure 4.8, pg. 88. A comparison of these powder patterns with the database for the International centre of diffraction data (ICDD, or JCPDS, No. 27-0465) showed that these NPs are composed of the tetragonal crystal structure 27-0465 as found for  $\text{KY}_3\text{F}_{10}$ . The reflections observed at  $2\theta = \sim 27^\circ, 31^\circ, 45^\circ$  and  $53^\circ$  are attributed to the (202) (220) (400) and (422) planes as given for the  $\text{KY}_3\text{F}_{10}$  crystal lattice in the literature. They are also somewhat reminiscent of those reflections observed for the  $\text{NaYF}_4$  crystal lattice, albeit it at much lower  $2\theta$  angles and the fact that they are different planes. The size of the K ion is larger than that of the Na ion and therefore it is expected that it would shift to smaller angles. Also apparent is that the small-scale syntheses sample seems to have some amorphous material associated with it as evidenced by the broad peak from  $2\theta = 10^\circ - 40^\circ$ . This sample appears to have split reflections at  $2\theta = 45^\circ$  and  $53^\circ$  which remains unaccounted for. The reflections are rather broad and this is attributed to the small size of the UCNPs since the smaller the NP, the broader the reflection. These patterns were also used to calculate the size of the NPs and they were determined to be 17 nm and 9 nm in size for the small-scale and upscaled samples, respectively (Table 4.1, pg. 78). A cursory glance at the two powder patterns indeed shows that the upscaled sample has broader signals than  $\text{KY}_x\text{F}_y:\text{Yb/Er}$  sample. The difference in concentration of the reactants within the reaction vessel seems to be the reason for these differences witnessed as it is the only difference between the us and ss samples. It has been reported that the structure of nanoparticle changes with the change in concentration of a reaction (Wang *et al.*, 2010). The true intensity of these reflections may be seen in Figure A4.11, pg. 142 in the appendix. Once again, the patterns here were magnified to enable comparisons to be made. The intensity of the reflections give an indication of the quality of the crystals.

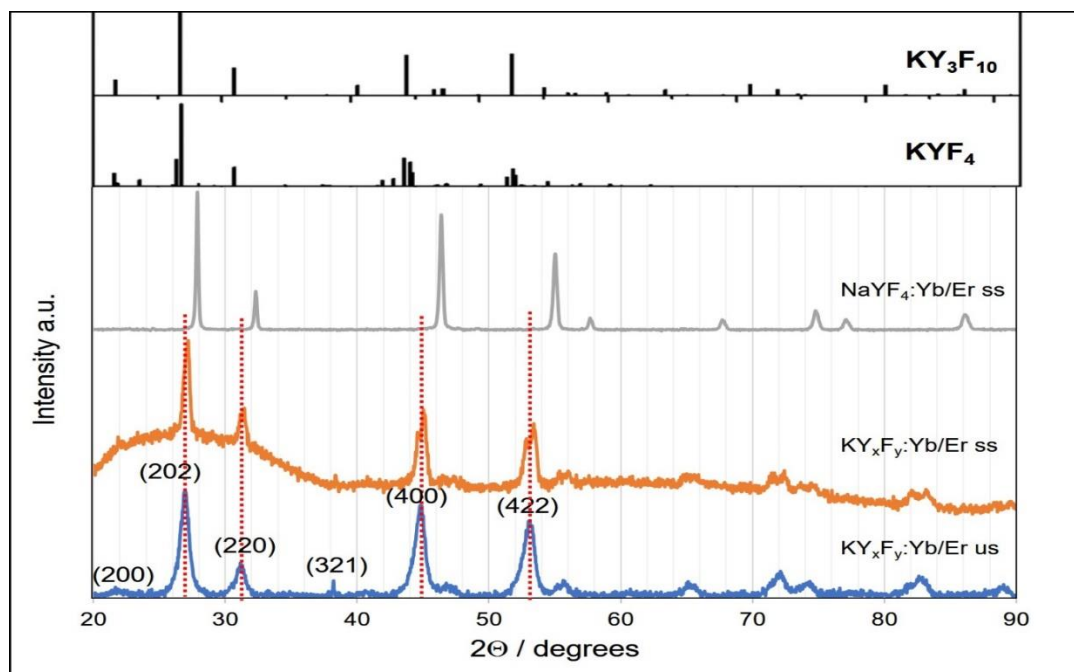


**Figure 4.8:** The XRD powder patterns obtained for the samples containing the  $KY_xF_y$  crystal lattice, together with the pattern for  $NaYF_4:Yb/Er$  ss and, for comparison, the reference data from JCPDS for the  $KYF_4$  and  $KY_3F_{10}$  patterns (Mahalingam *et al.*, 2009).

Overall, UCNPs with lower symmetry are expected to give better upconversion emissions. Unfortunately, most of the samples produced here belong to the cubic or  $\alpha$ -phase. However, conversion or transition to the lower symmetry hexagonal or  $\beta$ -phase may be successfully accomplished by calcination or annealing at temperatures around 500 °C (Klier *et al.*, 2015). Due to time constraints we were not able to carry out this additional step. An increase in upconversion (UC) emission is also expected with a decrease in cation size or unit cell volume, since these leads to a stronger crystal field (Wang *et al.*, 2009). Thus, it is expected that substitution of the Y in the  $NaYF_4$  crystal lattice with the smaller Sc cation, provided the nanocrystals are of suitable quality, should provide an enhanced UC emission. The same would be expected for the  $LiY_xF_y$  crystal lattice – however, the powder patterns revealed reflections of low intensity (Figure A4.1, pg. 137) and it is therefore expected that the nanocrystals are of poor quality.

### 4.2.3 Solid State NMR

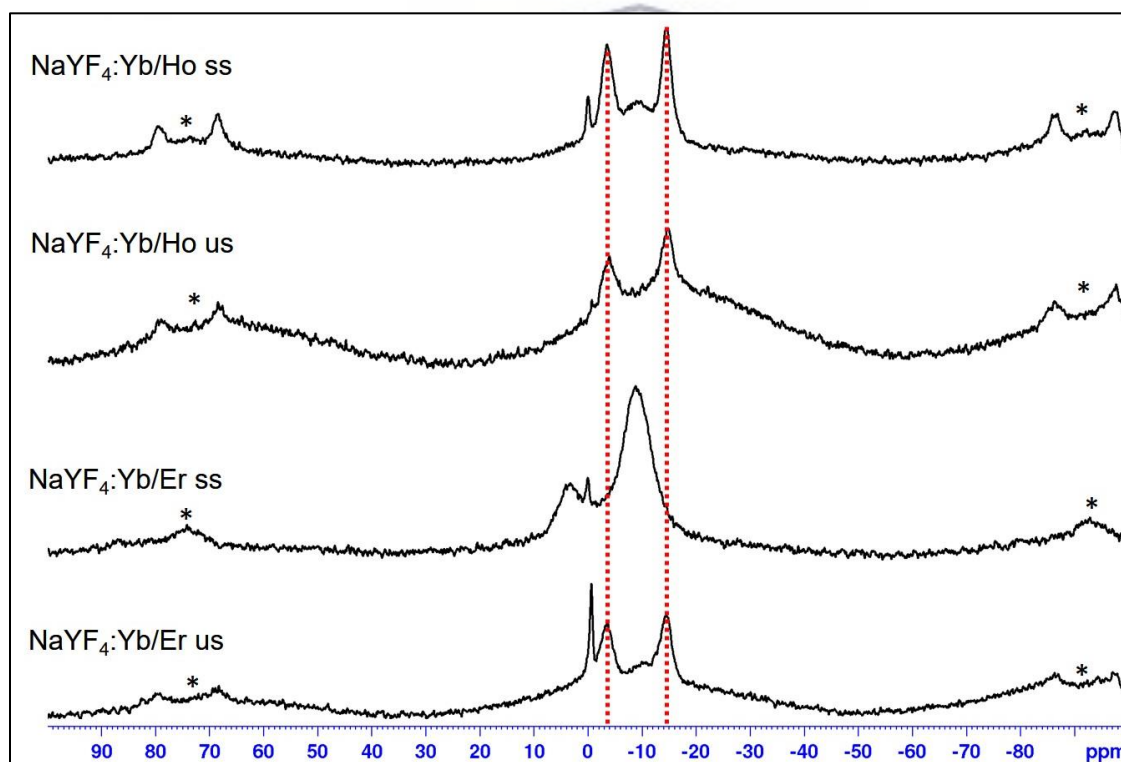
One of the few papers available in the literature is that of Arnold *et al.* (2013) who carried out structural investigations using solid state NMR on NaYF<sub>4</sub> UCNPs synthesized in the cubic phase. The authors prepared samples with 1 and 2 mol % Er<sup>3+</sup>, while a third sample remained undoped, and they were hoping to assess the quality of the crystals formed and to evaluate the effect the dopant ions the crystalline lattice parameters. The dopant levels were kept low enough to prevent paramagnetic relaxation and the subsequent quenching of the NMR signal.

A combination of <sup>23</sup>Na and <sup>45</sup>Sc NMR was used to try and provide some information on the structure of the NaYF<sub>4</sub> and NaScF<sub>4</sub> nanoparticles. With the natural abundance of the two isotopes is at 100%, even though they are quadrupolar nuclei possessing half-integer spins of  $I = 3/2$  and  $7/2$  for the <sup>23</sup>Na and <sup>45</sup>Sc isotopes, respectively, acquisition of the NMR data is particularly attractive. Data was not obtained for the K substituted NPs because the NMR frequency of the <sup>39</sup>K nucleus is expected to be at ~23 MHz (on a 500 MHz instrument) and the probes are only able to observe frequencies between 50 MHz and 202 MHz (<sup>31</sup>P nucleus) on the X/Y channel. Although the Li substituted NPs were analysed, the XRD and luminescence data obtained for the samples were not encouraging, and thus the <sup>7</sup>Li NMR data is also not included here.

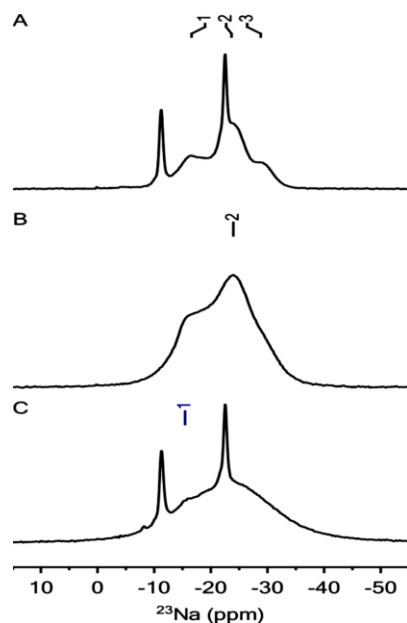
The <sup>23</sup>Na NMR data in particular is thought to be important since the <sup>23</sup>Na quadrupolar coupling constants ( $C_Q$ ) are expected to be sensitive to lattice distortion, while the <sup>23</sup>Na and <sup>45</sup>Sc chemical shifts are sensitive to the chemical environment. Er<sup>3+</sup>, Ho<sup>3+</sup> and Yb<sup>3+</sup> are paramagnetic and thus doping the nanoparticles (which is necessary for upconversion luminescence) is likely to affect the NMR signals observed through dipolar shift anisotropy and through increased paramagnetic relaxation. Paradoxically, this enables the localization of the dopant ions within a structure (Arnold *et al.*, 2013). However, the dopant levels are comparably low with respect to the matrix composition of the UCNPs.

Figure 4.9, pg. 90 shows the broad powder like patterns obtained for the <sup>23</sup>Na NMR spectra of the NaYF<sub>4</sub> UCNPs. The signals were distributed between 7 and -25 ppm, with maximum

intensities at  $-18.4$  ppm and a shoulder at  $-13.4$  ppm, as observed for all samples except the  $\text{NaYF}_4\text{:Yb/Er}$  ss sample. This  $\text{NaYF}_4\text{:Yb/Er}$  ss sample also showed two maximum intensity, sharp, signals at  $-0.5$  and  $-12.7$  ppm (which was the most intense), with the chemical shift of the latter at the same frequency as that of the shoulders for the remaining  $\text{NaYF}_4$  samples. The powder XRD pattern obtained for this sample did not point to any differences with respect to the  $\text{NaYF}_4$  samples which were deemed to be in the cubic phase, however, and this was unexpected. The spectra obtained here were similar to those obtained by Arnold *et al.* (2013) as shown in Figure 4.10, pg. 91. The authors suggested that these signals are due to impurities, although they were not able to identify the nature of these impurities, they did not rule out the possibility of a secondary crystalline phase in the UCNPs studied (Arnold *et al.*, 2013). The sharp signal at 0 ppm in Figure 4.9, pg. 90 is attributed to unreacted NaCl.



**Figure 4.9:**  $^{23}\text{Na}$  MAS NMR spectra obtained at a spinning speed of 11 kHz for the  $\text{NaYF}_4$  nanoparticles at 11.7 T. The parameters obtained for these spectra are listed in Table 4.2, pg. 93. \*indicate spinning side bands.



**Figure 4.10:**  $^{23}\text{Na}$  MAS NMR spectra of  $\text{NaYF}_4$  nanoparticles at 21.1 T (900 MHz) (A) undoped, (B) doped with 1 mol %  $\text{Er}^{3+}$ , (C) doped with 2 mol %  $\text{Er}^{3+}$  as reported by Arnold *et.al.* (2013).

The samples were spun at 11 kHz under MAS conditions, thus the heteronuclear dipolar interactions will be mostly averaged out and these spectra are therefore dominated by the second-order quadrupolar coupling and chemical shift interactions. Usually, the extent of their impact cannot be determined (and separated) in a 1D MAS spectrum, but with the availability of fitting program Sola in the Bruker Topspin software, a good estimation can be made. The actual peak position of a quadrupolar nucleus may not be at the maximum intensity of a signal but, due to quadrupolar coupling it has an induced shift and this is known as the quadrupolar induced shift ( $\delta_{\text{QIS}}$ ). The line broadening observed is due to second-order quadrupolar interaction effects and these decrease with increasing magnetic field, thus changing the magnetic field strength will change the position of a given peak (resulting from the quadrupolar induced shift  $\delta_{\text{QIS}}$ ) according to the following equation:

$$\delta_{\text{QIS}} = \delta_{\text{CG}} - \delta_{\text{iso}} = -25000(C_Q^2/\nu_0^2)(1 + \eta_Q^2/3) \quad (3.1)$$

where  $\delta_{CG}$  (ppm) is the peak position or center of gravity,  $\delta_{iso}$  (ppm) the true isotropic chemical shift in the absence of quadrupolar coupling,  $C_Q$  (MHz) the quadrupolar coupling constant,  $\nu_0$  (MHz) is the Larmor frequency of the observed nucleus, and  $\eta_Q$  the asymmetry parameter of the quadrupolar coupling tensor. These values were calculated for the UCNPs based on the one-dimensional MAS spectra shown in Figure 4.9, pg. 90 (and Figure 4.11, pg. 92) and are reported in Table 4.2, pg. 93.

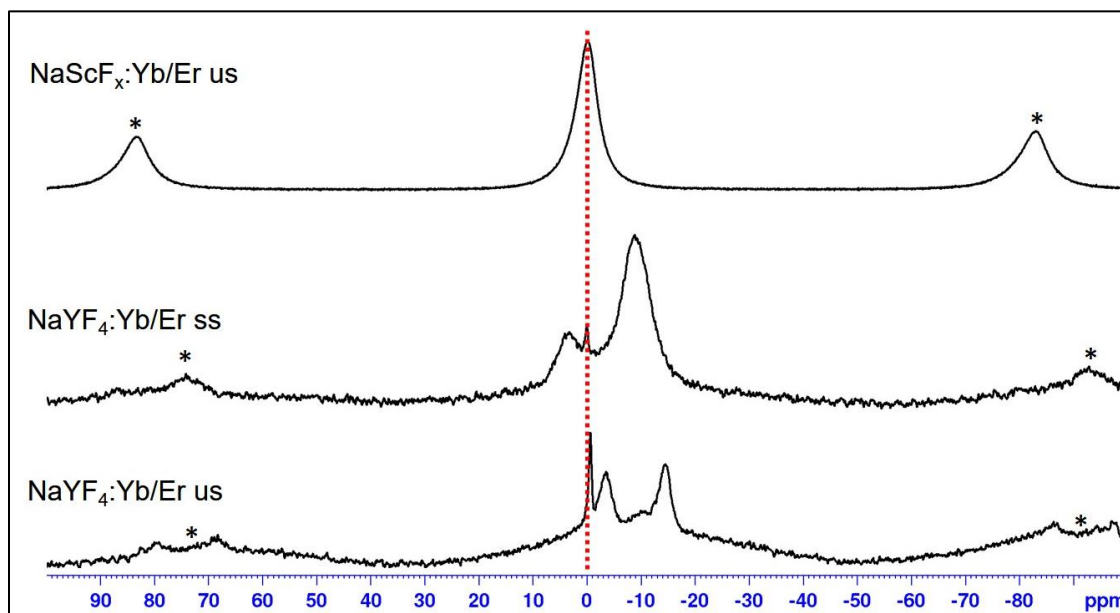


**Figure 4.11:**  $^{23}\text{Na}$  MAS NMR spectra obtained at a spinning speed of 11 kHz for the  $\text{NaYF}_4:\text{Yb/Er}$  NPs as a comparison and for the  $\text{NaScF}_4:\text{Yb/Er us}$  nanoparticles at 11.7 T. Spectra for the  $\text{NaScF}_4:\text{Yb/Er ss}$  sample was also obtained but subsequently lost due to hardware issues. The parameters obtained for these spectra are listed in Table 4.2, pg. 93. \*indicate spinning side bands.

Experiments such as multiple-quantum MAS (MQMAS) are able to separate the chemical shift and quadrupolar coupling effects in 2D. This is a robust experiment and is often employed by researchers. For our purposes, however, fitting of the acquired 1D spectra offered us a reasonable insight into the various parameters. The small quadrupolar coupling constants varied between 2 and 4 MHz for the  $\text{NaYF}_4$  samples (Table 4.2, pg. 93), in agreement with those obtained by Arnold et al. (2013). The chemical shifts ( $\delta_{iso}$ ) obtained for the  $\text{NaYF}_4$  nanocrystals varied between -7 and -25 ppm, which were also in agreement with those determined by Arnold et al.

(2013). A clear trend in  $^{23}\text{Na}$  chemical shift was shown by Bessada *et al.* (2009) when the authors showed that the chemical shift becomes more negative with increasing  $\text{YF}_3$  content i.e. when the number of  $\text{Y}^{3+}$  ion increases. This may explain the results obtained for the  $\text{NaScF}_4:\text{Yb}/\text{Er}$  samples, where the chemical shift obtained for the  $^{23}\text{Na}$  spectrum was determined to be -4.2 and -6.4 ppm for the  $\text{NaScF}_4:\text{Yb}/\text{Er}$  ss and  $\text{NaScF}_4:\text{Yb}/\text{Er}$  us samples (Figure 4.11, pg. 92), respectively (Table 4.2, pg. 93), since no  $\text{Y}^{3+}$  ions are present in the crystal lattice. The spectra obtained for the  $\text{NaScF}_4:\text{Yb}/\text{Er}$  ss is not shown, due to hardware difficulties encountered, however the data is listed in Table 4.2, pg. 93. With these results in mind, it appears, then, that  $^{23}\text{Na}$  is indeed very sensitive to the co-ordination environment within the crystal lattice, since no differences in the XRD powder patterns were observed for  $\text{NaYF}_4:\text{Yb}/\text{Er}$  ss, whereas the NMR spectra for this sample are clearly very different. The absence of the  $\text{Y}^{3+}$  ion in the crystal lattice was also observed to have an effect on the isotropic chemical shift.

**Table 4.2:** Isotopic Chemical Shifts  $\delta_{\text{iso}}$  (ppm), Quadrupolar Coupling Constants ( $C_Q$ , MHz) and Asymmetry ( $\eta$ ) parameters as extracted from  $^{23}\text{Na}$  and  $^{45}\text{Sc}$  one-dimensional NMR Spectra for the various upconversion nanoparticles.

Sample	Site	$^{23}\text{Na}$			$^{45}\text{Sc}$		
		$\delta_{\text{iso}}$ (ppm)	$C_Q$ (MHz)	$\eta$	$\delta_{\text{iso}}$ (ppm)	$C_Q$ (MHz)	$\eta$
$\text{NaYF}_4:\text{Yb}/\text{Er}$ ss	1	-4.2	1.5	0.99	-	-	-
	2	-13.9	1.0	0.84	-	-	-
$\text{NaYF}_4:\text{Yb}/\text{Er}$ us	1	-12.039	-0.013	0	-	-	-
	2	-22.712	0.069	1	-	-	-
	3	0.294	3.790	1	-	-	-
$\text{NaYF}_4:\text{Yb}/\text{Ho}$ ss	1	-12.178	0.279	0.535	-	-	-
	2	-23.237	0.333	0	-	-	-
	3	-19.198	0.357	0.158	-	-	-
$\text{NaYF}_4:\text{Yb}/\text{Ho}$ us	1	5.88	2.939	1	-	-	-
	2	-23.266	-0.082	0	-	-	-
	3	-5.453	3.864	0	-	-	-
$\text{NaScF}_4:\text{Yb}/\text{Er}$ ss	1	4.177	1.526	0.988	53.05	3.839	1
	2	-13.914	2.719	0.835	23.74	5.334	1
$\text{NaScF}_4:\text{Yb}/\text{Er}$ us	1	-6.363	1.025	0.929	23.864	4.278	0.983

Figure 4.12, pg. 94 shows the  $^{45}\text{Sc}$  MAS NMR spectra obtained for the  $\text{NaScF}_4:\text{Yb}/\text{Er}$  us nanoparticles at 11.7 T. This figure also shows the observed shifts in the spinning side bands at different MAS speeds showing the true chemical shift for the UCNP sample at  $\sim 16.8$  ppm, since the spinning side bands shift with different spinning speeds, while the isotropic chemical shift remains. A single broad peak was obtained for the  $\text{NaScF}_4:\text{Yb}/\text{Er}$  NPs us, with no apparent

shoulders (and therefore one site), and the  $\delta_{\text{iso}}$  was calculated to be 23.9 ppm, while the quadrupolar coupling constants were also small ( $\sim 4$  MHz) (Table 4.2, pg. 93). The powder pattern obtained for NaScF<sub>4</sub>:Yb/Er NPs ss sample was different however, as indicated by the contributions of the various parameters given in Table 4.2, pg. 93. Four possible sites were identified for the small scale sample with two main peaks and two apparent shoulders. This was expected as the XRD powder patterns obtained for the upscaled and small-scale sample were indeed very different. However, the XRD pattern seemed slightly more complex – as if more than one phase was present. Given that single peaks were obtained in both <sup>23</sup>Na and <sup>45</sup>Sc NMR, together with the sensitivity of the <sup>23</sup>Na nucleus to changes in its chemical environment, it is possible that one pure phase is present in the NaScF<sub>4</sub>:Yb/Er NPs us sample. In addition, excellent upconversion fluorescence data (discussed later in this chapter) made for great excitement.

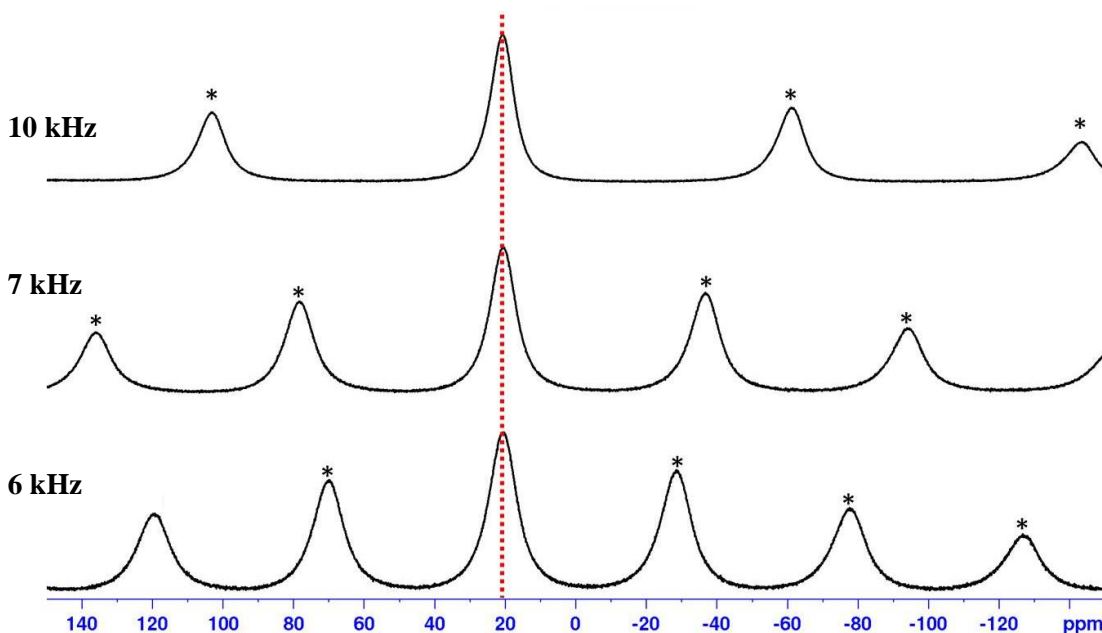


**Figure 4.12:** <sup>45</sup>Sc MAS NMR spectra obtained at various spinning speeds i.e. 6, 7 and 10 kHz for the NaScF<sub>4</sub>:Yb/Er NPs us as a comparison and for the NaScF<sub>4</sub>:Yb/Er us nanoparticles at 11.7 T.

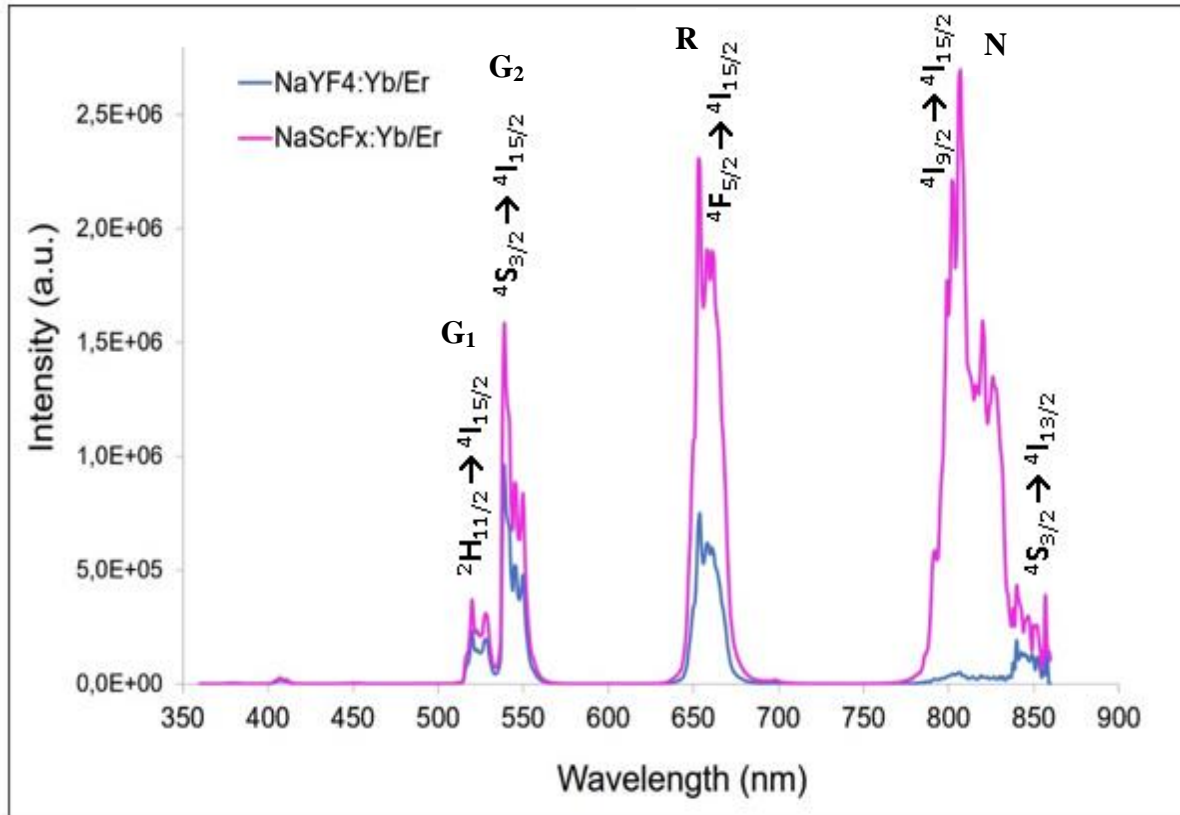
#### 4.2.4 Steady state fluorescence spectroscopy

The upconversion luminescence of the UCNPs synthesized were also studied using a 980 nm diode laser to excite the samples. The samples were analysed as both powders and in solution

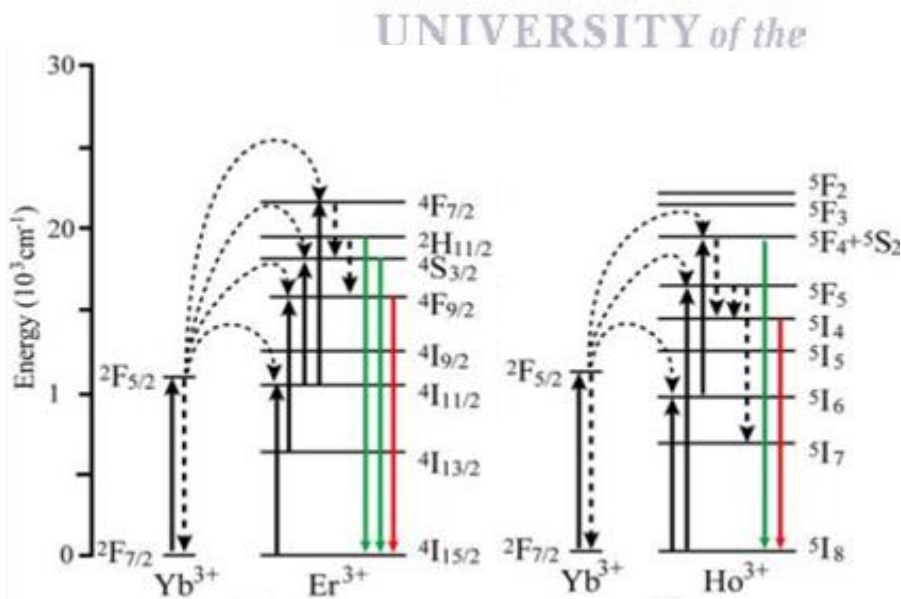
(using ethanol and water). Only the samples prepared using the upscaled method were analysed as 1 g of powder is required for analysis. Many of these powders were found to be hygroscopic, particularly the  $\text{KY}_x\text{F}_y$ , which formed a gel over time, and  $\text{LiY}_x\text{F}_y$ , which formed a paste when crushed. The samples were therefore heated in a drying oven at 150 °C for 2 h and ground.

Figure 4.13, pg. 96 shows the luminescence spectra obtained for all the samples at an  $\lambda_{\text{ex}} = 980$  nm. The intensity as well as the spectral distribution were found to differ for the individual samples. Stark level-related substructures (i.e. the fine splitting observed in the emission peaks) were also apparent within e.g. the green (G1 and G2) and the red (R) emission bands (Figure 4.13, pg. 96). The Stark splitting is caused by the crystal field of the ligands located around the Er cations in the host lattice (Suyver *et al.*, 2005; Eliseeva and Bunzli, 2010; Klier *et al.*, 2015).

Typically, three strong emission bands can be observed in the spectra corresponding to the green emission bands at  $\lambda_{\text{em}} = 525$  nm (G1, due to the  $^2\text{H}_{11/2} \rightarrow ^4\text{I}_{15/2}$  transition) and  $\lambda_{\text{em}} = 540$  nm (G2, due to the  $^4\text{S}_{3/2} \rightarrow ^4\text{I}_{15/2}$  transition), and the red emission band at  $\lambda_{\text{em}} = 660$  nm (R, due to the  $^4\text{F}_{9/2} \rightarrow ^4\text{I}_{15/2}$  transition). An additional strong emission band was observed for the  $\text{NaScF}_4$  sample centred at  $\lambda_{\text{em}} = 810$  nm (N, due to the  $^4\text{I}_{9/2} \rightarrow ^4\text{I}_{15/2}$  transition). These transitions are typically observed for Yb/Er doped crystal matrices and are clarified in Scheme 4.1A, pg. 96 below. It is quite striking to observe how intense the emission bands of the  $\text{NaScF}_4:\text{Yb/Er}$  sample is in comparison to the  $\text{NaYF}_4:\text{Yb/Er}$  (at least double in intensity) where the latter were considered to have the best quality crystals. It is also important to remember that the  $\text{NaYF}_4:\text{Yb/Er}$  nanocrystals are cubic phase, and therefore they are not expected to perform at its optimum. At this point the phase of the  $\text{NaScF}_4$  crystal lattice is uncertain and may very well be that of a lower symmetry than the cubic phase found for the  $\text{NaYF}_4$  lattice. As mentioned previously, the ionic radius of Sc is smaller than that of the Y ionic radius, and with the decrease in the unit cell lattice parameters, an increase in crystal field strength is expected to lead to an increase in upconversion emission (Wang *et al.*, 2010). Also, immediately noticeable is that the most intense emission for this nanocrystal is in the NIR region at  $\lambda_{\text{em}} = 810$  nm. This emission is either very weak for the  $\text{NaYF}_4$  sample, or it is non-existent.



**Figure 4.13:** Upconversion luminescence spectra for the NaYF<sub>4</sub>:Yb/Er and NaScF<sub>4</sub>:Yb/Er UCNPs under 980 nm laser excitation.



**Scheme 4.1:** Possible UC emission mechanisms for A) NaYF<sub>4</sub>:Yb/Er and NaScF<sub>4</sub>:Yb/Er UCNPs and B) NaYF<sub>4</sub>:Yb/Ho UCNPs under 980 nm laser excitation.

The transitions observed for the NaYF<sub>4</sub>:Yb/Ho samples also show four emission bands (Figure 4.14, pg. 97), however these are at slightly different wavelengths. For comparison, the UC spectrum for NaF<sub>4</sub>:Yb/Er sample is also shown in Figure 4.14, pg. 97 and this shows that the intensity of the emission bands are approximately 3 times less than that for Er sample. This was unexpected as the quality of the NaYF<sub>4</sub>:Yb/Ho crystals were deemed to be comparable to that of the NaYF<sub>4</sub>:Yb/Er samples according to the XRD data (Figure A4.1, pg. 137). The green emission bands are observed at  $\lambda_{em} = 540$  nm (G, due to the  $^5F_4, ^5S_2 \rightarrow ^5I_8$  transition), a red band at  $\lambda_{em} = 650$  nm (R, due to the  $^5F_5 \rightarrow ^5I_8$  transition), and NIR emission bands at  $\lambda_{em} = 750$  nm (N1, due to the  $^5F_4, ^5S_2 \rightarrow ^5I_8$  transition) and 805 nm (N2, due to the  $^4I_{9/2} \rightarrow ^4I_{15/2}$  transition). The emission band at  $\lambda_{em} = 750$  nm is not observed for the Er sample, while those bands at emission bands at  $\lambda_{em} = 810, 540$  and 650 nm are observed, although a slight shift is observed for the latter. Stark level-substructures are also observed for the Ho sample, although it is much clearer in the band at  $\lambda_{em} = 540$  nm compared to the others.

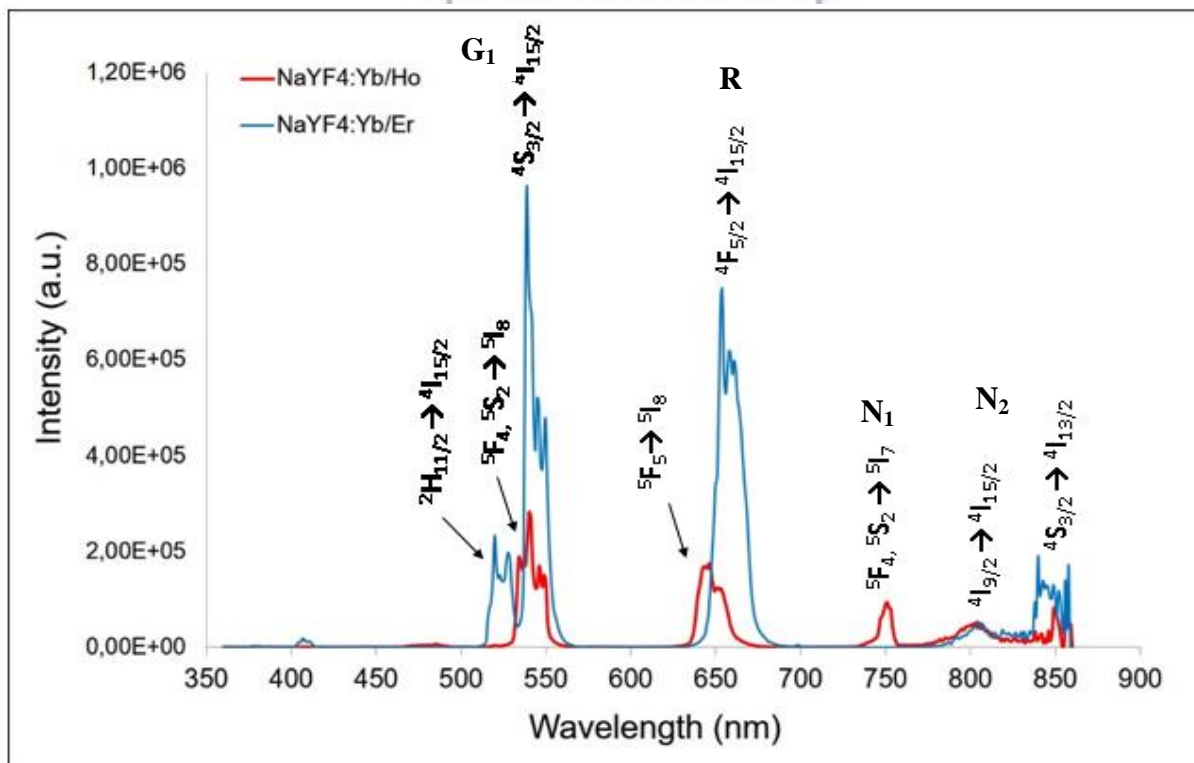


**Figure 4.14:** Upconversion luminescence spectra for the NaYF<sub>4</sub>:Yb/Ho and NaYF<sub>4</sub>:Yb/Er UCNPs under 980 nm laser excitation.

The upconversion luminescence spectra obtained for the  $\text{LiY}_x\text{F}_y:\text{Yb}/\text{Er}$  and  $\text{KY}_x\text{F}_y:\text{Yb}/\text{Er}$  UCNPs are shown in Figure 4.15, pg. 98. It is apparent that the  $\text{KY}_x\text{F}_y$  and  $\text{LiY}_x\text{F}_y$  samples gave almost no upconversion luminescence. Plotting the spectra on a log-scale reveals many small peaks which can be easily identified, and these spectra may be found in the appendices. The sloping background which increases with increasing wavelength is due to the scattered excitation light obtained as one approaches the excitation wavelength of 980 nm.

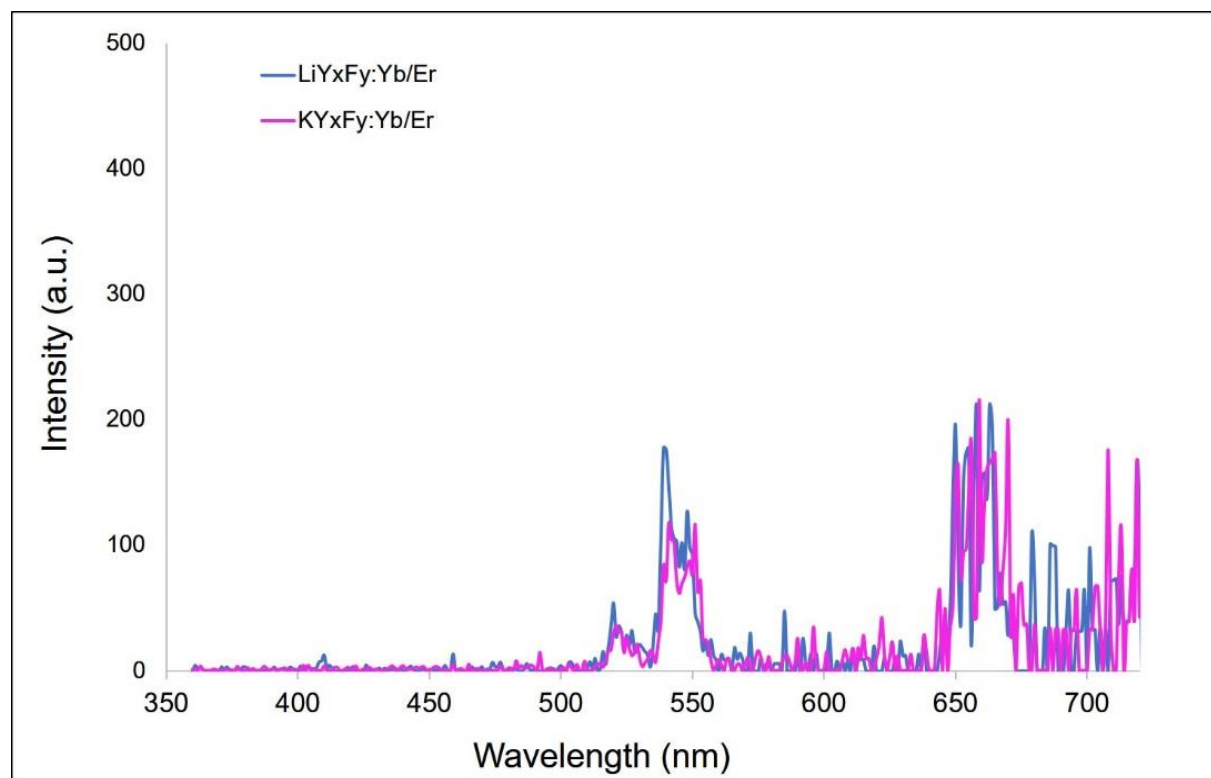


**Figure 4.15:** Upconversion luminescence spectra for the  $\text{KY}_x\text{F}_y:\text{Yb}/\text{Er}$  and  $\text{LiY}_x\text{F}_y:\text{Yb}/\text{Er}$  UCNPs powder samples under 980 nm laser excitation.

Upconversion luminescence spectra were also measured in solution. The solutions were made by adding 0.1 mmol powder by mass (ignoring dopants) in 10 ml of solvent (ethanol or water) and stirring for 2 h at room temperature. Unfortunately, some settling of the suspended powder occurred and was more pronounced in water. This means then that the actual concentration is considerably less and not known. The upconversion luminescence produced by all the solutions were weak compared to the powders, even though the laser power, monochromator bandpass and integration time were increased. The luminescence spectra for the  $\text{NaScF}_4$  UCNPs sample is

shown in Figure 4.16, pg. 99 as an example. The powder spectrum is also given, and the data are plotted on a logarithmic scale to reveal signals. The luminescence intensities for the ethanol solutions were slightly higher than the water solutions, though still very weak. This is due to the fact that ethylene glycol was used as the reducing and capping agent and is not likely to impart a great deal of solubility to the NPs. Future work would therefore involve the use of a polymer such as polyvinylpyrrolidone (PVP) in the synthetic reaction which should improve the concentration of the NPs in solution considerably. The spectra obtained for the other UCNPs may be seen in the appendix.

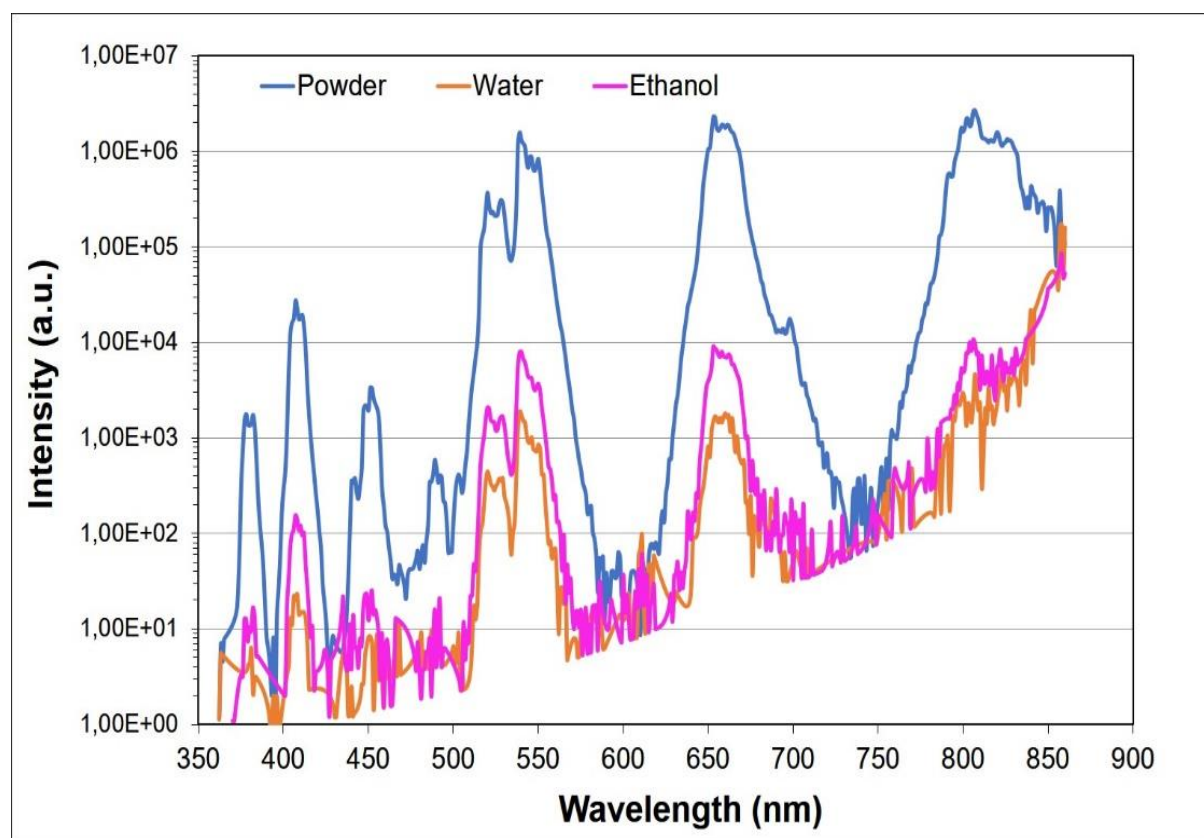


**Figure 4.16:** Upconversion luminescence spectra for the NaScF<sub>4</sub>:Yb/Er UCNP sample, in powder form as well as in ethanol and water, under 980 nm laser excitation. The graph is plotted on a logarithmic scale.

#### 4.2.4 Summary and Conclusion

The chapter revolved around the five different UCNPs synthesized with regards to their characterisation. The nanoparticles were synthesized with a Microwave solvothermal method which most notably utilised a shorter reaction time and lower temperature. There was also good reproducibility of the nanoparticles compared to the previous methods tested. The nanoparticles were synthesized on a small and larger scale. The physical appearance of the nanoparticles was a white powder except for the NaYF<sub>4</sub>:Yb/Ho, which yielded a pink colour, as well as the small scaled LiY<sub>x</sub>F<sub>y</sub>:Yb/Er and KY<sub>x</sub>F<sub>y</sub>:Yb/Er which yielded a brown colour. The KYF:Yb/Er nanoparticles had a “paste like” texture. The TEM results showed a lot of aggregation of the nanoparticles which was due to the ineffective capping agents. The average sizes obtained from the TEM images of the various UCNPs ranged from 10 nm – 80 nm. The XRD results on the other hand showed that the average size of the nanoparticle was between 9 – 45 nm. The crystalline structure of the nanoparticles obtained from the XRD results showed that the NaYF<sub>4</sub>:Yb/Er and NaYF<sub>4</sub>:Yb/Ho were in a cubic phase. The NaScF<sub>4</sub> nanoparticles appeared to be hexagonal but there was evidence of other phases as well for the upscaled sample. The KY<sub>3</sub>F<sub>10</sub>:Yb/Er nanoparticles were found to be in a tetragonal phase.

The solid state NMR data showed broad powder like patterns for the <sup>23</sup>Na NMR spectra of the NaYF<sub>4</sub> UCNPs. The <sup>23</sup>Na powder pattern obtained for NaScF<sub>4</sub>:Yb/Er NPs ss and us sample was found to be different however, and this was expected as the XRD powder patterns obtained for the upscaled and small-scale sample were indeed different. The XRD pattern seemed slightly more complex – as if more than one phase was present. Given that single peaks were obtained in both <sup>23</sup>Na and <sup>45</sup>Sc NMR, together with the sensitivity of the <sup>23</sup>Na nucleus to changes in its chemical environment, it is possible that one pure phase is present in the NaScF<sub>4</sub>:Yb/Er NPs us sample.

In the steady state fluorescence spectra, NaYF<sub>4</sub>:Yb/Er and NaScF<sub>4</sub>:Yb/Er nanoparticles showed three strong emission bands in the spectra corresponding to the green emission bands at  $\lambda_{em} = 525$  nm and  $\lambda_{em} = 540$  nm, and the red emission band at  $\lambda_{em} = 660$  nm. An additional very strong emission band was observed for the NaScF<sub>4</sub> sample centred at  $\lambda_{em} = 810$  nm. It was found that the emission bands for the NaScF<sub>4</sub>:Yb/Er sample was more intense in comparison to the

NaYF<sub>4</sub>:Yb/Er. The transitions observed for the NaYF<sub>4</sub>:Yb/Ho samples also showed four emission bands at slightly different wavelengths. The green emission bands are observed at  $\lambda_{em} = 540$  nm, a red band at  $\lambda_{em} = 650$  nm, and NIR emission bands at  $\lambda_{em} = 750$  nm and 805 nm. The KY<sub>3</sub>F<sub>10</sub> and LiY<sub>x</sub>F<sub>y</sub> samples gave almost no upconversion luminescence.



UNIVERSITY *of the*  
WESTERN CAPE

## Part B:

### Chapter 5: Synthesis and Characterisation of MPcs and the modified NP support

The following chapter will encompass the synthesis, characterisation and the photophysical properties of the phthalocyanine which has been named 4-(4-hydroxymethyl)phenyl Zinc phthalocyanine (**5**) (HMPZnPc) and AgNPs/Pc (**8**).

#### 5.1 Synthesis and characterization of MPcs

##### 5.1.1 Synthesis and characterisation of ZnPc (**4**) standard

The synthesis of the ZnPc was accomplished and confirmed with UV/Vis spectroscopy which resulted in a spectrum representative of a metallated zinc phthalocyanine as shown in Figure 5.1. A, pg. 103. FTIR spectroscopy was used to identify the characteristic peaks of functional groups found on the phthalocyanine in Figure 5.1. B, pg. 103. The functional groups identified was the aromatic C-H bonds at  $3014\text{ cm}^{-1}$  and  $3006\text{ cm}^{-1}$ . The stretches at  $1500\text{ cm}^{-1}$ ,  $1328\text{ cm}^{-1}$ ,  $1064\text{ cm}^{-1}$  and  $977\text{ cm}^{-1}$  correlated to the C=C bonds (Cakir *et al.*, 2015). The disappearance of the characteristic C≡N bond at  $\sim 2200\text{ cm}^{-1}$ , together with the UV/Visible absorption spectrum confirmed the successful formation of the ZnPc (**4**) standard.

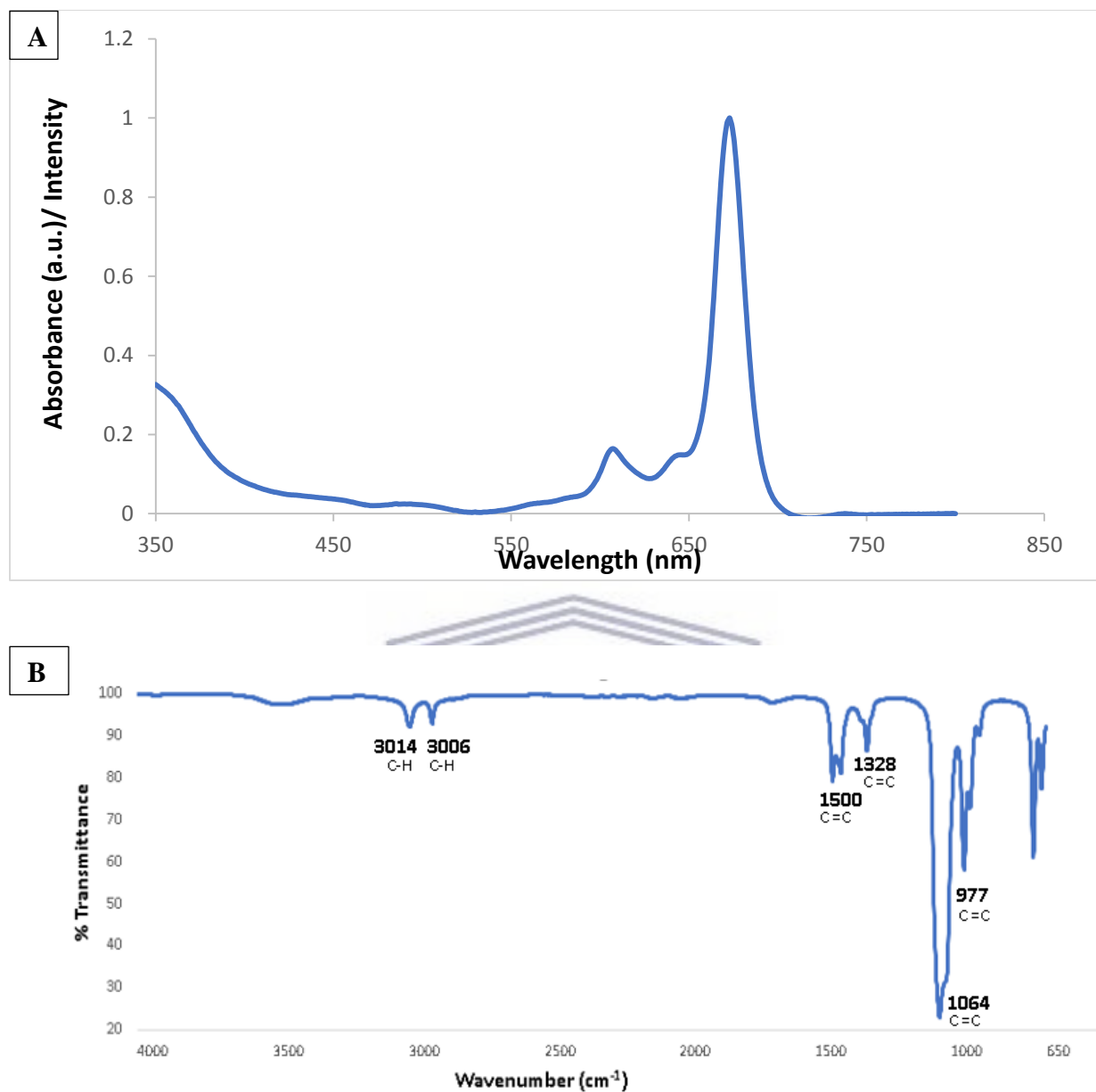
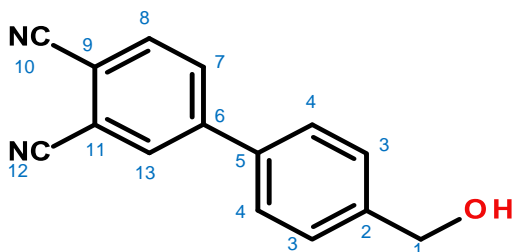


**Figure 5.1:** A) The UV/Visible spectrum of the ZnPc in DMSO and B) the FTIR spectrum of the ZnPc.

## 5.1.2 Synthesis and characterisation of 4-(4-hydroxymethyl)phthalocyanine Zn(II) (HMPZnPc) (**5**)

### 5.1.2.1 Synthesis and characterisation of phthalonitrile precursor 4-(4-hydroxymethyl)-phthalonitrile (**3**)



4-(4-hydroxymethyl)-phthalonitrile (**3**).

The desired phthalocyanine (HMPZnPc, complex **5**) required the initial synthesis of the phthalonitrile precursor, 4-(4-hydroxymethyl)phenyl-phthalonitrile (**3**). This was accomplished by using 4-iodophthalonitrile (**1**) and 4-(hydroxymethyl)phenyl boronic acid (**2**) in the presence of a palladium catalyst, Pd(PPh<sub>3</sub>)<sub>4</sub>. This reaction is known as the Suzuki-Miyaura carbon-carbon coupling reaction and it is considered the corner stone of organic chemistry these days. The Suzuki-Miyaura coupling reaction normally involves insertion of palladium into a sp<sup>2</sup>-hybridized C-X bond, and, unlike other synthetic methods, this reaction is often used with a variety of functional groups since the reaction utilizes mild conditions. Additionally, the method can be used in large scale syntheses (e.g. it is used in the pharmaceutical industry to produce Boscolid (Yan *et al.*, 2008, Dey *et al.*, 2010) and Losartan (Dey *et al.*, 2010)) due to the stability and commercial availability of a wide range of boronic acids, and especially the ease in working up the reaction (Felpin *et al.*, 2005).

Since good NMR spectra/data is notoriously difficult to obtain for phthalocyanines (due to solubility and aggregation issues), 1D and 2D NMR data was acquired for the synthesized phthalonitrile (**3**) and the data carefully interrogated. Given below in Figure 5.2, pg. 106 is the <sup>1</sup>H NMR data for each of the starting materials i.e. 4-iodophthalonitrile (**1**) in CDCl<sub>3</sub> (A) and 4-(hydroxymethyl)phenyl boronic acid (**2**) in DMSO-*d*<sub>6</sub> (D). Unfortunately, the solubility of these materials precluded the acquisition of the data in the same solvent, however, the phthalonitrile product was acquired in both CDCl<sub>3</sub> and DMSO-*d*<sub>6</sub> to enable comparison and

for clarity (Figure 5.2 B and C, pg. 106, respectively). The assignment of the proton signals is easily achieved for the iodophthalonitrile (**1**), since fine coupling ( $J < 2$  Hz) is observed for the aromatic meta protons in Figure 5.2 A, pg. 106, for the doublet of doublets  $\delta_{\text{H}}$  8.11 (H-7) and the doublet, which appears to be a singlet at first, at  $\delta_{\text{H}}$  8.14 (H-13). This then leaves the methine doublet at  $\delta_{\text{H}}$  7.50 (H-8). On the other hand, the  $^1\text{H}$  spectrum for the boronic acid (**2**) is decidedly complex at first (Figure 5.2 D, pg. 106). The reason for the complexity of the aromatic protons at  $\sim\delta$  7.3 (H-3) and  $\delta$  7.8 (H-3), is that boron has two NMR active isotopes with spin.  $^{11}\text{B}$  has a spin  $I = 3/2$  with a natural abundance of  $\sim 80\%$ , while  $^{10}\text{B}$  has a spin  $I = 3$  with a natural abundance of  $\sim 20\%$ . The NMR signals for boron compounds are often quite complicated due to the observed, strong,  $J$  coupling between the protons (as well as carbons) and both  $^{11}\text{B}$  and  $^{10}\text{B}$  isotopes. This means that a signal for a proton signal coupled to, or near a single boron would be the sum of two multiplets (a 1:1:1:1 quartet from  $^{11}\text{B}$  and a 1:1:1:1:1:1:1 septet from  $^{10}\text{B}$ ) in a  $\sim 4:1$  ratio according to their natural abundance. Thus, the observation of this complexity actually becomes a useful tool in Suzuki-Miyaura C-C coupling reactions, since the collapse of these complex signals to the expected two sets of aromatic signals would immediately indicate the successful formation of the phthalonitrile product (**3**), and this is what is indeed observed in Figure 5.2 C, pg. 106. In addition to the aromatic set of protons for the boronic acid, three broad signals which are attributed to the 3 hydroxyl moieties are also observed.



HMBC, Table 5.1, pg. 110), the signals at  $\delta_{\text{H}}$  7.47 and 7.80 were assigned to H-3 and H-4, respectively (Figure A5.2, pg. 148). The methylene signal on ring B is easily observed at  $\delta_{\text{H}}$  4.6 (2H), which is expected for a  $\text{CH}_2\text{-O}$  moiety. The multiplicity of this signal, a doublet, indicates that it has one neighbour, confirming that the methylene is next to the hydroxyl moiety. The triplet at  $\delta_{\text{H}}$  5.4 (1H) was at first confusing since the only signal that could account for this multiplicity is the  $\text{OH}$  moiety. Generally broad signals are observed for heteroatoms, but this was later confirmed using an HSQC experiment (Table 5.1, pg. 110, Figure A 4.2) which shows the correlations of the protons directly attached to carbon signals. The lack of a correlation confirmed that the triplet at  $\delta_{\text{H}}$  5.4, indeed confirmed that this was the  $\text{OH}$  proton. The chemical shifts, multiplicities and integration values are listed in Table 5.1, pg. 110.

The  $^{13}\text{C}$  (100 MHz) spectra for the phthalonitrile product (**3**) were also acquired in  $\text{CDCl}_3$  and  $\text{DMSO-}d_6$  to enable comparison with the starting materials **1** and **2**. These spectra are shown in Figure 5.3, pg. 108 and the data is listed in Table 5.1, pg. 110. Thirteen signals including one methylene, five methine and seven quaternary carbons were expected and observed. The success of the reaction was easily construed from the disappearance of the carbon signal at  $\delta_{\text{C}}$  99.7 which is characteristic for an aromatic carbon attached to an iodo group. This signal was not observed in the data acquired in either  $\text{CDCl}_3$  and  $\text{DMSO-}d_6$  for the product (**3**), indicating that the reaction had gone to completion. The methylene signal is observed at  $\delta_{\text{C}}$  62.5 which is characteristic for a  $\text{CH}_2\text{-OH}$  moiety. The intensity of the protonated carbons at  $\delta_{\text{C}}$  127.3 and 127.4 indicated that these signals belong to the chemically equivalent carbon atoms on ring B and could be assigned (based on the 2D data obtained, Table 5.1, pg. 110) to C-4 and C-3. The remaining protonated carbons, C-7, C-8 and C-13 which belong to ring A, were observed at  $\delta_{\text{C}}$  131.6, 134.7 and 131.9, respectively, based on the correlations observed in the HSQC (Figure 5.2, pg. 106) and HMBC (Figure 5.4, pg. 109) data (Table 5.1, pg. 110). The cluster of quaternary carbons observed between  $\delta_{\text{C}}$  112.8 and 116.3 are characteristic for phthalonitrile carbon signals i.e. C-9, C-10, C-11 and C-12. The remaining quaternary carbons unaccounted for are those of C-3 and C-6 and these are the crucial signals where correlations to these signals indicate the successful formation of the Suzuki-Miyaura C-C bond formation. The HMBC (Figure 5.4, pg. 109) experiment provided the vital correlations confirming the formation of this bond.

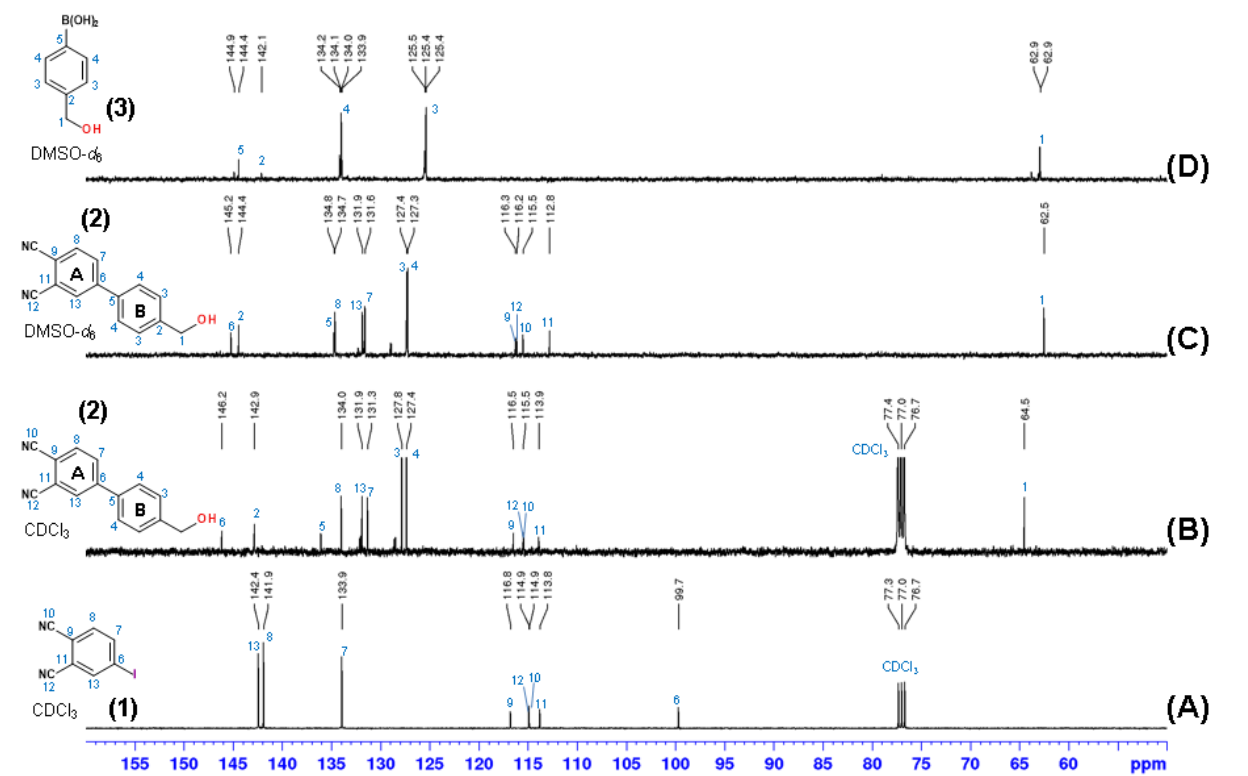


**Figure 5.3:**  $^{13}\text{C}$  NMR (400 MHz) data acquired at 298K for A) 4-iodophthalonitrile (**1**, in  $\text{CDCl}_3$ ), B) phthalonitrile product (**3**, in  $\text{CDCl}_3$ ), C) phthalonitrile product (**3**, in  $\text{DMSO}-d_6$ ) and D) 4-(hydroxymethyl)phenyl boronic acid (**4**, in  $\text{DMSO}-d_6$ ).

The 2D HMBC spectrum confirmed the assignments of the proton and carbon signals discussed above. More importantly, however, HMBC correlations observed from H-4 to C-6 and H-13 to C-3 (Figure 5.4, pg. 109) provided conclusive proof that the bond between ring A and ring B had indeed formed (Table 5.1, pg. 110). The pertinent HMBC correlations are also shown in Figure 5.5, pg. 109. Additional 2D spectra (COSY, HSQC) and the DEPT-135 spectra are included in the Appendix A4.1 – 4.3.

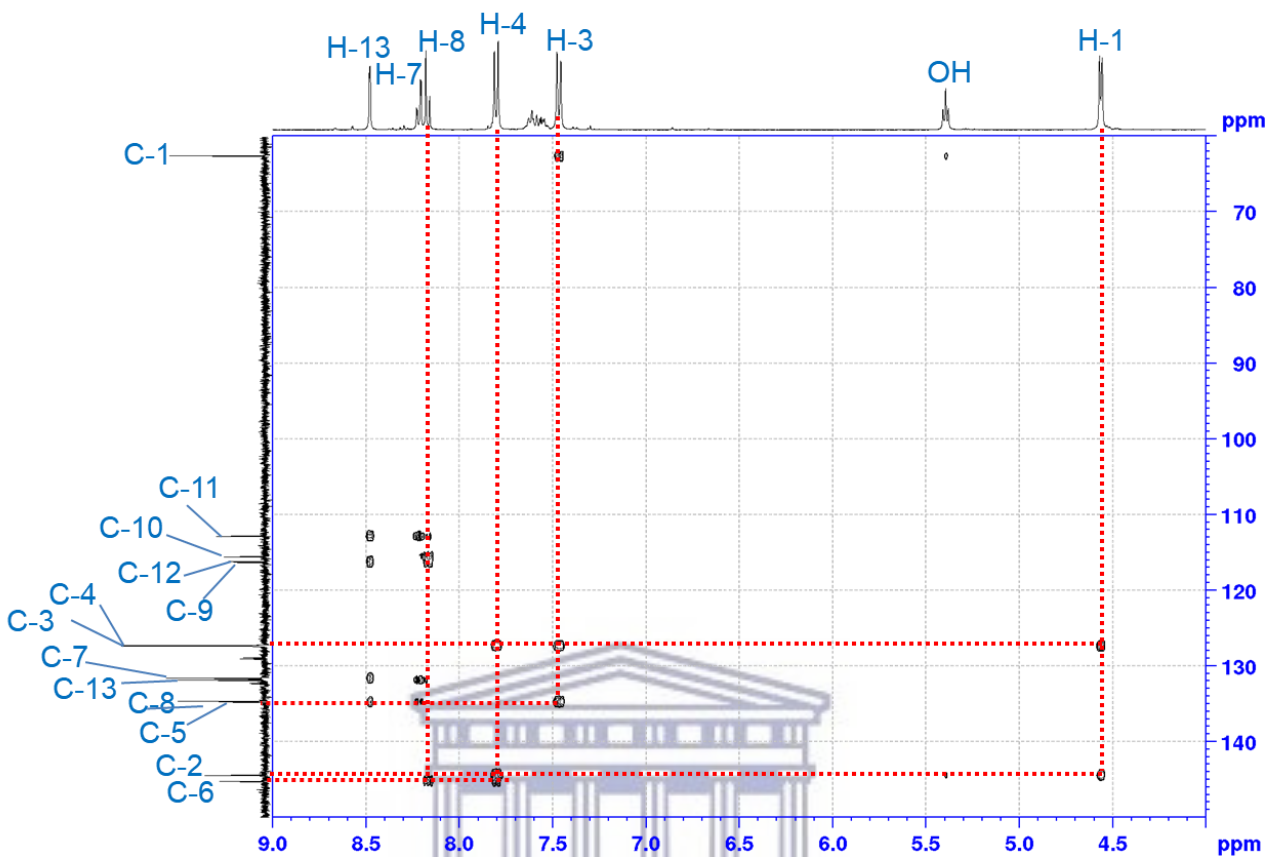


**Figure 5.4:** HMBC spectrum acquired on a 400 MHz NMR instrument at 298 K in DMSO- $d_6$ . Key correlations observed for compound **3** are shown.

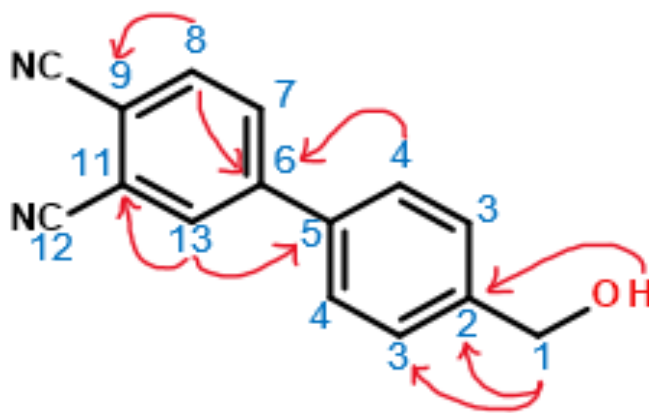


**Figure 5.5:** Important HMBC correlations observed for compound **3**.

**Table 5.1:**  $^1\text{H}$ ,  $^{13}\text{C}$ , HSQC, COSY and HMBC data acquired for 4-(4-hydroxymethyl)phthalonitrile (**3**) at 400 MHz in DMSO- $d_6$  at 298K. The correlations observed in the 2D spectra for the various proton signals.

Atom No.	$\delta_{\text{C}}$ (mult.)	$\delta_{\text{H}}$ (integ., mult., $J$ )	COSY	HMBC
1	62.5 (CH <sub>2</sub> )	4.57 (2H, d, $J = 5.7$ Hz)	H-3, OH	C-2, C-3
2	144.4 (C)	-	-	-
3	127.4 (CH)	7.47 (2H, d, $J = 8.0$ Hz)	H-1, H-4	C-1, C-3, <u>C-5</u>
4	127.3 (CH)	7.80 (2H, d, $J = 8.0$ Hz)	H-3	C-1, C-2, C-4
5	134.8 (C)	-	-	-
6	145.2 (C)	-	-	-
7	131.6 (CH)	8.22 (1H, dd, $J = 8.2, 1.7$ Hz)	H-13, H-8	C-11, C-13
8	134.7 (CH)	8.17 (1H, d, $J = 8.2$ Hz)	H-7	C-6, C-10
9	116.3 (C)	-	-	-
10	115.5 (C)	-	-	-
11	112.8 (C)	-	-	-
12	116.2 (C)	-	-	-
13	131.9 (CH)	8.48 (1H, d, $J = 1.7$ Hz)	H-7	C-5, C-7, <u>C-11</u> , C-12
OH	-	5.40 (1H, t, $J = 5.7$ Hz)	H-1	C-1, C-2

The NMR data in combination with the EI-MS data obtained for compound **3** at  $m/z$  235.2 (Calcd.  $m/z$  234.2) confirmed the identity of the product (**3**).

FTIR spectroscopy was used to identify the characteristic peaks of functional groups found on the phthalonitrile precursor in Figure 5.6, pg. 111. The functional groups identified was the OH peak at  $3500\text{ cm}^{-1}$ , aliphatic C-H at  $2934\text{ cm}^{-1}$  and  $2854\text{ cm}^{-1}$ , aromatic C-H bonds at  $3014\text{ cm}^{-1}$  and  $3006\text{ cm}^{-1}$ . The sharp stretches at  $2250\text{ cm}^{-1}$  is characteristic of the  $\text{C}\equiv\text{N}$  and the stretches at  $1600\text{ cm}^{-1}$  characteristic of  $\text{C}=\text{N}$ . The peaks at  $1500\text{ cm}^{-1}$ ,  $1328\text{ cm}^{-1}$ ,  $1064\text{ cm}^{-1}$  and  $792\text{ cm}^{-1}$  correlates to  $\text{C}=\text{C}$  bonds (Cakir *et al.*, 2015).

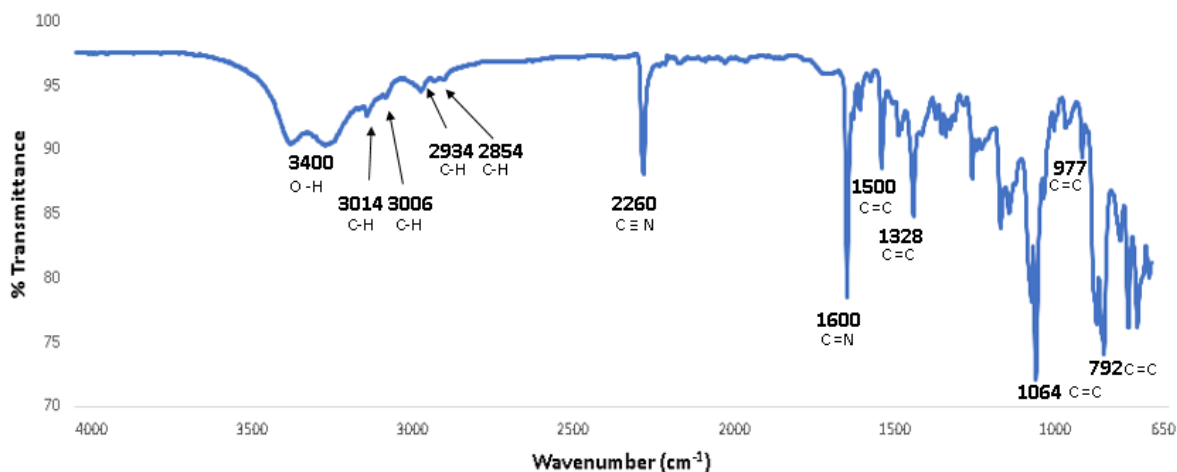
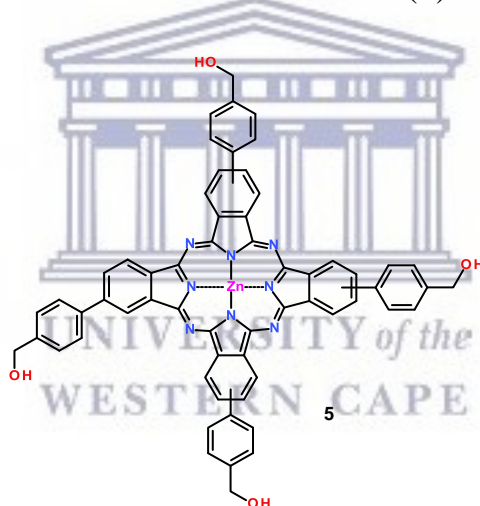


**Figure 5.6:** FTIR spectra of 4-(4-hydroxymethyl)phenyl-phthalonitrile (**3**).

### 5.1.2.2 Synthesis and characterisation of HMPZnPc (**5**)



4-[4-(hydroxymethyl)phenyl] Zinc Phthalocyanine (complex **5**).

As expected, the NMR data acquired for the phthalocyanine (**5**, HMPZnPc), even though it appeared to be highly soluble, was not good. The proton spectrum obtained for the Pc (**5**) in DMSO- $d_6$  at 323 K with water presaturation is shown in Figure 5.7, pg. 112. The temperature was increased to 50 °C in order to try and obtain a better spectrum. Two signals at approximately  $\delta_H$  4.6 integrating to 8, are attributed to the methylene group  $-CH_2-OH$ . The presence of two sets of  $CH_2$  signals is unusual and perhaps could be due to the fact that there are different isomers in tetrasubstituted phthalocyanines. Aromatic signals were observed in the region of  $\delta_H$  7.4 to 8.2 and these integrate to 28 protons as expected (without including the OH groups). A broad signal

which may be attributed to the hydroxyl moiety is observed at  $\delta_{\text{H}}$  9.3. Some impurities attributed to solvents are seen in the region of 2 ppm and below.

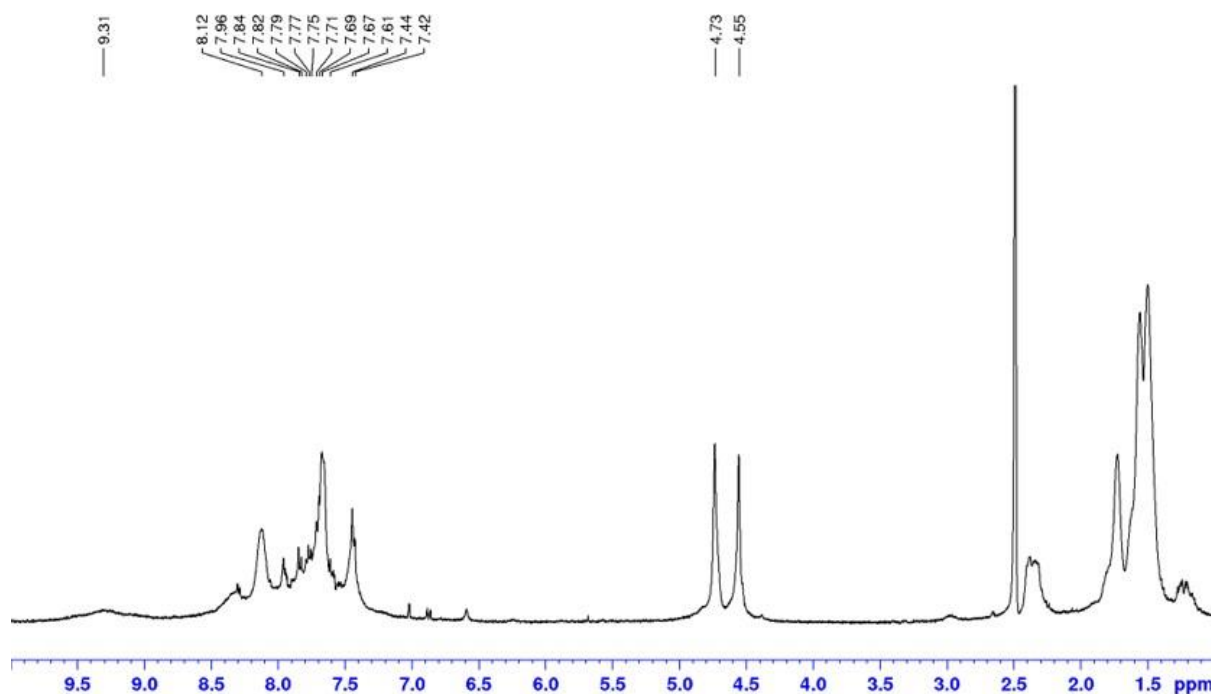


**Figure 5.7:**  $^1\text{H}$  NMR (400 MHz) spectrum acquired for complex **5** (HMPZnPc) in  $\text{DMSO-}d_6$  at 323 K with water presaturation.

Confirmation that the HMPZnPc (**5**) had indeed formed was also provided by MALDI-TOF MS where a molecular ion was observed in the negative ion mode at  $m/z$  998.5 amu (Calcd.  $m/z$  1002.4) corresponding to a loss of 4 hydrogens (most likely from the OH functional groups). The elemental analysis results revealed the presence of some water and Zinc oxide. This was initially puzzling, but upon receiving the results of the XRD analysis for the AgNPs supported on the HMPZnPc, the powder pattern (Figure 5.13, pg. 119) revealed the presence of Zinc oxide (discussed later in this chapter). Zinc oxide may have formed during the synthesis of the Pc where zinc acetate and pentanol was reacted at 150 °C, thus accounting for the low %C level observed. Elemental analysis revealed a composition of: C 60.0 %, H 5.1 %, N 12.1 % (Calcd. C 71.9 %, H 4.0 %, N 11.2 %, O 6.4 %, Zn 6.5 %). Since the main method of purification was precipitation and washing with copious amounts of solvents, it is possible that the Zinc oxide would precipitate during centrifugation. A white powder was not obviously apparent however.

Further characterisation of the HMPZnPc (**5**) was accomplished by the spectroscopic and photophysical studies as discussed in the next sections. FTIR spectroscopy was used to identify the characteristic peaks of functional groups found on the phthalocyanine in Figure 5.8, pg. 113. The functional groups identified was the OH peak at  $3500\text{ cm}^{-1}$ , aromatic C-H bonds at  $3014\text{ cm}^{-1}$  and  $3006\text{ cm}^{-1}$ . The peak at  $1600\text{ cm}^{-1}$  correlates to the C=N bond where the peak at  $1250\text{ cm}^{-1}$  correlates to the C-N bond. The peaks at  $1500\text{ cm}^{-1}$ ,  $1328\text{ cm}^{-1}$ ,  $1064\text{ cm}^{-1}$  and  $977\text{ cm}^{-1}$  correlates to C=C bonds found (Cakir *et al.*, 2015). More importantly, the disappearance of the sharp stretch at  $2260\text{ cm}^{-1}$  attributed to the C≡N has disappeared, confirming the successful formation of the Pc (**5**).

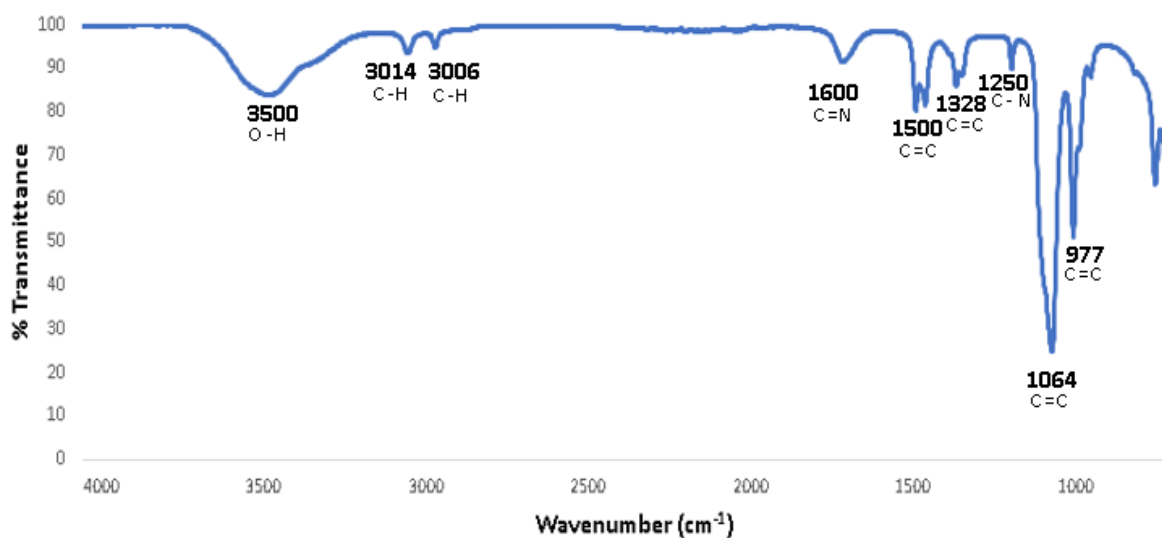
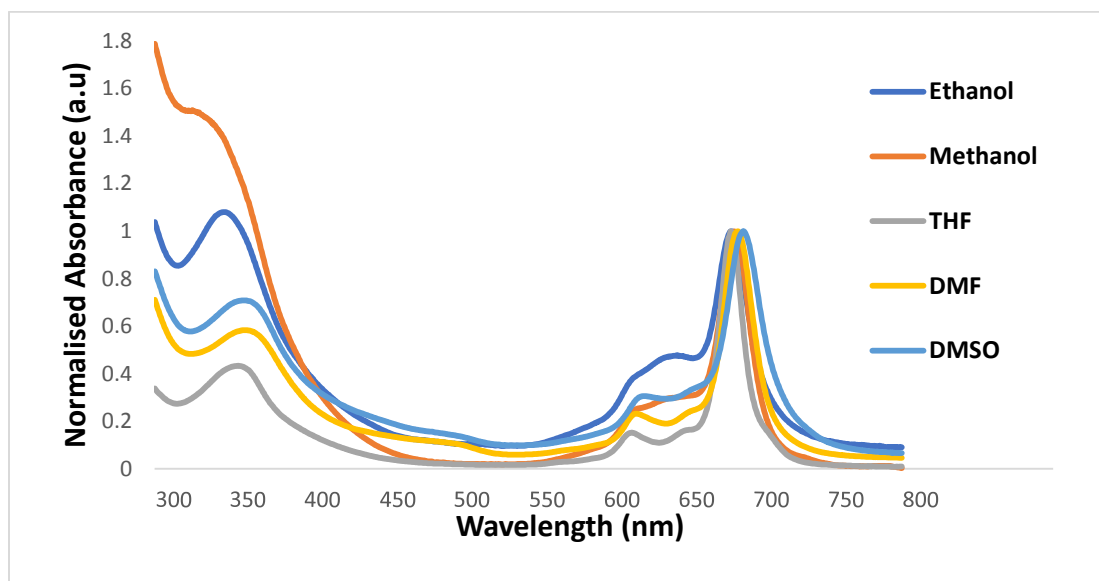


**Figure 5.8:** FTIR spectra of the synthesized phthalocyanine (**5**).

## 5.2 Ground state absorption spectra of MPCs and modified AgNPs/Pc (**8**) support

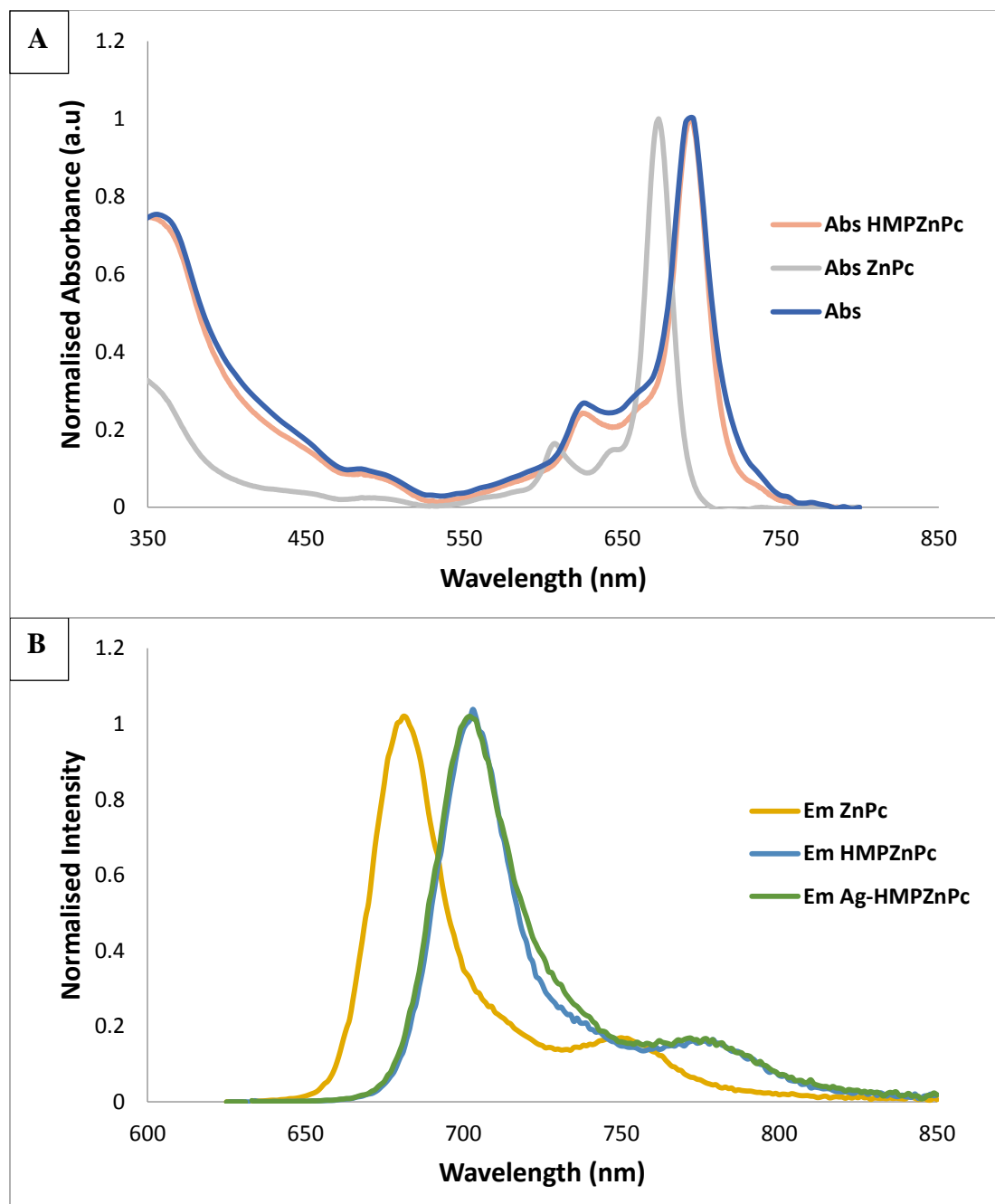
The normalized ground state absorption spectra for complex 4 in ethanol, methanol, THF, DMSO and DMF all shown in Figure 5.9, pg. 114. In all solvents, the complex showed typical metallophthalocyanine spectra with a Q band absorption at 686 nm (EtOH), 688 nm (MeOH), 693 nm (DMSO), 690 nm (DMF) and 686 nm (THF). The increase in the absorption of the B band in methanol could indicate a decrease in solubility for the sample in this solvent. For the most part, the Q band for the Pc remains sharp, pointing towards a lack of aggregation for this

Pc. The fact that this Pc displays no aggregation and it's soluble in polar solvents makes it quite attractive-particularly from a biocompatibility point of view. However, the Pc is sparingly soluble in water.



**Figure 5.9:** The spectra of the phthalocyanine (**5**) in different polar solvents which also show the slight shifting of the Q and B bands in the various solvents.

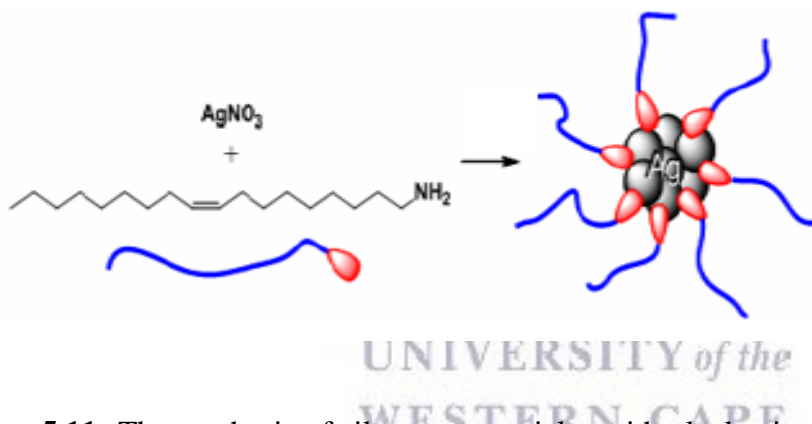
As a comparison, the absorption spectra for the synthesized Pcs (**4** and **5**) and the AgNPs/Pc (**8**) are shown in Figure 5.10, pg. 115. The increase in conjugation leads to a red shift for the Pc (**5**) as compared to the ZnPc (**4**). The Q band for complex **5** is also slightly broader than the ZnPc. Comparing the HMPZnPc (**5**) and the supported AgNPs (**8**), there is no observed shift in the Q band, although the Q band is somewhat broader.



**Figure 5.10:** Absorption (A) and emission (B) spectra of the MPcs (**4** and **5**) and the AgNPs/Pc (**8**) in DMSO to enable comparison.

### 5.3 Characterisation of AgNPs (6) and the AgNP supports (7) and AgNPs/Pc (8)

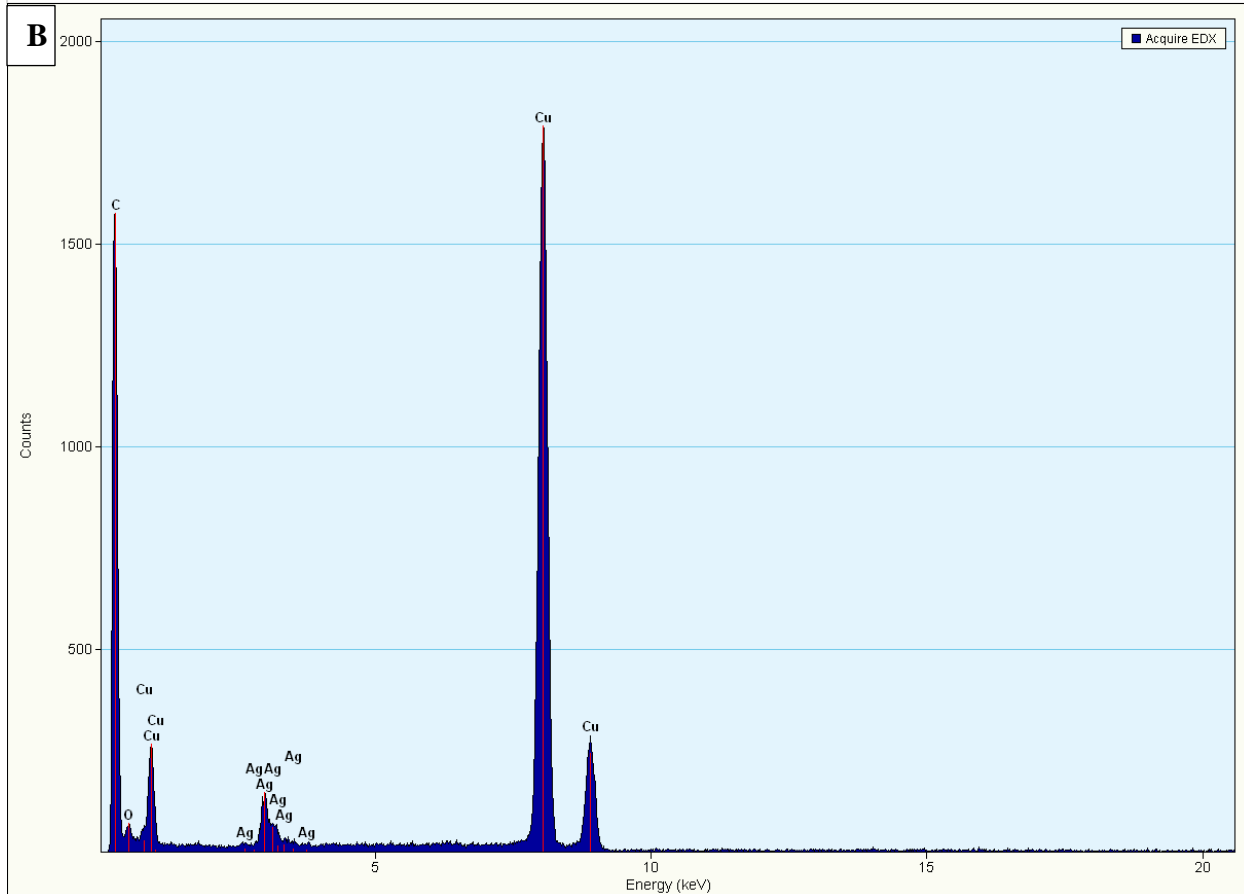
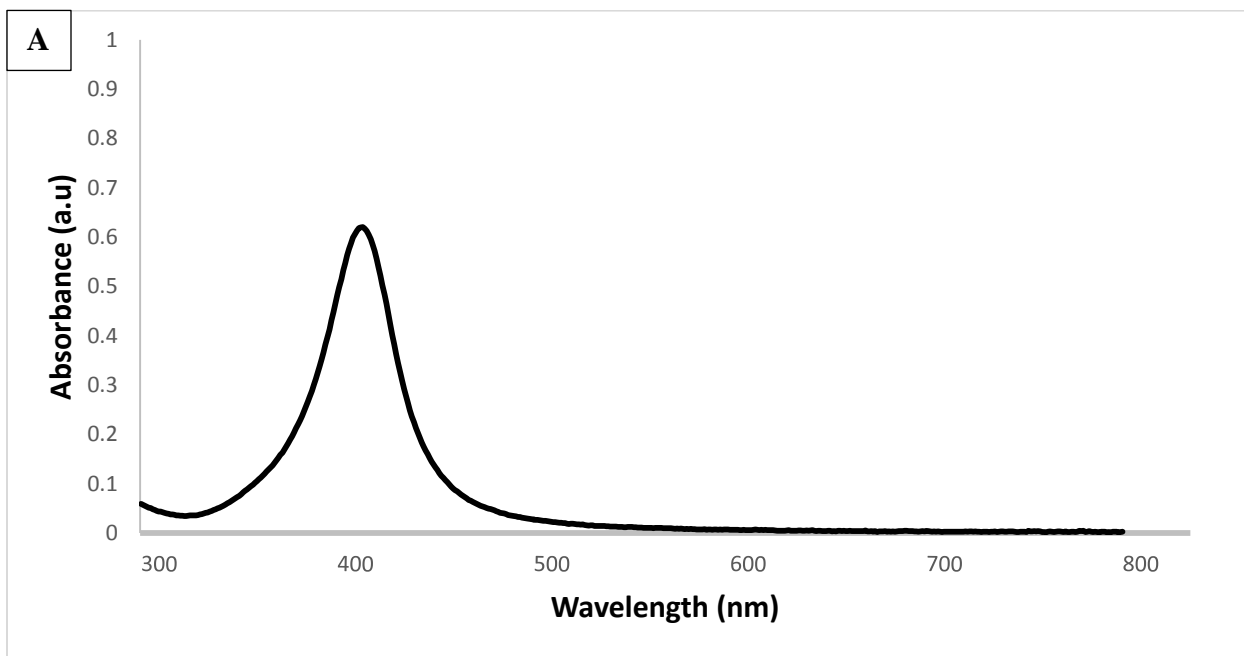
The synthesis of silver nanoparticles proved to be less intricate compared to the upconversion nanoparticles which is discussed later in the thesis. The synthesis procedure was straight forward and the temperature was found to be an important parameter when utilizing oleylamine as a reducing agent (Abbas *et al.*, 2013) and relatively high temperatures are required since oleylamine is a weak reducing agent. The amine, together with the hydrocarbons forming the aliphatic tail of oleylamine, are strong capping agents that coat the silver nanoparticles (Abbas *et al.*, 2013) as shown in Figure 5.11, pg. 116.



**Figure 5.11:** The synthesis of silver nanoparticles with oleylamine capping agent (Abbas *et al.*, 2012).

In Figure 5.12 A and B, pg. 117, the UV/Visible and EDX spectra showing the Ag element for the silver nanoparticles obtained were used to confirm the successful synthesis of the AgNPs. Figure 5.12 A shows the UV/Visible spectrum of the silver nanoparticles with an SPR band at 410 nm which is characteristic for AgNPs and coincides with reports from literature (Abbas *et al.*, 2012). The TEM images shown in Figure 5.12 C - E, pg. 118, give an idea of the size and morphology of the nanoparticles. The AgNPs are shown to be well dispersed with no agglomeration present. This can be attributed to the oleylamine capping agent on the surface of the nanoparticles. Figure 5.12 D, pg. 118, shows hexagonal and spherical shaped nanoparticles appearing to be approximately 10 nm in size, with a few smaller NPs. Figure 5.12 E, pg. 118 shows the

histogram and size distribution of the 160 nanoparticles measured. The sizes ranged from 4 – 15 nm, with an average NP size in the range of 10 – 12 nm.



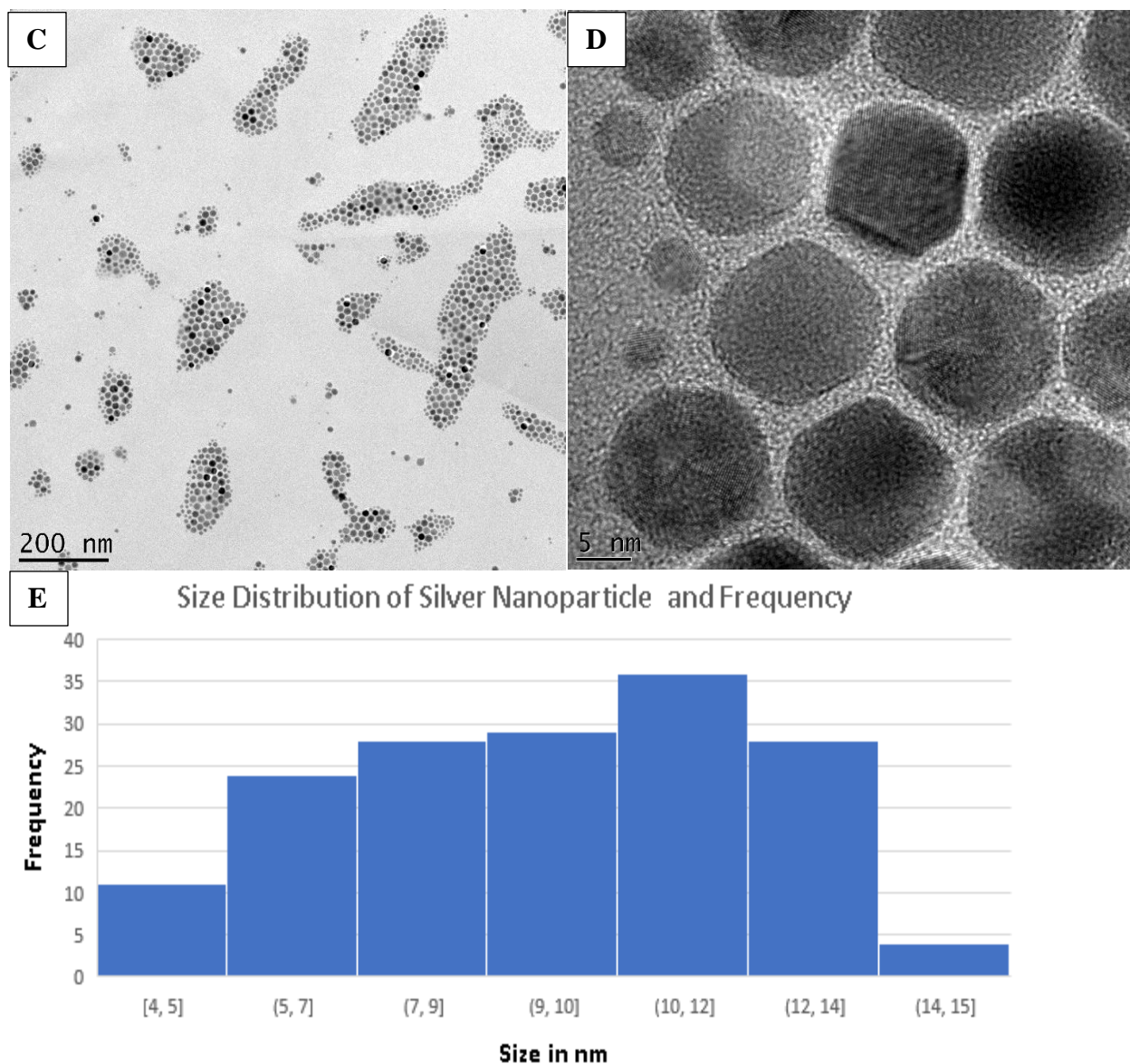
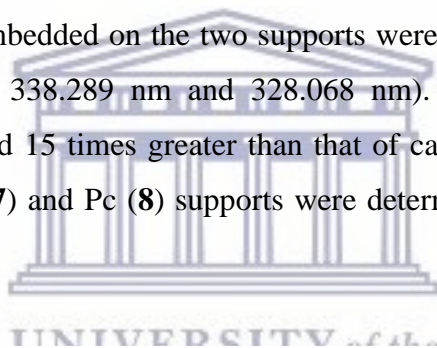


**Figure 5.12:** Spectra and images obtained for the synthesized silver nanoparticles. A) The UV/Visible spectrum of the AgNPs in hexane; B) EDX spectra for the AgNPs; and C – D) the TEM images of the synthesized silver nanoparticles and E) histogram illustrating the size distribution of the silver nanoparticles.

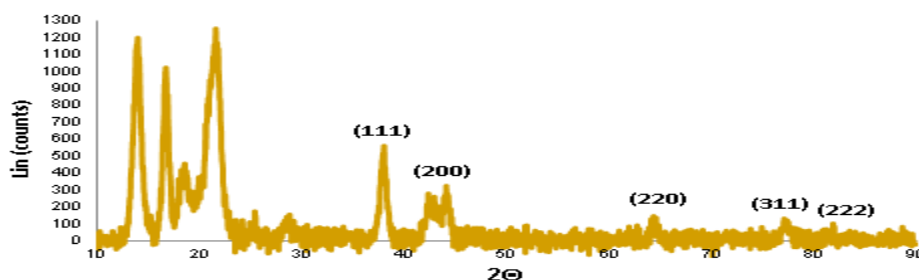
The XRD patterns for the AgNPs imbedded on a carbon support (AgNPs/C, **7**) and the phthalocyanine (AgNPs/Pc) synthesized are shown in Figure 5.13 A and B, pg. 119, respectively. The powder pattern for the AgNPs were not obtained since it was difficult to precipitate the NPs from the solution, even with centrifugation. The XRD patterns in Figure 5.13 A and B show the

five peaks which correspond to the crystalline face-centered cubic (fcc) phase of the AgNPs. The diffraction peaks were observed at  $2\theta = 38.1^\circ, 44.2^\circ, 64.3^\circ$  and  $77.6^\circ$  and can be attributed to the (111), (200), (220) and (311) crystalline planes of metallic silver, respectively (as per JCPDS 00-004-0783). The diffraction peaks (particularly the (111) peak which is most easily observed) show broadening which is expected for NPs. The broader the signal, the smaller the NP (Wang et al., 2010). The appearance of additional peaks in Figure 5.13 A, pg. 119 in the  $10 - 25^\circ$  region can be attributed to the carbon since commercial activated charcoal was used. The presence of additional peaks in Figure 5.13 B, pg. 119 at  $2\theta = 32^\circ, 34^\circ, 36^\circ, 47^\circ, 57^\circ, 63^\circ, 66^\circ, 68^\circ, 69^\circ, 77^\circ, 81^\circ$  and  $89^\circ$  all correspond to the presence of zinc oxide (Figure 5.13 D, pg. 120). Zinc oxide can be traced back to the synthesis of the phthalocyanine where the zinc salt reacted with the pentanol in the reaction to likely produce the ZnO material.

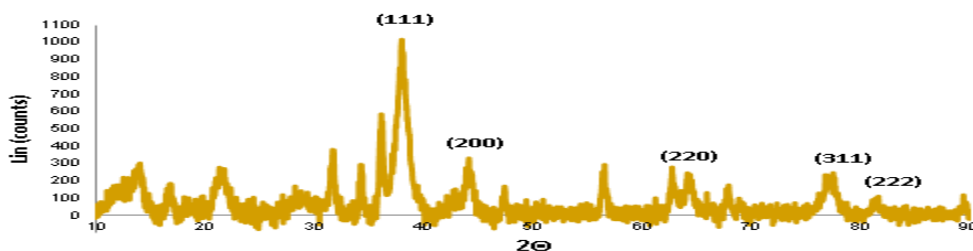
The concentration of AgNPs imbedded on the two supports were determined through the use of ICP-AES (at the wavelengths 338.289 nm and 328.068 nm). The concentration of AgNPs imbedded on the Pc was around 15 times greater than that of carbon at both wavelengths. The percentage Ag on the carbon (7) and Pc (8) supports were determined to be 0.15% and 2.23%, respectively.



**A**



**B**



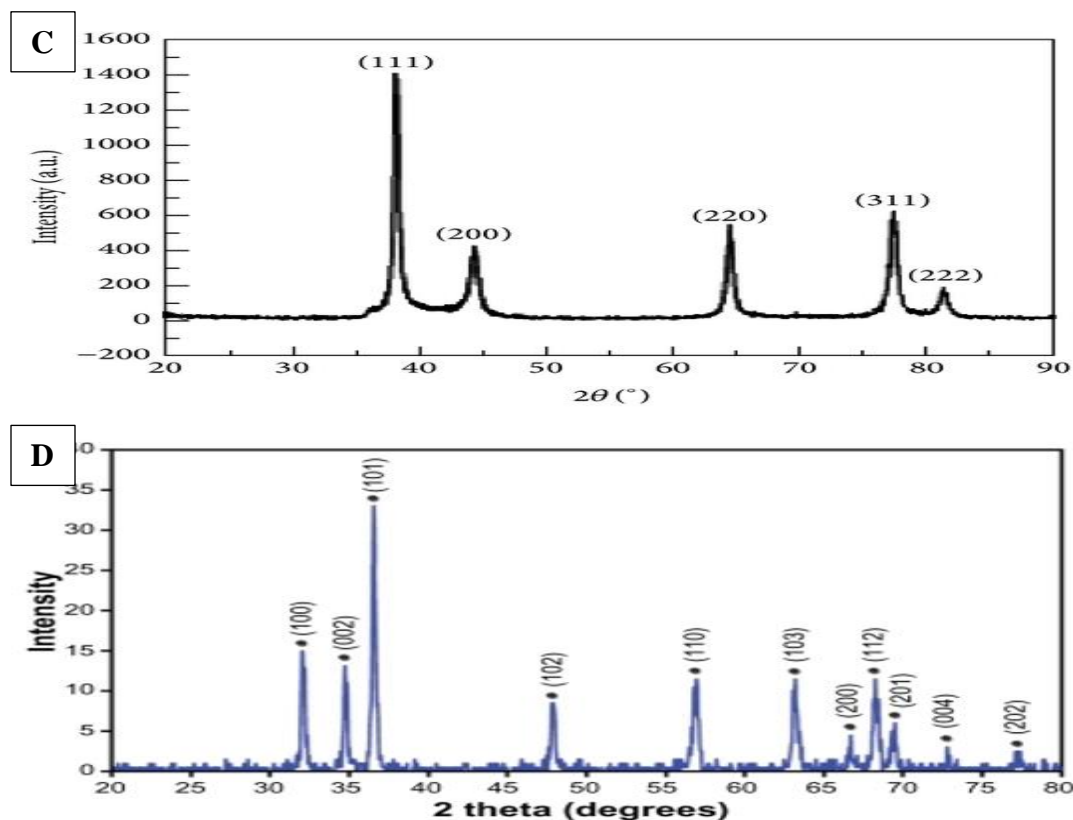


**Figure 5.13:** The XRD powder patterns obtained for silver nanoparticles on carbon and the phthalocyanine together with the standard reference pattern of silver (JCPDS 00-004-0783). A) AgNPs on carbon (**7**); B) AgNPs on the phthalocyanine (**8**); C) Standard reference pattern of silver (JCPDS 00-004-0783), and D) the standard reference pattern for ZnO (JCPDS 36-1451).

## 5.4 Photophysical characterization of MPCs and Modified AgNPs/Pc support (**8**)

The photophysical behavior of the synthesized phthalocyanine (**5**) and AgNPs on phthalocyanine (AgNPs/Pc, (**8**)) catalyst was studied using zinc phthalocyanine (**4**) as the standard. The photophysical parameters include determination of the fluorescence quantum yields, the extinction coefficient, singlet oxygen quantum yields and the fluorescence lifetimes (Table 5.2, pg. 121). The phthalocyanine was soluble in a variety of polar solvents, as shown in Figure 5.9, 114, and the photophysical parameters were determined in DMSO and DMF.

**Table 5.2:** Absorption and photophysical data obtained for complexes **4** and **5** as well as the ZnPc (**4**) standard.

	$\lambda_{\text{abs}}$ (nm)	$\lambda_{\text{emm}}$ (nm)	$\Phi_{\text{F}}$	$\tau_0$ (ns)	$\tau_{\text{F}}$ (ns)	$\Phi_{\Delta}$
<b>ZnPc</b>	675	683	/	/	/	/
<b>HMPZnPc (4)</b>	726	737	0.34	11.15	3.79	1.17
<b>AgNPs/Pc</b>	725	735	0.30	10.38	3.11	0.67

\*  $\lambda_{\text{exc}}$  – not determined as it appeared that the spectra generated were artifacts and not the actual excitation spectra for the Pcs.

#### 5.4.1 Extinction coefficient determination

The extinction coefficient for the 4-(4-hydroxymethyl)phenyl zinc phthalocyanine (**5**) was determined in DMSO and DMF. The Pc was prepared in the range of  $1.30 \times 10^{-5}$  M and  $2.00 \times 10^{-5}$  M, in DMSO and DMF respectively. These readings were observed to obey the Beer-Lambert law across all concentrations studied and the gradient was used to calculate the extinction coefficient (Figures 4.14 and 4.15). The extinction coefficients were calculated at the Q band, ~690 nm, ~606 nm and at ~350 nm (Table 5.3, pg. 121). The extinction coefficients in DMSO were calculated to have a  $\log \epsilon$  of 4.88 at 690 nm, 4.33 at 606 nm and 4.72 at 348 nm. In DMF, the  $\log \epsilon$  values were determined to be 4.75 at 684 nm, 4.06 at 604 nm and 4.48 at 350 nm.

**Table 5.3:** Log  $\epsilon$  determinations for complex **5** in DMSO and DMF

	<b>Log <math>\epsilon</math> (nm)</b>			
	<b>HMPZnPc (4)</b>	DMSO	4.88 (690)	4.33 (606)
	DMF	4.75 (684)	4.06 (604)	4.48 (350)

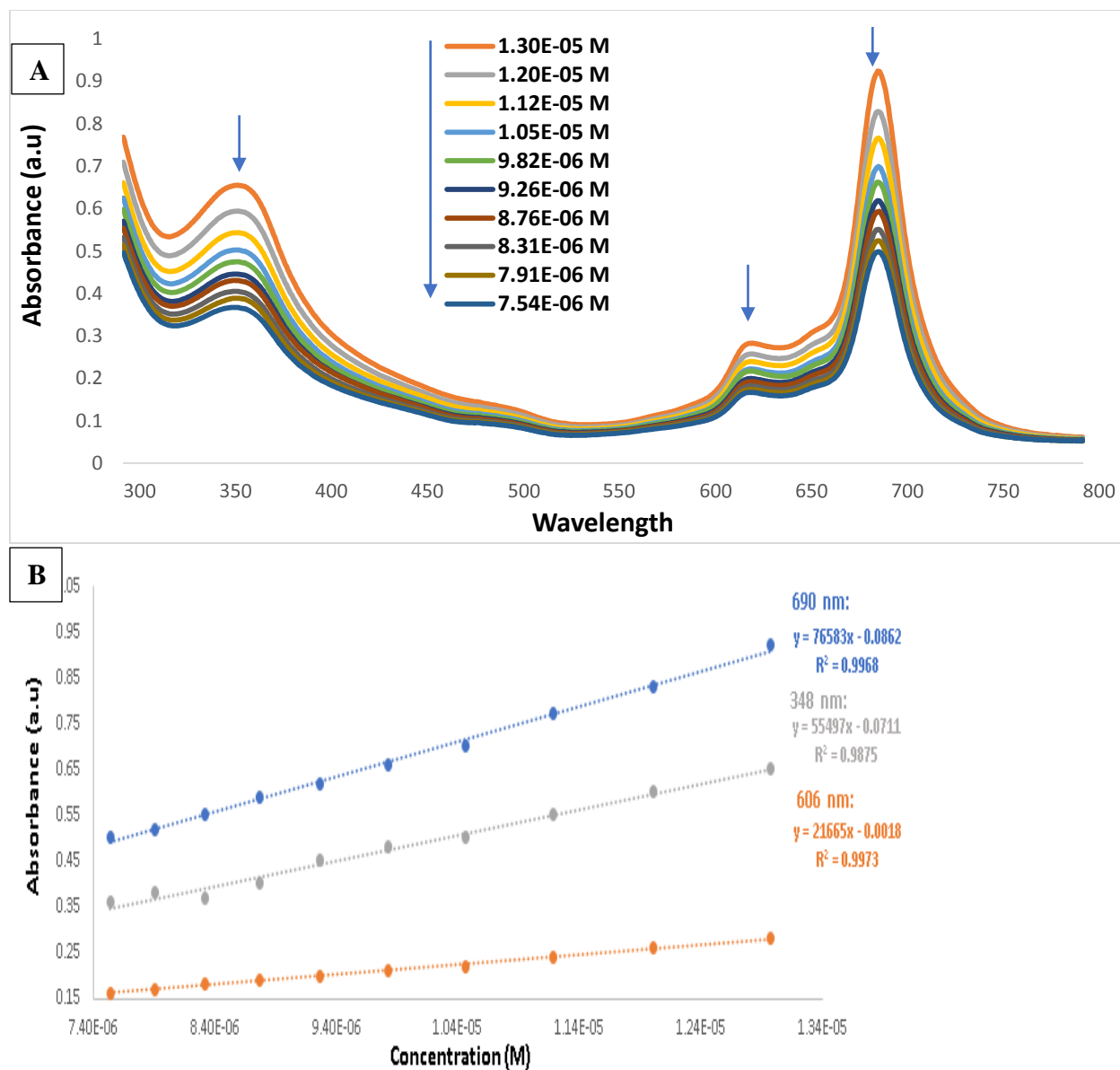


**Figure 5.14:** UV/Visible spectra (A) of a series of dilutions of complex **5** over a concentration range of  $1.30 \times 10^{-5}$  M to  $7.54 \times 10^{-6}$  M in DMSO. The linear behaviour of the absorbance vs concentration for the complex **5** at 690 nm, 606 nm and 348 nm was determined with the gradient used to calculate the extinction coefficient at each point.

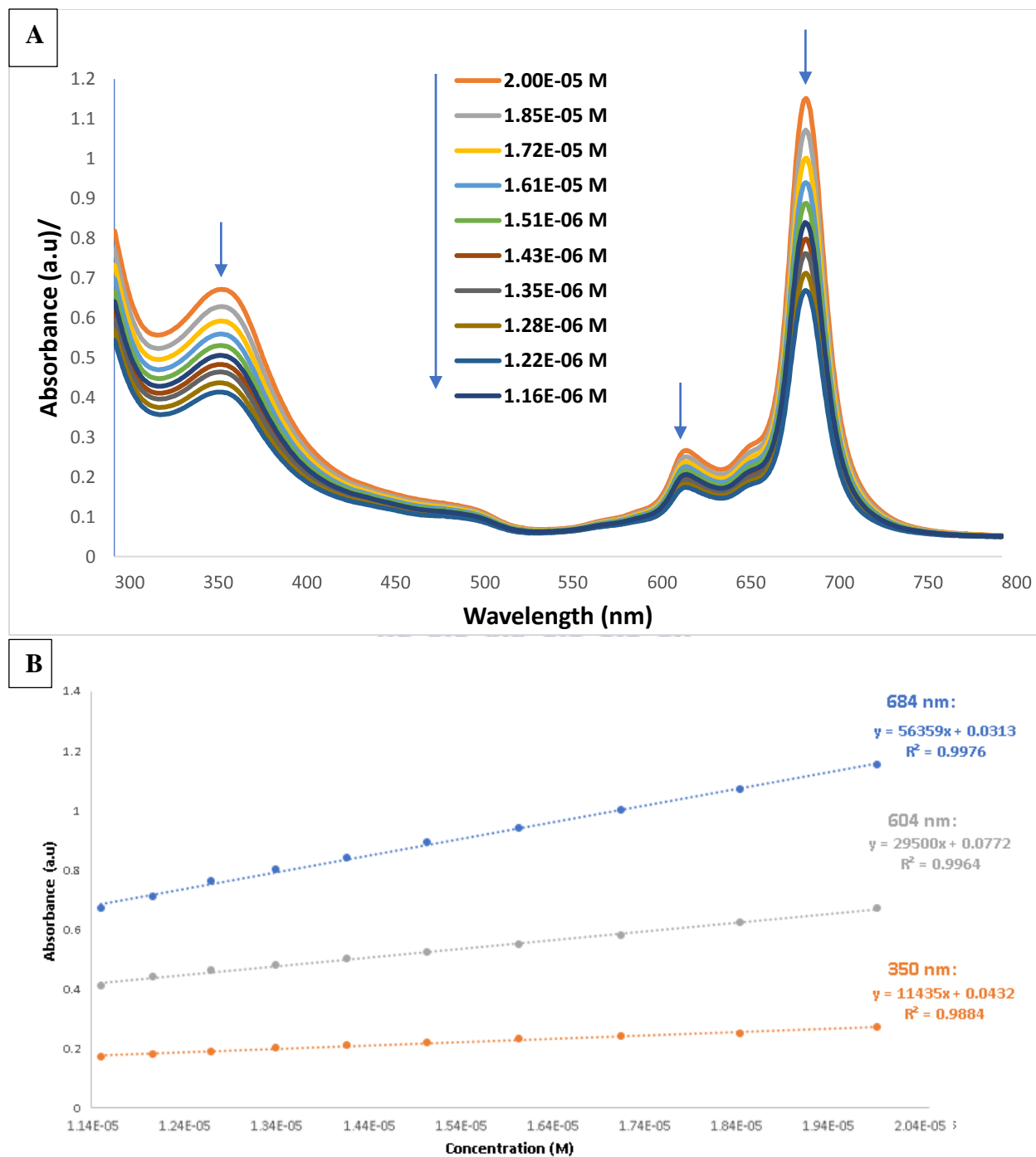


**Figure 5.15:** UV/Visible spectra (A) of a series of dilutions of complex 5 over a concentration range of  $2.00 \times 10^{-5}$  M to  $1.16 \times 10^{-6}$  M in DMF. (B) The linear behaviour of the absorbance vs concentration for the complex 5 at 684 nm, 604 nm and 350 nm was determined with the gradient used to calculate the extinction coefficient at each point.

### 5.4.2 Fluorescence quantum yield and lifetimes

The fluorescence emission spectra (as well as the absorbance spectra) for ZnPc (**4**) and the new Pc (**5**) are shown in Figure 5.16 A and B, pg. 124, respectively, in DMSO. Fluorescence spectra for the phthalocyanine (**5**), catalyst (**8**) as well as the zinc phthalocyanine (**4**) standard was prepared such that the absorbance of each at the excitation wavelength ( $\lambda_{\text{exc}} = 615\text{nm}$ ) was approximately 0.5. The area under the emission curves was used to determine the fluorescence quantum yields ( $\Phi_{\text{F}}$ ) which was calculated using Equation 2.2, where ZnPc (**4**) in DMSO ( $\Phi_{\text{F}} = 0.2$ ) as the standard (Gümrukçü *et al.*, 2014). The complex **5** was determined to have a  $\Phi_{\text{F}}$  of 0.34, while the AgNPs/Pc catalyst had a slightly lower  $\Phi_{\text{F}}$  at 0.30. As expected the emission  $\lambda_{\text{max}}$  occurs at longer wavelengths than absorption  $\lambda_{\text{max}}$  in accordance with Kasha's rule with Stokes shifts ranging from 8 nm to 11 nm in the two complexes as witnessed for the ZnPc (**4**) and HMPZnPc (**5**), respectively, while the AgNP/Pc catalyst (**8**) showed a shift of 10nm. The Stokes shifts observed for the complexes are typical for MPcs (Stillman and Nyokong, 1989).

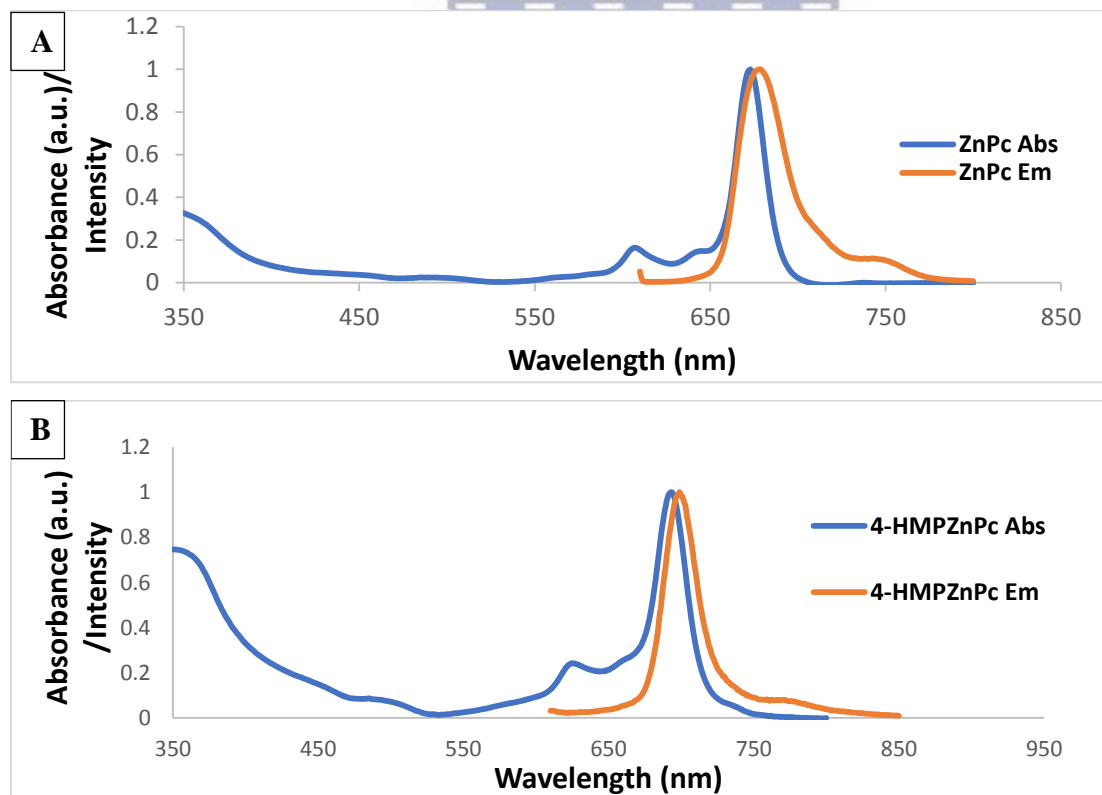


**Figure 5.16:** The absorbance and emission spectra for A) synthesized ZnPc (**4**), B) the HMPZnPc (**5**) and (C) the AgNPs/Pc (**8**) in DMSO.  $\lambda_{\text{exc}} = 615\text{nm}$ .

The fluorescence lifetime values of the phthalocyanines were determined in DMSO using the PhotochemCAD program and the values listed in Table 5.2, pg. 121. The  $\tau_F$  values were determined to be 3.79 ns and 3.11 ns for the HMPZnPc (**5**) and the AgNP/Pc (**8**) catalyst, respectively (Table 5.2, pg. 121). The  $\tau_F$  value of the complex and catalyst was found to be in accordance with the range of lifetimes found for different zinc phthalocyanines derivatives as reported by Kobayashi *et al.* (2003). The authors reported the lifetimes for eight zinc phthalocyanines with electron withdrawing substituents and eleven with electron donating substituents where eleven of these included oxygen derived substituents. The average lifetime for the phthalocyanines was found to be between 3 – 4 ns with four phthalocyanines having lifetimes below 3 ns and one above 4 ns. An unsubstituted zinc phthalocyanine is reported to have a longer lifetime (4.36 ns) compared to a substituted phthalocyanine. The natural radiative lifetimes ( $\tau_0$ ) for the complex **5** and the AgNPs/Pc (**8**) were calculated to be 11.15 ns and 10.39 ns respectively. The natural lifetimes indicates that lifetime which the molecule/system would have, if emission were the only decay process and so it is expected to be larger than the actual fluorescence time ( $\tau_F$ ).

#### 5.4.3 Singlet Oxygen quantum yield ( $\Phi_\Delta$ )

To assess the singlet oxygen production, an indirect method using DPBF as a chemical quencher was used to compare the rate of degradation promoted by the synthesized phthalocyanine (**5**) and the AgNPs/Pc (**8**) using the setup described in Chapter 3. The relationship between the rate of degradation of DPBF promoted by each of the samples, under the same conditions, can be used as an indicator of their photosensitizing properties. These studies were conducted in DMSO. The singlet oxygen quantum yield was calculated using Equation 2.4 with the singlet oxygen quantum yield of the standard (ZnPc, **4**) of 0.67 ( $\Phi_\Delta^{\text{Std}}$ ) (Durmus, 2012) and the R and  $R^{\text{Std}}$  equal to the gradient of the linear graph (Appendix A4.4). Figures 4.17 and 4.18 show the spectral changes observed during the photolysis of complex **5** and the AgNPs/Pc (**8**) catalyst respectively, in DMSO in the presence of DPBF. The disappearance of the DPBF (DPBF oxidizes as singlet oxygen is produced and thus we see a decrease in the absorption at 416nm is seen) was monitored using UV/Visible spectroscopy. There were no changes in the Q band intensities during the study, confirming that the Pc samples themselves do not degrade during the study.

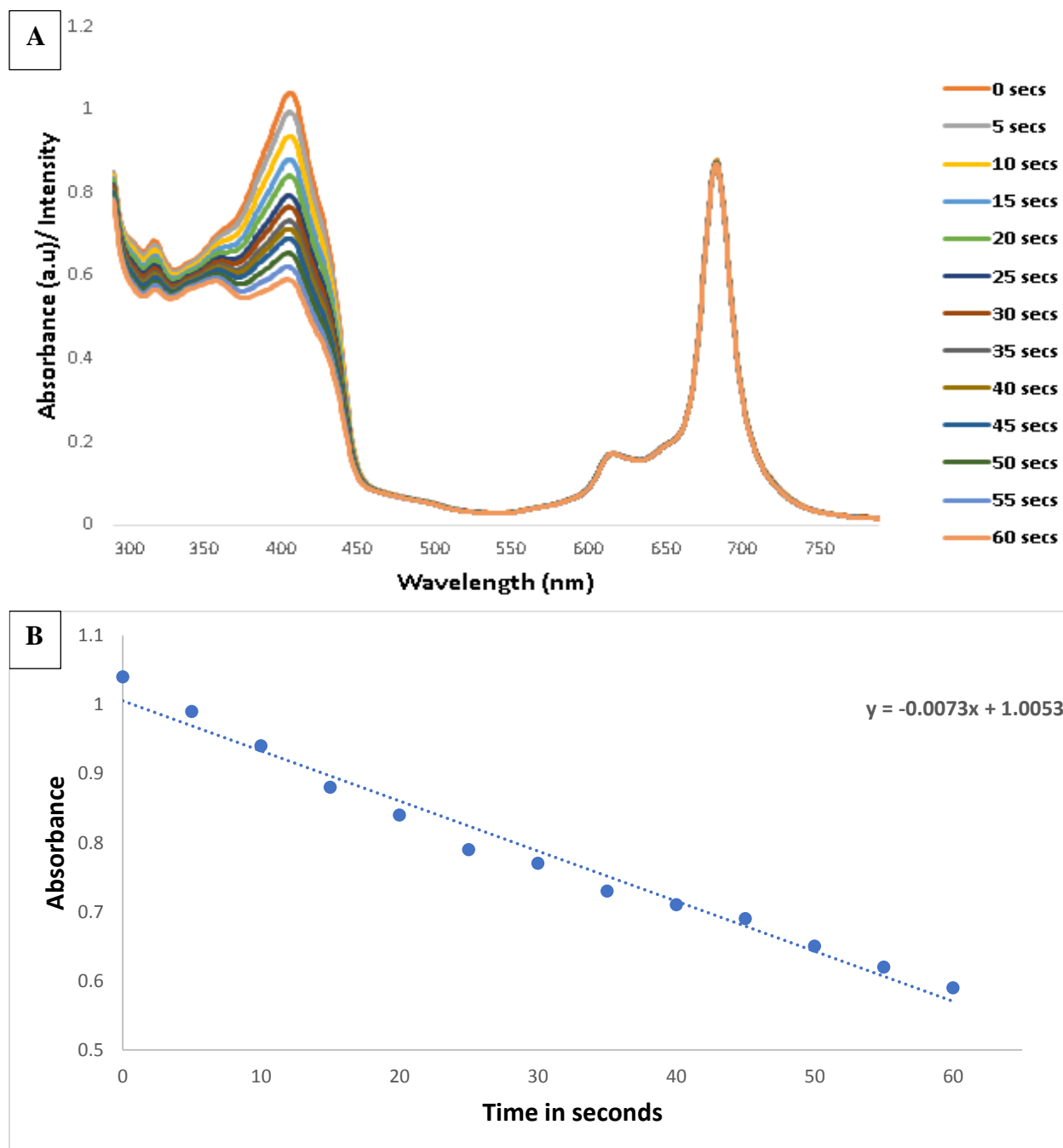


**Figure 5.17:** UV/Visible spectra for the determination of singlet oxygen quantum yields ( $\Phi_{\Delta}$ ) in DMSO using complex **5**.

The singlet oxygen quantum yields were found to be 1.17 and 0.67 for the HMPZnPc (**5**) complex and the AgNP/Pc catalyst (**8**) in DMSO, respectively. The  $\Phi_{\Delta}$  value for complex **5** is unusual as values above 1 are not expected since the photophysical processes are all ratios which

combined give a value of 1. This implies that additional reactions are taking place during photolysis and these reactions most likely involve free radicals. Unfortunately, due to time constraints, free radical studies to confirm this were not conducted. The  $\Phi_{\Delta}$  value obtained for the AgNPs/Pc (**8**) catalyst system is a fair one since a value greater than 1 (and due to possible involvement of free radicals by the Pc), it was not possible to determine whether the catalyst  $\Phi_{\Delta}$  value was higher than that of the Pc (**5**), which was expected, as numerous authors have reported the increase in  $\Phi_{\Delta}$  in the presence of AgNPs and AuNPs (Rapulenyane., 2012; Nombona., 2011). Intriguingly, it does seem then that the AgNPs are quenching any free radicals that the Pc (**5**) could be producing during photolysis – since the  $\Phi_{\Delta}$  value for the catalyst (**8**) is lower (Rapulenyane *et al.*, 2013). In any event, these values are considered high enough to be useful in PDT applications.

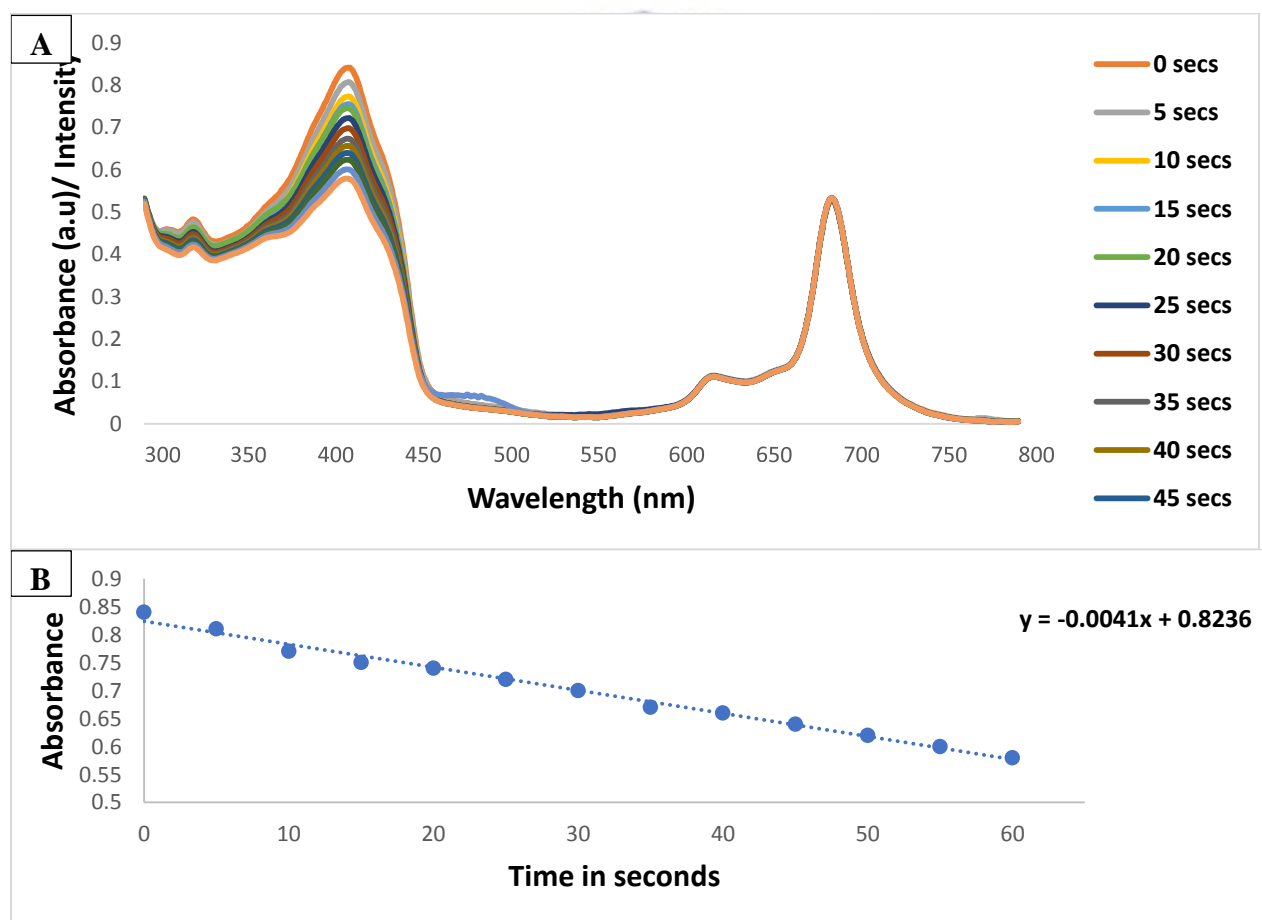


**Figure 5.18:** UV/Visible spectra for the determination of singlet oxygen quantum yields ( $\Phi_{\Delta}$ ) in DMSO using the AgNPs/Pc (**8**) catalyst.

#### 5.4.4 Summary and conclusions

The chapter revolved around the successful synthesis of the HMPZnPc (**5**) with various photophysical properties being tested as well as the synthesis of a catalyst utilising the compound. The synthesis of the HMPZnPc (**5**) was initiated by the synthesis of a phthalonitrile precursor (**3**) through a successful Suzuki-Miyaura carbon-carbon coupling reaction. The phthalocyanine showed interesting results with regards to its solubility in polar solvents, making it attractive for biological applications. The synthesis of one of the catalysts involved silver nanoparticles supported on the phthalocyanine (**8**), with the Pc acting as a support. The other catalyst involved silver nanoparticles imbedded on a carbon support (**7**). The silver nanoparticles had an average size of 10 – 12 nm, where it was found that the AgNPs/Pc (**8**) support contained 15 times the amount of Ag compared to the AgNPs/C (**7**). The catalytic ability of these two catalysts are compared in Chapter 5.

The Log  $\epsilon$  for the HMPZnPc (**5**) was found to be 4.88 (690 nm), 4.33 (606 nm) and 4.72 (348 nm) in DMSO. The Log  $\epsilon$  values in DMF was found to be 4.75 (684 nm), 4.06 (604 nm) and 4.48 (350 nm). The increase in conjugation for the HMPZnPc was found to lead to a red shift compared to that of the ZnPc. The HMPZnPc showed a broader Q band compared to the ZnPc. The photophysical characterisation of the HMPZnPc (**5**) and AgNPs/Pc (**8**) revealed typical results expected for phthalocyanines. The fluorescence quantum yield stokes shift and fluorescence lifetime for the HMPZnPc (**5**) was found to be 0.34, 11 nm and 3.79 ns, respectively, while the AgNPs/Pc (**8**) were found to have fluorescence quantum yields, stokes shifts and fluorescence lifetimes of 0.30, 10 nm and 3.11 ns, respectively. For the singlet oxygen quantum yield, a value of 1.17 was obtained for the HMPZnPc (**5**), suggesting the involvement of radicals, whereas the AgNPs/Pc (**8**) had a quantum yield of 0.67 which could be attributed to a quenching effect of free radicals as reported in the literature by AgNPs.

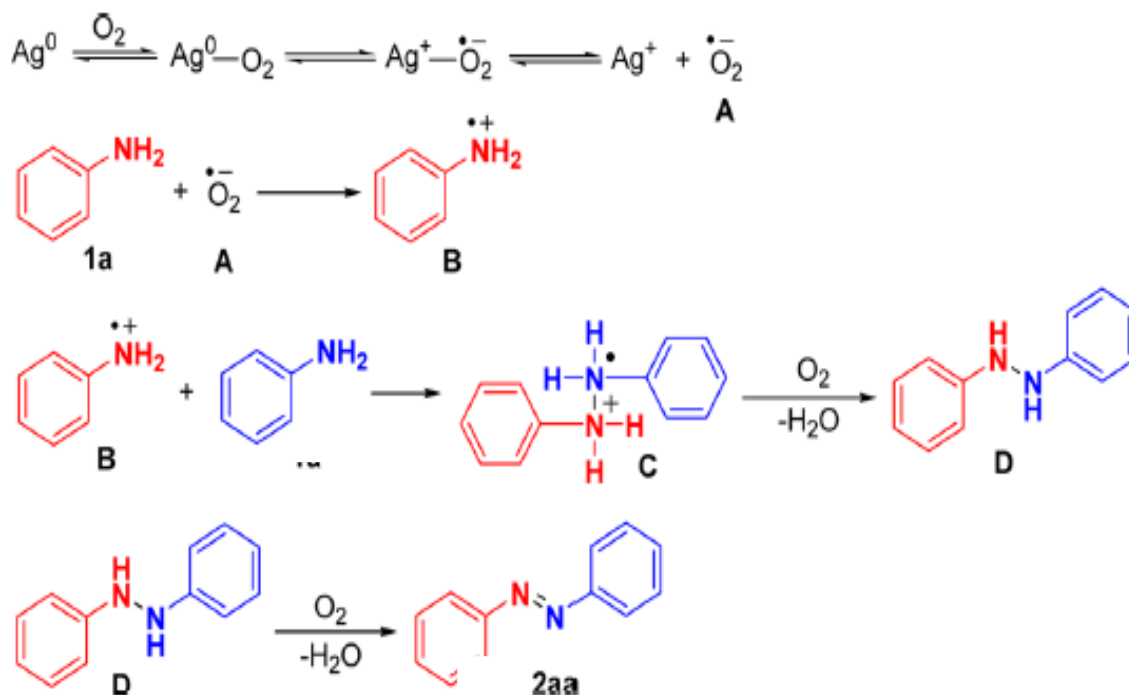
# Chapter 6: Catalytic reactions

## 6.1 Introduction

Metal nanoparticles are found in many industrial reactions and they are utilized as catalysts to synthesize many compounds. These range from dyes, pigments, food additives to pharmaceuticals containing aromatic azo compounds (Cai *et al.*, 2013). One of the most convenient ways of synthesizing azo compounds is by the oxidative coupling of anilines, although, there seems to be a lack of a generally applicable catalyst that is capable of oxidative coupling of aniline under mild conditions (Cai *et al.*, 2013). In this chapter we look at a preliminary study illustrating parameters which are important in the success of the catalytic reaction and the catalytic ability of the synthesized catalysts in synthesizing azo compounds. Evidence of the successful synthesis of the azo compounds will allow further studies to be done to confirm the presence of the azo compound.

## 6.2 Azobenzene catalytic reactions

The rationale of the catalytic reactions was based on the findings of Cai *et al.* (2013) where the authors showed that many types of metal NPs could efficiently activate molecular oxygen under aerobic conditions at room temperature. This finding led to the use of metal NPs in the catalytic synthesis of azo compounds *via* oxidative coupling of anilines (Cai *et al.*, 2013). The authors postulated that the reaction mechanism (Scheme 6.1, pg. 130) proceeds with the oxidation of the nitrogen atom of aniline by **A**, which gives rise to the aniline radical cation **B**. Subsequent coupling between **B** and an aniline molecule leads to the formation of a three-electron  $\sigma$  bond in intermediate **C**. In addition, one-electron oxidation of intermediate **C** led to hydrazine intermediate **D**, which was rapidly oxidized to the azo product (Cai *et al.*, 2013).



**Scheme 6.1:** Mechanism for Ag NPs-catalyzed oxidative coupling of aniline as proposed by Cai *et al.* (2013).

The catalytic ability of the synthesized AgNPs/C (7) catalyst was tested within the reported reaction conditions of Cai *et al.*, 2013. Parameters of the reaction were altered (see Table 6.1, pg. 131) in order to conclude the importance of these parameters within the reaction acting as control reactions. A negative control was also done, which did not include the catalyst under the reaction conditions. Successful formation of the azobenzene product is expected to show a molecular ion at  $m/z$  182 amu, in the GC-MS data obtained. Figure 6.1, pg. 131 shows the GC chromatogram for the product obtained under the standard catalytic conditions using the model AgNPs/C (7) catalyst.

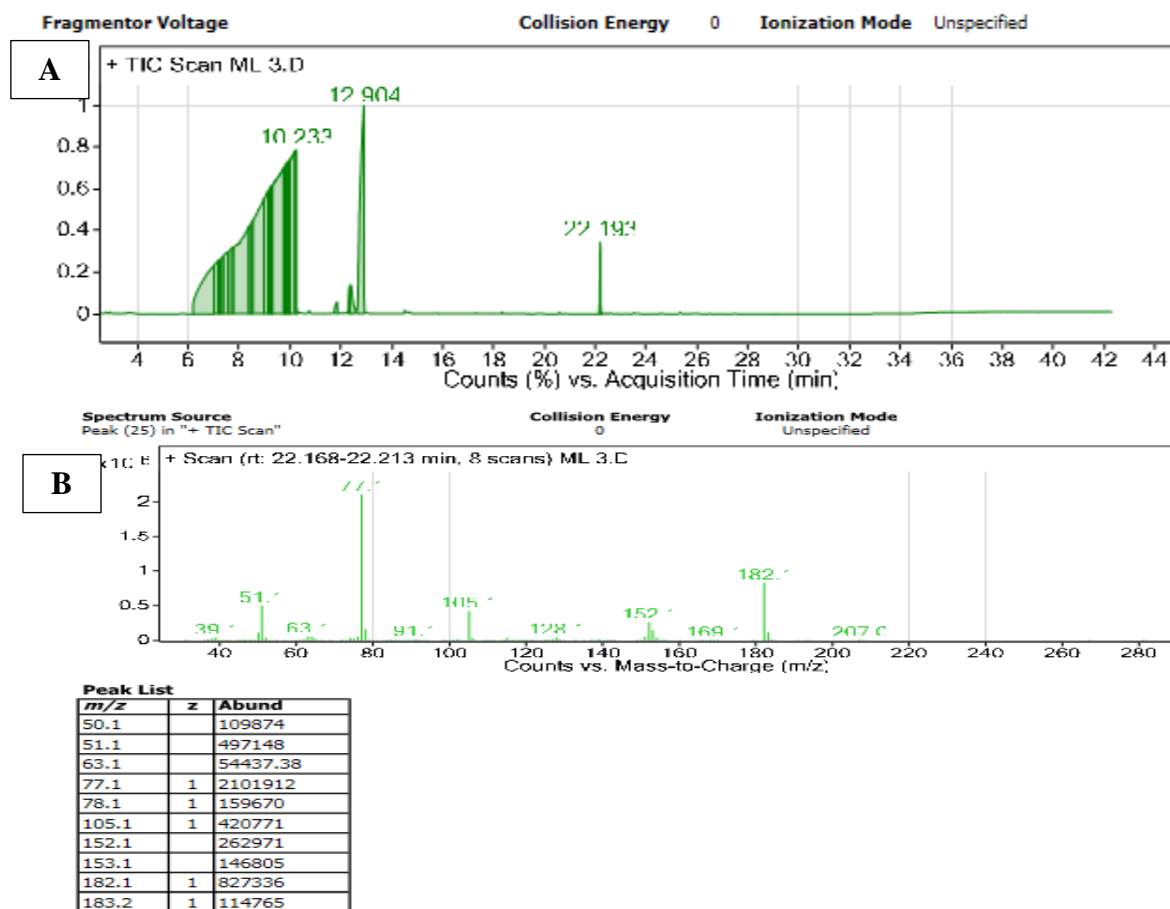
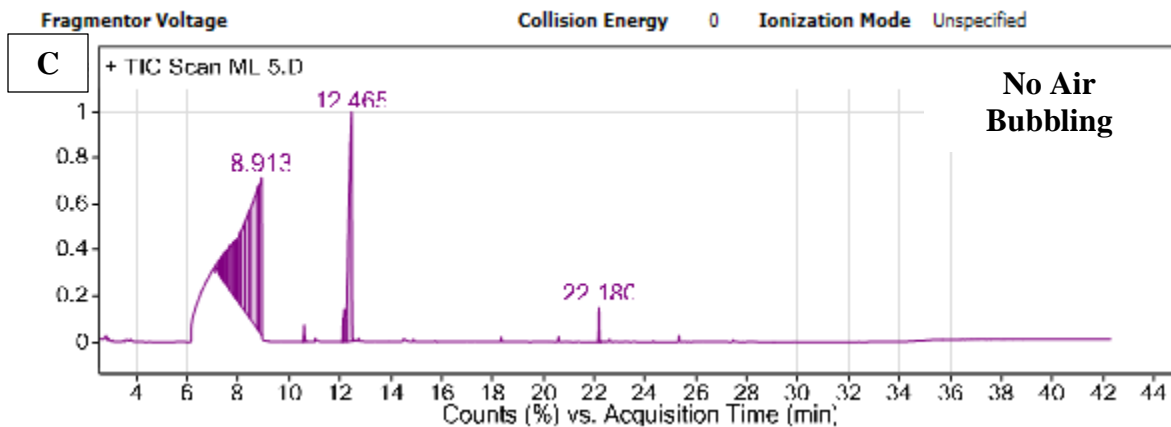
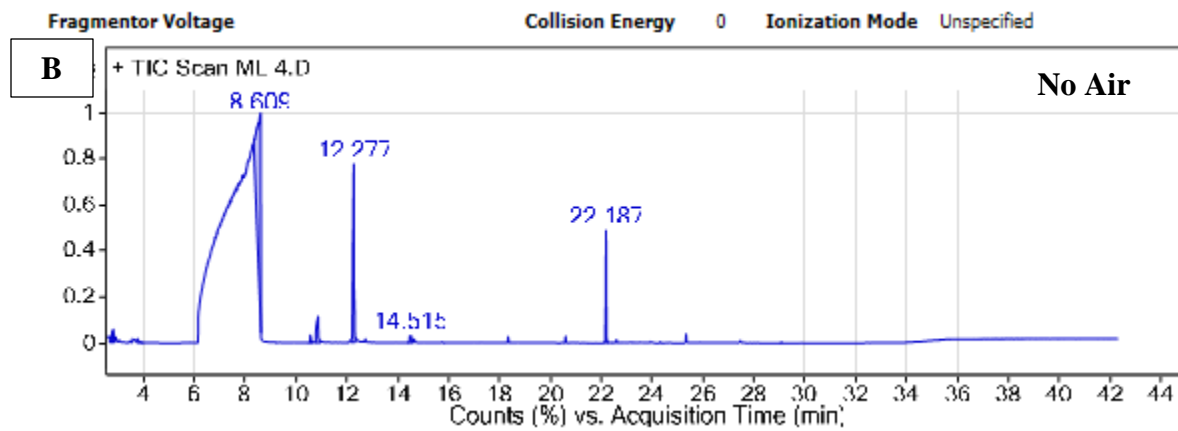
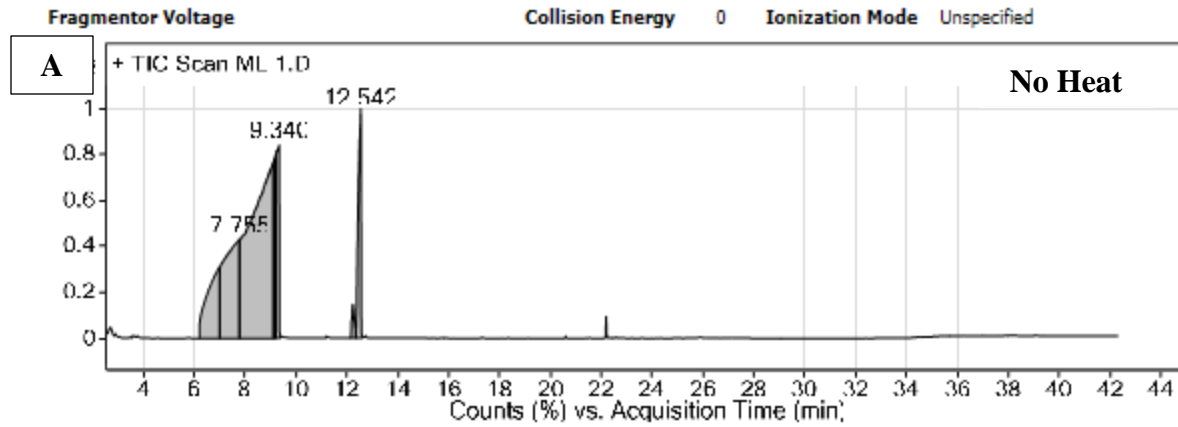


**Figure 6.1:** GC-MS results obtained for the standard catalytic reaction (Table 6.1, pg. 131, reaction 1) of aniline using AgNPs/C (7). A) Shows the total ion chromatogram (TIC) obtained for the product and B) shows the mass spectrum of the GC peak at a retention time of 22.2 min, indicating successful formation of the azobenzene product.

**Table 6.1:** Catalytic reaction conditions with varied parameters and product formation

Reaction	Catalyst	Heat	Air	Air Bubbling	Product Formed?
1	AgNPs/C	Yes	Yes	Yes	Yes
2	AgNPs/C	X	Yes	Yes	No
3	AgNPs/C	Yes	X	Yes	Yes
4	AgNPs/C	Yes	Yes	X	Yes
5	X	Yes	Yes	Yes	No
6	AgNPs/Pc	Yes	Yes	Yes	Yes

\* Standard reaction conditions (reaction 1): Catalyst (7/8), reaction temperature at 60 °C under air/bubbled through with air, reaction time (24 hours). \* X denotes parameter missing



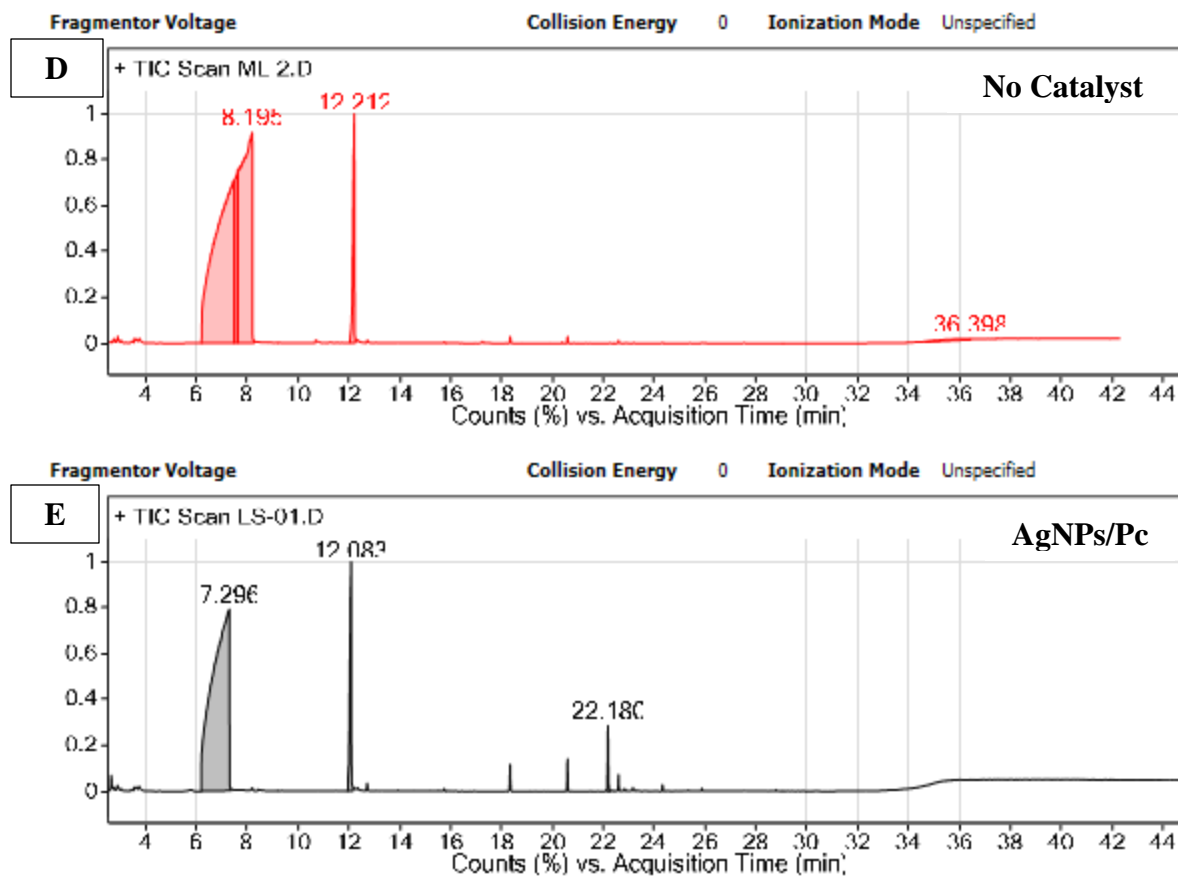


**Figure 6.2:** TICs obtained for the various catalytic reactions where parameters are changed (Table 6.1, pg. 131) for A) reaction 2. B) reaction 3. C) reaction 4. D) reaction 5. E) reaction 6. The azobenzene product has a retention time of 22.2 min and the aniline starting material retention time is at 12.1 min.

In contrast to Cai *et al.*, the azobenzene product was successfully formed even when under anaerobic conditions (Table 6.1, pg. 131 and Appendix A6.1). However, the reactions which did not produce the azobenzene product at 22.2 min (with a  $m/z$  182) were those which lacked the catalyst (i.e. the negative control reaction 5) and the reaction without heat (reaction 2) (Table 6.1, pg. 131). Reaction times was the only parameter kept constant. A total 10 GC chromatograms (TIC) were obtained and are shown in Figure 6.2, pg. 133. The mass spectra for each of these are found in Appendix A5.1. From these results, it can be concluded that oxidative dehydrogenative coupling of anilines for azobenzene synthesis can be carried out with AgNPs/C (7) as catalysts in the absence of air, but heat is an important parameter in the success of the reaction. It would

seem that there is another mechanism at play in the formation of the product. However, further studies are needed to confirm this. The AgNPs/Pc (**8**) catalyst was also tested to compare its catalytic ability in a reaction run under the standard conditions (reaction 6, Table 6.1, pg. 131). In Figure 6.2, pg. 133 the successful formation of the azobenzene product was again shown with the appearance of a molecular ion at  $m/z$  182. It seems however that reactions 1 and 3 were the most successful, while the AgNPs/Pc (**8**) catalyst was only moderately successful. The azobenzene compound was not isolated from the other side products present, as it was not part of the scope of the thesis.

### 6.3 Summary and conclusion

This chapter delves into the catalytic ability of the synthesized supports (**7** and **8**) with regards to the catalytic synthesis of azo compounds *via* oxidative coupling of anilines. The first reaction (Table 6.1, pg. 131) dealt with the catalytic synthesis of azobenzene utilizing the AgNPs/C (**7**) catalyst to successfully synthesize the azobenzene. The importance of the different parameters was then determined where heat and the catalysts were found to be important factors. It was also found that the catalytic reaction was a success in anaerobic conditions (reactions 3, Table 6.1, pg. 131) which could be attributed to another mechanism at work. The AgNPs/Pc catalyst (**8**) was also successful in synthesizing azobenzene, through to a lesser extent (reaction 6, Table 6.1, pg. 131). The catalysts would be AgNPs/Pc (**8**) and the AgNPs/C are all able to produce molecular oxygen and theoretically produce the azo compound according to the postulated mechanism. The HMPZnPc (**5**) catalytic ability was tested through a different reaction which included aniline as one of the starting materials. The final product was not synthesized successfully although the azobenzene molecular ion was present in the GC chromatogram of the reaction which could occur through two aniline molecules catalytically reacting with each other forming the azobenzene compound. This is also deemed possible as the HMPZnPc (**5**) catalyst has the ability to produce molecular oxygen and theoretically produce the azo compound according to the postulated mechanism.

## Chapter 7: Conclusion and future prospects

The synthesis of the various UCNPs yielded nanoparticles experiencing agglomeration. This made it difficult determining the structure and morphology of the small and upscaled synthesized nanoparticle. The XRD patterns yielded more information with regards to the crystalline structure of the nanoparticles. The small scale nanoparticles produced better quality nanoparticles except for the ss NaScF<sub>4</sub>:Yb/Er nanoparticles. The solid state NMR showed good crystalline structures within the Na host lattices in accordance with literature. The steady state fluorescence spectroscopy resulted in emissions in the green, red and near infrared regions. The NaScF<sub>4</sub>:Yb/Er nanoparticles showed the strongest emissions, whereas the bands for the NaYF<sub>4</sub>:Yb/Ho nanoparticles showed a slight shift in the region of their emissions.

The successful synthesis of the 4-(4-hydroxymethyl)-phthalonitrile (**3**) obtained through the Suzuki-Miyaura carbon-carbon coupling reaction acted as a precursor in the successful synthesis of the HMPZnPc (**5**), which was found to be soluble in polar solvents making it attractive from a biocompatibility point of view. The photophysical properties of the phthalocyanine obtained was as expected. The AgNPs/Pc (**8**) catalyst photophysical properties yielded similar results. There is however, contrasting results shown for the singlet oxygen quantum yield. The HMPZnPc (**5**) yielded a value above 1 which could be contributed to the presence of free radicals. The AgNPs/Pc (**8**) catalyst yielded a value lower than one which could elude to quenching effects by the AgNPs. The AgNPs/Pc (**8**) catalytic ability was tested in its ability to produce azo compounds *via* oxidative coupling of anilines. The AgNPs/C (**7**) catalyst was utilized to find the important parameters within the reaction which are necessary for the successful synthesis of azobenzene.

Future work for the phthalocyanine could include the determination of the production of free radicals by the phthalocyanine which would give clarification in the value above 1 for the singlet oxygen quantum yield. The application of the phthalocyanine and AgNPs/Pc (**8**) in fluorescence imaging and PDT in live cell cultures would reveal the effectiveness of the phthalocyanines. Further studies can be done to understand the mechanism of action in the production of azobenzene in anaerobic conditions. In various papers, different nanoparticles had different

reaction conditions, with regards to temperature and time, it would be good to optimize reaction conditions for all matrices. Capping the nanoparticles with polyvinylpyrrolidone for example will make the NPs hydrophilic, increasing its application, especially for biological applications.



UNIVERSITY *of the*  
WESTERN CAPE

## Appendix

### TEM/EDX data:

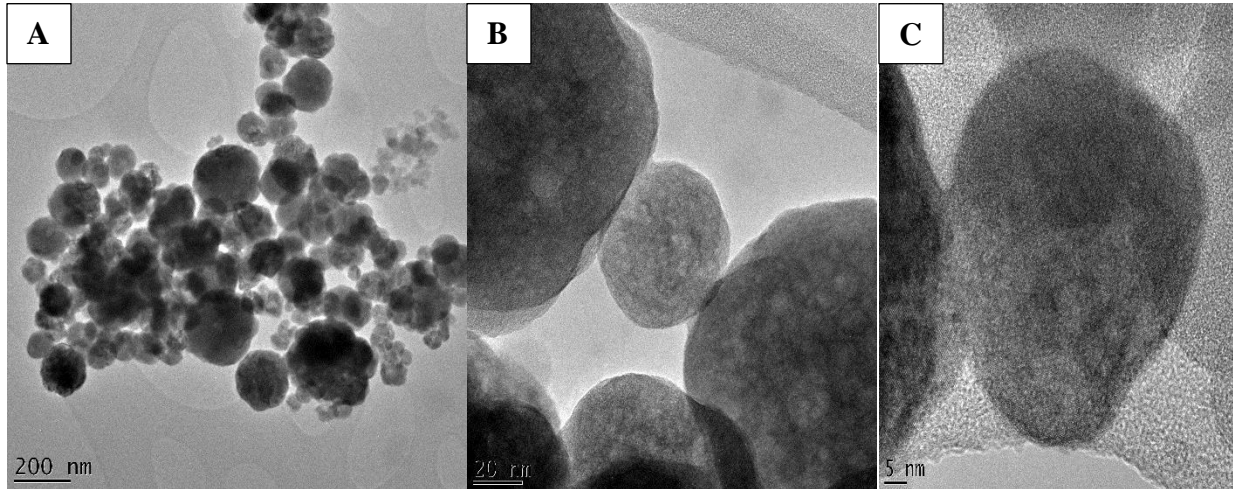


**Figure A4.1:** A - C) The TEM images of the upscaled synthesized NaYF<sub>4</sub>:Yb/Er upconversion nanoparticles.

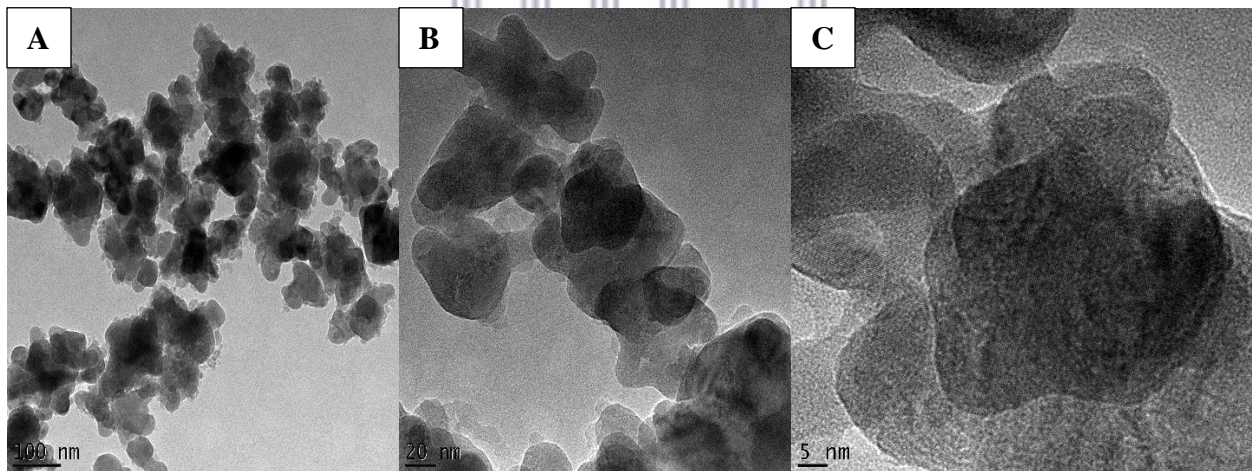


**Figure A4.2:** A - C) The TEM images of the upscaled synthesized NaYF<sub>4</sub>:Yb/Ho upconversion nanoparticles.

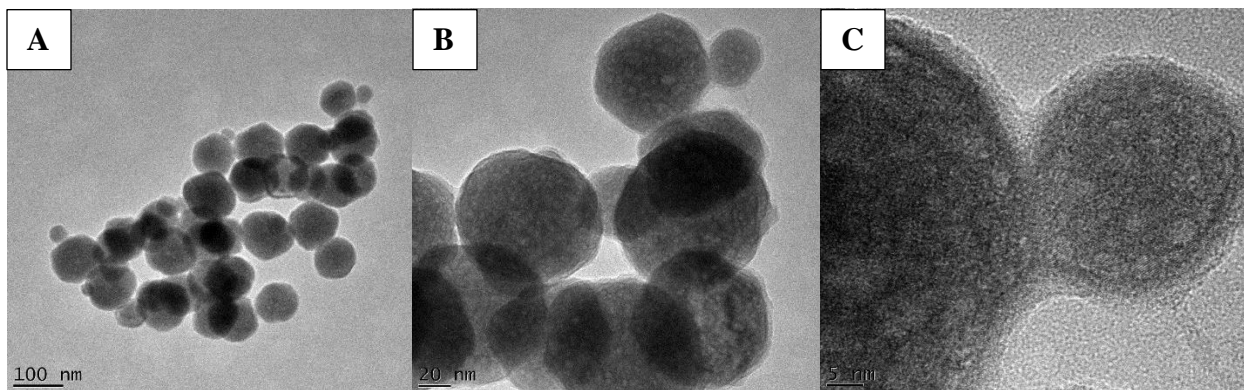


**Figure A4.3:** A - C) The TEM images of the synthesized NaScF<sub>4</sub>:Yb/Er upconversion nanoparticles.

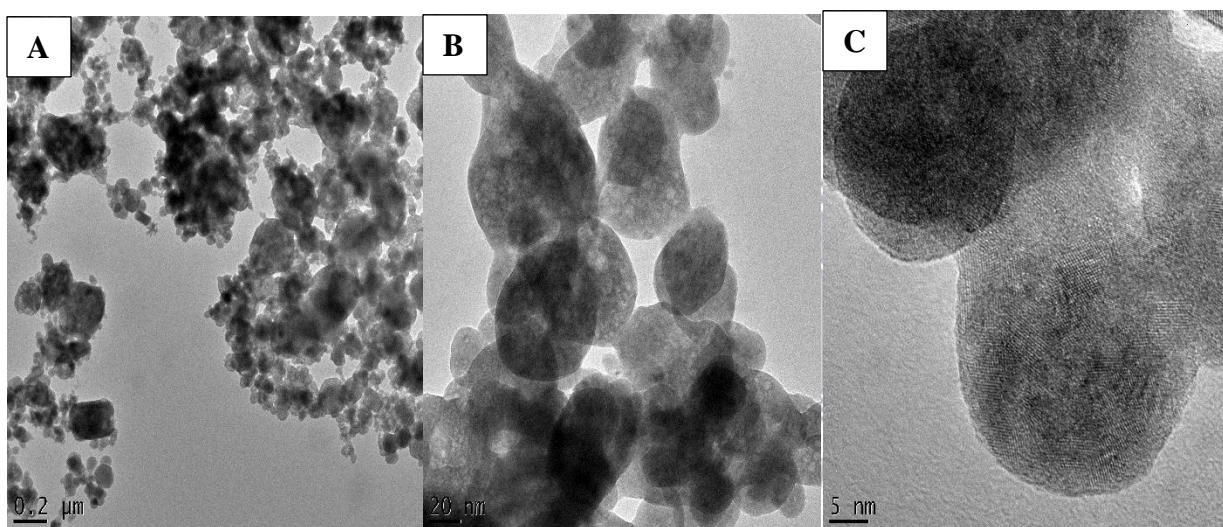


**Figure A4.4:** A - C) The TEM images of the upscaled synthesized LiY<sub>x</sub>F<sub>y</sub>:Yb/Er upconversion nanoparticles.

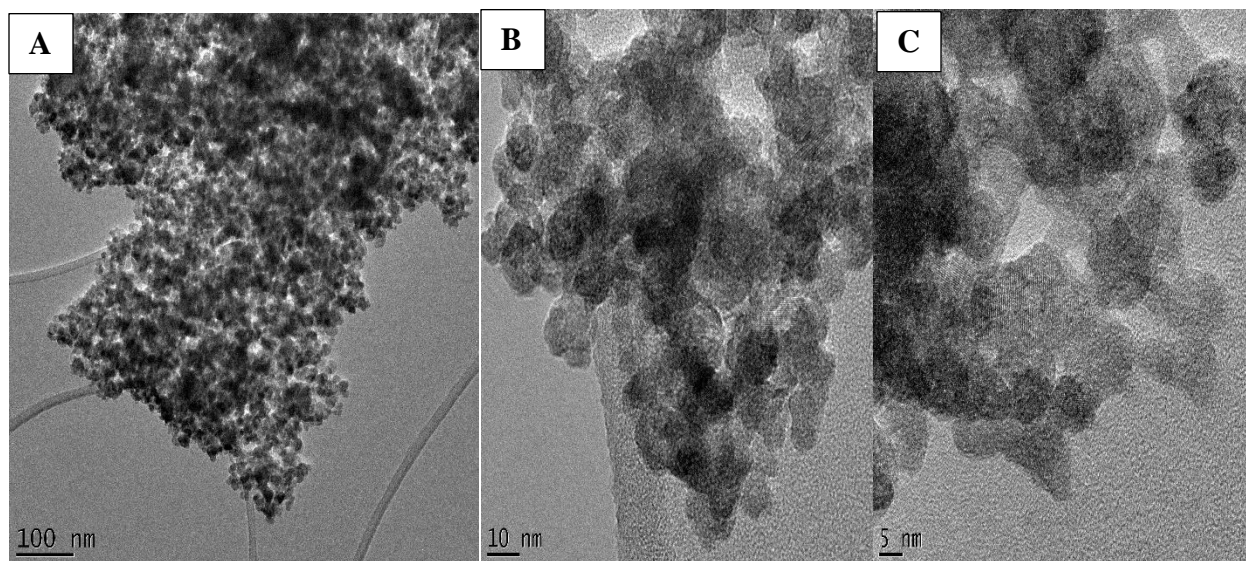


**Figure A4.5:** A - C) The TEM images of the upscaled synthesized  $KY_xF_y:Yb/Er$  upconversion nanoparticles.

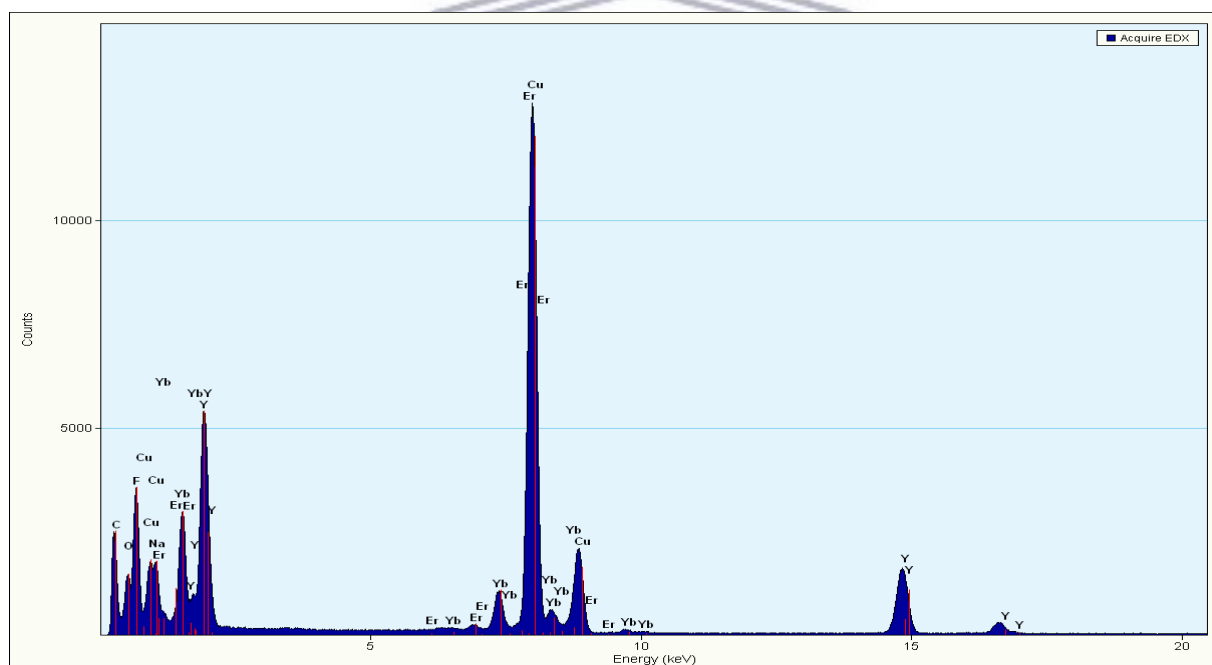


**Figure A4.6:** The EDX of the small scale synthesized  $NaYF_3:Yb/Er$  upconversion nanoparticles.

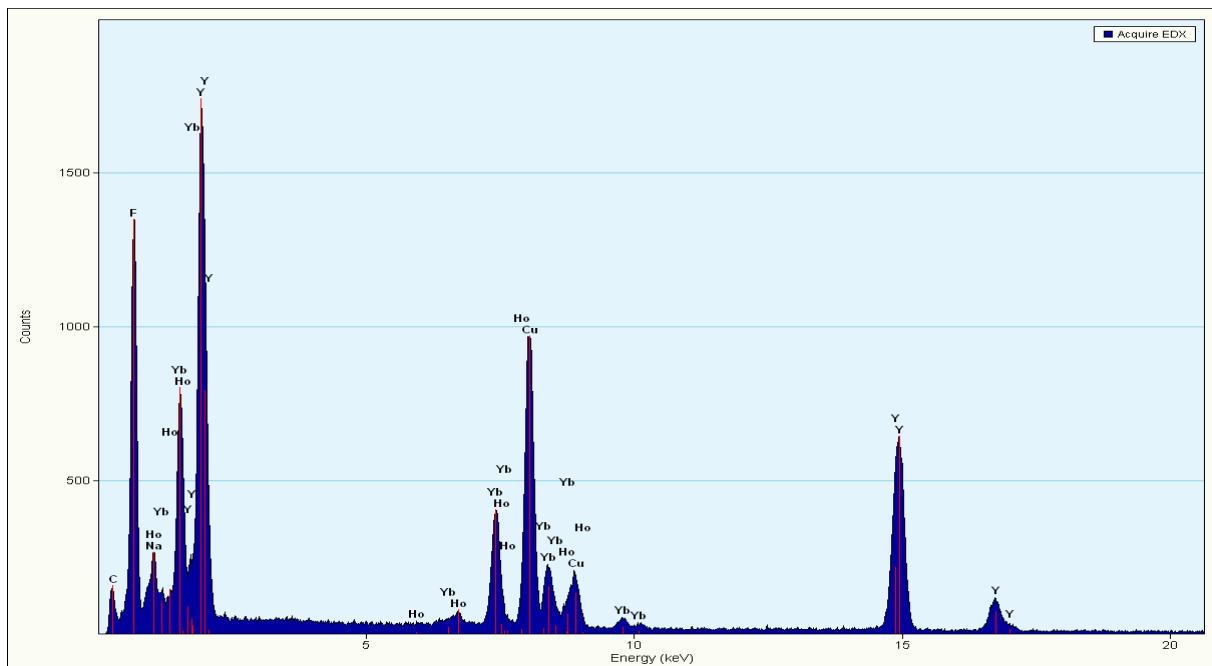


**Figure A4.7:** The EDX of the upscaled synthesized NaYF<sub>3</sub>:Yb/Ho upconversion nanoparticles.

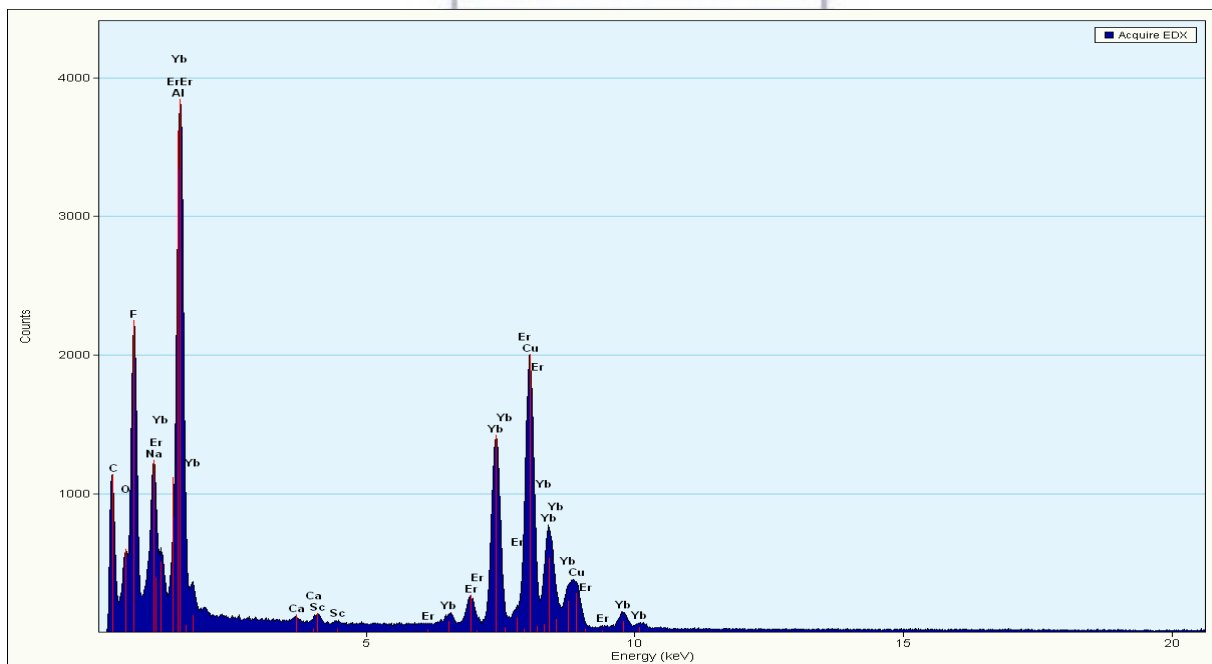


**Figure A4.8:** The EDX of the upscaled synthesized NaScF<sub>4</sub>:Yb/Er upconversion nanoparticles.

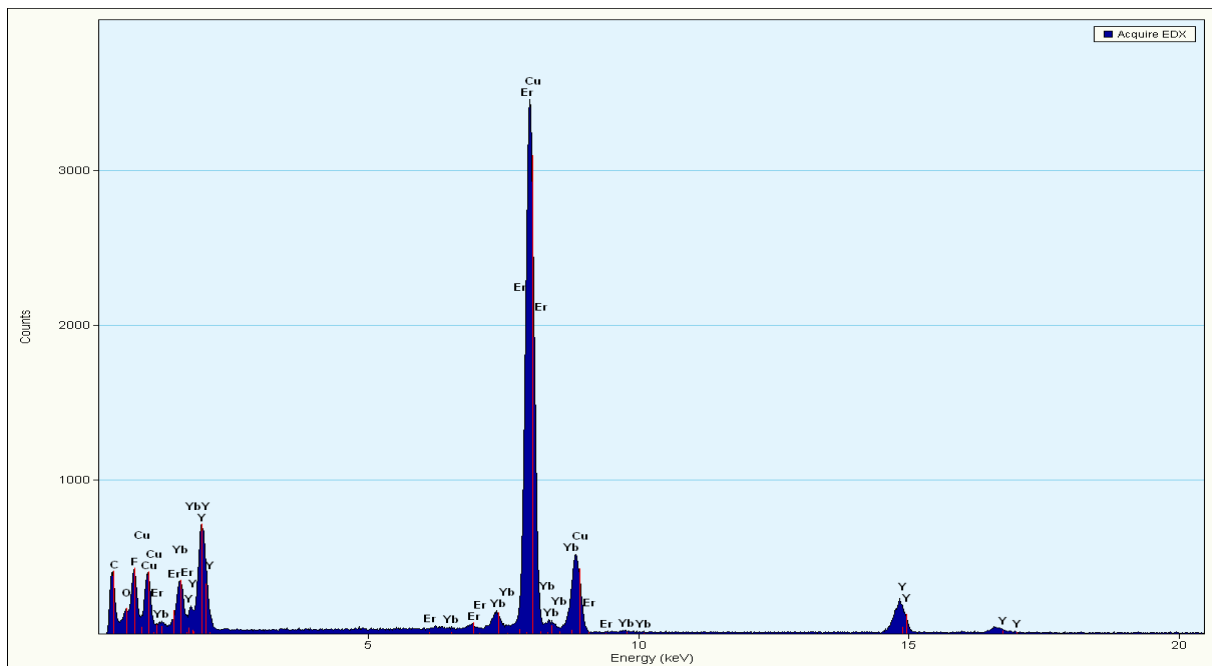


**Figure A4.9:** The EDX of the small scale synthesized  $\text{LiY}_x\text{F}_y:\text{Yb/Er}$  upconversion nanoparticles.

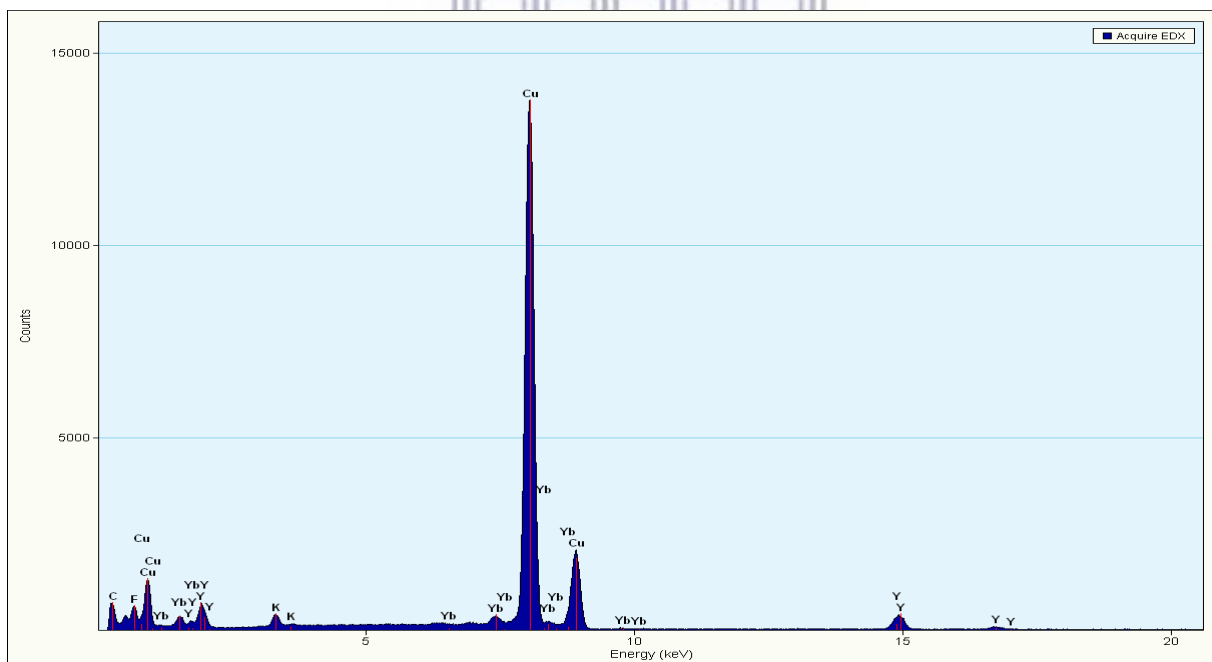


**Figure A4.10:** The EDX of the small scale synthesized  $\text{KY}_x\text{F}_y:\text{Yb/Er}$  upconversion nanoparticles.

**XRD data:**

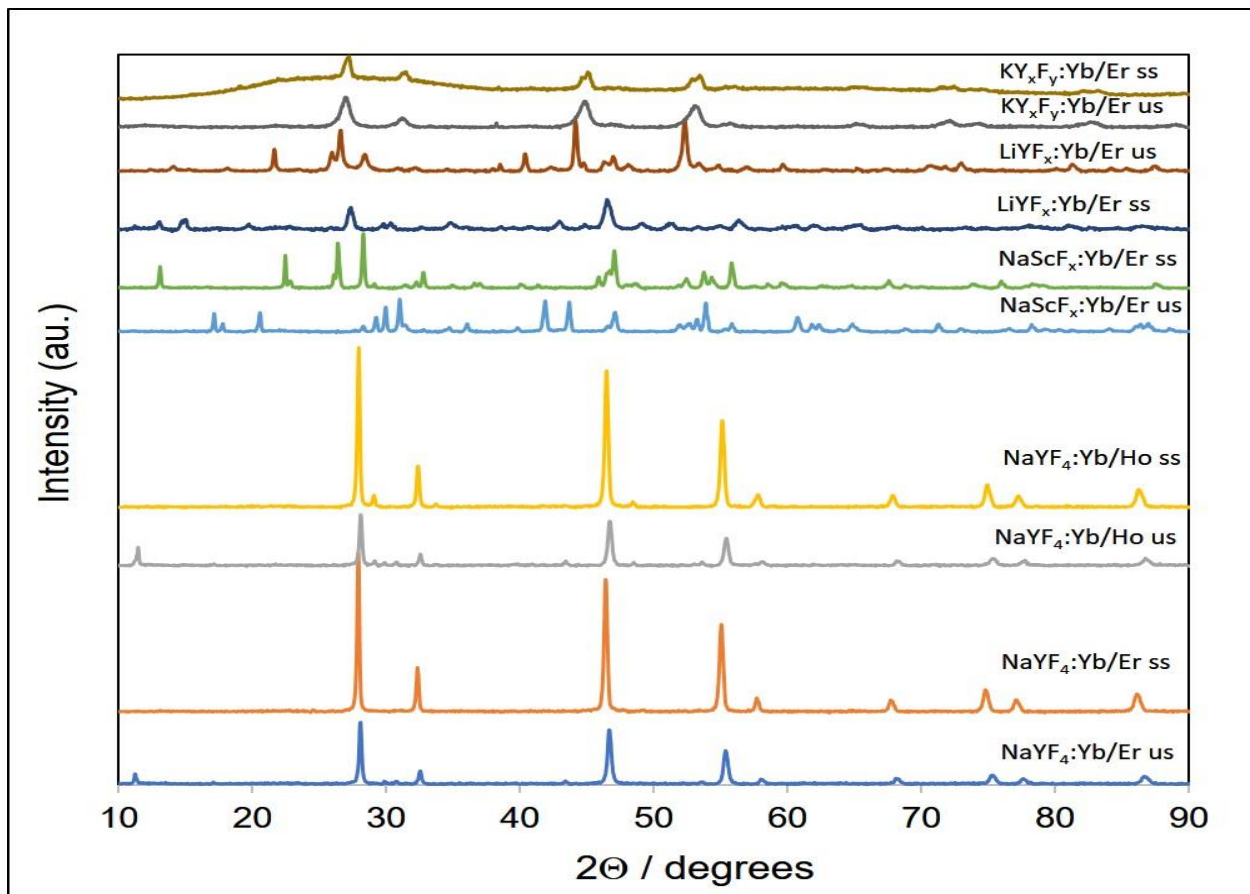


**Figure A4.11:** The XRD powder patterns obtained for the samples synthesized in this work showing the true intensities of the reflections obtained.

**Fluorescence emission data for UCNPs:**

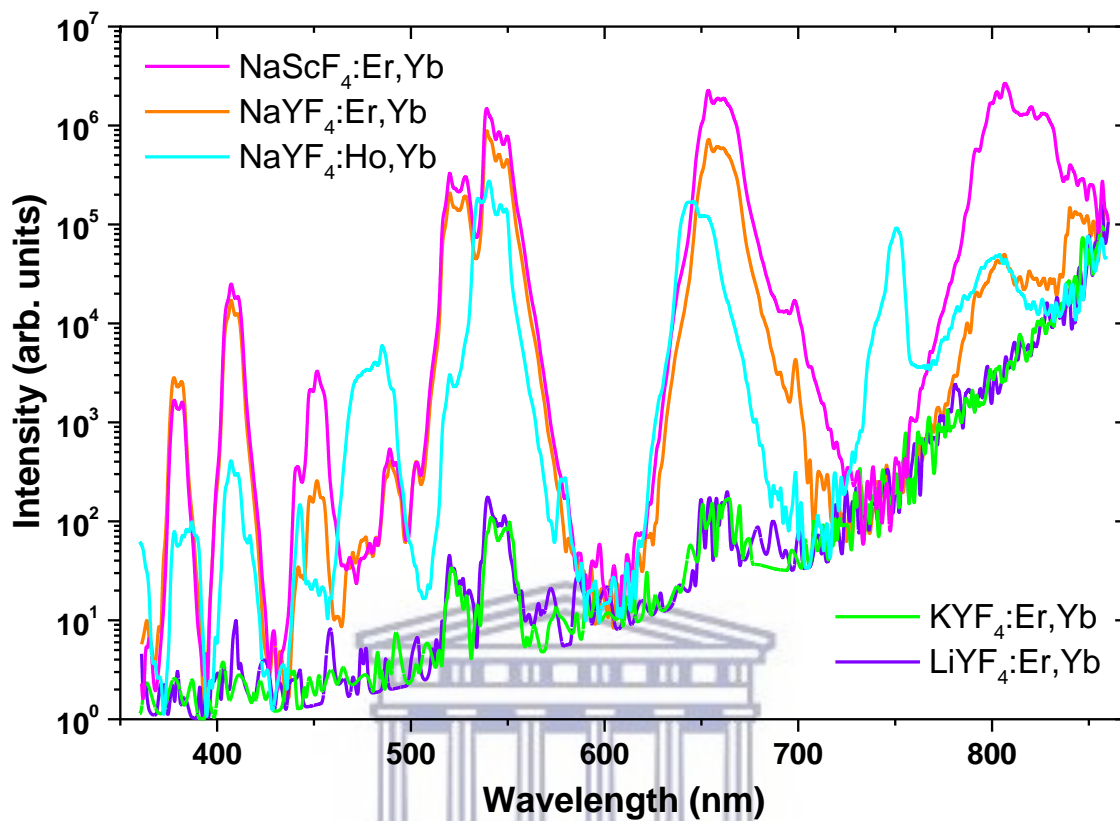


**Figure A4.12:** Upconversion luminescence spectra for all powdered UCNPs under 980 nm laser excitation. The graph is on a log-scale which enables small peaks to be identified.

UNIVERSITY OF  
WESTERN CAPE

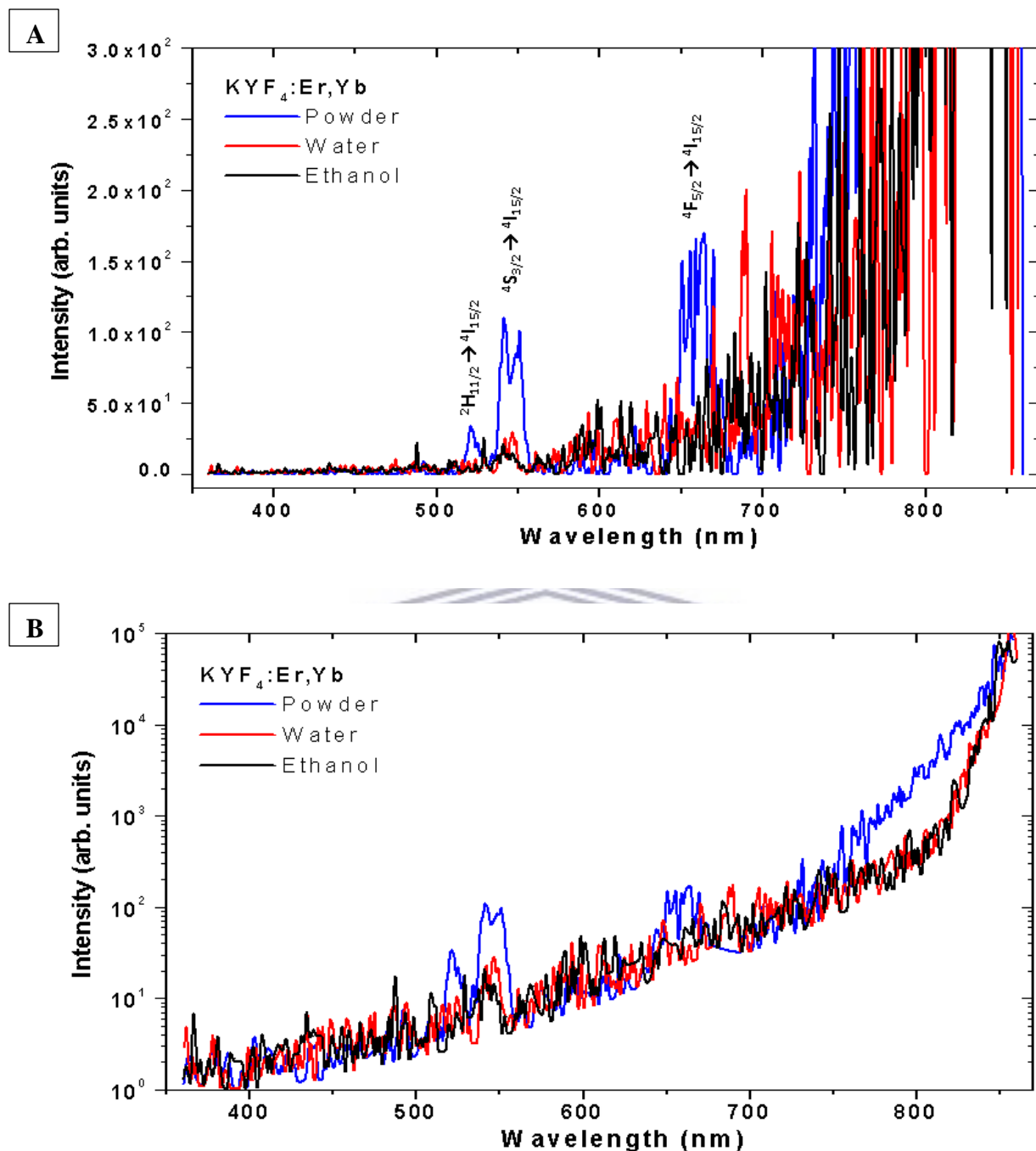


**Figure A4.13:** (A) Upconversion luminescence emission spectra of the  $\text{KY}_3\text{F}_{10}:\text{Yb/Er}$  nanoparticles synthesized in the powder form and the relevant transitions. (B) Logarithmic scaled emission spectra of the nanoparticles synthesized in the powder form.

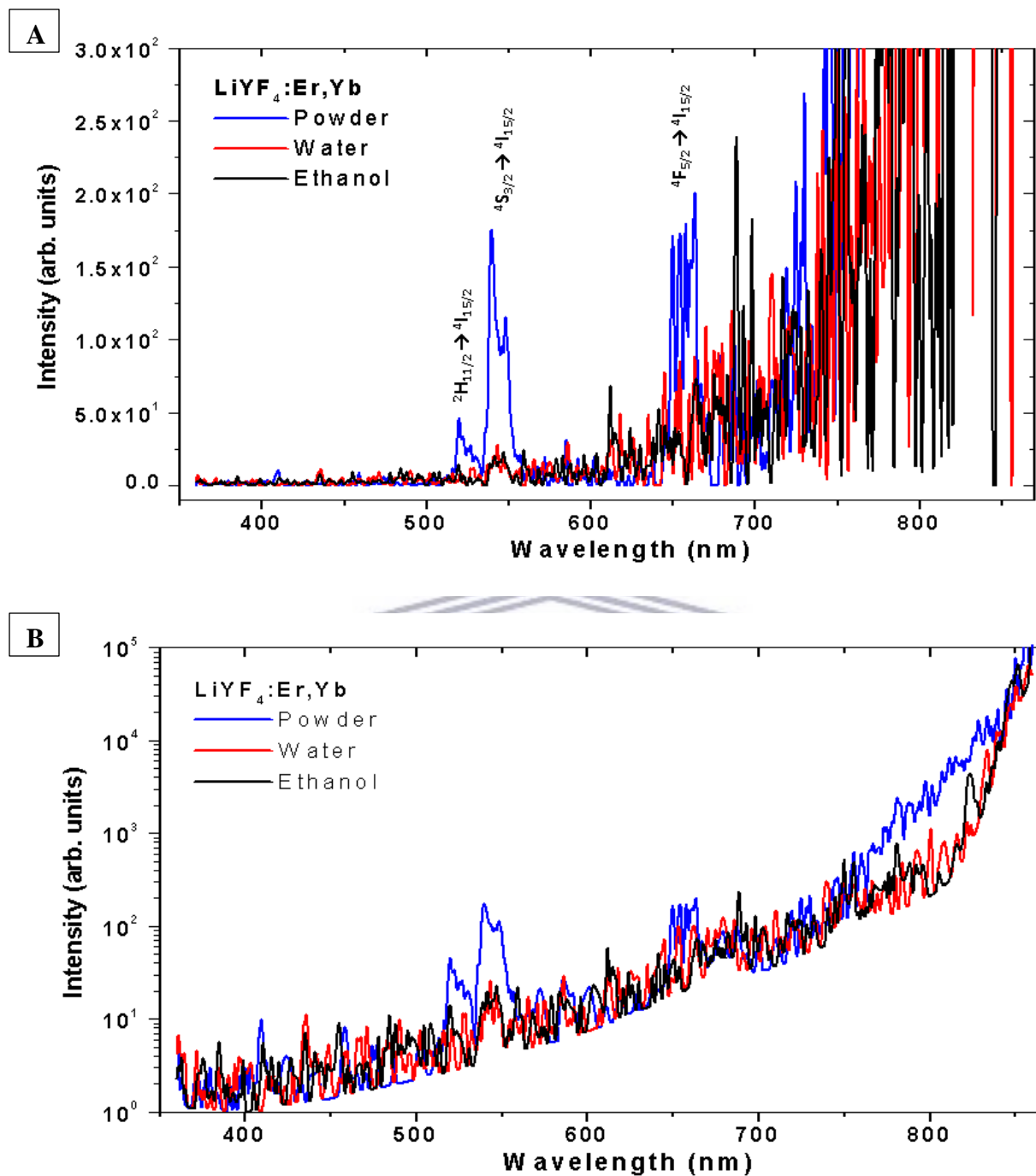


**Figure A4.14:** (A) Upconversion luminescence emission spectra of the  $\text{LiY}_x\text{F}_y:\text{Yb/Er}$  nanoparticles synthesized in the powder form and the relevant transitions. (B) Logarithmic scaled emission spectra of the nanoparticles synthesized in the powder form.



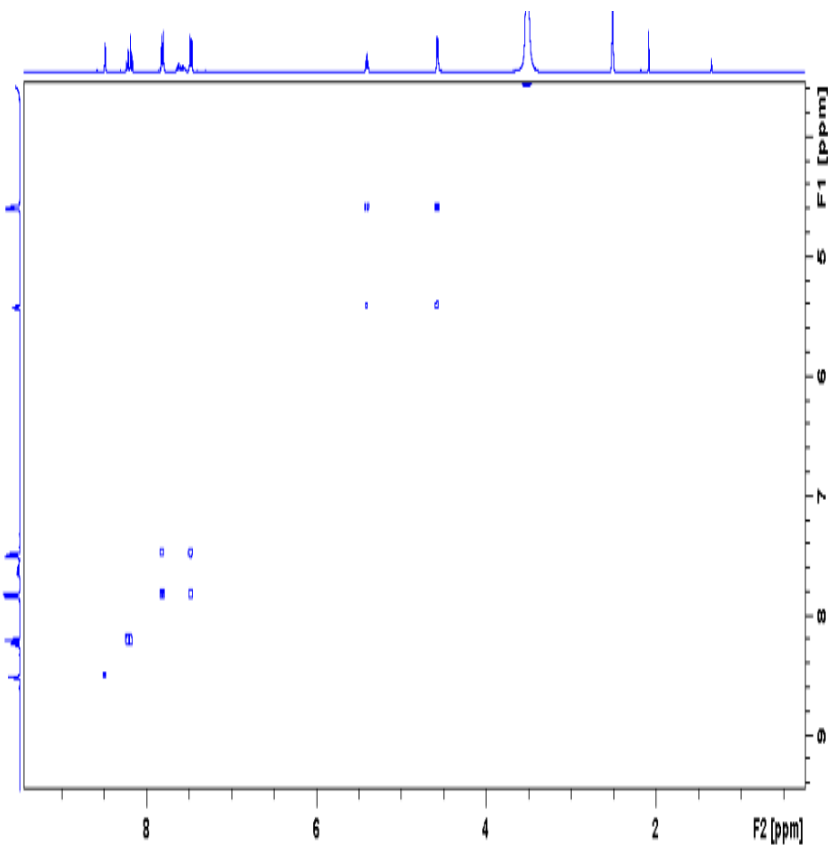
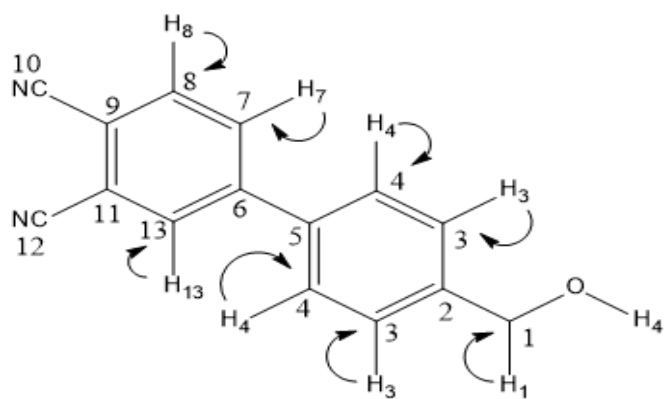


**Figure A5.1:** Cosy spectra of 4-(4-hydroxymethyl)-phthalonitrile (**3**) (400 MHz, DMSO-*d*<sub>6</sub>, 298 K).



**Scheme A5.2:** Illustration of correlating protons to the respective carbons found within the HSQC spectra (400 MHz, DMSO-*d*<sub>6</sub>, 298 K).

The HSQC spectra (in Figure A5.2, pg. 148) illustrate the protons correlating to the carbon which it is bonded to. There six protons bonded to carbons which are confirmed through the

spectra. The proton H4 (7.80 ppm) correlates to C4 (127.3 ppm). The proton H3 (7.47 ppm) correlates to C3 (127.4 ppm). The proton H1 (4.56 ppm) correlates to C1 (62.5 ppm). The proton H7 (8.21 ppm) correlates to C7 (131.6 ppm). The proton H8 (8.17 ppm) correlates to C8 (134.7 ppm). The proton H13 (8.48 ppm) correlates to C13 (131.9 ppm).

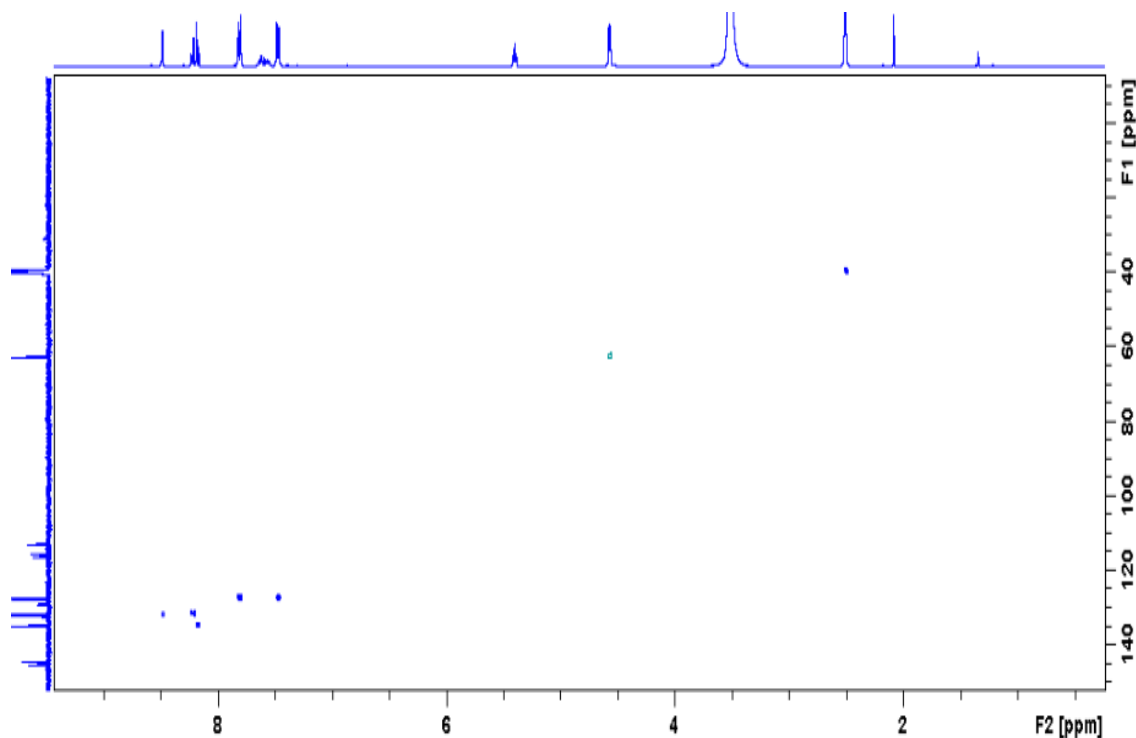


**Figure A5.2:** HSQC spectra of 4-(4-hydroxymethyl)-phthalonitrile (**3**) (400 MHz, DMSO- $d_6$ , 298 K).

The DEPT-135 spectra (in Figure A5.3, pg. 149) illustrates the non-quaternary carbons within the molecule which are either CH or CH<sub>2</sub>. The CH carbons are positive while the CH<sub>2</sub> carbons are negative within the spectra. As predicted the C1/6 – 127.3, C2/5 – 127.4, C9 -131.6, C10 - 134.7 and C13 – 131.9 are positive representing CH carbons. The negative peak represents the C4 – 62.5 which was predicted to be CH<sub>2</sub>.

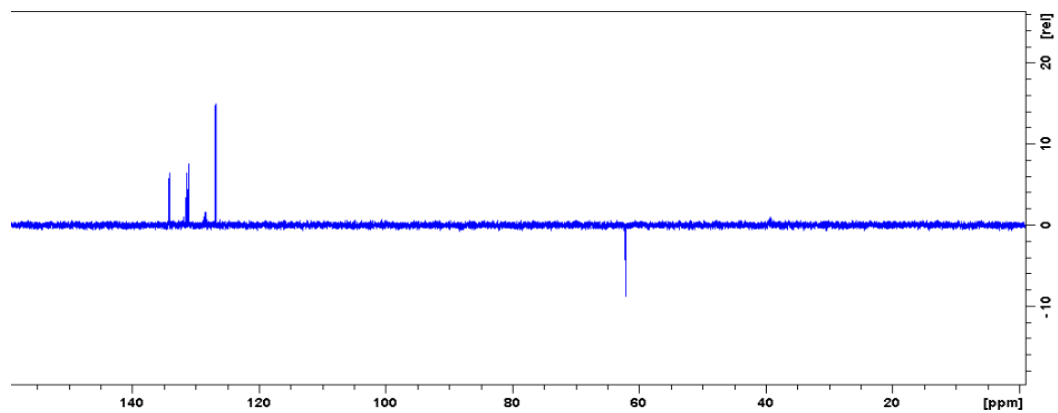


**Figure A5.3:** DEPT-135 spectra of 4-(4-hydroxymethyl)-phthalonitrile (**3**) (400 MHz, DMSO- $d_6$ , 298 K).

**UV/Visible Data:**

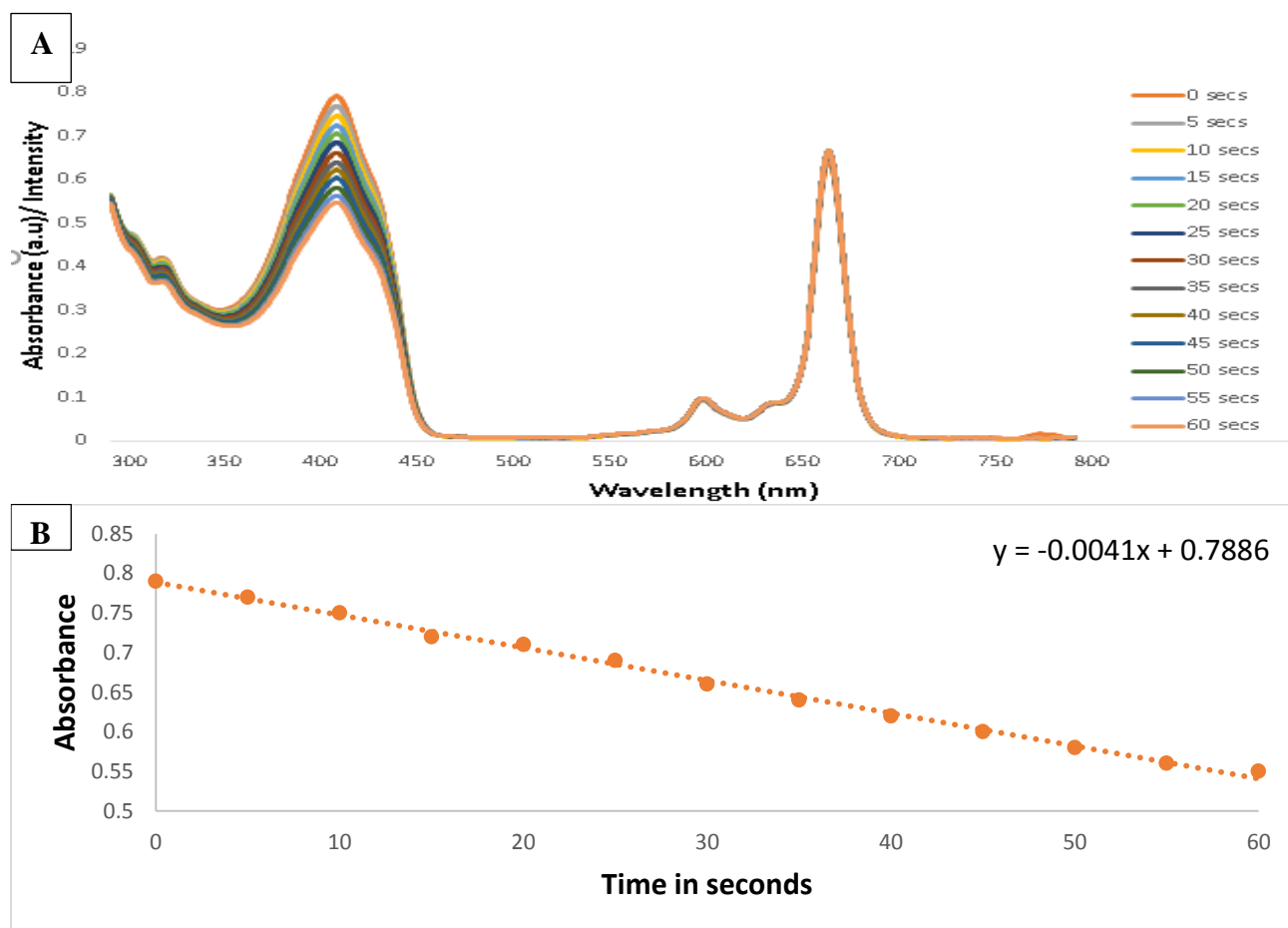
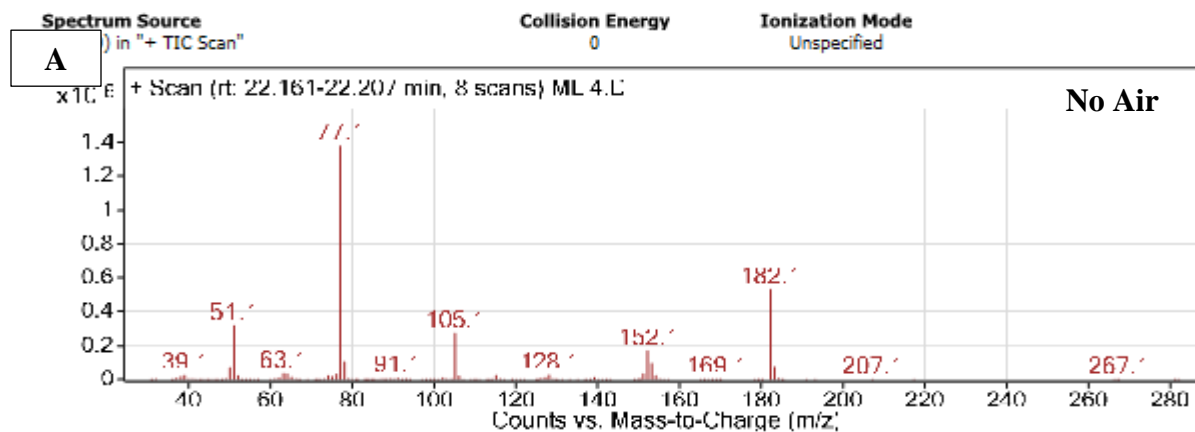


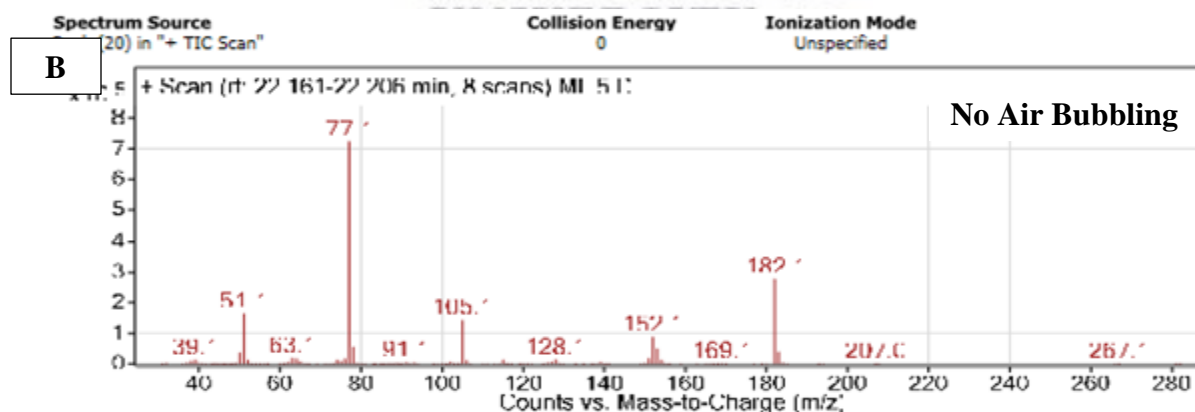
**Figure A5.4:** UV/Visible spectra for the determination of the  $R^{Std}$  in DMSO using the standard ZnPc, (complex **4**).

## GC-EIMS DATA:



### Peak List

m/z	z	Abund
50.1		69687.63
51.1		317125
63.1		34742.13
77.1	1	1377896
78.1	1	104056
105.1	1	272331
152.1		169167
153.1		94367
182.1	1	531008
183.1	1	73839.5



### Peak List

m/z	z	Abund
50.1		35223.38
51.1		162628
63.1		18054.13
77.1	1	723416
78.1	1	54482.63
105.1	1	141486
152.1		87371
153.1		48704.5
182.1	1	276588
183.1	1	38804.75

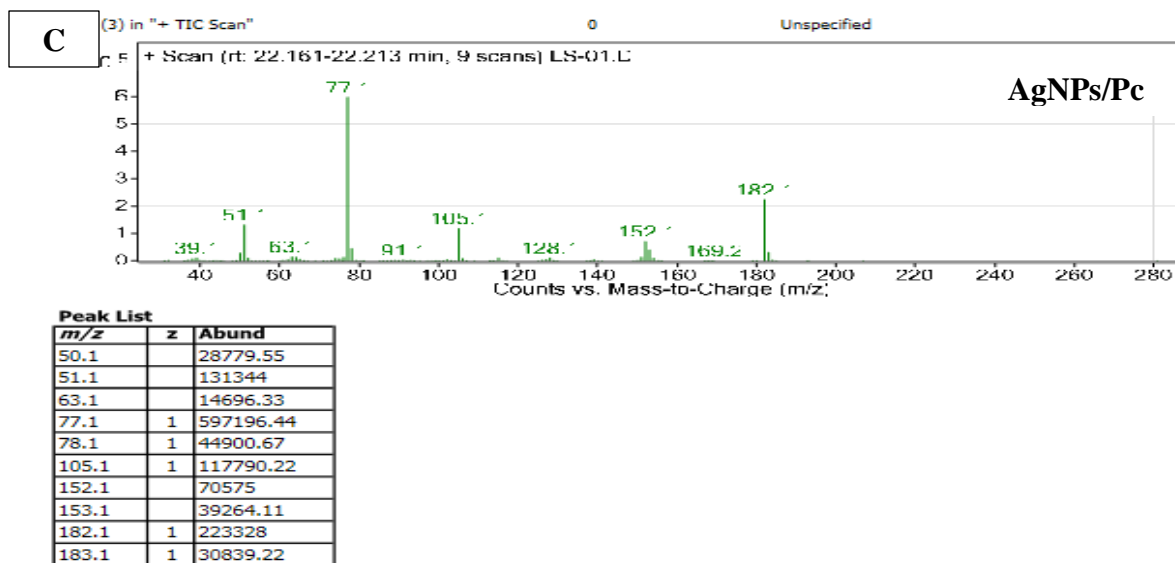
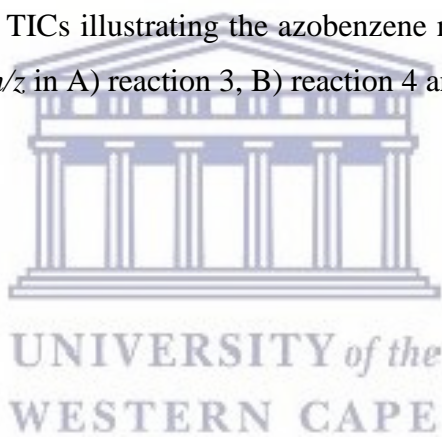


**Figure A6.1:** GC-EI MS chromatograms obtained for the catalyst reactions yielding the azobenzene molecular ion. The TICs illustrating the azobenzene molecular ion at the 22 minute time frame with a peak at 182 *m/z* in A) reaction 3, B) reaction 4 and C) with the reaction 6.



## References

- Abbas, M., Leitgeb, A., Kienberger, J. and Slugovc, C., 2013. Solvent-free synthesis of silver-nanoparticles and their use as additive in poly (dicyclopentadiene). *Chemical Society*. **35**(2), pp. 359–362.
- Ahamed, M., AlSalhi, M.S. and Siddiqui, M.K.J., 2010. Silver nanoparticle applications and human health. *Clinica Chimica Acta*. **411**(23), pp.1841–1848.
- Ai, Y., Tu, D., Zheng, W., Liu, Y., Kong, J., Hu, P., Chen, Z., Huang, M. and Chen, X., 2013. Lanthanide-doped NaScF<sub>4</sub> nanoprobes: crystal structure, optical spectroscopy and biodetection. *Nanoscale*, **5**(14), pp.6430-6438.
- Aichler, M. and Walch, A., 2014. MALDI imaging mass spectrometry: current frontiers and perspectives in pathology research and practice. *Laboratory Investigation*. **95**(4), pp. 422–431.
- Alivisatos, A.P., 1996. Semiconductor clusters, nanocrystals, and quantum dots. *Science*. **271**(5251), pp.933–937.
- Arnold, A.A., Terskikh, V., Li, Q.Y., Naccache, R., Marcotte, I. and Capobianco, J.A., 2013. Structure of NaYF<sub>4</sub> Upconverting Nanoparticles: A Multinuclear Solid-State NMR and DFT Computational Study. *The Journal of Physical Chemistry C*, **117**(48), pp.25733-25741.
- Bell, A.T., 2003. The impact of nanoscience on heterogeneous catalysis. *Science*. **299**(5613), pp.1688–1691.
- Berezin, M.Y. and Achilefu, S., 2012. Fluorescence lifetime measurements and biological imaging. *Chemical Reviews*. **110**(5), pp. 2641-2684.

Bessada, C., Rakhmatullin, A., Rollet, A.L. and Zanghi, D., 2009. High temperature NMR approach of mixtures of rare earth and alkali fluorides: An insight into the local structure. *Journal of Fluorine Chemistry*, **130**(1), pp.45-52.

Braslavsky, S.E., 2007. Glossary of terms used in photochemistry, (IUPAC Recommendations 2006). *Pure and Applied Chemistry*, **79**(3), pp.293-465.

Bréchnignac, C., Houdy, P. and Lahmani, M., 2008. *Nanomaterials and nanochemistry*. Springer Science & Business Media.

Bunzli, J.C.G., Comby, S. Chauvin, A.S and Vandevyer, C.D.B., 2007. New opportunities for lanthanide luminescence. *Journal of Rare Earths*. **25**(3), pp. 257-274.

Byrd, K.M., Subramanian, C., Sanchez, J., Motiwala, H.F., Liu, W., Cohen, M.S., Holzbeierlein, J. and Blagg, B.S., 2016. Synthesis and biological evaluation of Novobiocin core analogues as Hsp90 inhibitors. *Chemistry-A European Journal*. **22**(20), pp.6921-6931

Cai, S., Rong, H., Yu, X., Liu, X., Wang, D., He, W. and Li, Y., 2013. Room temperature activation of oxygen by monodispersed metal nanoparticles: Oxidative dehydrogenative coupling of anilines for azobenzene syntheses. *American Chemical Society Catalysis*. **3**(4), pp.478-486.

Çakır, V., Çakır, D., Göksel, M., Durmuş, M., Bıyıklıoğlu, Z. and Kantekin, H., 2015. Synthesis, photochemical, bovine serum albumin and DNA binding properties of tetrasubstituted zinc phthalocyanines and their water soluble derivatives. *Journal of Photochemistry and Photobiology A: Chemistry*, **299**(1), pp.138-151.

Calixto, G. M., Bernegossi, J., de Freitas, L. M., Fontana, C. R. and Chorilli, M., 2016. Nanotechnology-based drug delivery systems for photodynamic therapy of cancer: A Review. *Molecules*. **21**(3), pp 342.

Chen, G., Qiu, H., Prasad, P. N. and Chen, X., 2014. Upconversion nanoparticles: Design,

- nanochemistry, and applications in theranostics. *Chemical Reviews*. **114**(10), pp.5161–5214.
- Chen, J. and Zhao, J.X., 2012. Upconversion nanomaterials: Synthesis, mechanism, and applications in sensing. *Sensors*, **12**(3), pp.2414–2435.
- Chen, Z., Chen, H., Hu, H., Yu, M. and Li, F., 2008. Versatile synthesis strategy for carboxylic acid – functionalized upconverting nanophosphors as biological labels versatile synthesis strategy for carboxylic biological labels. *Journal of the American Chemical Society*. **130**(6), pp.3023–3029.
- Clennan, E.L. and Pace, A., 2005. Advances in singlet oxygen chemistry. *Tetrahedron*. **61**(28), pp.6665–6691.
- Davis, M.E., Chen, Z.G. and Shin, D.M., 2008. Nanoparticle therapeutics: An emerging treatment modality for cancer. *Nature reviews. Drug discovery*. **7**(9), pp.771–782.
- DeLuca, J.A., 1980. An introduction to luminescence in inorganic solids. *Journal of Chemical Education*. **57**(8), pp. 541-545.
- DeRosa, M.C. and Crutchley, R.J., 2002. Photosensitized singlet oxygen and its applications. *Coordination Chemistry Reviews*. **234**, pp.351–371.
- Dey, R., Sreedhar, B. and Ranu, B.C., 2010. Molecular sieves-supported palladium (II) catalyst: Suzuki coupling of chloroarenes and an easy access to useful intermediates for the synthesis of irbesartan, losartan and boscalid. *Tetrahedron*, **66**(13), pp.2301-2305.
- Dong, A., Ye, X., Chen, J., Kay, Y., Gordon, T., Kikkawa, J.M. and Murray, C.B., 2010. A generalized ligand-exchange strategy enabling sequential surface functionalization of colloidal nanocrystals. *Journal of the American Chemical Society*. **133**(4), pp.998–1006.
- Du, H., Fuh, R.C.A., Li, J., Corkan, A. and Lindsay, J.S., 1998. Technical and Software Note

PhotochemCADtt : A computer-aided design and research tool in photochemistry. *American Society of Photobiology*. **68**(2), pp.141–142.

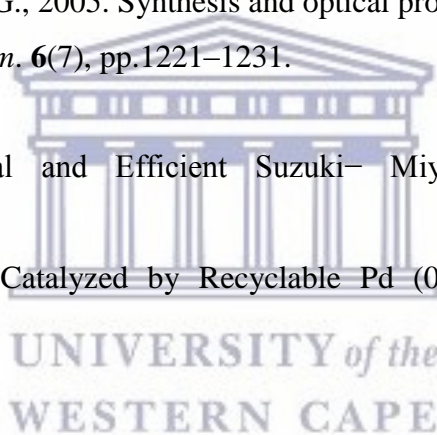
Durmuş, M., 2011. *Photosensitizers in medicine, environment, and security* (pp. 135-266). Springer Netherlands.

Eliseeva, S.V. and Bünzli, J.C.G., 2010. Lanthanide luminescence for functional materials and bio-sciences. *Chemical Society Reviews*, **39**(1), pp.189-227.

Engel, M.K. and Hokoku, K.R.K., 1997. Single-crystal and solid-state molecular structures of phthalocyanine complexes. *Porphyrin Handbook*. **20**, pp.11–54.

Evanoff, D.D. and Chumanov, G., 2005. Synthesis and optical properties of silver nanoparticles and arrays. *ChemPhysChem*. **6**(7), pp.1221–1231.

Felpin, F.X., 2005. Practical and Efficient Suzuki–Miyaura Cross-Coupling of 2-Iodocycloenones with Arylboronic Acids Catalyzed by Recyclable Pd (0)/C. *The Journal of organic chemistry*, **70**(21), pp.8575-8578.



Fenn, J.B., Mann, M., Meng, C.K., Wong, S.F. and Whitehouse, C.M., 1990. Electrospray ionization—principles and practice. *Mass Spectrometry Reviews*, **9**(1), pp.37-70.

Gainer, C.F. and Romanowski, M., 2014. A review of synthetic methods for the production of upconverting lanthanide nanoparticles. *Journal of Innovative Optical Health Sciences*. **7**(2), pp. 1–11.

Gao, W., Zheng, H., He, E., Lu, Y. and Gao, F., 2014. Luminescence investigation of Yb<sup>3+</sup>/Er<sup>3+</sup> codoped single LiYF<sub>4</sub> microparticle. *Journal of Luminescence*, **152**, pp.44-48.

González-Béjar, M., Francés-Soriano, L. and Pérez-Prieto, J., 2016. Upconversion nanoparticles

for bioimaging and regenerative medicine. *Frontiers in Bioengineering and Biotechnology*. **4**(47), pp. 1–9.

Gümrükçü, G., Karaoğlan, G. K., Erdoğmuş, A., Gül, A. and Avcıata, U., 2014. Photophysical, photochemical, and BQ quenching properties of zinc phthalocyanines with fused or interrupted extended conjugation. *Journal of Chemistry*. **2014**, pp. 1–11.

Guo, H., Qian, H., Idris, N.M. and Zhang, Y., 2010. Singlet oxygen-induced apoptosis of cancer cells using upconversion fluorescent nanoparticles as a carrier of photosensitizer. *Nanomedicine: Nanotechnology, Biology, and Medicine*. **6**(3), pp. 486-495.

Gusak, A.M., Hodaj, F. and Zaporozhets, T.V., 2011. Thermodynamics of void nucleation in nanoparticles. *Philosophical Magazine Letters*, **91**(12), pp.741-750.

Griffiths, J., 2008. A brief history of mass spectrometry. *Anal Chem*, **80**(15), pp.5678-5683.

Haase, M. and Schäfer, H., 2011. Upconverting nanoparticles. *Angewandte Chemie - International Edition*. **50**(26), pp.5808–5829.

Hao, S., Chen, G. and Yang, C. 2013. Sensing using rare-earth-doped upconversion nanoparticles. *Theranostics*. **3**(5), pp.331–345.

Heer, S., Kompe, K., Gudel, H.-U. and Haase, M., 2004. Highly efficient multicolour upconversion emission in transparent colloids of lanthanide-doped NaYF<sub>4</sub> nanocrystals. *Advanced Materials*. **16**(23-24), pp. 2102-2105.

Heer, S., Lehmann, O., Haase, M. and Güdel, H.U., 2003. Blue, green, and red upconversion emission from lanthanide-doped LuPO<sub>4</sub> and YbPO<sub>4</sub> nanocrystals in a transparent colloidal solution. *Angewandte Chemie International Edition*. **42**(27), pp.3179-3182.

Jiang, Z.J., Liu, C.Y. and Sun, L.W., 2005. Catalytic properties of silver nanoparticles supported

on silica spheres. *The Journal of Physical Chemistry*. **109**(5), pp.1730–1735.

Joshi, M., Bhattacharyya, A. and Ali, S.W., 2008. Characterization techniques for nanotechnology applications in textiles. *Indian Journal of Fibre and Textile Research*. **33**(3), pp.304–317.

Kasha, B.Y.M., 1950. Characterization of electronic transitions in complex molecules. *Discussions of the Faraday Society*. **9**, pp.14–19.

Kadish, K.M., Smith, K.M. and Guilard, R., 2000. *The Porphyrin Handbook: Inorganic, organometallic and coordination chemistry* (Vol. 3). Elsevier.

Keat, C. L., Aziz, A., Eid, A. M. and Elmarzugi, N. A., 2015. Biosynthesis of nanoparticles and silver nanoparticles. *Bioresources and Bioprocessing*. **2**(1), pp.47.

Kelly, K.L., Coronado, E., Zhao, L.L and Schatz, G.G., 2003. The optical properties of metal nanoparticles: the influence of size, shape, and dielectric moment. *Journal of Physical Chemistry*. **107**(3): pp. 668-677.

Klier, D.T. and Kumke, M.U., 2015. Analysing the effect of the crystal structure on upconversion luminescence in Yb<sup>3+</sup>, Er<sup>3+</sup>-co-doped NaYF<sub>4</sub> nanomaterials. *Journal of Materials Chemistry C*, **3**(42), pp.11228-11238.

Kobayashi, N., Ogata, H., Nonaka, N. & Luk, E. A., 2003. Effect of peripheral substitution on the electronic absorption and fluorescence spectra of metal-free and zinc phthalocyanines. *Chemistry-A European Journal*. **9**(20), pp. 5123-5134.

Kuznetsova, N.A., Gretsova, N.S., Kalmykova, E.A., Makarova, E.A., Dashkevich, S.N., Negrimovskii, V.M., Kaliya, O.L. and Luk'yanets, E.A., 2000. Relationship between the photochemical properties and structure of pophyrins and related compounds. *Russian Journal of General Chemistry*, **70**(1), pp.133-140.

- Lakowicz, J.R., 2006. *Principles of fluorescence spectroscopy*. Springer.
- Langford, J.I., Louër, D. and Scardi, P., 2000. Effect of a crystallite size distribution on X-ray diffraction line profiles and whole-powder-pattern fitting. *Journal of Applied Crystallography*, **33**(3), pp.964-974.
- Laws, D., Bitter, H.L. and Jerschow, A., 2002. Solid-State NMR spectroscopic methods in chemistry. *Angewandte Chemie (International ed. in English)*. **41**, pp.3096–3129.
- Li, Z., Zhang, Y. and Jiang, S., 2008. Multicolor core/shell-structured upconversion fluorescent nanoparticles. *Advanced Materials*. **20**(24), pp.4765–4769.
- Liang, Z., Zhao, S., Xu, Z., Qiao, B., Yang, Y., Zhu, W. and Xu, X., 2016. Controllable synthesis of tetragonal LiScF<sub>4</sub>:Yb<sup>3+</sup>, Er<sup>3+</sup> nanocrystals and its upconversion photoluminescence properties. *Optical Materials*, **62**, pp.255-260.
- Lichtman, J.W. and Conchello, J., 2009. Fluorescence microscopy. *Nature Methods*. **2**(12), pp.1–60.
- Lin, M., Zhao, Y., Wang, S.-Q. Liu, M., Duan, Z.-F. Chen, Y.-M., Li, F. Xu, F. and Lu, T.J., 2012, Recent advances in synthesis and surface modification of lanthanide-doped upconversion nanoparticles for biomedical applications. *Biotechnology Advances*. **30**(6): pp. 1551-1561.
- Lin, P. C., Lin, S., Wang, P. C. and Sridhar, R., 2014. Techniques for physicochemical characterization of nanomaterials. *Biotechnology Advances*. **32**(4), pp.711–726.
- Liu, Q., Guo, B., Rao, Z., Zhang, B. and Gong, J.R., 2013. Strong two-photon-induced fluorescence from photostable, biocompatible nitrogen-doped graphene quantum dots for cellular and deep-tissue imaging. *Nano Letters*. **13**(6): p. 2436-2441.

- Liu, X., Zhao, J., Sun, Y., Song, K., Yu, Y., Du, C., Kong, X. and Zhang, H., 2009. Ionothermal synthesis of hexagonal-phase  $\text{NaYF}_4:\text{Yb}^{3+},\text{Er}^{3+}/\text{Tm}^{3+}$  upconversion nanophosphors. *Chemical Communications*. **43**, pp.6628.
- Luykx, D.M., Peters, R.J., van Ruth, S.M. and Bouwmeester, H., 2008. A review of analytical methods for the identification and characterization of nano delivery systems in food. *Journal of agricultural and food chemistry*. **56**(18), pp.8231–8247.
- Mahalingam, V., Vetrone, F., Naccache, R., Speghini, A. and Capobianco, J.A., 2009. Colloidal  $\text{Tm}^{3+}/\text{Yb}^{3+}$ -doped  $\text{LiYF}_4$  nanocrystals: multiple luminescence spanning the UV to NIR regions via low-energy excitation. *Advanced Materials*. **21**(40), pp.4025-4028.
- Mi, C., Tian, Z., Cao, C., Wang, Z., Mao, C. and Xu, S., 2011. Novel microwave-assisted solvothermal synthesis of  $\text{NaYF}_4:\text{Yb},\text{Er}$  upconversion nanoparticles and their application in cancer cell imaging. *Langmuir*. **27**(23), pp.14632–14637.
- Mitsudome, T., Noujima, A., Mikami, Y., Mizugaki, T., Jitsukawa, K. and Kaneda, K., 2010. Supported gold and silver nanoparticles for catalytic deoxygenation of epoxides into alkenes. *Angewandte Chemie*. **122**(32), pp.5677-5680.
- Monshi, A., Foroughi, M.R. and Monshi, M.R., 2012. Modified Scherrer equation to estimate more accurately nano-crystallite size using XRD. *World Journal of Nano Science and Engineering*, **2**(3), pp.154-160.
- Morones, J.R., Elechiguerra, J.L., Camacho, A., Holt, K., Kouri, J.B., Ramírez, J.T. and Yacaman, M.J., 2005. The bactericidal effect of silver nanoparticles. *Nanotechnology*. **16**(10), pp.2346–2353.
- Muto, S. and Tatsumi, K., 2016. Detection of local chemical states of lithium and their spatial mapping by scanning transmission electron microscopy, electron energy-loss spectroscopy and hyperspectral image analysis. *Microscopy*, **66**(1), pp.39-49.

Na, H.B., Song, I.C. and Hyeon, T., 2009. Inorganic nanoparticles for MRI contrast agents. *Advanced Materials*. **21**(21), pp.2133–2148.

Nombona, N., Maduray, K., Antunes, E., Karsten, A. and Nyokong, T., 2012. Synthesis of phthalocyanine conjugates with gold nanoparticles and liposomes for photodynamic therapy. *Journal of Photochemistry and Photobiology B: Biology*. **107**, pp.35-44.

Ogilby, P.R. and Foote, C.S., 1983. Chemistry of singlet oxygen. 42. Effect of solvent, solvent isotopic substitution, and temperature on the lifetime of singlet molecular oxygen. *Journal of the American Chemical Society*, **105**(11), pp.3423-3430.

Olesik, J.W., 1991. Elemental analysis using ICP-OES and ICP/MS. *Analytical Chemistry*. **63**(1), pp.12A-21A.

Pang, M., Zhai, X., Feng, J., Song, S., Deng, R., Wang, Z., Yao, S., Ge, X. and Zhang, H., 2014. One-step synthesis of water-soluble hexagonal NaScF<sub>4</sub>:Yb/Er nanocrystals with intense red emission. *Dalton Transactions*, **43**(26), pp.10202-10207.

Petritsch, K., Dittmer, J.J., Marseglia, E.A., Friend, R.H., Lux, A., Rozenberg, G.G., Moratti, S.C. and Holmes, A.B., 2000. Dye-based donor/acceptor solar cells. *Solar energy materials and solar cells*, **61**(1), pp.63-72.

<http://www.photochemcad.com/pages/chemcad/chem-home.html>

Plohl, O., Majaron, B., Ponikvar-Svet, M., Makovec, D. and Lisjak, D., 2015. Influence of the synthesis parameters on the properties of NaYF<sub>4</sub>:Yb<sup>3+</sup>,Tm<sup>3+</sup> nanoparticles. *Acta Chimica Slovenica*. **62**(4), pp.789–795.

Poole Jr, C.P. and Owens, F.J., 2003. *Introduction to nanotechnology*. John Wiley & Sons.

Prabhu, S. and Poulouse, E.K., 2012. Silver nanoparticles: mechanism of antimicrobial action,

- synthesis, medical applications, and toxicity effects. *International Nano Letters*. **2**(1), pp.32.
- Qin, X., Yokomori, T. and Ju, Y., 2007. Flame synthesis and characterization of rare-earth ( $\text{Er}^{3+}$ ,  $\text{Ho}^{3+}$ , and  $\text{Tm}^{3+}$ ) doped upconversion nanophosphors. *Applied Physics Letters*. **90**(7), pp. 21 - 23.
- Rai, M., Yadav, A. and Gade, A., 2009. Silver nanoparticles as a new generation of antimicrobials. *Biotechnology Advances*. **27**(1), pp.76–83.
- Rapulenyane, N., Antunes, E., Masilela, N. and Nyokong, T., 2012. Synthesis and photophysical properties of novel zinc phthalocyanines mono substituted with carboxyl containing functional groups. *Journal of Photochemistry and Photobiology A: Chemistry*. **250**, pp.18-24.
- Rapulenyane, N., Antunes, E. and Nyokong, T., 2013. A study of the photophysical and antimicrobial properties of two zinc phthalocyanine–silver nanoparticle conjugates. *New Journal of Chemistry*. **37**(4), pp.1216-1223.
- Ronda, C.R., 2008. *Luminescence: from theory to applications*. John Wiley & Sons.
- Ronda, C.R., Justel, T. and Nikol, H., 1998. Rare earth phosphors: fundamentals and applications. *Journal of Alloys and Compounds*. **275**, pp. 669-676.
- Sakamoto, K. and Ohno-Okumura, E., 2009. Syntheses and functional properties of phthalocyanines. *Materials*. **2**(3), pp.1127–1179.
- Schwartz, E., Blazewicz, S., Doucett, R., Hungate, B.A., Hart, S.C. and Dijkstra, P., 2007. Natural abundance  $\delta^{15}\text{N}$  and  $\delta^{13}\text{C}$  of DNA extracted from soil. *Soil Biology and Biochemistry*. **39**(12), pp.3101–3107.
- Sekkat, N., Bergh, H.v.d., Nyokong, T and Lange, N., 2012. Like a bolt from the blue: phthalocyanines in biomedical optics. *Molecules*. **17**, pp. 98-144.

- Snow, A.W. and Griffith, J.R., 1984. Syntheses and characterization of heteroatom-bridged metal-free phthalocyanine network polymers and model compounds. *Macromolecules*. **17**(8), pp.1614–1624.
- Sorokin, A.B., 2013. Phthalocyanine metal complexes in catalysis. *Chemical Reviews*. **113**(10), pp.8152–8191.
- Stillman, M.J., Nyokong, T., Leznoff, In Phthalocyanines: properties and applications, eds. C.C. and Lever, A.B.P., 1989. Phthalocyanines: properties and applications. C.C Leznoff, A.B.P Lever, VCH Publishers, New York, Vol 1, p.133.
- Sun, Y., Peng, J., Feng, W. and Li, F., 2013. Upconversion nanophosphors NaLuF<sub>4</sub>: Yb,Tm for lymphatic imaging *in vivo* by real-time upconversion luminescence imaging under ambient light and high-resolution X-ray CT. *Theranostics*. **3**(5), pp.346–353.
- Suyver, J.F., Grimm, J., Krämer, K.W. and Güdel, H.U., 2005. Highly efficient near-infrared to visible up-conversion process in NaYF<sub>4</sub>: Er<sup>3+</sup>, Yb<sup>3+</sup>. *Journal of luminescence*, **114**(1), pp.53-59.
- Thompson, J.A., Murata, K., Miller, D.C., Stanton, J.L., Broderick, W.E., Hoffman, B.M. and Ibers, J.A., 1993. Synthesis of high-purity phthalocyanines (pc): High intrinsic conductivities in the molecular conductors H<sub>2</sub> (pc) I and Ni (pc) I. *Inorganic Chemistry*. **32**(16), pp.3546-3553.
- Torres, G.D.L., Vazquez, P., Agullo-Lopez, F. and Torres, T., 1998. Phthalocyanines and related compounds: organic targets for nonlinear optical applications. *Journal of Materials Chemistry*. **8**(8): p. 1671-1683.
- Uchida, H., Reddy, P.Y., Nakamura, S. and Toru, T., 2003. Novel efficient preparative method for phthalocyanines from phthalimides and phthalic anhydride with HMDS. *The Journal of organic chemistry*. **68**(22), pp.8736-8738.

- Valeur, B. and Berberan-Santos, M.N., 2012. *Molecular fluorescence: principles and applications*. John Wiley & Sons.
- Walch, A., Rauser, S., Deininger, S.O. and Höfler, H., 2008. MALDI imaging mass spectrometry for direct tissue analysis: A new frontier for molecular histology. *Histochemistry and Cell Biology*. **130**(3), pp.421–434.
- Wang, F., Banerjee, D., Liu, Y., Chen, X. and Liu, X., 2010. Upconversion nanoparticles in biological labeling, imaging, and therapy. *The Analyst*. **135**(8), p.1839.
- Wang, F. and Liu, X., 2009. Recent advances in the chemistry of lanthanide-doped upconversion nanocrystals. *Chemical Society Reviews*. **38**, pp. 976-989.
- Wang, H.Q., Tilley, R.D. and Nann, T., 2010. Size and shape evolution of upconverting nanoparticles using microwave assisted synthesis. *CrystEngComm*. **12**(7), pp.1993.
- Wang, L. and Li, Y., 2007. Controlled synthesis and luminescence of lanthanide doped NaYF<sub>4</sub> Nanocrystals. *Chemistry of Materials*. **19**(4), pp.727–734.
- Wang, M., Abbineni, G., Clevenger, A., Mao, C. and Xu, S., 2011. Upconversion nanoparticles: synthesis, surface modification and biological applications. *Nanomedicine: Nanotechnology, Biology and Medicine*. **7**(6), pp.710-729
- Watrous, J.D., Alexandrov, T. and Dorrestein, P.C., 2011. The evolving field of imaging mass spectrometry and its impact on future biological research. *Journal of Mass Spectrometry*. **46**(2), pp.209–222.
- Whitesides, G. M., 2005. Nanoscience, nanotechnology, and chemistry. *Small*. **1**(2): p. 172–179.
- Wilhelm, S., Kaiser, M., Würth, C., Heiland, J., Carrillo-Carrion, C., Muhr, V., Wolfbeis, O.S., Parak, W.J., Resch-Genger, U. and Hirsch, T., 2015. Water dispersible upconverting

nanoparticles: effects of surface modification on their luminescence and colloidal stability. *Nanoscale*. **7**(4), pp.1403–1410.

Wöhrle, D., Schnurpfeil, G., Makarov, S.G., Kazarin, A. and Suvorova, O.N., 2012. Practical applications of phthalocyanines—from dyes and pigments to materials for optical, electronic and photo-electronic devices. *Macroheterocycles*. **5**(3), pp.191–202.

Xia, Y., Yang, H. and Campbell, C.T., 2013. Nanoparticles for catalysis. *Accounts of Chemical Research*. **46**(8), pp.1671–1672.

Yan, F.Y., Liu, D.Q., Sima, L.F., SHI, H. and HU, X., 2008. Boscalid, a novel carboxamide aka anilide class of fungicides. *PESTICIDES-SHENYANG-*, **47**(2), p.132.

Yang, C.Q., Li, A.J., Guo, W., Tian, P.H., Yu, X.L., Liu, Z.X., Cao, Y. and Sun, Z.L., 2016. Paramagnetism and improved upconversion luminescence properties of NaYF<sub>4</sub>: Yb, Er/NaGdF<sub>4</sub> nanocomposites synthesized by a boiling water seed-mediated route. *Frontiers of Materials Science*, **10**(1), pp.38-44.

Yanık, H., Al-Raqa, S.Y., Aljuhani, A. and Durmuş, M., 2016. The synthesis of novel directly conjugated zinc(II) phthalocyanine *via* palladium-catalyzed Suzuki–Miyaura cross-coupling reaction and its quaternized water-soluble derivative: Investigation of photophysical and photochemical properties. *Dyes and Pigments*. **134**, pp.531–540.

Yi, G., Sun, B., Yang, F., Chen, D., Zhou, Y. and Cheng, J., 2002. Synthesis and characterization of high-efficiency nanocrystal up-conversion phosphors: Ytterbium and erbium codoped lanthanum molybdate. *Chemistry of Materials*. **14**(7), pp.2910–2914.

Zeng, Q., Xue, B., Zhang, Y., Wang, D., Liu, X., Tu, L., Zhao, H., Kong, X. and Zhang, H., 2013. Facile synthesis of NaYF<sub>4</sub>: Yb, Ln/NaYF<sub>4</sub>: Yb core/shell upconversion nanoparticles *via* successive ion layer adsorption and one-pot reaction technique. *CrystEngComm*, **15**(23), pp.4765-4772.

Zhou, B., Shi, B., Jin, D. and Liu, X., 2015. Controlling upconversion nanocrystals for emerging applications. *Nature nanotechnology*. **10**(11), pp.924-936

Zhou, J., Sun, Y., Du, X., Xiong, L., Hu, H. and Li, F., 2010. Dual-modality *in vivo* imaging using rare-earth nanocrystals with near-infrared to near-infrared (NIR-to-NIR) upconversion luminescence and magnetic resonance properties. *Biomaterials*. **31**(12), pp.3287–3295.



UNIVERSITY *of the*  
WESTERN CAPE